

ON-SURFACE SYNTHESIS OF ORGANOMETALLIC AND CARBON- BASED NANOSTRUCTURES IN ULTRAHIGH VACUUM

Par
Penghui Ji

Thèse présentée pour l'obtention du grade de
Philosophiae Doctor (Ph.D.)
en Sciences de l'énergie et des matériaux

Jury d'évaluation

Président du jury et
examinateur interne

Emanuele Orgiu
INRS-EMT

Examinateur externe

Louis Cuccia
Département de chimie et biochimie
Concordia University

Examinateur externe

Antonella Badia
Département de chimie
Université de Montréal

Directeur de recherche

Federico Rosei
INRS-EMT

Codirecteur de recherche

Lifeng Chi
Soochow University

Acknowledgements

First of all, I would thank Prof. Federico Rosei and Prof. Lifeng Chi, they offer me the opportunity to start this Ph.D. and to unfold my academical career. I feel so fortunate that my Ph.D. can be supervised by these two experts in surface science. I also feel so grateful to get their guidance in the initial stages of my academical career, which will definitely be a big fortune in my future work. As my co-supervisors, they encouraged me to have my own idea and gave me a lot of scientific freedom to verify these ideas. In the process of my projects, I can always receive their sufficient support, patience and trust when my projects faced any kind of difficulty.

Since I'm a joint Ph.D. student, I had the chance to work at INRS and FUNSOM (Soochow university). At INRS, I would firstly thank Oliver who had involved almost every detail in my work. He spent lots of time to conduct theoretical works, correct my papers and help me a lot in the English writing, etc. In addition, I would thank Maryam, Gianluca, Fabrizio, Daling, Dominik and Lei Jin for their kindness in training me or helping me adapt the life at INRS and in Montreal. They are always glad to share me with their experiences and provide valuable suggestions to my research. As well, I would thank all the other members in NanoFemtoLAB. At Soochow university, I would thank Haiming and Kewei who brought me to the world of science and taught me experiment skills hand by hand. I would also thank Junjie, Xiaodong, Yajun, Qigang, Biao, Zhongmiao, Xuechao and Yanning who accompany me in the life at Soochow university.

During my lifetime, friends always play a critical role. When my project proceeded slowly and the experiment didn't go as smooth as expected, my friends (both in China and new friends in Montreal) were always glad to hear me and showed their great encouragements to me. They will appear whenever I feel depressed. It is them who help me insist to accomplish all the projects and finish the degree.

I would show a big thank you to My family, especially to my parents. 5 years are not a short time, they never questioned me if it is worthy to spend such a long time to finish a degree. They showed their great love, firm support and trust to me without any reservation and any consideration.

In the end, I would thank all who helped and influenced me in my growth,

TABLE OF CONTENTS

List of figures	xi
List of table	xvii
List of equations.....	xviii
Chapter 1. Introduction	21
1.1 On-surface chemical reactions in UHV	21
1.2 Surface-confined Ullmann-type coupling.....	26
1.3 The effects of externally introduced co-adsorbates on surface-confined reaction.....	33
1.4 Thesis objectives and organization	46
Chapter 2. Experimental methods and techniques	49
2.1 Scanning tunneling microscopy	49
2.2 Scanning tunneling spectroscopy.....	53
2.3 Single-crystal surfaces	56
2.4 X-ray photoelectron spectroscopy	58
Chapter 3. Oxygen-Induced 1D to 2D Transformation of On-Surface Organometallic Structures	63
3.1 Introduction.....	63
3.2 Results and Discussions	66
3.2.1 OM structural transformation achieved by introducing DBTP and O ₂ on Cu(111).....	66
3.2.2 Size and symmetry controlling by using shorter precursor dBB and adjusting the substrates with Cu(111) and Cu(100)	73
3.3 Conclusions.....	78
3.4 Experimental and Theoretical Methods	79
Chapter 4. Oxygen-Promoted Synthesis of Armchair Graphene Nanoribbons on Cu(111).....	81
4.1 Introduction.....	81
4.2 Results and Discussions	83
4.2.1 The synthesis of 3P sub-family AGNRs on Cu(111).....	83
4.2.2 The effects of oxygen on the synthesis of 3P sub-family AGNRs on Cu(111).....	86

4.2.3	STS measurements of 3P sub-family AGNRs on Au(111) & Cu(111)	93
4.3	Conclusions.....	98
4.4	Experimental and Theoretical Methods	99
Chapter 5.	Tandem Desulfurization/C-C Coupling Reaction of Tetrathienylbenzenes on Cu(111): Synthesis of Pentacene and an Exotic Ladder Polymer	101
5.1	Introduction.....	102
5.2	Results and Discussions	103
5.2.1	Synthesis of pentacene on Cu(111) with T1TB	104
5.2.2	Synthesis of ladder polymer on Cu(111) with T2TB.....	106
5.3	Conclusions.....	114
5.4	Experimental and Theoretical Methods	114
Chapter 6.	Conclusions and Future Plans	117
6.1	Conclusions.....	117
6.2	Steering the formation of 2DCPs with 2DOM network templating	118
6.3	Chiral transfer from 2DOM networks to 2DCPs	120
6.4	Surface-confined reactions of molecules functionalized with thiophene groups.....	120
Résumé:	Synthèse en surface de nanostructures organométalliques et carbonées sous ultravide	123
References.....		154
APPENDIX.....		170

RÉSUMÉ

Les nanomatériaux à base de carbone de faible dimension ont attiré une grande attention en raison de leurs propriétés attrayantes, notamment des bandes interdites accordables et des mobilités de porteurs de charge élevées. Au cours des dernières décennies, la synthèse en surface a été identifiée comme une stratégie prometteuse pour produire des nanomatériaux de faible dimension avec la structure et les propriétés ciblées. Dans cette thèse, nous avons étudié la synthèse en surface en utilisant le microscope à effet tunnel et la spectroscopie photoélectronique à rayons X, soutenue par des calculs et des simulations de la théorie fonctionnelle de la densité.

En raison de sa polyvalence dans la synthèse de polymères conjugués atomiquement précis, le couplage de type Ullmann a été l'une des réactions de surface les plus étudiées. Le dépôt d'halogénures d'aryle sur Cu(111) entraîne la formation d'un intermédiaire organométallique (OM), qui peut ensuite se transformer en polymères couplés C-C après chauffage. Cependant, seuls quelques travaux ont examiné les influences de co-adsorbats supplémentaires sur le couplage de type Ullmann. Par conséquent, l'un de nos objectifs est d'étudier les effets de l'oxygène co-adsorbé sur le couplage de type Ullmann confiné en surface. En introduisant de l'oxygène chimisorbé avant ou après le dépôt de 4,4'-dibromo-p-terphényle sur Cu(111), au lieu de la formation de polymère unidimensionnel (1D) en l'absence d'oxygène, les chaînes OM formées se transforment en réseaux OM bidimensionnels (2DOM), où les clusters Cu-O en tant que nœuds connectent les segments OM. La même transformation en réseaux 2DOM mais avec des unités répétitives plus petites peut être réalisée avec un précurseur plus court, le 1,4-dibromobenzène. De plus, nous avons étudié les effets de la symétrie du substrat sur cette transformation structurelle sur Cu(100) symétrique quadruple. En conséquence, la taille et la symétrie des réseaux 2DOM peuvent être ajustées de manière flexible, illustrant une technique de modélisation de surface polyvalente avec des applications potentielles dans la chimie hôte-invité.

En tant que principal exemple de nanomatériaux de carbone accessibles par couplage de type Ullmann, les nanorubans de graphène (GNRs) ont gagné en popularité en raison de leurs applications potentielles dans les dispositifs à semi-conducteurs et la spintronique. Ici, nous avons réalisé la synthèse de GNR à bords de fauteuil (AGNRs) par cyclodéshydrogénéation latérale de poly-para-phénylène (3-AGNR) sur

Cu(111). Inspirés par l'effet de l'oxygène sur l'activation de C-H, nous avons introduit de l'oxygène avant la cyclodéshydrogénéation latérale du 3-AGNR. Cela a permis à la fusion latérale de se produire à une température inférieure de 180 K, mettant en évidence un effet catalytique prometteur de l'oxygène.

Au-delà des GNR, nous avons exploré de nouvelles méthodes pour synthétiser différentes nanostructures à base de carbone. Nous avons utilisé la réaction de désulfuration des dérivés du thiophène pour synthétiser des polymères pi-conjugués et des acènes, qui peuvent être considérés comme les GNR à bords en zigzag les plus étroits. Nous avons démontré la formation de pentacène par désulfuration et cyclisation intramoléculaire du tétrathiénylbenzène sur Cu(111). Cependant, le nonacène ne se forme pas par cyclisation intramoléculaire répétée à partir du congénère étendu tétrakis(dithiényl)benzène. Au lieu de cela, des polymères en échelle exotiques 1D composés d'une alternance de fragments anthracène et annulène fusionnés sont produits par une combinaison de couplage C-C intra- et intermoléculaire.

En un mot, nous avons exploré de nouvelles stratégies pour construire des nanostructures sur des surfaces et démontré la formation de réseaux organométalliques, de nanorubans de graphène et de polymères conjugués.

Mots clés: synthèse en surface, couplage de type Ullmann confiné en surface, nanorubans de graphène, polymères pi-conjugués, réaction de désulfuration, microscopie à effet tunnel, spectroscopie photoélectronique à rayons X, théorie de la fonctionnelle de la densité

ABSTRACT

Low-dimensional carbon-based nanomaterials have drawn great attention due to their appealing properties including tunable bandgaps and high charge carrier mobilities. In recent decades, on-surface synthesis has been identified as a promising strategy to produce low-dimensional nanomaterials with the targeted structure and properties. In this thesis, we studied on-surface synthesis using scanning tunneling microscopy and X-ray photoelectron spectroscopy, supported by density functional theory calculations.

Owing to its versatility in synthesizing atomically precise conjugated polymers, Ullmann-type coupling has been one of the most investigated surface reactions. Deposition of aryl halides on Cu(111) drives the formation of organometallic (OM) intermediates, which can further transform to C-C coupled polymers after heating. However, only a few works have examined the influences of additional co-adsorbates on Ullmann-type coupling. Therefore, one of our goals is to investigate the effects of co-adsorbed oxygen on surface-confined Ullmann-type coupling. By introducing chemisorbed oxygen before or after the deposition of 4,4"-dibromo-p-terphenyl on Cu(111), instead of the formation of one-dimensional (1D) polymer in the absence of oxygen, the formed OM chains transform to two-dimensional OM (2DOM) networks, with Cu-O clusters as the nodes connecting OM segments. The same transformation to 2DOM networks but with smaller repeating units can be achieved with a shorter precursor, 1,4-dibromobenzene. In addition, we studied the effects of substrate symmetry on this structural transformation on fourfold symmetric Cu(100). As a result, the size and symmetry of the 2DOM networks can be flexibly tuned, illustrating a versatile surface patterning technique with potential applications in host–guest chemistry.

As the leading example of carbon nanomaterials accessible by Ullmann-type coupling, graphene nanoribbons (GNRs) have gained increasing popularity due to their potential applications in semiconductor devices and spintronics. Here, we achieved the synthesis of armchair-edged GNRs (AGNRs) through lateral cyclodehydrogenation of poly-para-phenylene (3-AGNR) on Cu(111). Inspired by the effect of oxygen on C-H activation, we introduced oxygen before the lateral cyclodehydrogenation of 3-AGNR. This enabled the lateral fusion to occur at a temperature lower by 180 K, highlighting a promising catalytic effect of oxygen.

Beyond GNRs, we explored new methods to synthesize different carbon-based nanostructures. We used desulfurization reaction of thiophene derivatives to synthesize π -conjugated polymers and acenes, which can be viewed as the narrowest zigzag-edged GNRs. We demonstrated the formation of pentacene through desulfurization and intramolecular cyclization of tetrathienylbenzene on Cu(111). However, nonacene does not form by repeated intramolecular cyclization from the extended congener tetrakis(dithienyl)benzene. Instead, 1D exotic ladder polymers composed of alternating anthracene and fused annulene moieties are produced through a combination of intra- and intermolecular C-C coupling.

In a word, we explored new strategies to construct nanostructures on surfaces and demonstrated the formation of organometallic networks, graphene nanoribbons and conjugated polymers.

Key words: on-surface synthesis, surface-confined Ullmann-type coupling, graphene nanoribbons, π -conjugated polymers, desulfurization reaction, scanning tunneling microscopy, x-ray photoelectron spectroscopy, density functional theory

LIST OF FIGURES

FIGURE 1. 1 STM IMAGES AND CORRESPONDING STRUCTURAL MODELS OF DIFFERENT PRODUCTS OF GLASER-TYPE COUPLING FROM ALKYNE PRECURSORS ON Au(111).....	23
FIGURE 1. 2 STM IMAGES OF ALKANE CHAIN POLYMERIZATION ON Au(110) AND Au(110)-(1×3) RECONSTRUCTED GROOVES.....	24
FIGURE 1. 3 STRUCTURAL MODELS OF THE RE-CONSTRUCTION OF (1×2)-Au(110), (1×3)-Au(110) AND TOP VIEW OF THE (11-1) PLANE.....	25
FIGURE 1. 4 SCHEME OF SCHIFF-BASE REACTION WITH DIFFERENT REACTANTS.....	25
FIGURE 1. 5 GENERALLY ACCEPTED MECHANISM OF THE CLASSICAL ULLMANN REACTION.....	27
FIGURE 1. 6 SCHEMATIC DIAGRAM OF TIP-INDUCED SYNTHESIS OF BIPHENYL MOLECULES ON Cu(111).....	28
FIGURE 1. 7 STEERING OF THE SYNTHESIS OF POLYMERS WITH DIFFERENT DIMENSIONALITIES BY ADDING END GROUPS IN DIFFERENT SITES OF THE PORPHYRIN-BASED PRECURSORS.....	29
FIGURE 1. 8 SCHEME OF THE SYNTHESIS OF ZGNRs ON Au(111).....	30
FIGURE 1. 9 FAST XPS INVESTIGATIONS OF THE EFFECTS OF MOLECULAR COVERAGE ON THE ULLMANN-TYPE COUPLING ON Cu(110), AND SCHEMATIC DIAGRAM OF THE RATIO BETWEEN THE 1D, 2D OM PHASES AND POLYMER.....	31
FIGURE 1. 10 FAST XPS MEASUREMENTS OF C 1s CORE LEVEL BY ANNEALING PRECURSORS FUNCTIONALIZED WITH DIFFERENT HALOGEN ATOMS ON Cu(110).....	32
FIGURE 1. 11 SCHEME OF HIERARCHICAL ULLMANN-TYPE COUPLING FROM PRECURSORS WITH BROMINE AND PRECURSOR ON Au(111).....	32
FIGURE 1. 12 STRUCTURAL MODELS OF GOLD (1×1) MONOLAYER AND ADDITIONAL (1×3) BILAYER ON TITANIA SURFACE GROWN ON Mo(112) SURFACE, AND THE VARIATION OF TURNOVER FREQUENCY WITH THE GOLD COVERAGE.....	34
FIGURE 1. 13 SCHEME OF CONTROLLING POLYMER STRUCTURE BY Cu-DIRECTED TEMPLATE.....	35
FIGURE 1. 14 MONTE CARLO SIMULATION OF THE FORMATION OF POLYMERIZED CHAINS AFTER HEATING 120 MINUTES AT 400K.....	36
FIGURE 1. 15 SCHEME OF THE FORMATION OF 2D COVALENT ORGANIC FRAMEWORKS WITH EXTERNALLY INTRODUCED Cu ON Au(111) IN A HIERARCHICAL MANNER, AND STM IMAGES OF THE ARYL CHLORIDE DIMERS, DECHLORINATED PRODUCTS AND FINAL 2D NETWORKS, RESPECTIVELY.....	37
FIGURE 1. 16 SCHEME OF Ho-CATALYZED COUPLING OF TERMINAL ALKYNES ON Ag(111).....	38

FIGURE 1. 17 SCHEME OF THE FORMATION OF 1D AND 2D METAL-ORGANIC STRUCTURES DUE TO THE MODIFICATION OF DEHYDROGENATED PRECURSORS BY DIFFERENT EXTERNALLY INTRODUCED METAL ATOMS.....	39
FIGURE 1. 18 SCHEME OF STRUCTURAL TRANSFORMATION AND STABILIZATION OF Ni-CENTERED METAL-ORGANIC MOTIFS INDUCED BY THE DOPING OF IODINE, AND SCHEMATIC DIAGRAM OF THE INTERCALATION OF A IODINE MONOLAYER BETWEEN 2D POLYMERS AND Au(111) OR Ag(111) SURFACES.....	41
FIGURE 1. 19 SCHEME OF ULLMANN-TYPE COUPLING ON Cu(111) OR Cu(110) SURFACE AND FURTHER CLEANING UP OF Br BYPRODUCTS BY INTRODUCING HYDROGEN.	43
FIGURE 1. 20 TWO STEPS OF O ₂ GAS MEDIATED FORMATION OF ALKYNYL-SILVER NETWORKS ON Ag(111). STEP1: O ₂ GAS PROMOTES THE C-H ACTIVATION. STEP 2: THE DISSOCIATED ALKYNYL RADICALS BOND THE Ag ADATOMS TO FORM OM NETWORKS..	44
FIGURE 1. 21 SKELETAL STRUCTURE OF 7-AGNRs. STM IMAGE AND STS MEASUREMENTS OF A 7-AGNR ON AN NaCl ISLAND SUPPORTED BY Au(111)	46
FIGURE 2. 1 SCHEMATIC DIAGRAM OF THE SCANNING TUNNELING MICROSCOPE.....	49
FIGURE 2. 2 SCHEMATIC DIAGRAM OF A ONE-DIMENSIONAL METAL-VACUUM-METAL TUNNELING JUNCTION.	50
FIGURE 2. 3 ENERGY DIAGRAM OF THE TIP AND SAMPLE STATES WHEN A POSITIVE BIAS IS APPLIED ON THE SAMPLE, CAUSING THE ENERGY OF THE STATES IN THE SAMPLE TO DECREASE. IT IS ASSUMED THAT ALL ENERGY LEVELS ARE FILLED UP TO THE FERMI LEVEL AND EMPTY ABOVE FERMI LEVEL.....	52
FIGURE 2. 4 DIAGRAM OF THE FIRST DERIVATIVE OF THE I-V CURVE. A MODULATED VOLTAGE IS ADDED AROUND THE CENTER VALUE V ₁ OR V ₂ . THE MEASURED AMPLITUDE OF THE RESULTING MODULATED CURRENT BY ADDING A MODULATED VOLTAGE IS PROPORTIONAL TO THE SLOPE OF THE I-V CURVE.....	55
FIGURE 2. 5 dI/dV SPECTRA ACQUIRED ON A CLEAN TERRACE (SOLID LINE) AND STEP EDGE (DASHED LINE) OF Cu(111).	55
FIGURE 2. 6 INITIAL, TRANSITION AND FINAL STATES OF SLIDING DIFFUSION AND FLIPPING DIFFUSION OF PHENYL ON Au(111), Ag(111), AND Au(111) AND THE CORRESPONDING ENERGY DIAGRAMS. AND THE ENERGY DIAGRAM OF THE IS, TS AND FS OF DEHALOGENATION PROCESS ON Au(111), Ag(111) AND Cu(111).	56
FIGURE 2. 7 TOP-VIEW OF (100), (110) AND (111) SURFACES IN A FACE CENTERED CUBIC CRYSTAL. THE ARROWS INDICATE THE BASIC VECTORS IN DIFFERENT SURFACES.	57
FIGURE 2. 8 SCHEMATIC DIAGRAM OF X-RAY PHOTOELECTRON SPECTROSCOPY, SHOWING THE BASIC COMPONENTS OF THE SYSTEM. .	59

FIGURE 2. 9 OMICRON UHV VARIABLE-TEMPERATURE STM, INTEGRATED WITH XPS, LEED AND ORGANIC MOLECULAR BEAM EPITAXY FACILITIES, AND OMICRON UHV LOW-TEMPERATURE STM WITH OMBE SYSTEMS.....	61
FIGURE 3. 1 SCHEME OF THE TRANSFORMATION OF ORGANOMETALLIC (OM) STRUCTURES FROM 1D TO 2D BY INTRODUCING O ₂ INTO SURFACE-CONFINED ULLMANN-TYPE COUPLING.....	64
FIGURE 3. 2 LT STM IMAGES OF THE HEXAGONAL OM NETWORKS ON Cu(111).....	65
FIGURE 3. 3 HIGH-RESOLUTION STM IMAGES OF OM CHAINS FORMED BY DBTP ON Cu(111)	66
FIGURE 3. 4 LT STM IMAGES OF OM CHAINS AND POLY-PARA-PHENYLENE (PPP) WIRES.....	67
FIGURE 3. 5 OVERVIEW LT STM IMAGE AFTER FURTHER ANNEALING THE HEXAGONAL NETWORKS AT 497 K.....	67
FIGURE 3. 6 IDENTIFICATION OF TWO DISTINCT VERTICES IN THE 2D DBTP NETWORK.....	68
FIGURE 3. 7 OBLIQUE VIEW OF THE DFT OPTIMIZED MODELS OF DBTP AND DBB 2D NETWORKS ON Cu(111). THE O ATOMS ARE ABOVE CU ADATOMS IN A THREE-FOLD BONDING ENVIRONMENT, ANALOGOUS TO A HOLLOW SITE ON THE SURFACE. THE REMAINING C ATOMS ARE IN BLACK AND H IN WHITE.....	69
FIGURE 3. 8 COPPER-OXYGEN CLUSTERS CONSIDERED IN ON-SURFACE DFT CALCULATIONS FOR THE DBTP 2D OM NETWORK.....	69
FIGURE 3. 9 LT STM IMAGES FOR DEPOSITION OF O ₂ BEFORE DBTP ON Cu(111).....	70
FIGURE 3. 10 OVERVIEW RT STM IMAGES OF TRANSFORMATION FROM 1D OM CHAINS TO 2D HEXAGONAL NETWORKS.....	71
FIGURE 3. 11 C 1s AND O 1s XPS SPECTRA OBTAINED DURING THE TRANSFORMATION FROM OM CHAINS OBTAINED WITH DBTP TO 2D HEXAGONAL NETWORKS ON Cu(111).....	72
FIGURE 3. 12 O 1s XPS SPECTRA OBTAINED DURING A SEQUENTIAL ANNEALING WITHOUT PRECURSORS DBTP ON Cu (111).....	73
FIGURE 3. 13 RT STM IMAGES FOR 2D NETWORK FORMATION FROM DBB ON Cu(111).....	74
FIGURE 3. 14 C 1s AND O 1s XPS SPECTRA OBTAINED DURING THE TRANSFORMATION FROM 1D OM CHAINS (FROM DBB) TO 2D HEXAGONAL NETWORKS.....	75
FIGURE 3. 15 DFT-CALCULATED STRUCTURES AND ENERGIES OF PHASES BETWEEN 1D OM CHAINS AND 2D OM NETWORKS FORMED BY DBB.....	76
FIGURE 3. 16 CHARGE DENSITY DIFFERENCES INDUCED BY OXYGEN ATOMS IN THE 2D OM NETWORK AND CHEMISORBED ON THE BARE SUBSTRATE.....	77
FIGURE 3. 17 RT STM IMAGES FOR 2D NETWORK FORMATION FROM DBB ON Cu(100).	78

FIGURE 4. 1 SYNTHESIS OF 3P-AGNRs ON THE PURE Cu(111) AND PARTIALLY OXIDIZED Cu(111). BONDS FORMED DURING LATERAL FUSION ARE SHOWN IN RED.....	82
FIGURE 4. 2 LT STM IMAGES (T = 4.6 K) OF THE SYNTHESIS OF 3P-AGNRs ON Cu(111).....	83
FIGURE 4. 3 LT STM IMAGE OF ANNEALING 3-AGNR ON Cu(111) AT 533 K. AS A RESULT, ONE 3-AGNR LIES ABOVE THE Br ATOMS TO EXHIBIT INCREASED HEIGHT AND CONTRAST.....	84
FIGURE 4. 4 CALCULATED STRUCTURES FOR THE INITIAL SELF-ASSEMBLY OF 3- AGNRs AND Br ATOMS, AND AFTER INTERCALATION OF ONE Br ATOM. SIMULATED STM IMAGES FOR THE CORROSPONDING STRUCTURES	85
FIGURE 4. 5 PROPOSED MODEL OF 9-AGNR ON TOP OF Br ATOMS. Br ATOMS ARE DISTRIBUTED AS THE KNOWN ($\sqrt{3} \times \sqrt{3}$) R30° OVERLAYER STRUCTURE ON Cu(111) AND THE LATTICE MATCHES WELL WITH THE LONGITUDINAL PERIODICITY OF 9-AGNR	85
FIGURE 4. 6 CALCULATED STRUCTURES AND STM SIMULATIONS FOR ATOM INTERCALATION BELOW 3-AGNRs.....	86
FIGURE 4. 7 LT STM IMAGES (T = 4.6 K) OF 3P-AGNRs SYNTHESIZED ON Cu (111) WITH THE INTRODUCTION OF O ₂	87
FIGURE 4. 8 MAGNIFIED STM IMAGE AFTER DOSING O ₂ ON Cu(111) DECORATED WITH 3-AGNR AT 403 K, LEADING TO THE FORMATION OF OXIDIZED Cu PHASE.....	87
FIGURE 4. 9 LT-STM IMAGE OF ANNEALING 3-AGNR ON OXIDIZED Cu(111) AT 423 K, LEADING TO THE ONSET OF Br INTERCALATION. INSET IS MAGNIFIED IMAGE.	88
FIGURE 4. 10 LT STM IMAGE OF 3P-AGNRs ON Au(111). 6, 9 AND 12-AGNRs ARE FORMED BY ZIPPING OF 3-AGNRs.....	88
FIGURE 4. 11 RT STM IMAGES OF THE SYNTHESIS OF 3P-AGNRs ON Cu(111).	89
FIGURE 4. 12 RT STM IMAGES OF THE SYNTHESIS OF 3P-AGNRs ON OXIDIZED Cu(111).	90
FIGURE 4. 13 C 1s XPS SPECTRA OF THE SYNTHESIS OF 3P-AGNRs ON Cu(111) AT INCREASING TEMPERATURES, AND C 1s AND O 1s XPS SPECTRA OF THE SYNTHESIS OF 3P-AGNRs ON Cu(111) WITH OXYGEN INTRODUCED.	91
FIGURE 4. 14 C 1s AND O 1s XPS SPECTRA OF INTRODUCING OXYGEN ON THE SAMPLE HELD AT RT AFTER THE FORMATION OF 3-AGNRs, AND CORRESPONDING RT STM IMAGES.	92
FIGURE 4. 15 STS MEASUREMENTS OF 6-AGNR AND 9-AGNR ON Au(111).	93
FIGURE 4. 16 STS MEASUREMENTS OF THE ELECTRONIC STRUCTURE OF 12-AGNR ON Au (111) SUBSTRATE.....	94
FIGURE 4. 17 STS MEASUREMENTS OF THE ELECTRONIC STRUCTURE OF 6, 9, 12-AGNR ON Cu (111) SUBSTRATE.	96
FIGURE 4. 18 STM IMAGES BEFORE AND AFTER DRAGGING A 6-AGNR ON Cu(111) BY STM TIP MANIPULATION. THE SURFACE UNDER	

THE DRAGGED RIBBON EXHIBITS THE APPEARANCE OF OXIDIZED Cu(111).	97	
FIGURE 4. 19 STS MEASUREMENTS OF THE ELECTRONIC STRUCTURE OF 3, 6, 9-AGNRs ON Au (111) SUBSTRATE.	98	
FIGURE 5. 1 SURFACE-CONFINED REACTIONS OF FUSED TETRATHIENOANTHRACENE MOLECULES ON DIFFERENT METAL SURFACES, PRODUCING PENTACENE OR H-SHAPED PRODUCTS, AND SURFACE-CONFINED REACTION OF T1TB PRODUCING PENTACENE ON Cu(111) AND C) OF T2TB PRODUCING A 1D LADDER POLYMER INSTEAD OF NONACENE ON Cu(111).	103	
FIGURE 5. 2 S 2P AND C 1s XPS SPECTRA OBTAINED WHEN T1TB WAS DEPOSITED ON Cu(111) SURFACE HELD AT 453 K OR AT RT FOLLOWED BY A SEQUENCE OF ANNEALING. STM IMAGES OF DEPOSITING T1TB ON Cu(111) HELD AT 453 K.		104
FIGURE 5. 3 STM IMAGES AFTER DEPOSITION OF T1TB ON Cu(111) AT RT, AND ANNEALING THE SAMPLE AT 453 K, LEADING TO THE FORMATION OF ISOLATED, DISORDERED MONOMERS. STM IMAGE OF THE FORMATION OF PENTACENE FROM T1TB ON Cu(111), WHICH ARE CO-ASSEMBLED WITH DISSOCIATED SULFUR ATOMS.	104	
FIGURE 5. 4 S 2P AND C 1s XPS SPECTRA OBTAINED WHEN T2TB WAS DEPOSITED ON Cu(111) SURFACE HELD AT 393, 473 AND 573 K, OR AT RT FOLLOWED BY ANNEALING AT 393 K.....	105	
FIGURE 5. 5 STM IMAGES AFTER A) DEPOSITION OF T2TB ON Cu(111) AT RT, AND ANNEALING THE SAMPLE AT 393 K, LEADING TO THE FORMATION OF RANDOMLY COUPLED STRUCTURES.	106	
FIGURE 5. 6 OVERVIEW AND MAGNIFIED STM IMAGES AFTER DEPOSITING T2TB ON Cu(111) HELD AT 393 K. TOP AND SIDE VIEW OF DFT OPTI-MIZED MODEL. CALCULATED ELECTRONIC BAND STRUC-TURE FOR THE FREESTANDING 1D POLYMER.	107	
FIGURE 5. 7 A SERIES OF STM IMAGES AFTER DEPOSITING T2TB ON Cu(111) AT 343 K, 363 K, 393 K, 463 K, 493 K AND 573 K ...	108	
FIGURE 5. 8 TWO POSSIBLE RESONANT STRUCTURES FOR THE 1D LADDER POLYMER.....	109	
FIGURE 5. 9 TOP-VIEW OF THE DENSITY FUNCTIONAL THEORY (DFT) OPTIMIZED MODEL AND STM SIMULATION FOR THE Cu ADATOM STABILIZED STRUCTURE, AND FOR THE STRUCTURE WITHOUT Cu ADATOMS.	109	
FIGURE 5. 11 PROPOSED SKELETAL MODELS OF THE REACTION PATHWAYS FOR THE TRANSFORMATION FROM T1TB TO PENTACENE AND T2TB TO 1D EXTENDED POLYMER.....	110	
FIGURE 5. 10 TOP- AND SIDE-VIEWS OF DFT OPTIMIZED STRUCTURES CONSIDERED FOR THE 1D POLYMER AND THE CORRESPONDING STM SIMULATIONS.	110	
FIGURE 5. 12 DFT CALCULATED STRUCTURE FOR THE FLAT FREE-STANDING POLYMER. DFT CALCULATED STRUCTURES AND ENERGIES OF H-SATURATED POLYMERS IN GAS PHASE.	111	

FIGURE 5. 13 C 1S AND S 2P XPS SPECTRA OBTAINED AFTER T2TB WAS DEPOSITED ON Ag(111) SURFACE AT 423 K AND 573 K, OR ON Ag(111) AT RT FOLLOWED BY A SEQUENTIAL ANNEALING.....	112
FIGURE 5. 15 C 1S AND S 2P XPS SPECTRA OBTAINED WHEN T2TB WAS DEPOSITED ON Au(111) SURFACE HELD AT RT OR HIGHER TEMPERATURE.....	113
FIGURE 5. 14 DFT CALCULATIONS FOR POSSIBLE STRUCTURES OF THE UNREACTED CHAIN TERMINUS ON Cu(111).	113
 FIGURE 6. 1 PROPOSED SCHEME OF THE FORMATION OF 2DCPs FROM A PRECURSOR FUNCTIONALIZED WITH HALOGENATED ACETYLENE GROUPS.....	118
FIGURE 6. 2 PROPOSED SCHEMES OF THE FORMATION OF 2DOM NETWORKS WITH DIFFERENT CHIRALITY FROM A V-SHAPED PRECURSOR, AND THE FORMATION OF 2DCPs FROM A V-SHAPED PRECURSOR FUNCTIONALIZED WITH HALOGENATED ACETYLENE GROUPS.....	119
FIGURE 6. 3 ON-SURFACE SYNTHESIS OF DODECABENZOCORONENE FROM THIOPHENE-BASED PRECURSORS. A: RING OPENING AND DESULFURIZATION. B: INTRAMOLECULAR CYCLIZATION.....	121
FIGURE 6. 4 ON-SURFACE SYNTHESIS OF ARMCHAIR-EDGED GNRs FROM THIOPHENE-BASED PRECURSORS. A: C-C COUPLING INDUCED BY DEHALOGENATION. B: RING OPENING AND DESULFURIZATION. C: INTRAMOLECULAR CYCLIZATION	121

LIST OF TABLE

TABLE 4. 1 TABLE OF THE BAND GAPS (EXPERIMENTAL VS THEORETICAL) IN THE AGNRs WITH DIFFERENT WIDTHS ON Au(111). 95

LIST OF EQUATIONS

$-\frac{\hbar^2}{2m} \frac{\partial^2 \psi_n(z)}{\partial z^2} + V(z)\psi_n(z) = E\psi_n(z)$	2. 1	51
$k = \frac{\sqrt{2m(E-V(z))}}{\hbar}$	2. 2	51
$\psi_n(z) = \psi(0)e^{\pm ikz}$	2. 3	51
$\psi_n(z) = \psi(0)e^{\pm \kappa z}$	2. 4	51
$P \propto \psi(z) ^2 = \psi(0) ^2 e^{-2\kappa d}$	2. 5	51
$I \propto \sum_{E_f - eV}^{E_f} \psi(0) ^2 e^{-2\kappa d}$	2. 6	51
$\rho_s(z, E) = \frac{1}{\epsilon} \sum_{E-\epsilon}^E \psi(z) ^2$	2. 7	52
$I \propto V \rho_s(0, E_f) e^{-2\kappa d}$	2. 8	52
$\omega_{tip,i \rightarrow sample,f} = \frac{2\pi}{\hbar} M_{fi} ^2 \delta(E_{sample,f} - E_{tip,i})$	2. 9	52
$M_{fi} = \frac{\hbar^2}{2m} \int_{S_{tip/sample}} [\psi_{tip,i}(R) \nabla \psi_{sample,f}^*(r) - \psi_{sample,f}(R) \nabla \psi_{tip,i}^*(r)] \cdot dS$	2. 10	53
$\omega_{tip \rightarrow sample} = \frac{2\pi}{\hbar} \sum_{i,f} M_{fi} ^2 \delta(E_f - E_i)$	2. 11	53
$I = \frac{4\pi e}{\hbar} \sum_{i,f} M_{fi} ^2 \delta(E_f - E_i)$	2. 12	53
$I = \frac{4\pi e}{\hbar} \int_0^{eV} \rho_{tip}(\epsilon - eV) \rho_{sample}(\epsilon) M(\epsilon) ^2 d\epsilon$	2. 13	53
$I = \frac{4\pi e}{\hbar} \int_0^{eV} [f(E_f - eV + \epsilon) - f(E_f + \epsilon)] \times \rho_s(E_f - eV + \epsilon) \rho_t(E_f + \epsilon) M(\epsilon) ^2 d\epsilon$	2. 14	53
$I = \frac{4\pi e}{\hbar} \int_0^{eV} [f(E_f - eV + \epsilon) - f(E_f + \epsilon)] \times \rho_s(E_f - eV + \epsilon) \rho_t(E_f + \epsilon) M(\epsilon) ^2 d\epsilon$	2. 15	54
$I = \int_0^{eV} \rho_{tip}(\epsilon - eV) \rho_{sample}(\epsilon) d\epsilon$	2. 16	54
$\frac{dI}{dV} \propto \rho_{sample}(E_F - eV)$	2. 17	54
$E_{binding} = E_{photo} - E_{kinetic} - \emptyset$	2. 18	60

List of ABBREVIATIONS

1D	one-dimensional
2D	two-dimensional
1DOM	one-dimensional organometallic
2DOM	two-dimensional organometallic
AC	alternating current
AFM	atomic force microscopy
AGNRs	armchair graphene nanoribbons
BE	binding energy
CB	conduction band
dB _B	1,4-dibromobenzene
DBTP	4,4"-dibromo-p-terphenyl
DFT	density functional theory
fcc	face centered cubic
GGA	Generalized-gradient approximation
HOMO	highest occupied molecular orbital
K	Kelvin
KMC	kinetic Monte Carlo
LDOS	local density of state
LT	low temperature
LUMO	lowest unoccupied molecular orbital
MOCNs	metal organic coordination networks
OM	organometallic
PAW	projector augmented wave
ph	phenylene
PPP	poly para-phenylene
RT	room temperature
SIMS	secondary-ion mass spectrometry
STM	scanning tunneling microscopy
STS	scanning tunneling spectroscopy
T1TB	1,2,4,5-Tetra(thiophen-2-yl)benzene

T2TB	1,2,4,5-Tetra([2,2'-bithiophen]-5-yl)benzene
UHV	ultrahigh vacuum
UPS	ultraviolet photoelectron spectroscopy
VASP	Vienna Ab-initio simulation package
VB	valence band
vdW	van der Waals
XPS	x-ray photoelectron spectroscopy
ZGNRs	zigzag graphene nanoribbons

Chapter 1. Introduction

1.1 On-surface chemical reactions in UHV

Graphene, a two-dimensional sheet of carbon atoms, has attracted great attention due to its remarkable properties that arise from electron confinement. However, its lack of a bandgap is detrimental to electronics and photonics applications. Low-dimensional carbon-based nanomaterials have been predicted as excellent alternatives owing to their tunable electronic structures and high charge carrier mobilities.¹ Besides conventional electronics, there are several emerging research areas that make low-dimensional polymers intriguing, including topological insulators, carbon magnetism, and quantum information processing.² A promising strategy to produce low-dimensional nanomaterials with atomically precise structures is to confine covalent coupling reactions to a crystal surface, a bottom-up approach referred to as “on-surface synthesis.” The related field of on-surface self-assembly seeks to produce complex nanostructures linked by weaker non-covalent interactions, offering a higher degree of order and greater structural flexibility.

The in-depth investigation of on-surface self-assembly and surface-confined chemical reactions had been made possible by the development of a range of surface characterization techniques, including photoelectron spectroscopies, scanning electron microscopy (SEM), Raman spectroscopy, atomic force microscopy (AFM), and in particular scanning tunneling microscopy (STM).³⁻¹² Supported by these techniques, the reactants, products and even different phases of intermediates of the surface-confined reactions can be directly visualized in real space with sub-molecular or even atomic resolution (mainly by STM), and indirectly confirmed by the characterization of their unique electronic structures. As a complement to STM imaging, X-ray photoelectron spectroscopy (XPS) can provide information on the elemental composition and electronic state of the elements. In recent years, non-contact (NC)-AFM with qPlus sensors has become increasingly popular in surface science due to its capability of resolving chemical bonds and to compensate for the deficiency of STM when the sample is non-conducting. Beyond experimental techniques, density functional theory (DFT) calculations are frequently used to help understand the reactions. In addition to simulating the structures’ geometries and adsorption sites, DFT calculations can predict the energy barriers between different states during the reaction and model the optimal reaction pathways.

On this basis, on-surface self-assembly and surface-confined chemical reactions have been widely applied to produce different low-dimensional functional nanostructures. Compared to self-assembly, more robust structures can be synthesized by surface-confined reactions, which is also known as on-surface synthesis. In contrast to traditional in-solution chemistry, surface-confined reactions avoid problems with insolubility and aggregation of the products, and enables them to be investigated with the range of surface analysis techniques described above.

In this thesis, we will focus on surface-confined reactions occurring in an ultrahigh vacuum (UHV) environment, i.e., at a solid-vacuum interface. Beyond just supporting the molecules, the metal atoms of the substrates can act as catalysts to promote the reaction, which could also lead to the formation of different intermediates and products compared to traditional in-solution chemical reactions. During the last 15 years, a number of traditional chemical reactions (Ullmann-type coupling, Glaser-type coupling, Schiff-base condensation, Bergman cyclization, Sonogashira coupling, alkane polymerization, etc.) have been studied on a range of single-crystal surfaces with different lattices and properties, including insulating, semiconducting and metallic substrates. In this thesis, the research was conducted on single-crystal metal surfaces, such as Au(111), Cu(111) and Cu(100).

Among all the reactions, on-surface Ullmann-type coupling has been the most investigated as a promising strategy to produce various conjugated polymers with desired structures and properties. This reaction will be described comprehensively in the next section. Here, I will introduce a few representative surface-confined coupling reactions to illustrate the promising role of on-surface synthesis in material science.

Glaser-type coupling is another classic reaction where alkyne groups link to butadiynes via oxidative coupling.^{13, 14} When this reaction is applied on surfaces, it exhibited great potential in synthesizing desired polymers by designing the functionalized precursors with alkyne groups. Glaser-type coupling of terminal alkyne can induce the cyclization at the end sites of each precursor molecule, contributing to the synthesis of potential conjugated nanomaterials. In addition, compared with Ullmann-type coupling, surface-confined Glaser-type coupling is halogen free, which can eliminate the side effects of the halogen byproducts; that is, the dissociated halogen atoms can inhibit the detailed characterization of the target products.¹⁵ In 2012, combining STM characterization with DFT calculations, Zhang *et al.* first reported the

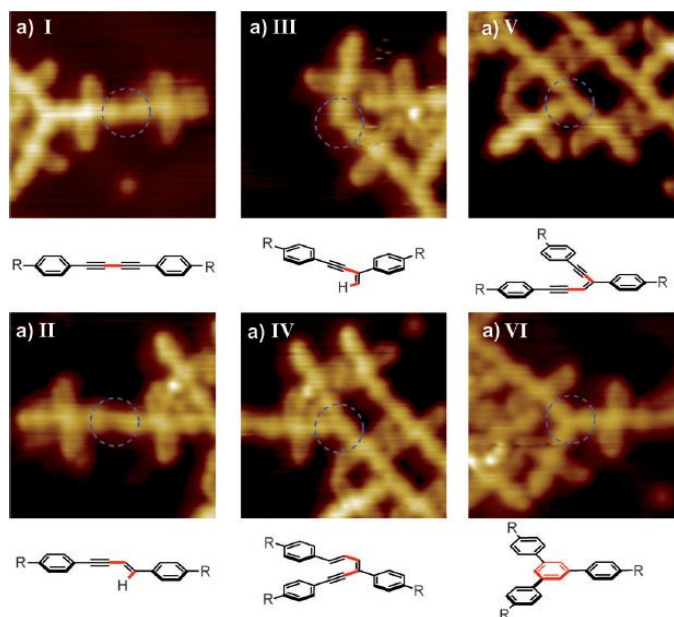


Figure 1. STM images and corresponding structural models of different products of Glaser-type coupling from alkyne precursors on Au(111). Adapted from Ref.¹⁷ with the permission of John Wiley and Sons.

surface-assisted terminal alkyne C_{sp} - H bond activation and homo-coupling to 2D covalent networks on Ag(111).¹⁶ In 2013, Gao *et al.* reported Glaser-type coupling on Au(111).¹⁷ As shown in Figure 1.1, annealing alkyne functionalized precursors can drive the formation of different polymerized products including trimerized connections, revealing the possibility of synthesizing cyclic conjugated polymers by Glaser-type coupling. Furthermore, they compared Glaser-type coupling on different surfaces including Au(111), Ag(111), and Cu(111), illustrating the substrate sensitivity of surface-confined Glaser-type coupling.¹⁸ Among these substrates, Cu(111) was identified as the least efficient substrate for Glaser-type coupling, while on Ag(111) there was a lower proportion of side reactions than Au(111).

In contrast to the sp hybridized carbon in alkynes, alkanes are saturated hydrocarbons with all- sp^3 -hybridized carbon atoms, which have tremendous industrial importance as a basic component in petroleum, natural gas, etc. In the polymerization processes of alkanes, functionalized derivatives are commonly used as precursors, which however sharply increases the cost. Therefore, it is desirable to directly use the alkanes as precursors, though they are relatively inert. Compared to in-solution chemistry, the selectivity of the reaction sites can be more easily controlled when the reaction is confined on surfaces, which is a key challenge in alkane polymerization. Zhong et al. remarkably achieved predictable and direct surface-confined alkane polymerization in UHV (as shown in Figure 1.2),¹⁹ which has never been achieved in

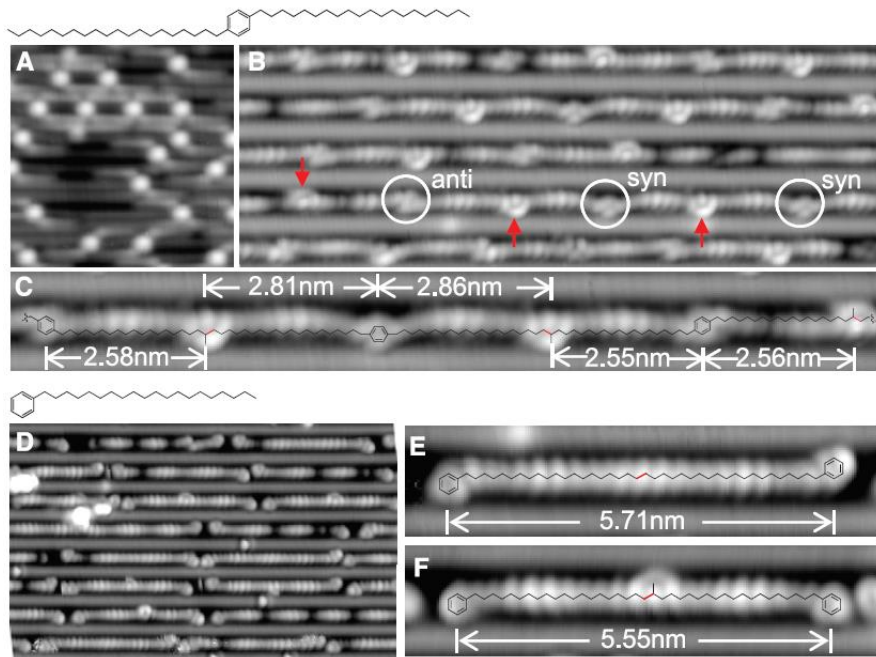


Figure 1. 2 STM images of alkane chain polymerization. **a)** Deposited alkane monomers on Au(110). **b)** Polymerized alkane chains located on Au(110)-(1×3) reconstructed grooves. **c)** Polymerized chains with superimposed skeletal model. **d)** Dimerized (eicosyl) benzene. **e-f)** Terminal C–C coupling and terminal/penultimate C–C coupling. Adapted from Ref. ¹⁹ with the permission of the American Association for the Advancement of Science.

traditional in-solution chemistry. They used the anisotropic Au(110) surface, which provides one-dimensional channels with the proper width to constrain the alignment of long-chain ($>C_{20}$) linear alkanes. Through STM characterizations and DFT calculations, the highly selective C–H activation and subsequent C–C coupling were confirmed after annealing the sample at around 529K. This work opens up a new direction in the area of alkane polymerization on surfaces, strengthening the catalytic versatility of single-crystal metal substrate. Based on this work, Sun *et al.* further comprehensively investigated the mechanism of alkane polymerization on Au(110).²⁰ Through either manually applying an electron beam onto the surface or introducing branched methylidene groups on both sides of the alkane chain, the (1×2)-Au(110) can be totally or partially reconstructed into (1×3)-Au(110), as shown in [Figure 1.3](#). With STM images and DFT calculations, they demonstrated that due to the extra row of gold atoms in the channel, the alkane chains adsorbed on (1×3)-Au(110) are more reactive than those on pristine (1×2)-Au(110). This work illustrates the importance and specific catalytic ability of reconstructed structure of substrates in surface science. In addition, Zhang *et al.* reported the step-edge assisted alkane coupling on Cu(100), where the C–H activation barrier is very low due to the low-coordinated surface atoms at the step edge.²¹ These achievements in

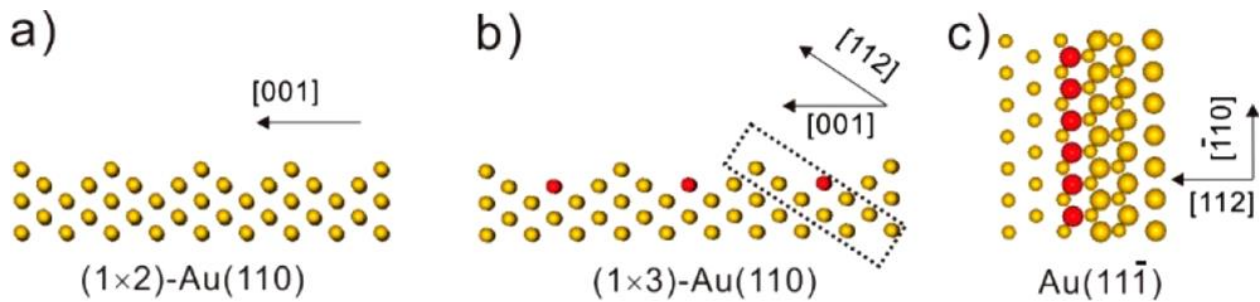


Figure 1. 3 Structural models of the re-construction of a) (1×2)-Au(110) b) (1×3)-Au(110). c) Top view of the (11-1) plane.
Adapted from Ref.²⁰ with the permission of the American Chemical Society.

surface-confined alkane polymerization in UHV reveal the unique catalytic properties of metal substrates with narrow channels or reactive step edges, which could promote the development of industrial fuel synthesis.

Another widely investigated reaction on surfaces is the Schiff-base reaction, which is defined as an addition reaction between aromatic amines and carbonyl compounds to form an imine. This reaction is reversible in solution, enabling the formation of layered stacking 2D polymer and even 3D networks.²² One challenge is that ordered covalent-bonded structures with thinner layers and lower dimensions are difficult to achieve from Schiff-base reaction in solution. Constraining this reaction to proceed on single-crystal surfaces may enable the formation of low-dimensional nanomaterials with single layer and atomically precise structure. In 2007, Weigelt *et al.* first reported the synthesis of imine from an aldehyde and an amine on Au(111) in UHV.²³ Furthermore, they reported the synthesis of 2D branched polymer nanostructures on Au(111) through Schiff base reaction.²⁴ In addition, on the basis of Schiff-base reaction on Au(111) in UHV,

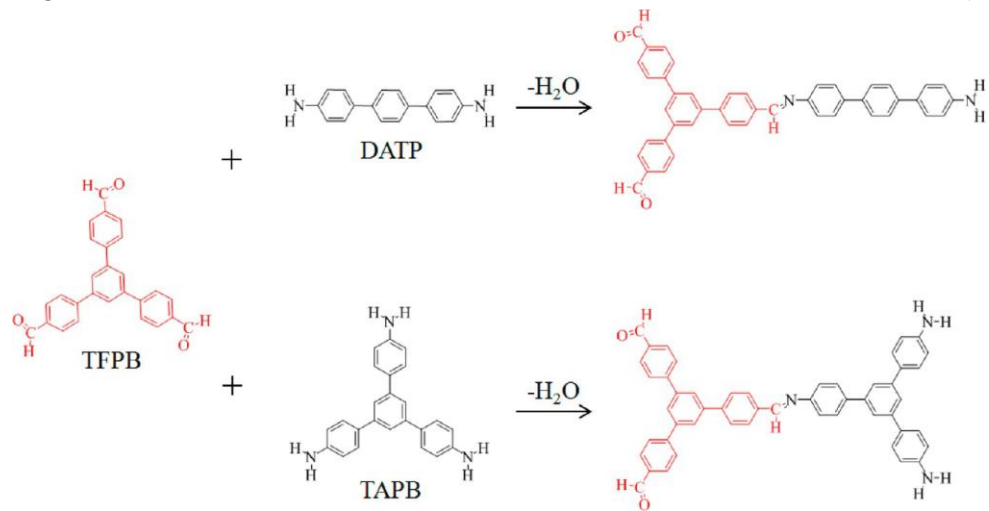


Figure 1. 4 Scheme of Schiff-base reaction with different reactants. Adapted from Ref.²⁵ with the permission of the American Chemical Society.

Gong *et al.* constructed various oligomer products by rationally adjusting the stoichiometric proportions of the reactants (see scheme in [Figure 1.4](#)).²⁵ As well, Jiang *et al.* investigated the synthesis of 1D oligomers on Ag(111) by optimizing the stoichiometry ratio between tetraketone and tetraamine monomers.²⁶ Due to the irreversibility of Schiff-base reaction on surfaces in UHV, defects lead to random connections between the reactive sites, which impedes the formation of large-scale structures. By combining the in-solution and on-surface chemistries, the reversible Schiff-base reaction can be achieved on solid-liquid interface.¹¹ Hence, designing the molecular building blocks and optimizing the balance between reaction kinetics and thermodynamics could be a plausible way to achieve the synthesis of desired polymers with larger domain size. In 2018, it has been proved that grafted aryl species can act as defects to steer the Schiff-base reaction at the solid-liquid interface.²⁷ The aryl species can be subsequently removed to start the 2D polymer healing process.

Besides the aforementioned reactions that have been widely studied, there are many other surface-confined chemical reactions have been investigated with the supporting of modern surface characterizing techniques. Thanks to these powerful techniques, I expect that more surface-confined reactions will be studied in-depth and therefore better-ordered low-dimensional nanomaterials with desired structures and properties can be synthesized in the future.

1.2 Surface-confined Ullmann-type coupling

Among all the surface-confined reactions mentioned in the previous section, on-surface Ullmann-type coupling is the most investigated, owing to its potential to precisely synthesize different conjugated polymers with specific dimensionality, structures and properties. The basic strategies to steer this reaction include the design of the functionalized precursors, the optimization of the reaction parameters (molecular coverage, annealing temperature, etc.), and the selection of the substrate and its symmetry.

The classical Ullmann reaction was first put forward by Germany chemist Fritz Ullmann in 1901.²⁸ He observed that a copper-containing compound can catalyze the coupling of two aryl halides into bi-aryl moieties. In the following several years, Ullmann further applied this reaction to synthesize N-aryl amines and ethers.^{29, 30} After continued investigation of the Cu species in the Ullmann reaction, researchers

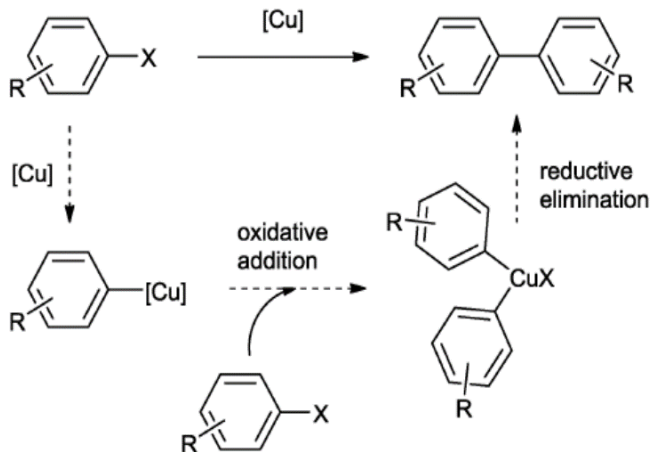


Figure 1.5 Generally accepted mechanism of the classical Ullmann reaction. Adapted from Ref. ⁴¹ with the permission of The Royal Society of Chemistry.

concluded that the initial states of the Cu source in the reaction are not crucial because the copper will always transfer to the same state during the oxidation/reduction processes. However, the mechanism of Ullmann reaction underwent a long period of dispute from the first hypothesis in the 1960's,³¹⁻³³ the focus of which was on whether the final products were generated in solution or on the surface of the copper species. Nowadays, the general accepted mechanism (as shown in [Figure 1.5](#)) is that the Cu species catalyze the dissociation of aryl halides into halogen atoms and phenylene radicals, which immediately couple Cu atoms to form organometallic (OM) intermediates in the solution. After reductive elimination, the OM species transform into final polymerized products.

To eliminate the side effects of contaminants present in solution and obtain a deeper understanding of the reaction mechanism, the investigation of the traditional Ullmann reaction was switched from solution to solid interfaces (solid-vacuum). Different from the behavior of homogeneous catalysis where the reactions occur in the same phase (liquid), the precursors and intrinsic adatoms are constrained in low dimension when the Ullmann-type reaction takes place on interfaces, bearing as well the characteristics of heterogeneous catalysis. This could promote the different reaction pathways and the understanding of reactions in different aspects. Combined with UHV atmosphere and low temperature (LT) cooling, modern surface characterization techniques are able to provide insights into different states of this reaction in atomic or sub-molecular scale. In 1992, for the first time, Xi and Bent investigated surface-confined Ullmann-type coupling with the precursor iodobenzene on Cu(111) in UHV.³⁴ They further illustrated the relationship between the molecular coverage and the reaction mechanism,³⁵ making the point that the coverage would

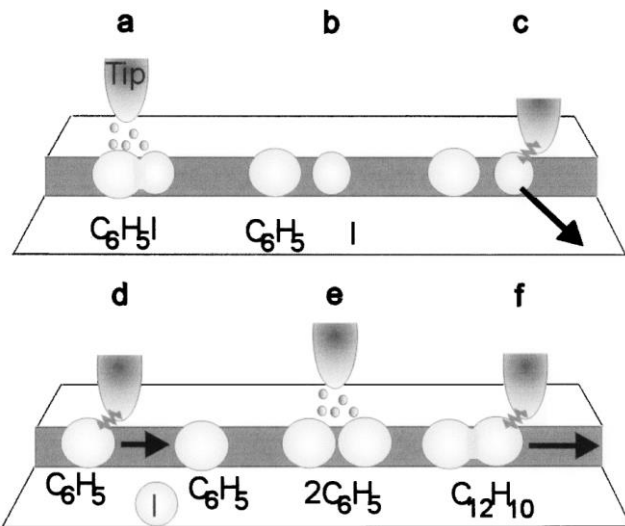


Figure 1.6 Schematic diagram of tip-induced synthesis of biphenyl molecules on Cu(111). a)-b) Dissociation of iodobenzene induced by electrons emitted from the tip. c)-d) Removal of the iodine atoms and lateral manipulation of two phenyls together. e) Electron-induced chemical combination of two phenyls into biphenyl. f) Further confirmation of the association of biphenyl by lateral manipulation. Adapted from Ref.³⁶ with the permission of the American Physical Society.

affect the orientation of iodobenzene molecules on surface and therefore the subsequent coupling. In 2000, Hla *et al.* reported STM tip-induced Ullmann-type coupling on Cu(111), demonstrating the feasibility of “welding” molecules manually.³⁶ As shown in [Figure 1.6](#), the dissociation of the precursor iodobenzene into phenyl and iodine can be induced by placing the tip above the molecule and applying a bias. Two phenyl groups can be laterally dragged closer by tip manipulation and then coupled into biphenyl by further tip-excitation. In the following several years, different aspects of on-surface Ullmann-type coupling have been studied, including the synthesis of conjugated polymers with desired structures and properties,^{5, 9, 37-45} the effects of different halogen substituents in the precursor,⁴⁶⁻⁴⁹ formation of different intermediate states,^{40,} ⁵⁰⁻⁵⁴ the influence of different substrates,⁵⁵ and hierarchical dehalogenation using the different activation energies for C-Br, C-Cl and C-I bonds.⁵⁶⁻⁶²

Based on surface-confined Ullmann-type reaction, a pioneering work reported by Grill *et al.* in 2007 contributed to the synthesis of a large number of functional covalently bonded structures.³⁷ Porphyrin building blocks with Br substituents were deposited on Au(111) at RT. After thermal activation, carbon radicals are generated with the dissociation of Br atoms, and carbon-carbon (C-C) coupling then occurs at those predefined points. Through the design of the active sites, the reaction can be steered to the desired product (as shown in [Figure 1.7](#)). As a result, dimers, 1D polymers and 2D polymers could be obtained

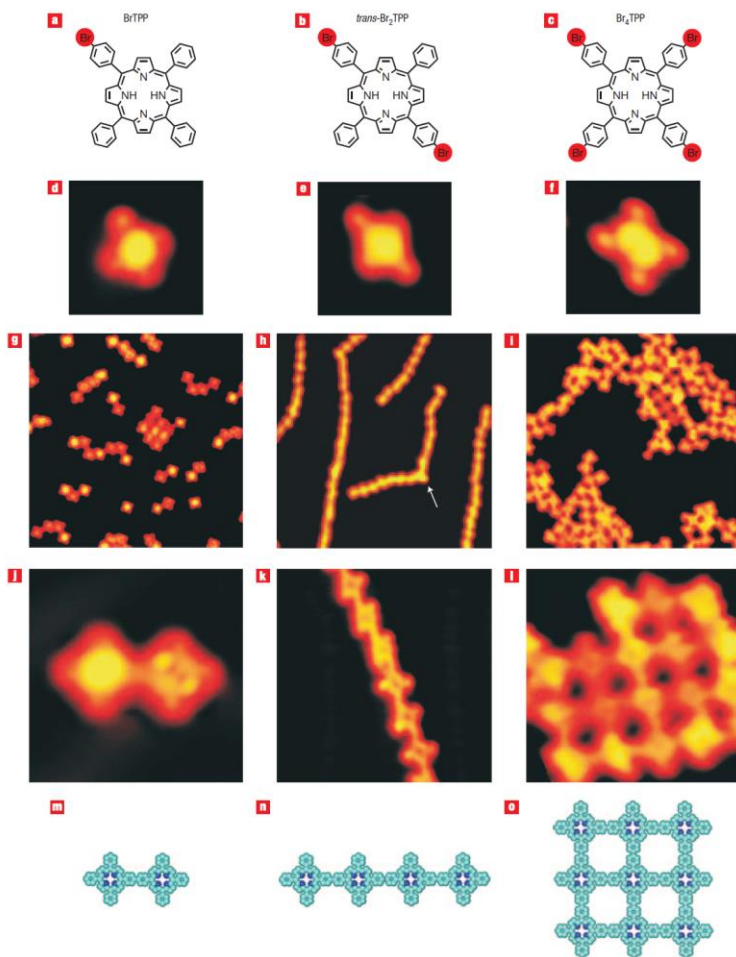


Figure 1.7 Steering of the synthesis of polymers with different dimensionalities by adding end groups in different sites of the porphyrin-based precursors. Adapted from Ref.³⁷ with the permission of Springer Nature.

respectively. After this work, the surface-confined Ullmann-type coupling was mainly focused on the synthesis of different large-scale functional conjugated polymers, such as quasi-1D graphene nanoribbons (GNRs) and 2D semiconducting, graphene-like polymers.

In 2010, Cai *et al.* first reported the synthesis of armchair-edged GNRs with atomically precise topology and controllable width through a bottom-up approach, enabling the further precise investigation of their electronic structures.³⁹ With a finely designed halogenated precursor, the first synthesis of atomically precise zigzag-edged GNRs through Ullmann-type coupling and subsequent cyclodehydrogenation on Au(111) followed several years later, in 2016 (the scheme is shown in Figure 1.8).⁴² On top of the synthesis of GNRs, with bromine-functionalized heterotriangulene precursors, Galeotti *et al.* achieved the synthesis of large-scale (greater than $100 \times 100 \text{ nm}^2$) 2D conjugated polymers with semiconducting properties on Au(111) in 2020.⁴⁵ These representative works highlight the importance of surface-confined Ullmann-type

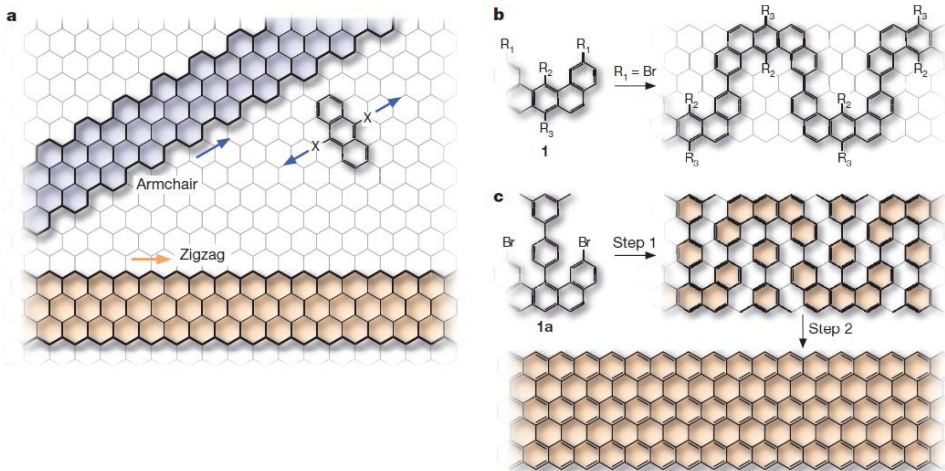


Figure 1.8 Scheme of the synthesis of ZGNRs on Au(111). a) Structural models of AGNRs and ZGNRs, which depends on the orientation of aryl–aryl coupling. **b)** Ullmann-type coupling of Br functionalized U-shaped precursors into a snake-like polymers. **c)** Synthesis of ZGNRs with precursor 1a through Ullmann-type coupling and following intro-cyclodehydrogenation. Adapted from Ref.⁴² with the permission of Springer Nature.

coupling in the synthesis of more functional nanomaterials with different dimensions, edge structures, symmetries and unique properties.

Before the formation of the final conjugated polymers, there are a number of intermediate states during the surface-confined Ullmann-type coupling process. Not only can these intermediate states themselves have unique properties, an understanding of their evolution could enable the reaction to be steered to the desired final polymerized products. Fan *et al.* reported a surface-adatom-induced phase transformation of intermediate states at 113 K on Cu(111) and at 103 K on Ag(111).⁵² Deposition of the precursor 4,4"-dibromo-m-terphenyl on Cu(111) at 90 K with subsequent annealing to 113 K can transform the halogen-bonded intermediate phase to a coordination-bonded one. A similar transformation can also be achieved by depositing the precursors on Ag(111) with subsequent heating from 88 K to 103 K.

Among all the intermediate states, OM phases are the most commonly observed and play a crucial role in the subsequent polymerization.^{40, 50, 51, 53} In 2013, by using STM and XPS, Di Giovannantonio *et al.* first gave insight into the OM intermediate of on-surface Ullmann-type coupling on Cu(110) and its evolution to polymers.⁴⁰ In the same year, Fan *et al.* demonstrated the formation of different OM intermediate states from single category of precursor but with different coverage on Cu(111).⁵¹ In addition, in 2019, Galeotti *et al.* reported an unexpected 2D OM intermediate that coexisted with the traditional 1D OM phase when the precursor 1,4-dibromobenzene was deposited on Cu(110).⁵³ As shown in Figure 1.9, with the increase

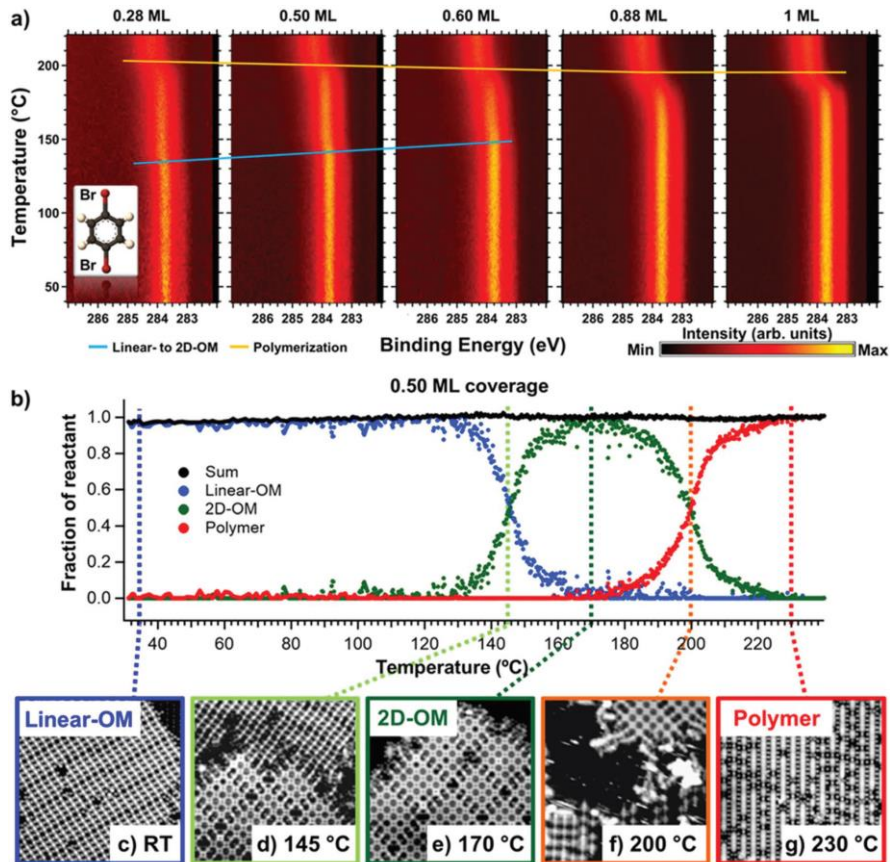


Figure 1.9 a) Fast XPS investigations of the effects of molecular coverage on the Ullmann-type coupling on Cu(110), up to 1 monolayer (ML). b) Schematic diagram of the ratio between the 1D, 2D OM phases and Polymer during sample annealing from RT to 230 °C. Corresponding STM images are also included. Adapted from Ref. ⁵³ with the permission of The Royal Society of Chemistry.

of annealing temperature to 170 °C, the ratio of 2D OM phase, which contains a four-copper-adatom cluster as the node, reaches its peak. With higher annealing, the 2D OM phase transforms into 1D polymers through Ullmann-type coupling as previously reported. During the continuous investigation of Ullmann-type coupling, more OM intermediate states have been found, suggesting the research of intermediate phases in Ullmann-type coupling has not reached its end. Greater efforts are required to achieve the rational control over the structures of OM phases to take advantage of them to steer the formation of polymers.

The choice of halogen atoms in the precursor is another key factor which plays a critical role in steering the on-surface Ullmann-type coupling. In 2017, Galeotti *et al.* systematically analyzed the influence of halogen type on the molecular superstructures, reaction temperatures and kinetics using STM, fast XPS and near edge X-ray absorption fine structure spectroscopy.⁴⁷ From the fast XPS data, the starting and ending temperatures in different reaction steps can be easily interpreted (as shown in Figure 1.10). The onset and

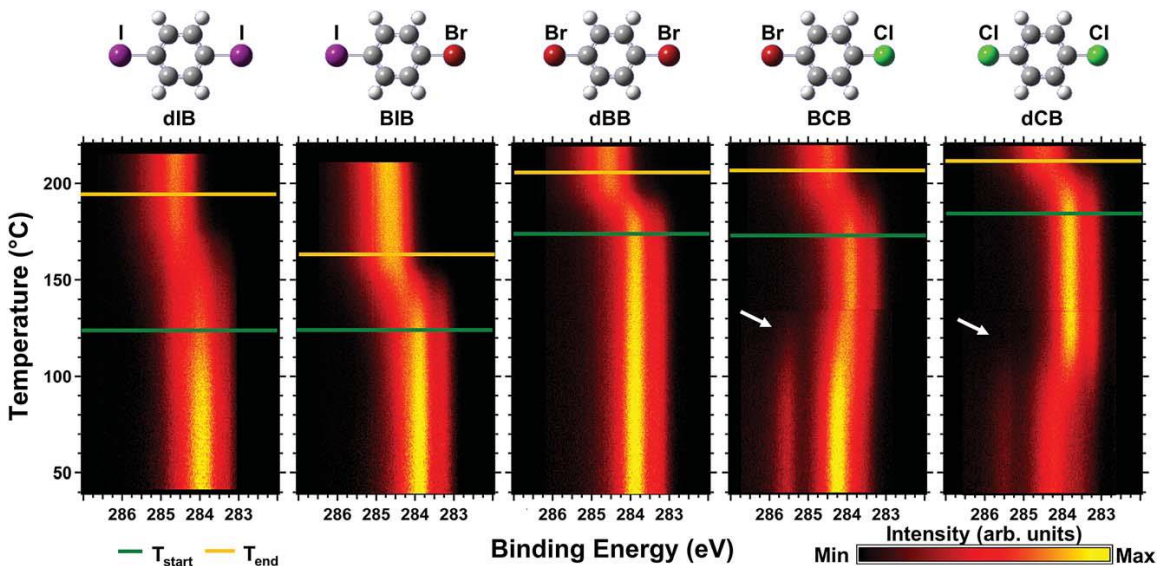


Figure 1. 10 Fast XPS measurements of C 1s core level by annealing precursors functionalized with different halogen atoms on Cu(110). Adapted from Ref. ⁴⁸ with the permission of The Royal Society of Chemistry.

range of reaction temperature are clearly different for different halogenated precursors. In addition, in 2018, Di Giovannantonio *et al.* reported that iodine functionalized monomers lead to the growth of longer GNRs than brominated ones.⁴⁸ By taking advantages of the different temperature thresholds for cleaving different C-halogen bonds, multiple halogen substituents can be added in particular sites within the same precursor to steer the process of surface-confined Ullmann-type coupling. On this basis, a hierarchical polymerization protocol was achieved by introducing C-Br and C-I bonds in the same precursors.⁵⁷ As Figure 1.11 shows, C-I bonds can be cleaved at RT on Au(111), whereas the cleavage of C-Br bonds requires heating to at least 185 °C. By optimizing the annealing temperature, the defects of the polymers can be efficiently decreased.

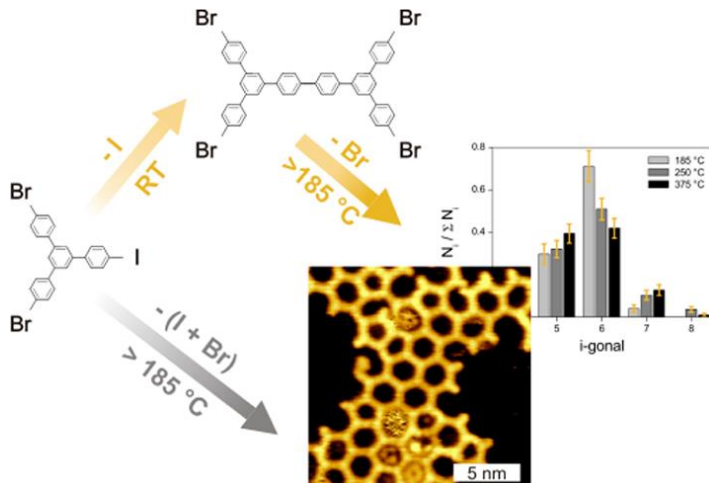


Figure 1. 11 Scheme of hierarchical Ullmann-type coupling from precursors with bromine and precursor on Au(111). Adapted from Ref. ⁵⁷ with the permission of the American Chemical Society.

In the future, I expect that more and more functional nanostructures can be synthesized by this hierarchical protocol with precisely designed halogenated precursors.

Although surface-confined Ullmann-type coupling has been widely investigated and applied in synthesizing functionalized conjugated polymers, more efforts are required to improve the quality and domain size of the structures of OM intermediates and products, and to adjust the structures to explore more interesting quantum phenomena. Beyond the synthesis on catalytic metal substrates, to achieve potential applications in actual devices, more progress is needed to be made to achieve conjugated polymers on non-metallic surfaces with surface-confined Ullmann-type coupling. Very recently, using an atomic force microscope tip for activation, Zhong *et al.* reported a versatile approach for building low-dimensional covalently bonded structures block by block on bilayer sodium chloride films on Cu(111).⁶³ In addition, post-synthetic transfer might be an alternative solution to realize conjugated polymers on non-metallic surfaces. In this thesis, to decouple the interactions from the metal substrate, we will explore the feasibility of oxidizing upper layers of Cu(111) substrate to render them semiconducting, without a detrimental effect on the products.

1.3 The effects of externally introduced co-adsorbates on surface-confined reaction

Owing to the extremely clean atmosphere, the UHV environment enables the investigation of on-surface self-assembly and reactions with practically no influence of contaminants. In addition, UHV makes it possible to prepare atomically flat single-crystal substrates through cycles of ion sputtering and annealing. One further advantage that remains underexplored is that extrinsic co-adsorbates can be controllably introduced into the UHV environment along with the (intrinsic) molecular building blocks to modify their self-assembly and reaction. This strategy represents a potential versatile technique to control surface-confined nanostructures by adjusting the phase, the amount and the adsorption rate of introduced species. In general, the atomic co-adsorbates can be divided into two categories, metals (including small atomic clusters) and non-metals (e.g., hydrogen, oxygen and halogens).

Metals are known to play a critical role in traditional chemistry as catalysts or essential components of the products (such as metal-organic frameworks). As mentioned above, in surface-confined Ullmann-type

reactions, the intrinsic metal atoms abstracted from the substrates can also hinder the C-C coupling by forming organometallic intermediates. This highlights the important role of the metal atoms in surface reactions. It is noteworthy here that whether the metal atoms are abstracted from the terraces or come from step edges is still under debate.⁶⁴ Besides the intrinsic metal atoms abstracted from the substrates, metals can be controllably introduced externally onto the surface through specific metal evaporators. The metals can then steer the reactions in two main ways, acting as catalysts to facilitate the reactions which exhibits the characteristics of heterogeneous catalysis or participating in the construction of final structures in a specific form (e.g., as the connecting nodes in the 2D metal-organic networks).⁶⁵⁻⁶⁹

Since 1990s, scientists in the area of catalysis have been focused on the investigation of the role of surface-supported gold particles on chemical reactions. As reported, although gold is less active than the other transition metals, gold particles dispersed on TiO₂ surface exhibit an extraordinarily high activity for catalyzing various reactions, such as the reduction of nitrogen oxides, the oxidation of hydrocarbons, etc.⁷⁰ A typical example is that surface-supported gold clusters can promote the oxidation of carbon monoxide at low-temperature (for example at 40 K). The catalytic activity is highly related to the choice of substrates, fabrication methods and size of the gold clusters. The turnover frequencies of the oxidation undergo a steep decrease when the diameters of the Au clusters fall below 3.5 nm.⁷¹ Based on this, in 1998, D. W.

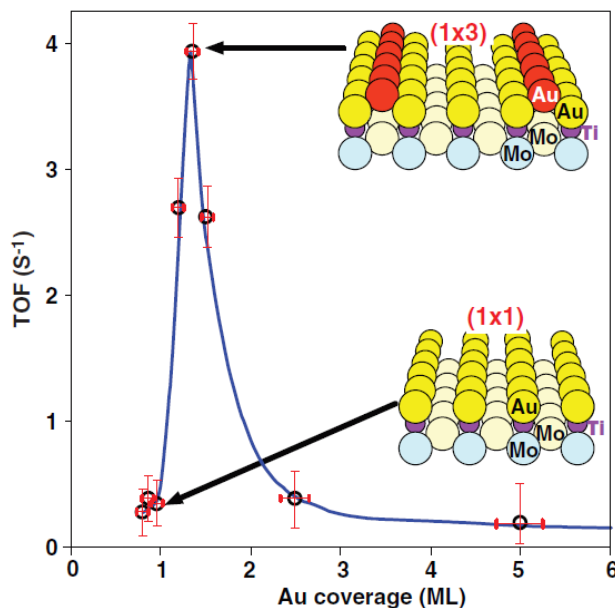


Figure 1.12 Structural models of gold (1×1) monolayer and additional (1×3) bilayer on titania surface grown on Mo(112) surface, and the variation of turnover frequency with the gold coverage. Adapted from Ref. ⁷¹ with the permission of the American Association for the Advancement of Science.

Goodman's team further investigated the catalytic activity of gold clusters supported by a single-crystal titania surface at the atomic level by using STM and scanning tunneling spectroscopy (STS), revealing the quantum size effect regarding the thickness of the gold clusters. Gold clusters with two layers were demonstrated as the most efficient structures in catalyzing the oxidation of carbon monoxide. In addition, the proper band gaps (0.2-0.6 V) are possessed by two-layer gold with diameters ranging from 2.5 to 3.0 nm. This is consistent with the Au/TiO₂ model with maximum activity in catalysts, implying the potential relationship between the catalytic properties and metal-nonmetal transitions induced by quantum-size effects. Furthermore, to eliminate the effects from the shape of the clusters and the supporting substrate, they created a (1×1) monolayer and a (1×3) bilayer gold that fully cover the titania surface grown on Mo(112) surface. The structural model of the gold layers and their relationship to turnover frequency are shown in [Figure 1.12](#), suggesting that (1×3) bilayer gold is significantly more active than the monolayer structures by an order of magnitude. Besides gold, several other metal clusters (such as copper, platinum, Palladium, etc.) supported on specific surfaces also exhibit unique catalytic properties.⁷¹⁻⁷³

With STM, more traditional organic reactions have been studied in-depth on surfaces at the molecular scale. As well, the catalytic properties of metals on these reactions have been investigated in detail. In many surface reactions, the intrinsic metal atoms from the substrate play a role as catalysts. To more flexibly

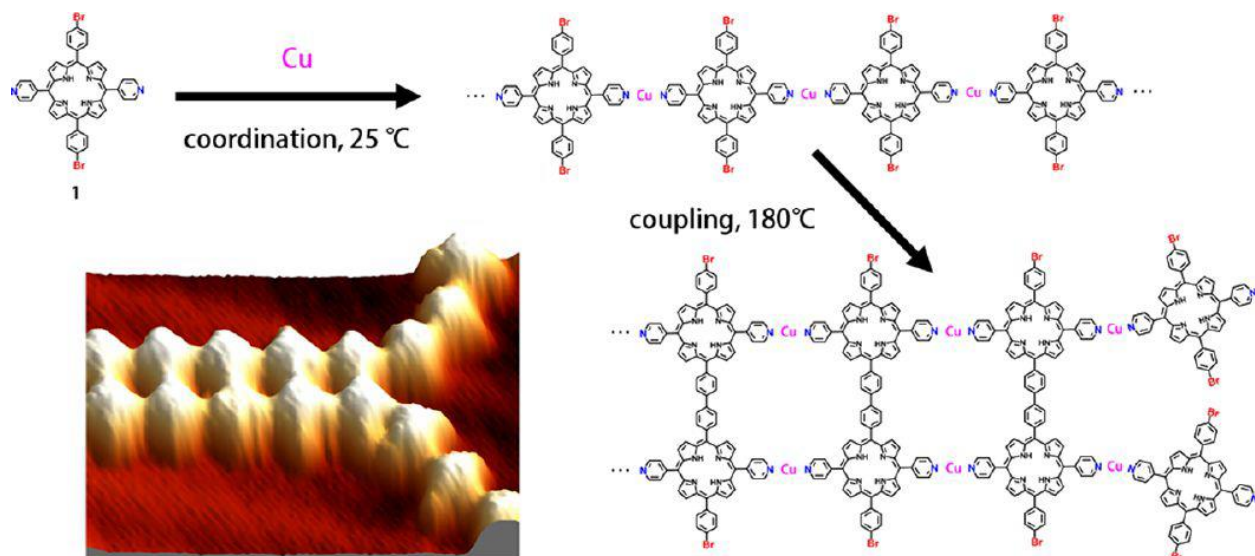


Figure 1.13 Scheme of controlling polymer structure by Cu-directed template. Deposition of porphyrin derivative precursors with pyridyl and bromine end groups on Au(111) pre-decorated with Cu atoms forms a 1D coordination structure, which further steers the following polymerization through annealing. Adapted from Ref. ⁶⁵ with the permission of the American Chemical Society.

investigate the catalytic mechanism, compare the catalytic properties of different metals, and steer the reaction pathway and formation of different products, the desired metals can be externally introduced on the surface at specific steps of the reactions. By introducing Cu atoms onto the more inert Au(111) surface, Lin *et al.* achieved Cu-mediated Ullmann-type coupling with a porphyrin precursor containing pyridyl and bromine end groups (the scheme is shown in [Figure 1.13](#)).⁶⁵ Besides their catalytic effect, the introduced Cu atoms play an additional role in this reaction, forming coordination structures that act as a template to guide the further C-C coupling, which will be discussed below. Based on this work and considering the excellent catalytic activity of palladium (Pd) in wet chemistry,⁷⁴ they further investigated and compared Pd and Cu-catalyzed homocoupling of aryl bromide on Au(111).⁶⁶ There are two main steps in this reaction, activation of C-Br bonds and subsequent C-C coupling. Comparing the same reaction on Au(111) in the absence of additional metal atoms, the introduction of Pd or Cu can both lower the activation temperature and yield more and longer polymers, yet the catalytic mechanisms of Cu and Pd are distinctive. Based on the statistical results of the length distribution of the polymer products and a kinetic Monte Carlo (KMC) algorithm (as shown in [Figure 1.14](#)), the sample with Pd atoms has a lower energy for activation of C-Br bonds in the precursor than the Cu-containing sample, leading to a decrease in the extent of un-activated species. As a result, the activated monomer has a smaller chance to encounter un-activated species, which

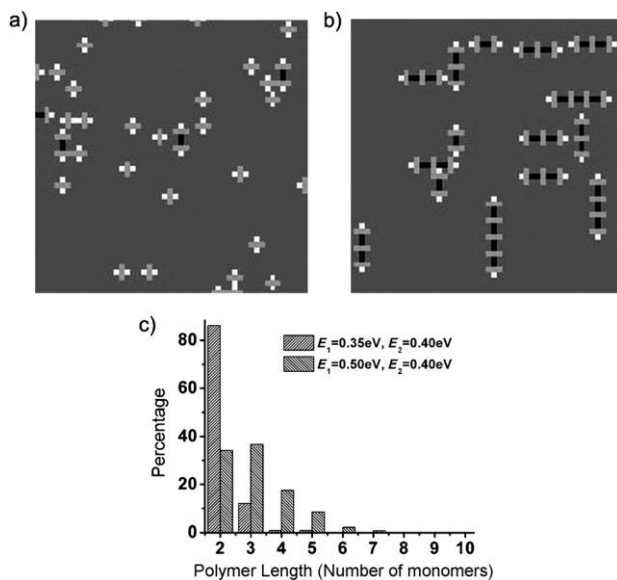


Figure 1.14 Monte Carlo simulation of the formation of polymerized chains after heating 120 minutes at 400K. E_1 is the activation energy of halogenated precursor. E_2 is the energy of subsequent C-C coupling. Accordingly, a smaller E_1 leads to shorter polymers. Adapted from Ref. ⁶⁶ with the permission of John Wiley and Sons.

impedes the following C-C coupling. Therefore, in this case, Cu is more favorable than Pt in catalyzing the C-C coupling and promoting the formation of longer polymerized chains.

Based on the investigation of Cu-catalyzed Ullmann-type reaction on Au(111) and the different activation energies of C-Br and C-Cl bonds, 2D covalently bonded networks can be synthesized in a hierarchical manner with a precursor containing both Br and Cl atoms.⁷⁵ As the scheme and STM images in Figure 1.15 show, annealing the precursor on pure Au(111) at 453 K leads to the debromination and formation of dimers with intact C-Cl bonds. After introducing Cu atoms and annealing the sample at 413 K, C-C coupling can be triggered through dechlorination. The formation of the final 2D covalent organic frameworks can be induced by a higher annealing at 553 K. This work further confirmed the advantages of introduced metal catalysts in programmed on-surface synthesis. Besides metal substrates, Pd and Cu were demonstrated to catalyze the Ullmann-type reaction on hexagonal boron nitride layers, further confirming the catalytic activity of Pd and Cu on chemically inert surfaces.⁶⁸ In addition to Cu and Pd, Cu(111)-supported cobalt (Co) nanoparticles can catalyze Ullmann-type coupling at a lower temperature.⁷⁶ Although most of the mentioned investigations of metal-catalyzed surface-confined reactions focused on Ullmann-type coupling due to its widespread and flexible applications in synthesizing conjugated polymers, there are a few studies examining other organic reactions. Zhang *et al.* reported Pd-catalyzed Sonogashira cross-coupling reactions on Au(111) surface. Pd was introduced onto the sample externally after the formation of different

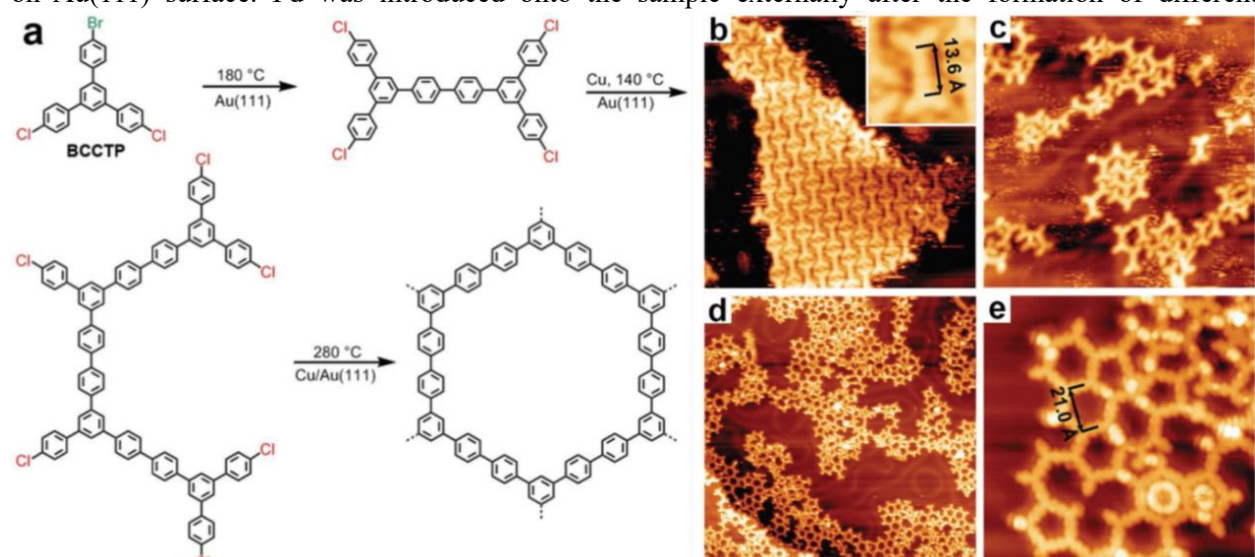


Figure 1.15 a) Scheme of the formation of 2D covalent organic frameworks with externally introduced Cu on Au(111) in a hierarchical manner. b)-e) STM images of the aryl chloride dimers, dechlorinated products and final 2D networks, respectively. Adapted from Ref. ⁷⁵ with the permission of The Royal Society of Chemistry.

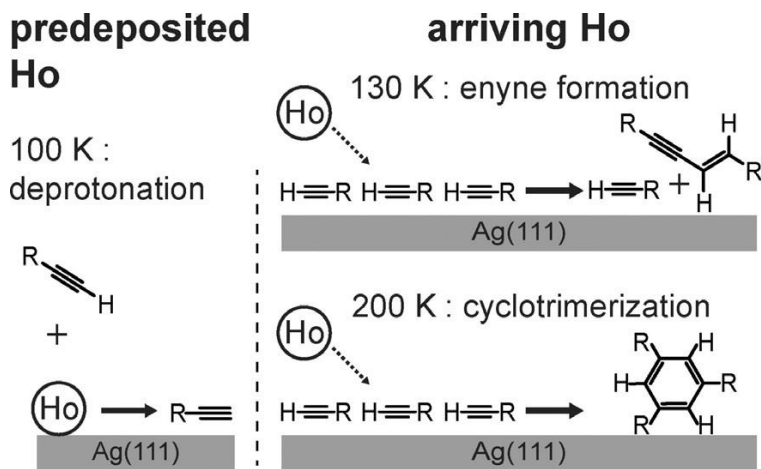


Figure 1.16 Scheme of Ho-catalyzed coupling of terminal alkynes on Ag(111). Adapted from Ref.⁸⁰ with the permission of John Wiley and Sons.

coordinated structures linked by Fe or Cu, contributing to the yield of different Sonogashira cross-coupled products.⁶⁹ As well, the introduction of Pd can assist the Heck reaction of aryl bromides with alkenes on Au(111).⁷⁷

Besides the d-block transition metals, f-block lanthanide metals and corresponding metal oxides play a critical role in surface-confined coordination chemistry and industrial catalysis. Remarkably, lanthanum ions are reported to promote the formation of 3D graphene by catalyzing the carbonization of ethylene or acetylene.⁷⁸ Recently, lanthanide metals have also been demonstrated to be excellent catalysts for surface-confined reactions. Externally introduced dysprosium (Dy) atoms can promote the debromination of 4,4"-dibromo-p-terphenyl (DBTP) on Ag(111).⁷⁹ Even at room temperature, the addition of Dy can drive the transformation of the self-assembly phase of intact DBTP on Ag(111) to an organometallic phase. This transformation is caused by the debromination of DBTP and subsequent incorporation of Dy in C-Dy-C bonds. As a comparison, the debromination of DBTP and formation of the organometallic phase on pure Ag(111) requires a higher annealing temperature of 340 K. However, only dimers can be synthesized after further annealing the Dy-containing sample, implying a detrimental effect of Dy on Ullmann-type coupling. On the other hand, the rational control over the length of C-C coupled polymers by the externally introduced Dy provides a potential approach for designing polymers with constrained dimension on surfaces. As well, another lanthanide metal holmium (Ho) was demonstrated to catalyze the coupling of alkyne-containing monomers.⁸⁰ Ho acted as mobile isolated adatoms on weakly reactive Ag(111) surface at low temperature, through the reaction scheme shown in [Figure 1.16](#). The co-adsorption of Ho atoms and monomers on the

$\text{Ag}(111)$ leads to the deprotonation of the alkyne at low temperature (100 K). Importantly, the extrinsic Ho atoms on monomer-covered $\text{Ag}(111)$ can trigger the enyne-linked dimerization and cyclotrimerization at 130K and 200 K, respectively. In the future, the investigation of more lanthanide metals on different noble metal substrates or 2D material decorated surfaces are called for, to explore their catalytic properties on different reaction and steer the formation of more novel nanostructures.

Beyond acting as catalytic species, the extrinsic metal atoms can also participate in the coupling reaction by passivating the radials to form organometallic intermediates (with *covalent* carbon-metal bonds).⁶⁸ Instead of the more common intrinsic surface metal adatoms, different metal atoms can be selected to form specific OM structures on more inert surfaces. In addition to the formation of OM intermediates, the extrinsic metal atoms can link the building blocks at the designed functional sites to form targeted metal-organic, *coordinated* structures. These weaker linked structures could further act as templates to steer the subsequent formation of covalently coupled structures. Until now, $-\text{COOH}$, $-\text{C}\equiv\text{N}$, $-\text{C}=\text{NH}$, $-\text{OH}$, $-\text{C}=\text{O}$ and pyridine are the most common groups used in the ligand to coordinate with specific metal adsorbates, including Fe, Co, Cu, Ni, and lanthanide metals.^{65, 67, 69, 81-97}

The properties (e.g., size, symmetry and chirality) of metal-organic coordinated structures can be rationally controlled by adjusting the number and active sites of coordination groups in the building blocks and by using different metal atoms. In 2002, Klaus *et al.* reported the formation of chiral metal-organic structures on $\text{Cu}(001)$ using an achiral precursor 1,3,5-tricarboxylic benzoic acid with co-deposited Fe atoms.⁸¹ The cavity size of $-\text{C}\equiv\text{N}$ and Co-coordinated structures can be adjusted by using monomers with

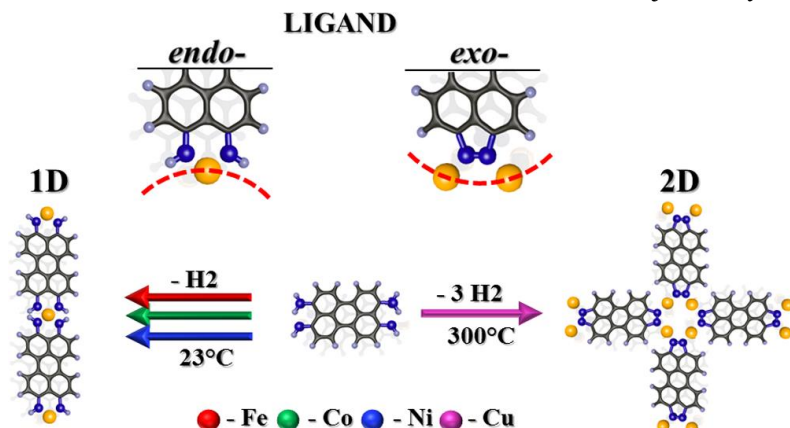


Figure 1.17 Scheme of the formation of 1D and 2D metal-organic structures due to the modification of dehydrogenated precursors by different externally introduced metal atoms. Adapted from Ref. ⁹⁰ with the permission of the American Chemical Society.

different lengths.⁸² The simplest way to change the symmetry of metal-organic structures is to use organic monomers with different symmetry, such as square structures from fourfold monomers and hexagonal structures from threefold monomers. In addition, the symmetries of metal-organic structures can also be tuned by using different metal centers (Co or Fe) and functional groups (-C≡N or -OH).⁸³ However, the intrinsic symmetries of coordinated structures stay stable over the influences from different substrate symmetry, implying their higher thermal stability and structural flexibility than hydrogen-bonded 2D networks.⁸³ Besides traditional 1D chains or 2D networks, the externally introduced Fe atoms can coordinate pyridine functionalized 120° V-shaped monomers to form fifth-order Sierpiński triangles, which is a classic fractal structure with 1.58 Hausdorff dimension.⁹¹ The dimensionality of the metal-organic structure can also be controlled by tuning the metal atoms, as shown in [Figure 1.17](#).⁹⁰ The dehydrogenation of nitrogen-containing functional groups in the monomers can be modified by different metals, contributing to the formation of metal-organic structures with different dimensions. The 1D and 2D structures can be formed from an endo-ligand and an exo-ligand, respectively. In addition, the metal-organic structures can be applied in the area of constitutional dynamics, which relies on the breaking of equilibrium in reversible formation to achieve continuous adjustments in constitution by reorganization of components.⁶⁷ By co-depositing organic building blocks and Ni atoms on Au(111), the reversible structural transformation of on-surface metal-organic structures can be realized.

Due to the structural flexibility of on-surface metal-organic structures stabilized by the externally introduced metals, multiple active groups could be added in the ligand precursor to further steer the formation of coupled structures in a hierarchical manner. As mentioned before, externally introduced Cu atoms can catalyze the Ullmann-type coupling of brominated porphyrin precursors on Au(111), as shown in [Figure 1.13](#). By including both pyridyl and bromine end groups in the precursor and adjusting their sites, deposition of the precursor on Au(111) at RT leads to the formation of metal-organic structures stabilized by pyridine – Cu interactions. Further annealing leads to the debromination and subsequent C-C coupling in the perpendicular direction. The structure of final polymer is determined by the pre-formed metal-organic structures that work as a template in this reaction.⁶⁵ By changing the numbers and sites of pyridine groups and using different metal centers, Zhang *et al.* demonstrated the formation of different metal-organic

structures and their application as templates to steer the Sonogashira cross-coupling reactions on Au(111).⁶⁹

In addition, a variety of metal-organic networks can be used as templates with unique electronic properties in host-guest chemistry.^{98, 99}

In conclusion, externally introduced metal species (including d-block transition metals and f-block lanthanide metals) can either catalyze surface-confined reactions or coordinate functionalized ligands to form metal-organic structures on surfaces. Combined with finely designed precursors, the co-adsorbed metal atoms could be further applied in steering the pathways of reactions. In the future, as the field of on-surface synthesis continues to develop rapidly, I expect externally introduced metals to play a larger role as a versatile approach to catalyze new coupling reactions, optimize the reaction pathways, and produce novel nanostructures.

Apart from metal species, externally introduced nonmetals (e.g., halogens, oxygen, hydrogen, sulfur, NaCl) can also play an important role in surface-confined reactions, which have been more widely studied in recent years. Nonmetallic species are introduced into UHV in the gas phase to steer the reactions by mainly interacting with the pristine reactants in molecular or atomic phase.

As mentioned in the discussion of metal species, constitutional dynamics can be implemented on a solid surface by adding either the metal atoms or ligand molecules in the metal-organic coordination structures.

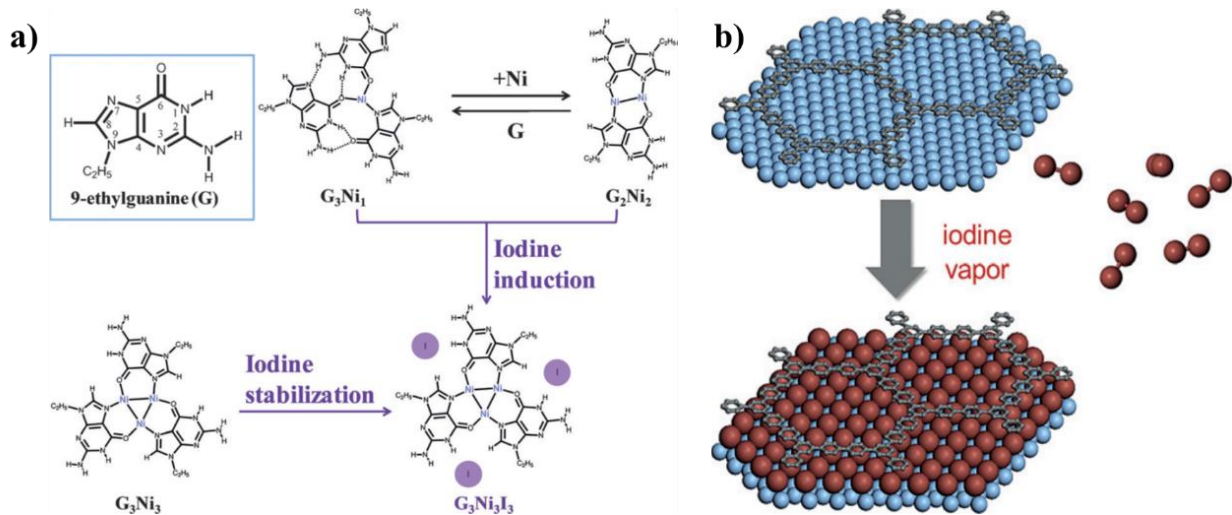


Figure 1.18 a) Scheme of structural transformation and stabilization of Ni-centered metal-organic motifs induced by the doping of iodine. Adapted from Ref. with the permission of John Wiley and Sons. **b)** Schematic diagram of the intercalation of a iodine monolayer between 2D polymers and Au(111) or Ag(111) surfaces. Adapted from Ref.¹⁰⁰ with the permission of John Wiley and Sons.

In this context, Xie *et al.* investigated the effects of different halogen atoms (I, Br, Cl) on metal–organic systems.¹⁰⁰ As the scheme in [Figure 1.18a](#) shows, by introducing iodine atoms on Au(111), the pristine Ni-coordinated structures can be transformed entirely to three Ni-atom centered coordination motifs. This coordinated structure is stabilized by iodine atoms via electrostatic interactions, and along with hydrogen bonding leads to the formation of a 2D honeycomb structure. The coordination structural transformation and stabilization induced by iodine atoms were demonstrated also for Cl and Br atoms and other coordination systems, showing the versatility of this approach.

A different application of iodine is to controllably decouple the interaction between surface-confined polymers and metal substrates, as demonstrated for 2D conjugated polymers on Ag(111) and Au(111).¹⁰¹ This work was motivated by the detachment of covalently bonded structures on metal substrates induced by intrinsic dissociated iodine atoms. In 2016, using STM, XPS and DFT calculations, Rastgoo-Lahrood *et al.* demonstrated that the externally introduced iodine atoms can overcome the interaction between the polymers and substrates to penetrate through and remain under the 2D polymers on Ag(111) or Au(111), through the scheme shown in [Figure 1.18b](#).^{102, 103} The decoupling of electronic interactions between the polymers and substrates due to the intercalation of iodine monolayer was supported by simulation of the partial density of electronic states (PDOS). Compared to the gas-phase PDOS, the PDOS projected on the polymer supported by bare Ag(111) changes significantly, whereas there is little change for the polymer above intercalated iodine atoms. This suggests that iodine intercalation could enable the investigation of the intrinsic properties of the surface-supported polymers. In addition, the STM images show that the decoupled polymers on Au(111) exhibit similar features to the spatial distribution of frontier molecular orbitals, providing further evidence of the de-hybridization of the electronic states between molecules and metal surface. On top of the decoupling effect, the externally introduced iodine monolayer can be used as an inert substrate that can still be imaged by STM. The C-C coupling on the I-passivated Au(111) was obtained by the generation and deposition of radicals, demonstrating a potential approach to realize coupling on inert surfaces.¹⁰⁴

Beyond halogen atoms, the effects of several other inorganic species (such as H, S and O) on surface-confined reactions have also been investigated. Hydrogen plays a critical role in traditional chemical

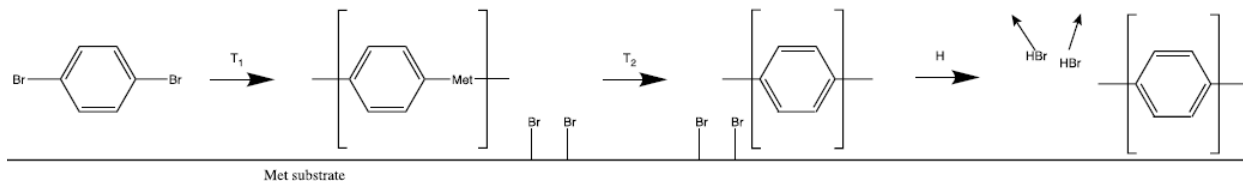


Figure 1.19 Scheme of Ullmann-type coupling on Cu(111) or Cu(110) surface and further cleaning up of Br byproducts by introducing hydrogen. Adapted from Ref. ¹⁰⁷ with the permission of the American Chemical Society.

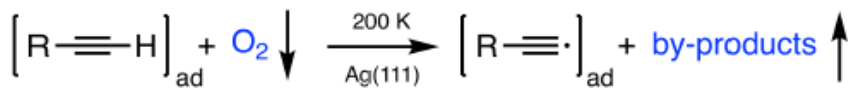
reactions, mainly as a reductant, and is involved in a number of surface-confined hydrogenation and dehydrogenation reactions. This motivated the investigations of the effects of externally introduced hydrogen on surface-confined reactions. Using temperature-programmed desorption and complementary DFT calculations, C. Bronner *et al.* demonstrated that the bromine byproducts generated during the synthesis of GNRs on Au(111) can be removed by introducing molecular hydrogen.¹⁰⁵ Specifically, atomic H generated by the dissociation of molecular hydrogen on Au(111) could subsequently couple the adsorbed bromine and desorb as molecular HBr. The dosing of molecular hydrogen and removal of Br byproducts after the formation of polyanthrylene chains has no detrimental influence on the further cyclodehydrogenation to GNRs, implying that this strategy is a general and safe method to remove the halogen byproducts. Based on this work, V. Tran *et al.* demonstrated that in Ullmann-type coupling on Au(111) and Cu(111), thermal activation with concurrent H-dosing treatment can promote the C-C coupling at lower temperature with improved structural ordering, together with the elimination of halogen byproducts.¹⁰⁶ In 2019, using STM and XPS, Abyazisani *et al.* further systematically investigated the effects of atomic hydrogen on surface-confined Ullmann-type coupling.¹⁰⁷ After exposing the surface to atomic hydrogen at RT, the bromine atoms that were aligned between polymers could be totally removed (see scheme in [Figure 1.19](#)), which led to the polymers becoming more randomly distributed. Therefore, this implies that the absorbed bromine atoms can drive the ordered alignment of the linear polymers. Very recently, Sun *et al.* reported that externally introduced silicon can play the similar role as hydrogen in removing the bromine byproducts generated during the synthesis of GNRs.¹⁵ Introducing silicon atoms after the formation of 5-AGNRs can trigger the formation of highly volatile silicon tetrabromine even at RT, which can desorb from the Au(111) substrate by mild annealing. Beyond removing the halogen byproducts, the externally introduced atomic hydrogen can passivate the radicals during the transformation from OM intermediates to C-C coupled polymers.¹⁰⁸ This strategy can be used to constrain the elongation of the

polymer to obtain ribbons with the desired length. Therefore, modification of the structures and lengths of synthesized GNRs can be achieved, which could further controllably tune the electronic properties of the GNRs. Besides its influence on surface-confined Ullmann-type coupling, H can change the chemical structure and nature of an active layer adsorbed on Pd(111), an allyl cyanide self-assembly, through hydrogenation of the ligand precursor.¹⁰⁹

In addition, the effects of H₂S and H₂ on Ullmann-type coupling were also investigated.¹¹⁰ Ullmann-type coupling on Au(111) can be completely inhibited by initially decorating the substrate with H₂S gas to passivate the free Au atoms in the form of S–Au complexes. Coupling can then be switched on again by exposure to H₂ gas at 673 K. This work highlights the on-off switching of a coupling reaction using gaseous adsorbates.

Oxygen is one of the most common elements in daily life and broadly involved in traditional in-solution reactions. As well, oxygen plays a critical role in many surface-confined reactions, such as promoting C-H activation. In 2017, Niu *et al.* reported oxygen-promoted methane activation on Cu(111) precovered with oxygen atoms.¹¹¹ According to the DFT calculations, the dissociated CH₃ and hydrogen are formed from a transition state which is stabilized by a dipole–dipole attraction, leading to a relatively low activation energy barrier of 137 kJ/mol. Beyond C(sp³) - H activation, Orozco *et al.* demonstrated the catalytic role of co-adsorbed oxygen on Glaser coupling on Ag(100).¹¹² Through DFT calculations, they demonstrated that the catalytic effect is due to an oxygen-induced exothermic reaction pathway involving the formation of OH as the reaction-initiating step. Moreover, this catalytic role of oxygen is also reflected in the Ag-particle-catalyzed Glaser–Hay coupling in solution.¹¹² In addition, Zhang *et al.* reported the fabrication of

Step i (O₂-mediated terminal alkyne deprotonation):



Step ii (on-surface alkynyl–Ag–alkynyl bond formation):



Figure 1. 20 Two steps of O₂ gas mediated formation of Alkynyl-Silver Networks on Ag(111). Step1: O₂ gas promotes the C-H activation. Step 2: the dissociated alkynyl radicals bond the Ag adatoms to form OM networks. Adapted from Ref. ¹¹³ with the permission of the American Chemical Society.

micrometer scale OM honeycomb alkynyl–silver networks on Ag(111), which is mediated by the C(sp) - H activation induced by O₂ gas (shown as [Figure 1.20](#)).¹¹³ Furthermore, they demonstrated that this reaction cannot be achieved by the introduction of CO or H₂O. This work opens a new gate of the combination of UHV surface-confined reactions and gas induced chemical modification. Taking advantage of the high structural flexibility of organic ligands and the high mobility of metal centers in metal-organic coordination networks (MOCNs), Fabris *et al.* reported the oxygen-induced structural modification of MOCNs, mimicking functions of the cofactors of non-heme enzymes.¹¹⁴ DFT calculations revealed that the mechanism of the dissociation of introduced O₂ gas is related to the cooperative catalytic action of the two Fe²⁺ centers. The effects of O₂ exposure in UHV on the self-assembly structures and polymerization process of melanin monomers on Au(111) and Ag(111) have also been explored.^{115, 116} Due to the oxidation via O₂ exposure, the hydroxyl group in the melanin monomer allows for redox reactions, , resulting in molecular rearrangement.

Last but not least, the chemisorption of oxygen on copper single-crystal surfaces can drive the formation of different reconstructed phases,^{117, 118} which could further affect the behaviors of deposited molecules. Oxidized copper is a semiconducting material, so oxidation of the surface after surface-confined synthesis of the target nanomaterial is a potential approach to decouple the interaction of the metallic substrate and investigate the material’s intrinsic properties.¹¹⁹ Compared to the monolayer of iodine or thin layers of NaCl, which have similar effects, oxidized copper is more straightforward.

Although a great number of investigations of oxygen in surface chemistry have been reported, the effects of oxygen on Ullmann-type coupling had not yet been studied. Therefore, we systematically examined the influence of externally introduced oxygen on different steps of Ullmann-type coupling on Cu(111), which is the subject of Chapter 3 and Chapter 4.

Beyond atomic or gaseous species introduced on surfaces to steer reaction pathways, layers of the metal compound NaCl have been demonstrated to work as insulating layers to decouple the electronic interactions between the metal surfaces and synthesized materials. This strategy has been widely applied in investigating the electronic structures of GNRs by STS.^{120, 121} As shown in [Figure 1.21](#), following the introduction of NaCl islands after the formation of 7-AGNR, the 7-AGNR can be dragged onto the NaCl layer by STM

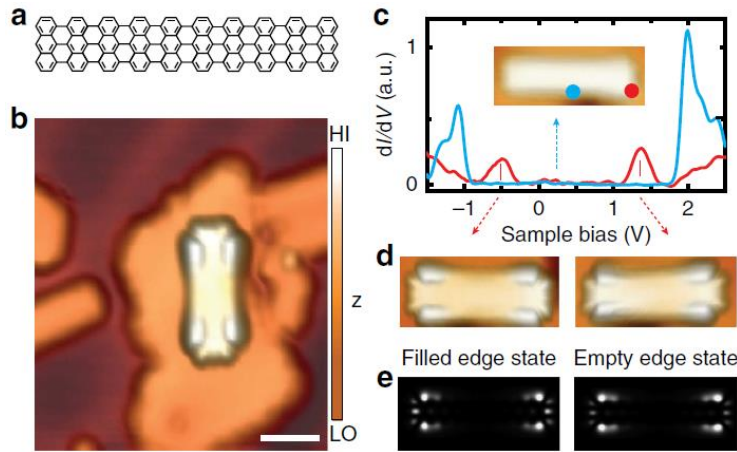


Figure 1.21 a) skeletal structure of 7-AGNRs. b) STM image showing a 7-AGNR on an NaCl island supported by Au(111). c) STS measurements taken in the center (blue) and at a zigzag end (red) of the ribbon. d)-e) STM topography images and corresponding local density of empty and filled states at the edge of the ribbon. Adapted from Ref. ¹²¹ with the permission of Springer Nature.

manipulation. As a result, STS measurements demonstrated that the intrinsic electronic properties can be obtained.

In conclusion, externally introduced inorganic co-adsorbates play an important role in surface organic chemistry by catalyzing or mediating the process of reactions, tuning the structures of products, removing the reaction byproducts or decoupling the electronic affections from the metal substrates. In the future, to contribute to the development of surface science from the aspects of both fundamental and applied science, more systematic investigations of the effects of inorganic species on surface-confined reactions are called for to examine factors including new co-adsorbates, different chemical reactions, and the stoichiometry of the co-adsorbates vs. reactants.

1.4 Thesis objectives and organization

Surface-confined reactions represent a compelling approach to synthesize low-dimensional carbon-based materials that are inaccessible by traditional chemistry due to insolubility or aggregation. The focus of my thesis lies on the investigation of surface-confined reactions on single-crystal metal surfaces, where the reactions are catalyzed and confined in low dimensions by the supporting metal substrates. By using advanced techniques (e.g., STM, AFM) for surface characterization, one of our goals is to reveal the effects of externally introduced oxygen on surface-confined reactions, specifically Ullmann-type coupling and the

synthesis of graphene nanoribbons (GNRs). Due to its symmetry and moderately high reactivity, Cu(111) was chosen as the target substrate. First, we will examine oxygen introduced between different steps of Ullmann-type coupling to study how it will affect and steer the reaction. Secondly, we will consider oxygen introduced after the formation of narrow GNRs to explore if it could promote the synthesis of wider GNRs by lateral cyclodehydrogenation. The premise of this investigation is the successful synthesis of GNRs on Cu(111) through lateral fusion, which has never been achieved before. In the future, to achieve the synthesis of more functionalized nanostructures, we will extend our investigation with more diverse externally introduced co-adsorbates and more elaborately designed precursors.

To expand the versatility of surface-confined reactions, we set out to explore potential reactions beyond the well-studied types, that could lead to the formation of different conjugated polymers. Hence, our second goal is to study the coupling reaction triggered by desulfurization of thiophene-contained molecules (Provided by Prof. Dmitrii F. Perepichka). The radicals generated by desulfurization of thiophene groups could undergo either intra- or intermolecular coupling on surfaces, contributing to the formation of different polymerized products.

Chapter 2

Introduces the main experimental techniques and facilities we used in our projects, including scanning tunneling microscopy operated in UHV and its extended function scanning tunneling spectroscopy, and X-ray photoelectron spectroscopy.

Chapter 3

Reports the effects of oxygen on the surface-confined Ullmann-type coupling. On a bare Cu(111) surface, 4,4"-dibromo-p-terphenyl (DBTP) de-halogenates and extracts copper adatoms to form 1D OM chains at room temperature (RT). However, with the introduction of oxygen before the deposition of precursors or after the formation of OM chains, the 1D OM chains transform to a 2D ordered hexagonal networks after annealing, instead of the formation of 1D polymers that occurs in the absence of oxygen. Using STM, XPS and supported by DFT calculations, the 2D networks were confirmed as an OM phase where the OM segments are connected by oxygen-copper clusters.

Chapter 4

First, the synthesis of 3P sub-family AGNRs with DBTP on Cu(111) is introduced. After step-by-step annealing, wider ribbons (6, 9 and 12-AGNRs) can be synthesized by lateral polymerization of the poly para-phenylene (3-AGNRs). After the formation of wider ribbons, the intercalation of dissociated Br atoms under the ribbons is observed. Second, the effects of oxygen on the synthesis were explored by introducing O₂ gas after the formation of 3-AGNRs. The catalytic effect of oxygen was demonstrated as it lowered the temperature of lateral polymerization by 180 K.

Chapter 5

In this chapter, a new coupling reaction is investigated. We build on the concept of desulfurization of thiophene to develop a cascade of tandem desulfurization/cyclization reactions with unsaturated oligoene intermediates, creating a polycyclic acene structure and novel polymers from simple molecular precursors. The unexpected 1D polymer stands out for its unusual electronic properties and its exotic ladder structure that was not previously observed in either solution or surface-confined polymerization.

Chapter 6

Conclusions of this thesis are given. In addition, future work and perspectives are considered in light of the achievements of this work.

Chapter 2. Experimental methods and techniques

2.1 Scanning tunneling microscopy

Scanning tunneling microscopy (STM) is a category of microscope that can measure surface-supported structures at sub-molecular or even atomic scale. It was invented in 1981, by the German physicist Dr. Gerd Binnig and Swiss physicist Dr. Heinrich Rohrer at IBM Zürich. For their invention, they were awarded the Nobel Prize in Physics in 1986. The working principle of STM is shown in [Figure 2.1](#), and is based on a sharp metal tip that can be precisely controlled by piezoelectrics in three perpendicular dimensions. In the present work, sharp tips were produced by electrochemical etching of tungsten wires. When the tip is sufficiently close to the sample, the applied bias drives electrons to tunnel through the potential barrier between the tip and sample and generate a tunneling current. This process is known as the quantum tunneling effect, the details of which will be further discussed below. In general, the tunneling current is related to the applied bias, the height of the tip relative to the surface and the local density of states (DOS) of the surface material. Therefore, when the tunneling current and applied bias are set at a fixed value, the height can be adjusted by feedback electronics to ensure a constant current value. When the tip is scanned across the surface in this mode, the acquired image will thus contain a convolution of topographical and electron density information. Similarly, STM can also work in constant-height mode where the height of tip and applied bias are fixed. Operation in constant height mode is faster than constant current mode, but

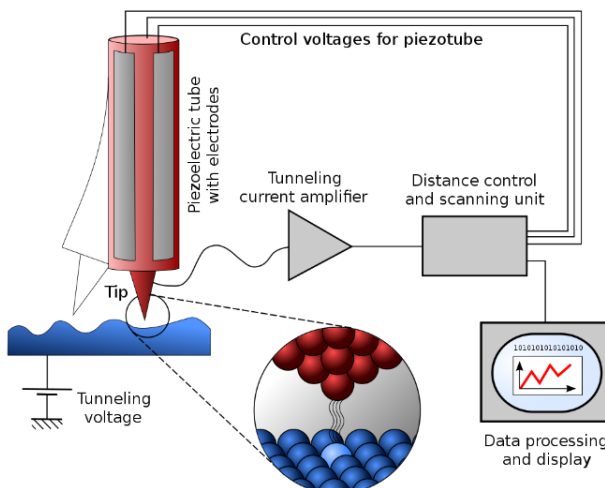


Figure 2. 1 Schematic diagram of the scanning tunneling microscope. The image is available under the Creative Commons Attribution-ShareAlike License of Wikipedia.

the tip will have a higher risk of crashing.

Compared to other, conventional microscopes, the striking advantage of STM is the ultrahigh resolution in both the lateral and depth dimensions (ideally, 0.1 nm lateral resolution and 0.01 nm depth resolution, referred to Wikipedia item of “Scanning tunneling microscope”). The actual resolution is highly related to the radius of curvature of the scanning tip. The ideal single-atom sharp tip is always essential for good quality imaging. To keep the tip in a good condition and reduce the probability of being contaminated, the extremely clean environment of UHV is beneficial. However, STM can also be performed in ambient conditions, which defines the second main working mode of STM. A good tip can survive and be regenerated for more than one year in UHV with proper preservation, whereas the tip needs to be replaced every day in ambient STM (typically by fine cutting of Pt-Ir wire). In addition, the methods of preparing the sample and the focus of investigation in UHV and ambient STM are different. In ambient STM, the sample is prepared in air, typically by drop-casting the solution of interest. In this thesis, all the experiments were conducted in UHV, where the sample was prepared by depositing reactants on clean surfaces, in the same chamber as the STM head or a separate molecular beam epitaxy chamber.

One of the main limitations of STM is that in order to generate a tunneling current, the substrate must be conductive (such as metal substrates or highly oriented pyrolytic graphite) or semiconductive (such as silicon substrate). The substrates used in our projects will be comprehensively introduced in the next section.

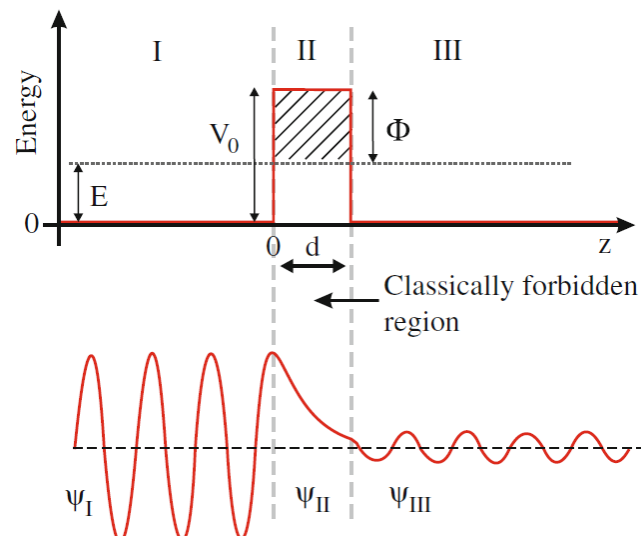


Figure 2. 2 Schematic diagram of a one-dimensional metal-vacuum-metal tunneling junction. Adapted from Ref. ¹²² with the permission of Springer.

As mentioned before, the basic physics behind STM is the quantum tunneling effect, which I will now introduce in more depth. First, I will consider a 1-dimensional case to solve the problem of the tunneling junction (tip-gap-sample), as shown in [Figure 2.2](#).¹²² A potential barrier $V(z)$ is assumed with height V_0 above the bottom of the potential ($V = 0$) in the gap area between $z = 0$ & d . An electron of energy E is incident upon an energy barrier of height V_0 . The potential is time-independent, so the energy levels $\psi_n(z)$ of the electrons can be expressed as the solution of Schrödinger's equation:

$$-\frac{\hbar^2}{2m} \frac{\partial^2 \psi_n(z)}{\partial z^2} + V(z) \psi_n(z) = E \psi_n(z) \quad 2.1$$

If we assume a travelling plane wave e^{ikz} as a solution of the equation, we obtain

$$k = \frac{\sqrt{2m(E-V(z))}}{\hbar} \quad 2.2$$

In the area of tip or sample (i.e., region I and III), $V(z) = 0$, so the solution should be an oscillating wave:

$$\psi_n(z) = \psi(0) e^{\pm ikz} \quad 2.3$$

, where $k = \frac{\sqrt{2mE}}{\hbar}$, When inside the barrier (region II), $V = V_0$ and $E - V(z) < 0$, and the wave function satisfying the Schrödinger's equation is a decaying wave:

$$\psi_n(z) = \psi(0) e^{\pm \kappa z} \quad 2.4$$

, where $\kappa = \frac{\sqrt{2m(V_0-E)}}{\hbar}$, In the process of electron tunneling, the wave functions of the tip and sample overlap. Thus, the probability to find an electron in $z = d$ of the barrier should be the square of the wave function overlap between the tip and sample:

$$P \propto |\psi(z)|^2 = |\psi(0)|^2 e^{-2\kappa d} \quad 2.5$$

Then the tunneling current can be expressed as:

$$I \propto \sum_{E_f-eV}^{E_f} |\psi(0)|^2 e^{-2\kappa d} \quad 2.6$$

Since the electrons in the occupied states of one electrode need to tunnel into the unoccupied states of the other electrode, tunneling occurs mainly with electrons near the Fermi level. Summing P between $E_f - eV$ and E_f yields the local density of state (LDOS) per unit volume near Fermi level, and the LDOS ($\rho_s(z, E)$) in the interval ϵ can be written:

$$\rho_s(z, E) = \frac{1}{\epsilon} \sum_{E-\epsilon}^E |\psi(z)|^2 \quad 2.7$$

The LDOS is independent with the volume, so the current can more suitably be expressed in terms of LDOS (at an applied bias V) rather than wave functions. This yields that the tunneling current is proportional to LDOS:

$$I \propto V \rho_s(0, E_f) e^{-2\kappa d} \quad 2.8$$

However, this approach to calculate the tunneling current fails to include the rate of electron tunneling through the barrier between the tip and sample, which can be solved by Fermi's Golden Rule with the

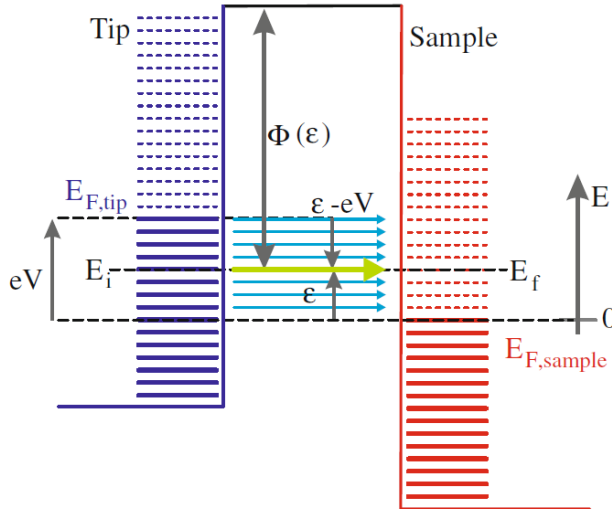


Figure 2.3 Energy diagram of the tip and sample states when a positive bias is applied on the sample, causing the energy of the states in the sample to decrease. It is assumed that all energy levels are filled up to the Fermi level and empty above Fermi level, so that tunneling with energy conservation can only take place in the area between the Fermi level of tip and sample. Adapted from Ref.¹²² with the permission of Springer.

appropriate tunneling matrix element. John Bardeen solved this problem by proposing a model of “metal-insulator-metal tunneling junctions” to simulate the tunneling case (as shown in [Figure 2.3](#)). He considered the “tip & barrier” and “sample & barrier” as two separated systems.

Fermi's Golden Rule shows that the transition rate for an electron from the initial state i of tip to final sample state f can be written as:

$$\omega_{tip,i \rightarrow sample,f} = \frac{2\pi}{\hbar} |M_{fi}|^2 \delta(E_{sample,f} - E_{tip,i}) \quad 2.9$$

The matrix element is given as:

$$M_{fi} = \frac{\hbar^2}{2m} \int_{S_{tip/sample}} [\psi_{tip,i}(r) \nabla \psi_{sample,f}^*(r) - \psi_{sample,f}(r) \nabla \psi_{tip,i}^*(r)] \cdot dS \quad 2.10$$

Where S is the separation surface between the tip and the sample. The total rate for the transition from any initial state to any final state, is given as:

$$\omega_{tip \rightarrow sample} = \frac{2\pi}{\hbar} \sum_{i,f} |M_{fi}|^2 \delta(E_f - E_i) \quad 2.11$$

Take the spin degeneracy into account, the tunneling current can be given:

$$I = \frac{4\pi e}{\hbar} \sum_{i,f} |M_{fi}|^2 \delta(E_f - E_i) \quad 2.12$$

Since the sum of the tip and sample states is an abstract entity, the energy-dependent approximation of the Bardeen model is applied here by introducing the energy-dependent density of states of tip and sample, which can be given as:

$$I = \frac{4\pi e}{\hbar} \int_0^{eV} \rho_{tip}(\epsilon - eV) \rho_{sample}(\epsilon) |M(\epsilon)|^2 d\epsilon \quad 2.13$$

So far, we assumed the model in an ideal situation, i.e., the model was considered in low-temperature which means all the energy levels above Fermi level are empty and are filled up below the Fermi level. To account for a finite temperature, the Fermi functions can be included, giving:

$$I = \frac{4\pi e}{\hbar} \int_0^{eV} [f(E_f - eV + \epsilon) - f(E_f + \epsilon)] \times \rho_s(E_f - eV + \epsilon) \rho_t(E_f + \epsilon) |M(\epsilon)|^2 d\epsilon \quad 2.14$$

where $f(x)$ is the Fermi-Dirac distribution function, and the density of states of the sample and tip are ρ_s and ρ_t , respectively.

In sum, considering the LDOS in the tip is ideally constant, the tunneling current is proportional to the applied bias V and the LDOS in the sample, and is exponentially related to the distance between tip and sample, meaning the current is much more sensitive to the movement of the tip in the height direction.

2.2 Scanning tunneling spectroscopy

Besides obtaining the morphology of surface-supported structures, STM can be extended to measuring the electronic states, which is known as scanning tunneling spectroscopy (STS). In general, STS can provide information on the LDOS of surface materials as function of the energy. Basically, when the STM tip is placed at a desired lateral site of the surface in constant-height mode (i.e., the height of tip relative to the sample is constant and the feedback loop is disabled), the electron tunneling current will vary with the

change of applied voltage between the tip and substrate. As a result, a simple spectrum for the tunneling junction can be recorded which we call it the I-V curve. According to the modified Bardeen transfer Hamiltonian method that was discussed in the previous section, the tunneling current can be described as:

$$I = \frac{4\pi e}{\hbar} \int_0^{eV} [f(E_f - eV + \epsilon) - f(E_f + \epsilon)] \times \rho_s(E_f - eV + \epsilon) \rho_t(E_f + \epsilon) |M(\epsilon)|^2 d\epsilon \quad 2.15$$

$f(x)$ is the Fermi function, the LDOS of sample and tip are ρ_s and ρ_t , respectively. M_{fi} is the tunneling matrix element, which depends only on the values of the tip and sample wave functions on the separation surface. If the absolute temperature were infinitesimally close to 0 K, the tunneling current could be simplified to:

$$I = \int_0^{eV} \rho_{tip}(\epsilon - eV) \rho_{sample}(\epsilon) d\epsilon \quad 2.16$$

It should be noted here that in real operation of STS, absolute 0 K is impossible to achieve and the temperature of the system needs to be as low as possible. Liquid helium is the most commonly used refrigerant, which can cool the system to about 4.5 K, guaranteeing the result ultimately close to the intrinsic property of detected materials. The LDOS of tip is assumed to be constant and already known, hence the data of STS reflects the variation of LDOS in the sample. Therefore, based on the assumptions and approximation, the deviation of the tunneling current dI/dV is proportional to the LDOS of the sample at the energy eV relative to the Fermi level of the sample, expressed as:

$$\frac{dI}{dV} \propto \rho_{sample}(E_F - eV) \quad 2.17$$

From the operational point of view, to detect the change in current versus bias with greater sensitivity, in STS an AC signal can be generated by using an oscillator (part of the lock-in amplifier technique) to add a small bias voltage modulation dV to the original applied bias. The resulted current can be read using a preamplifier. As shown in [Figure 2.4](#), a small modulated bias is added around the centered bias V_1 and V_2 , and the resulting modulated tunneling current is proportional to the slope of the dI/dV curve at each point. For example, when a modulated bias V_M is added around the center voltage V_1 , the amplitude of the resulting modulated current $I_{M,1}$ is proportional to the slope of dI/dV curve. As [Figure 2.4](#) shows, the measured slope is averaged over the amplitude of the modulated voltage. Therefore, ideally, the larger the amplitude of the modulation voltage, the higher energy resolution and precision of the measured dI/dV

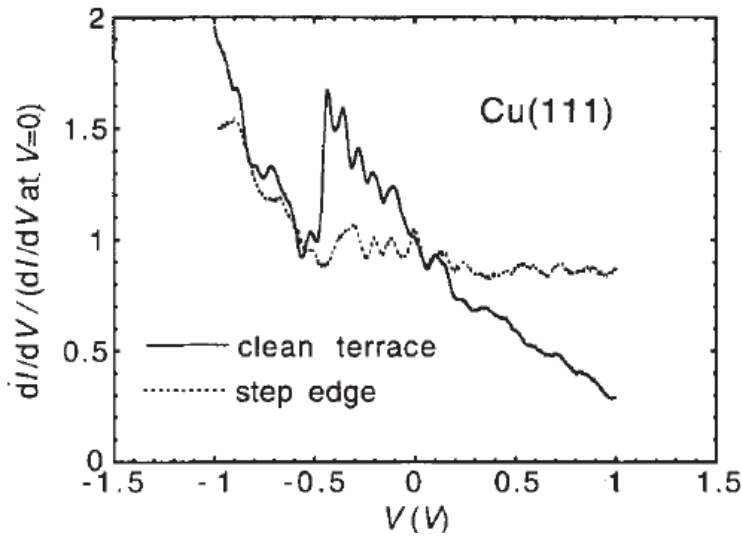


Figure 2.4 dI/dV spectra acquired on a clean terrace (solid line) and step edge (dashed line) of Cu(111). Adapted from Ref. ¹²³ with the permission of Nature Publishing Group.

curves in STS.

Once the LDOS of the sample over a range of energies is already known, the positions of different energy states (including the conductive and valence bands) can be interpreted. As a result, the band gap of the surface material at a specific site can be determined. In single-molecule studies, the conductive and valence bands are ascribed to the lowest unoccupied molecular orbital (LUMO) and the highest occupied molecular orbital (HOMO). Furthermore, based on this technique, we can conduct a grid of dI/dV curves and combine them to form a 2D STS map, where the distributions and features of LDOS along the grid at

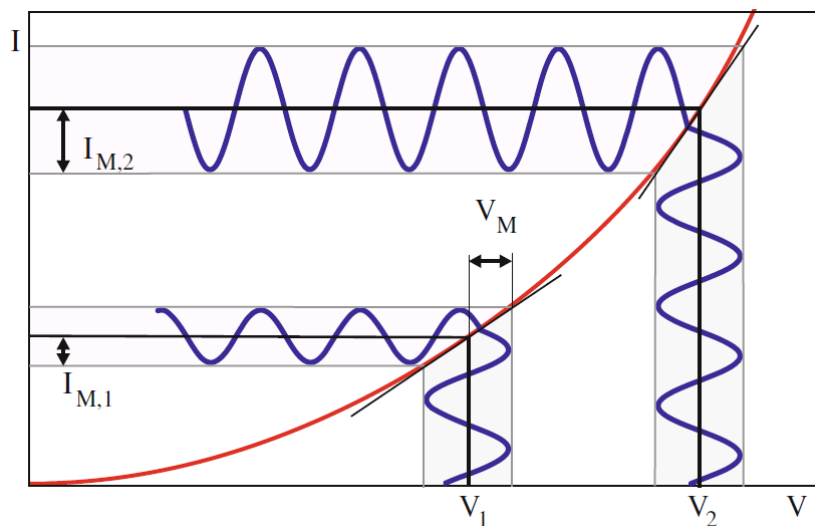


Figure 2.5 Diagram of the first derivative of the I-V curve. A modulated voltage is added around the center value V_1 or V_2 . The measured amplitude of the resulting modulated (tunneling) current $I_{M,1}$ by adding the modulated voltage V_M is proportional to the slope of the I-V curve (dI/dV) at V_1 . Adapted from Ref. ¹²² with the permission of Springer.

different bias are more easily read. It is also possible to conduct dI/dV mapping, where the spatial distribution of the DOS can be detected at any desired energy (e.g., in the position of HOMO or LUMO), which is of great benefit to distinguish structures with different electronic features.

In addition, the quality and accuracy of dI/dV spectra are very sensitive to the tip. A tiny change or contamination occurring on the head of the tip may ruin a good tip for dI/dV spectra. So, to ensure the tip is well structured for measurements on the desired surface materials, it is always conducted on a region of the clean surface to obtain a dI/dV curve to match the known results. For example, Crommme *et al.* reported a surface state in clean terrace of Cu(111) at about -0.5 eV (as shown in Figure 2.5).¹²³ Hence, as long as the dI/dV curves recorded on clean Cu(111) match this reported one, the tip is suitable for STS measurements. Besides Cu(111), this strategy works for other surfaces, including Ag(111) and Au(111).

2.3 Single-crystal surfaces

Due to the requirement of a tunneling current through the barrier between the tip and substrate, metal or semiconductive substrates are essential. In this thesis, I focused on reactions taking place on metal substrates. To achieve ultrahigh resolution, a single crystal surface with atomic flatness and extreme cleanliness is necessary. Among all the metals, coinage metal substrates (Au, Ag and Cu) and conductive HOPG are the most commonly used in surface science, considering the nature of the substrates (including

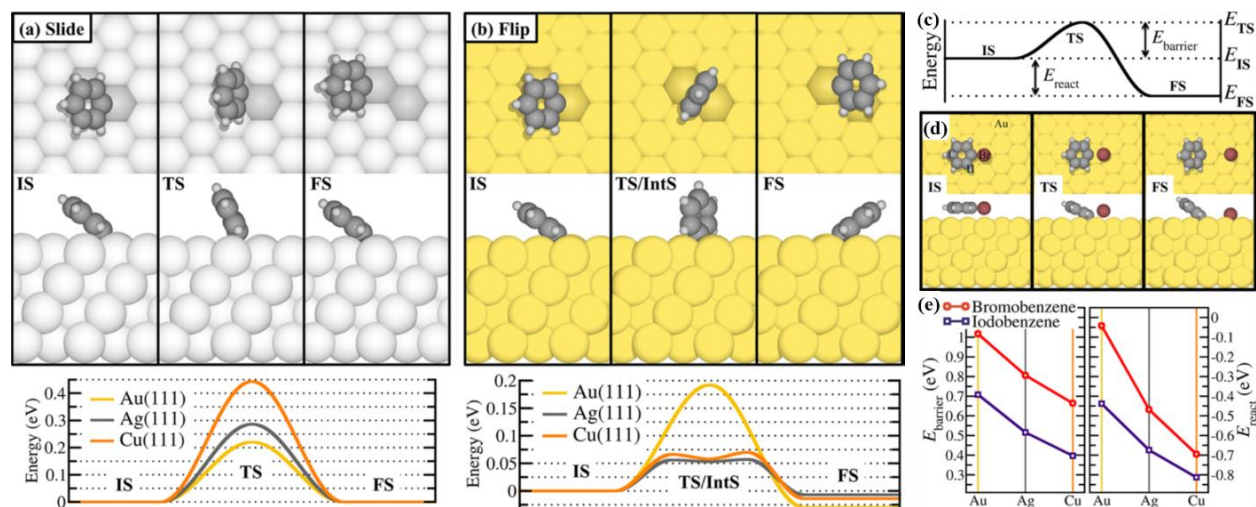


Figure 2.6 Initial (IS), transition (TS) and final states (FS) of a) sliding diffusion and b) flipping diffusion of phenyl on Au(111), Ag(111), and Cu(111) and the corresponding energy diagrams. c) energy diagram of the IS, TS and FS of dehalogenation process and d)-e) energy comparison of debromination and deiodination on Au(111), Ag(111) and Cu(111). Adapted from Ref.¹²⁵ with the permission of the American Chemical Society.

the melting temperature, hardness, and the cost, etc.), adsorption features, reactivity of the adsorbates (initial activation and the formation of different intermediates) and catalytic properties. In general, most adsorbates interact through comparably weaker physisorption on Au versus chemisorption on Ag and Cu.¹²⁴¹²⁵ Among Au, Ag and Cu, besides the differing interaction between the adsorbates and substrates, there are large differences in the diffusivity of supported materials and activation energy of different reactions. As shown in [Figure 2.6a-b](#), there are two possible modes for the diffusion of phenyl on Au(111), Ag(111), and Au(111). In slide diffusion mode, Cu(111) has the highest barrier, whereas Au(111) has the highest barrier in flip diffusion mode. As shown in [Figure 2.6c-e](#), the energy barrier for the dehalogenation is also different for these three substrates. In general, the dehalogenation reaction can be most easily triggered on Cu(111).

Surfaces with different facets also play a critical role in the behaviors of surface-supported materials. Different facets with specific lattice vectors are manufacturable by precisely cutting the single crystals. [Figure 2.7](#) shows the atomic distributions of the low-index facets typically used in surface science, including (111), (110) and (100). Even for the same material, the different lattice dimensions and symmetries of these surfaces can lead to strikingly different properties. Besides the most common low-index facets, higher-index facets normally have narrower terraces according to the crystal properties, which may impede the extension of 2D ordered structures across the step edges. However, they could be used to constrain the synthesized extended 1D structures with a uniform orientation. For example, the synthesis of armchair graphene nanoribbons on Au(788) can produce spatially well-aligned ribbons, which could enable the further investigation of their electronic structures by angle resolved photoemission spectroscopy.¹²⁶ Similarly, the low-index facet (110) can also constrain the material alignment by its narrow grooves. To

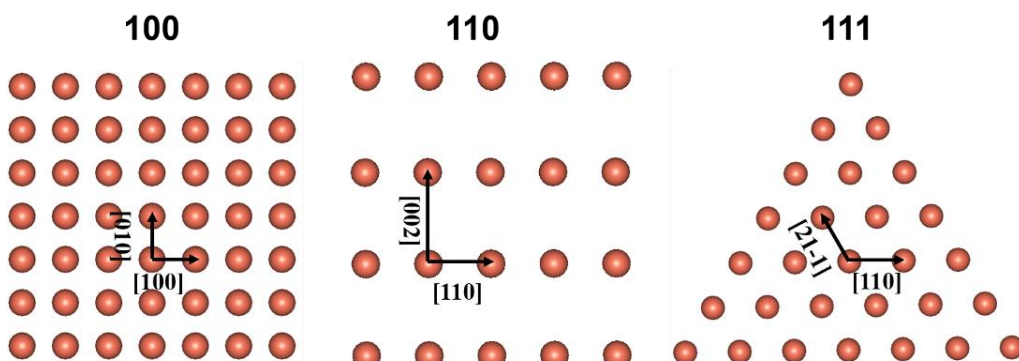


Figure 2.7 Top-view of (100), (110) and (111) surfaces in a face centered cubic crystal. The arrows indicate the basic vectors in different surfaces.

obtain extended 2D structures with larger domains, (111) and (100) are the ideal choices in surface chemistry.

In this thesis, my first project mainly focused on investigating the effects of oxygen on surface-confined Ullmann-type coupling. Considering the low energy barrier of activating carbon-halogen bonds, copper substrates are the preferences at the initial stage of our project. Further considering the unique adsorption features of oxygen, we chose Cu(111) as the main target surface.¹²⁷ As reported, at low coverage the dissociated atomic oxygen atom adsorbs preferentially on the hollow sites on Cu(111).¹²⁷ While higher coverage of oxygen leads to the formation of different oxidized phases under different conditions.^{118, 128} In the course of our investigations, adsorption of atomic oxygen on Cu(111) was observed to affect the Ullmann-type coupling on Cu(111). Therefore, in this project, we adsorbed a small amount of chemisorbed oxygen atoms on the Cu(111) surface. Furthermore, to investigate the effects of surface symmetry on the intermediate states of surface-confined Ullmann-type coupling, we conducted the experiments on the fourfold symmetric Cu(100) surface in addition to the threefold symmetric Cu(111) surface. It is noteworthy here that because of the lattice commensurability between Poly(p-phenylene) (PPP) segments and specific direction (mainly the close-packed direction) of the surface, Cu(111) is preferred in our project. Furthermore, to distinguish from the synthesis of GNRs on Au(111), we chose Cu(111) as the target surface to investigate the feasibility of synthesizing GNRs via lateral fusion and the effects of oxygen on the synthesis.

In addition, we investigated the reactions of tetrathienylbenzenes precursors on Cu(111), Ag(111) and Au(111). The activation energy of desulfurization of thiophene rings in the precursors and the ability of molecular diffusion are different on these surfaces, leading to formation of different products. These investigations further exemplify the significant role of the substrates on surface chemistry.

2.4 X-ray photoelectron spectroscopy

STM exhibits its great advantages in imaging molecular self-assembly structures, different states of the reactions and even dynamic process (through high-speed STM) of chemical reactions in real space with sub-molecular resolution. However, information on the chemical states, elemental composition and chemical bonding of materials on the surface cannot be discerned from STM. Hence, STM measurements

are usually conducted along with other surface spectroscopic techniques, such as X-ray photoelectron spectroscopy (XPS), Auger electron spectroscopy (AES), Low energy electron diffraction (LEED), Secondary-ion mass spectrometry (SIMS) and Raman spectroscopy. In this thesis, STM was complemented with XPS to analyze chemical states and elemental compositions. Another benefit of XPS is that it collects information across the surface, whereas STM can only measure small areas (typically less than one micrometer), so XPS can support that the surface structures observed by STM are representative of the global structures.

The basic physics of XPS is the photoelectric effect, which was first advanced by German physicist Heinrich Rudolf Hertz in 1887 and then explained by German-born physicist Albert Einstein in 1905, for which Einstein was awarded the 1921 Nobel Prize in Physics. The basic principle of photoelectric effect is that when the light source (X-rays in XPS) reaches or exceeds the threshold frequency, it will excite electrons in the materials to emit photoelectrons with a certain energy. In other words, the emission of a photoelectron can only take place when the electron can acquire enough energy from the incident photon to overcome the binding energy and the work function of the sample.

XPS is known as electron spectroscopy for chemical analysis, which is a quantitative spectroscopic technique applied mainly on surface-supported materials to characterize the elemental composition and chemical states of the elements. The collision of high-voltage accelerated charged particles (electrons in XPS) on an anode metal target (most often Mg and Al) reflects X-rays with particular energy (known as

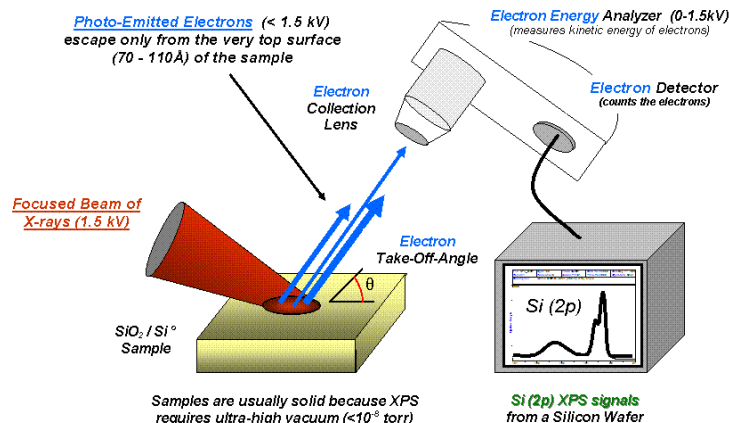


Figure 2. 8 Schematic diagram of X-ray photoelectron spectroscopy, showing the basic components of the system. With the permission of Wikimedia Commons.

Bremsstrahlung effect), which are then focused as the incident light source onto the surface of measured sample, as shown in [Figure 2.8](#). X-rays irradiate the surface of materials to excite electrons in the core level of different elements, which are emitted as photoelectrons. The kinetic energy and intensity of the induced photoelectrons are then measured by an analyzer and detector, respectively. According to the photoelectric effect, the binding energy of electrons can be determined by the following equation:

$$E_{binding} = E_{photo} - E_{kinetic} - \emptyset \quad 2.18$$

where E_{photo} is the energy of the X-rays, $E_{kinetic}$ is the detected kinetic energy of the emitted photoelectrons, and \emptyset is the work function of the sample. By scanning the kinetic energy permitted to pass through the analyzer, a plot can be acquired of the intensity of electrons versus the binding energy of detected electrons. Different elements have different set of XPS peaks at distinctive binding energy values, which can be used to identify the elemental composition of the materials (except for hydrogen). In addition, the intensity can be used to quantify different elements in the surface of material. Furthermore, deconvolution of the peaks can be used to deduce the ratio of the same element in different chemical environments.

There are some other unique features of the XPS technique which should not be ignored. The detector can only measure the photoelectrons that escape from the surface of material, while the electrons in the materials which are much deeper than the surface will experience more inelastic collisions, excitation of the sample and trapping in various excited states. As a result, they cannot reach the detector. As reported, these effects are exponentially related to the depth. Hence, XPS technique is of high surface sensitivity, however, which can be further used to eliminate the depth effects in multilayered materials. In addition, there is a nontrivial distance between the detector and the surface of sample, thus it is essential for the machine to work in UHV to minimize the loss of detected photoelectrons due to collisions with background gas.

In this thesis, the instrument we used is a variable-temperature (VT) STM which integrates the STM, XPS, as well as the sample preparation facilities in the same UHV system, as shown in [Figure 2.9a](#). In this machine, the prepared sample can be analyzed by STM or XPS in the same chamber without being taken out of UHV environment, which would contaminate the sample. We also used an Omicron UHV LT-STM

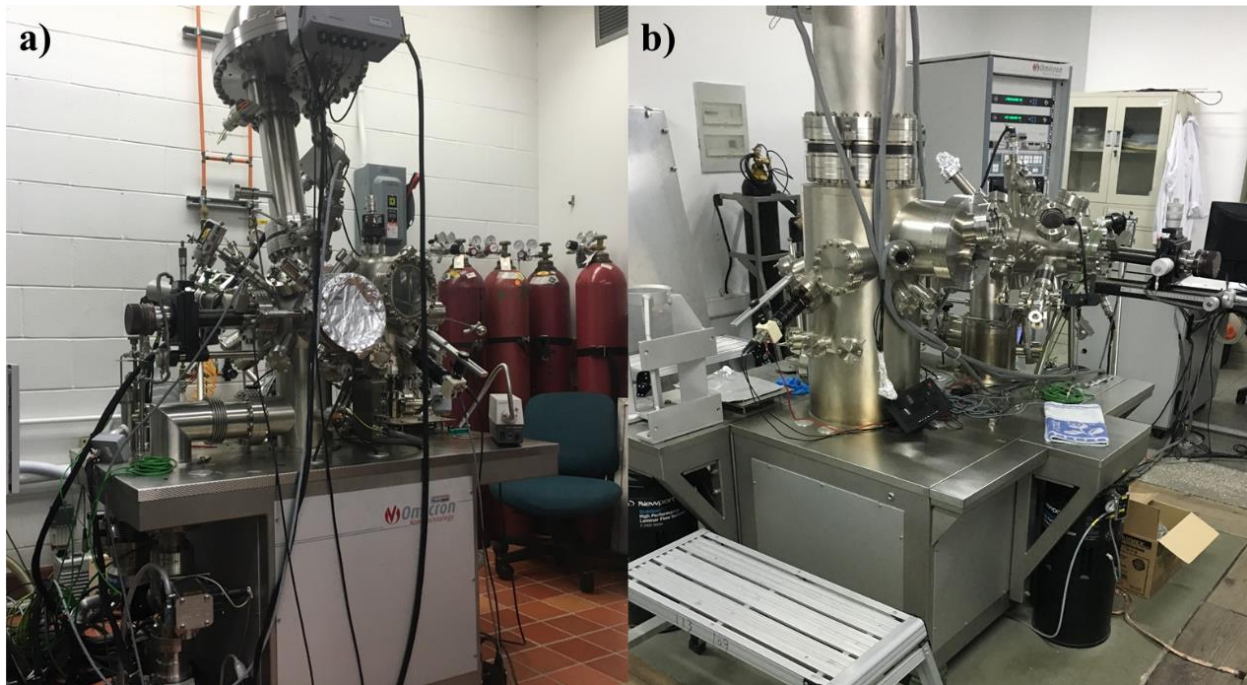


Figure 2.9 a) Omicron UHV variable-temperature (VT) STM, integrated with XPS, low-energy electron diffraction (LEED) and organic molecular beam epitaxy (OMBE) facilities. b) Omicron UHV low-temperature STM with OMBE systems.

equipped with a separate organic molecular beam epitaxy (OMBE) chamber and lock-in module to perform STS measurements. This machine can work at 4.6 K with the use of liquid helium. In addition, different ultrapure gases can be externally introduced to both of these two machines, enabling the investigation of the effects of different gas species on surface chemistry.

Chapter 3. Oxygen-Induced 1D to 2D Transformation of On-Surface Organometallic Structures

Penghui Ji, Gianluca Galeotti, Fabrizio De Marchi, Daling Cui, Kewei Sun, Haiming Zhang, Giorgio Contini, Maryam Ebrahimi, Oliver MacLean, Federico Rosei, and Lifeng Chi.

Authors' contribution: L. Chi, G. Contini and F. Rosei initiated and supervised the project. P. Ji conducted the experiments and the data processing. P. Ji wrote the initial manuscript. O. MacLean performed DFT simulation. All the authors modified the manuscript.

3.1 Introduction

On-surface synthesis is a promising approach to fabricate 2D organic nanomaterials with unique properties arising from their reduced dimensionality, including properties that are specific to planar π -conjugated bonds.^{3, 5, 6, 8-10, 12, 24, 45, 129-135} The surface can act both as a template to confine the reactants and as a catalyst to drive reactions to proceed along a different pathway than in traditional solution chemistry.^{19, 115, 136, 137} On-surface Ullmann-type coupling, involving dehalogenation reactions and subsequent C-C coupling of aromatic halides, is a widely investigated reaction due to its potential to synthesize π -conjugated polymers with control over the size, symmetry, chirality, dimensionality and therefore the properties.^{4, 37, 38, 43, 44, 47, 53, 138-141} This is exemplified by quasi 1D graphene nanoribbons, where the edge structure and width, and therefore the electronic properties, can be rationally controlled by the choice of the halogenated precursors.^{120, 142-145}

The focus of much of the previous work using on-surface Ullmann-type coupling has been to investigate different precursors and optimize the thermally activated reaction parameters. Few reports have explored the influence of different atomic adsorbates on surface-confined Ullmann-type coupling, which could alter reaction pathways to enable the synthesis of new nanostructures or provide further insights into the Ullmann-type reaction mechanism. Recently, atomic hydrogen was reported to remove the halogen byproducts of Ullmann-type coupling on Cu(111) and Cu(110),¹⁰⁵⁻¹⁰⁸ while iodine atoms can decouple covalent polymers from the Ag(111) and Au(111) surfaces to promote the investigation of intrinsic

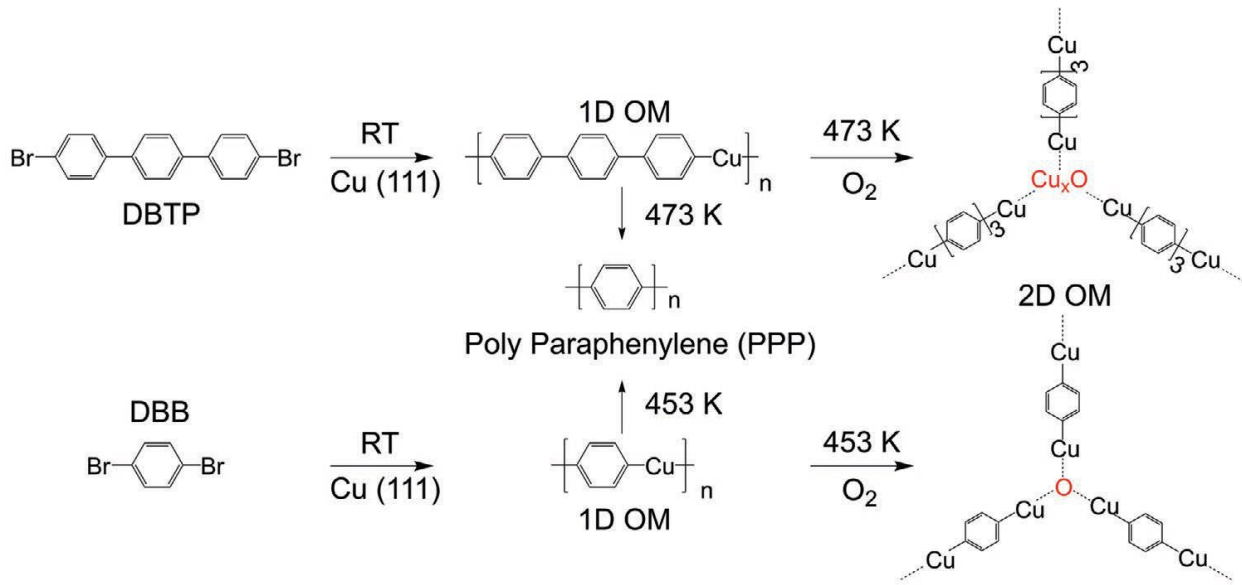


Figure 3.1 Scheme of the transformation of organometallic (OM) structures from 1D to 2D by introducing O_2 into surface-confined Ullmann-type coupling.

electronic properties.^{102, 103} In addition, H_2S was observed to suppress Ullmann-type coupling on $Au(111)$, while the reaction could be reactivated by subsequent exposure to H_2 .¹¹⁰ Oxygen plays a critical role in many surface-confined chemical reactions,^{113-116, 146} such as C-H activation,^{112, 147, 148} yet its effects on the Ullmann-type reaction has not been investigated. Moreover, the oxidation of the substrate to a semiconducting metal oxide could be a simple method to remove the influence of the metal surface,^{149, 150} facilitating the characterization of the intrinsic properties of surface-supported materials.

Here, we report the effects of co-adsorbed oxygen on surface-confined Ullmann-type coupling introduced before or after deposition of the halogenated precursors on $Cu(111)$ and $Cu(100)$. As shown in [Figure 3.1](#), OM intermediates are formed after the deposition of 4,4"-dibromo-p-terphenyl (DBTP, or $Br-(ph)_3-Br$) or 1,4-dibromobenzene (dB B , $Br-ph-Br$) on $Cu(111)$ at RT. An increase of the temperature gives, by Ullmann-type coupling, poly para-phenylene (PPP) wires; instead, in the presence of co-adsorbed oxygen on the surface, subsequent annealing causes the reaction to proceed along an unexpected pathway in which the 1D OM chains transform into 2D OM networks with copper–oxygen clusters as the connection nodes. Following the same approach on $Cu(100)$, 2D copper–oxygen OM networks with square symmetry are obtained. Ultrahigh vacuum (UHV) scanning tunneling microscopy (STM) and *in situ* X-ray photoelectron spectroscopy (XPS) were used to study the 2D network structures, complemented by density functional theory (DFT) calculations. Our investigations provide insights into the role of oxygen in surface-

confined Ullmann-type coupling, which has a detrimental effect on polymer synthesis, yet enables the formation of 2D nanostructures with tunable size and shape. The concept could be further employed in host–guest chemistry as quantum well templates providing specific electronic environments.⁹⁸

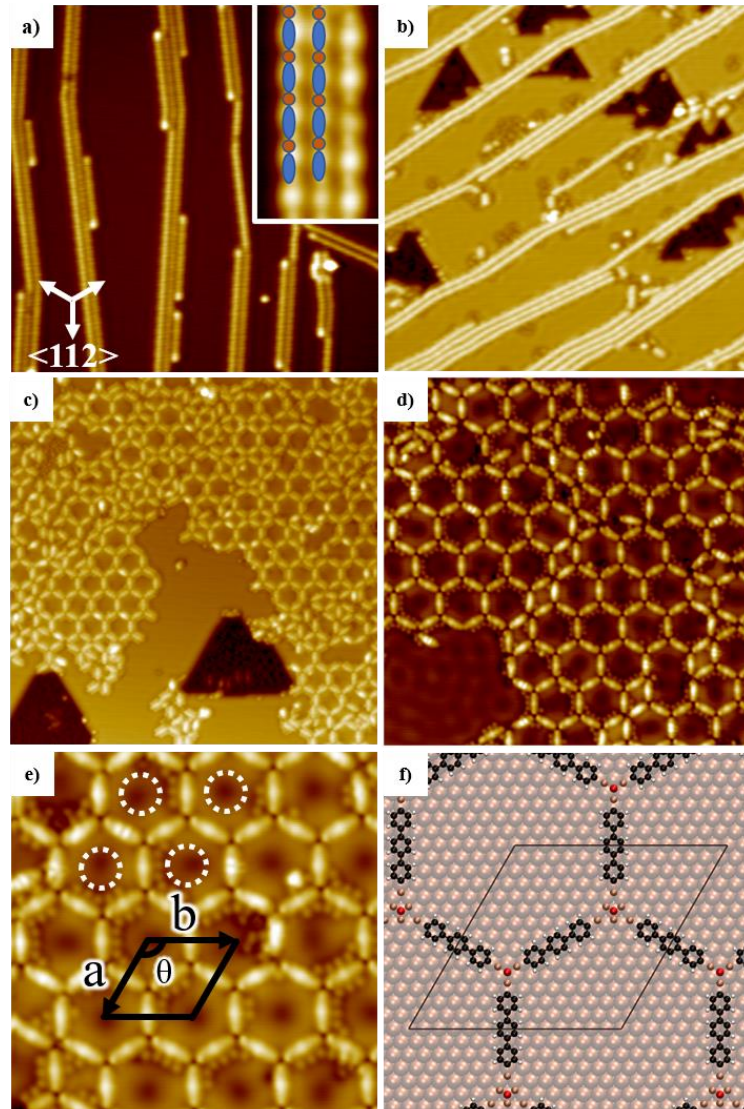


Figure 3. 2 LT STM images of the hexagonal OM networks on Cu(111). a) Overview STM image of $(\text{ph})_3\text{-Cu-(ph)}_3$ OM chains formed by deposition of DBTP on Cu(111). Brown circles and blue ellipses indicate copper atoms and terphenyl segments in the magnified image in the inset ($V_t = -1$ V, $I_t = 0.1$ nA; inset: $V_t = 1$ V, $I_t = 1$ nA). The orientation is indicated by arrows and is the same for all images. b) STM image after dosing O₂ on Cu(111) with pre-synthesized OM chains at RT. ($V_t = -1$ V, $I_t = 0.1$ nA) c–e) Large- and small-scale STM images of hexagonal networks formed by annealing at 473 K. (c: $V_t = -1$ V, $I_t = 0.1$ nA); d,e): $V_t = 0.05$ V, $I_t = 1.5$ nA). f) DFT optimized model of the networks. (red: oxygen, brown: copper, grey: carbon, white: hydrogen). (Image sizes of (a–e) and inset in (a) are 50×50 , 50×50 , 50×50 , 29×29 , 14.9×14.9 , 8×4.5 nm², respectively)

3.2 Results and Discussions

3.2.1 OM structural transformation achieved by introducing DBTP and O₂ on Cu(111)

When depositing DBTP on Cu(111) at RT, we observe the formation of linear OM chains consisting of alternating terphenyl segments and copper atoms (as shown in [Figure 3.2a](#)) through direct dehalogenation of DBTP molecules catalyzed by the metal substrate.^{40, 50, 51} The periodic structure of terphenyl segments and copper atoms can be identified in magnified STM images (inset in [Figure 3.2a](#)).

Following the formation of OM chains, O₂ gas was dosed on the sample held at RT. A large amount of O₂ gas would fully oxidize the upper layers of Cu(111) surface, leading to the formation different copper oxidized phases. In contrast, small amount of O₂ gas can just partially oxidized the copper surface. As reported, O₂ dissociates above 170 K on Cu(111) to adsorb as single atoms or small atomic clusters on the terraces as well as in dark triangular islands formed by the extraction of surface copper atoms (as shown in [Figure 3.2b](#)).^{127, 151-153} The overall STM image in [Figure 3.2b](#) and high resolution STM images (as shown in [Figure 3.3](#)) show that the OM chains largely remain intact after the introduction of O₂ gas at RT, without any changes in the length and order.

In the absence of oxygen, heating the OM chains induces C-C coupling to form covalent polymers, and we observed the formation of poly para-phenylene (PPP) wires after annealing to 473 K (as shown in [Figure 3.4](#)).⁵⁰ However, at the same annealing temperature, the presence of adsorbed oxygen induces an unexpected structural transformation, in which the 1D OM chains convert to 2D ordered hexagonal networks, as shown

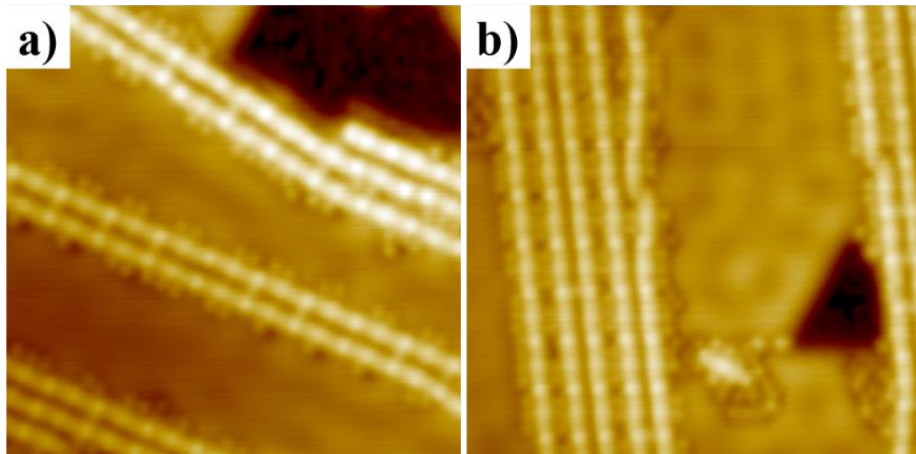


Figure 3. 3 High-resolution STM images of OM chains formed by DBTP on Cu(111). The OM chains remained intact after being exposed to O₂ gas at room temperature. Bromine atoms adjacent to the chains can also be observed in the images. (a-b: V_t = -0.02 V, I_t = 2.0 nA; 15 × 15 nm²)

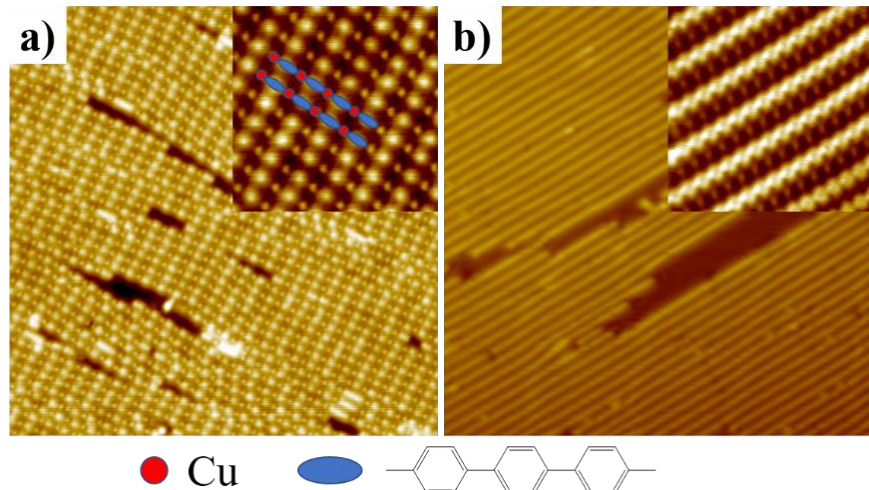


Figure 3. 4 LT STM images of OM chains and poly-para-phenylene (PPP) wires. a) Overview and magnified (inset) STM images of (ph)₃-Cu OM chains formed as DBTP deposited on Cu (111). ($V_t = 1$ V, $I_t = 0.1$ nA) b) Poly para-phenylene (PPP) wires are formed by annealing OM chains at 473 K for 20 minutes, which is same as reported results. ($V_t = -1$ V, $I_t = 0.1$ nA; inset: $V_t = -0.05$ V, $I_t = 1$ nA) [Image size: a) 40×40 nm², inset: 10×10 nm²; b) 40×40 nm², inset: 6×6 nm²]

in [Figure 3.2c-e](#). The vertices in the 2D networks appear as depressions, and the small bright dots adjacent to the hexagons are assigned to dissociated bromine atoms chemisorbed on Cu(111).^{51, 154} In addition, the contrast variation within the pores (marked by white dashed circles in [Figure 3.2e](#)) is attributed to the confinement of surface states on the copper surface, which could be further used as a quantum well template for host–guest systems.^{98, 155} The unit cell vectors of the 2D networks ($a = b = 3.53 \pm 0.05$ nm, $\theta = 120^\circ \pm 2^\circ$) correspond with 14 copper atoms (3.57 nm) in the close-packed directions $<110>$ of Cu(111). The alignment of the structures was determined by comparison with the edges of the dark triangular islands

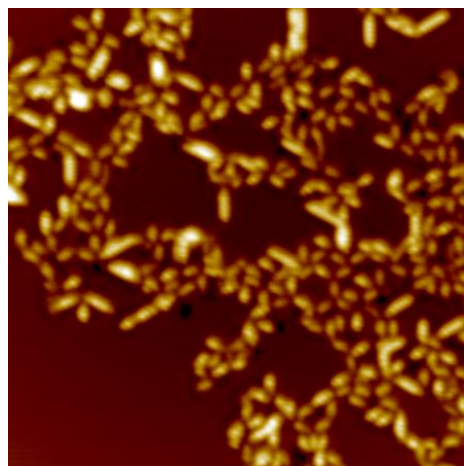


Figure 3. 5 Overview LT STM image after further annealing the hexagonal networks at 497 K. ($V_t = -1.0$ V, $I_t = 10$ pA 50 × 50 nm²) As observed in the image, in general, the networks transformed to disordered segments. There are also some wider and brighter segments that can be attributed to oligomeric chains. However, no ordered polymer can be formed.

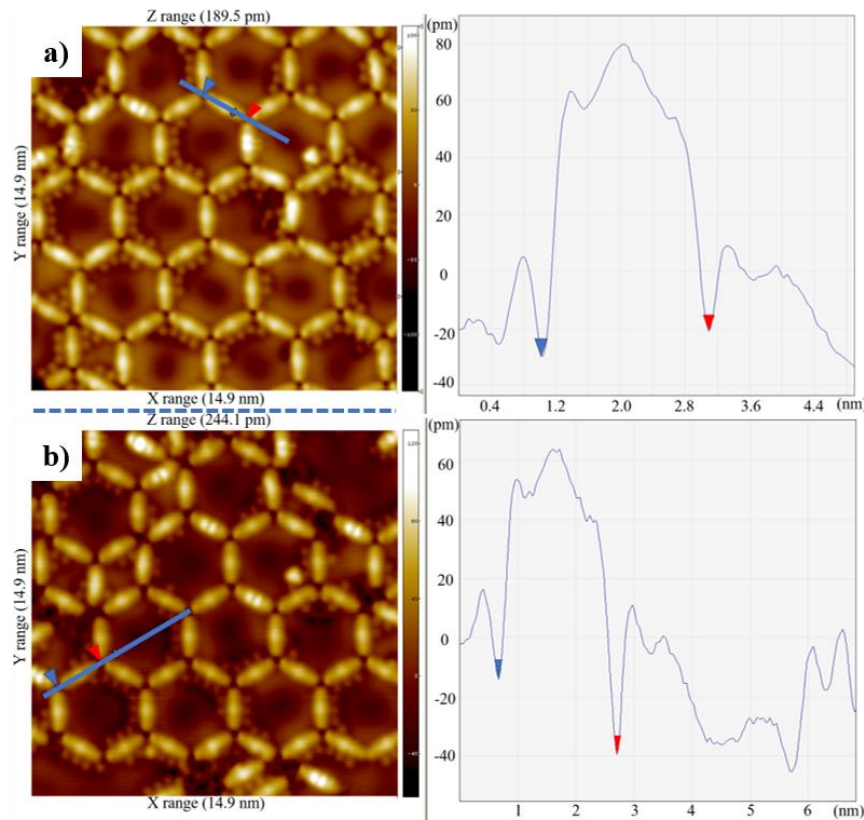


Figure 3.6 Identification of two distinct vertices in the 2D DBTP network. a,b) Two examples of LT STM images (left) and height profiles (right) along one OM segment belonging to the 2D hexagonal networks formed from DBTP. The red and blue arrows indicate the center of the vertices, which are depressions that are slightly different in height. The difference for DBTP of 11.0 ± 3.0 pm was observed in at least 10 pairs of vertices in different STM images. The observation of a distinct appearance of alternating vertices supports the conclusion that these are formed by two different copper-oxygen clusters.

formed during oxygen deposition (as shown in [Figure 3.2c](#)), which is reported to also align along the close-packed directions of Cu(111). The stabilization of the 2D OM phase suppresses the polymerization at 473 K, but coupling can be induced by further annealing to 493 K. However, the slightly higher annealing yields only disordered oligomeric chains rather than long polymers (as shown in [Figure 3.5](#)).

Density functional theory calculations were performed to identify the structure of the 2D OM phase. Experimental observations suggest that the 2D networks are composed of two distinct vertices: the edge length and alignment of the hexagonal network indicates that the vertices are centered at different surface adsorption sites. In addition, the alternating vertices appear as depressions with a small difference in height of 11 ± 3 pm (as shown in [Figure 3.6](#)). This height difference was observed in over 10 pairs of vertices with different orientations in different STM images. [Figure 3.2f](#) shows one of two computed structures consistent with these observations (shown in an oblique view in [Figure 3.7a](#)), which has a Cu₃O vertex centered at an

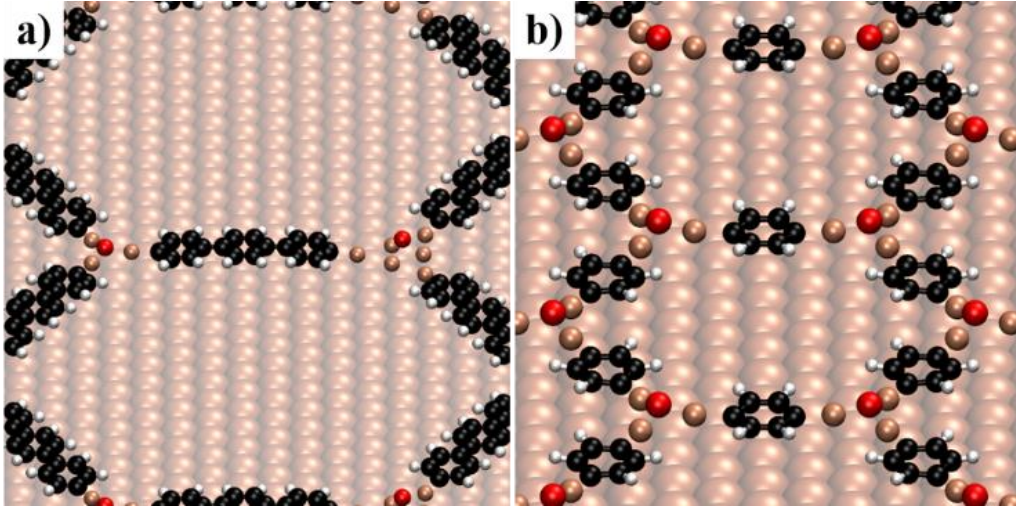


Figure 3.7 Oblique view of the DFT optimized models of a) DBTP and b) dBB 2D networks on Cu(111). The O atoms (red) are above Cu adatoms (copper) in a three-fold bonding environment, analogous to a hollow site on the surface. The remaining C atoms are in black and H in white.

fcc (face-centered cubic) hollow site and a Cu_6O vertex at a top site. A second structure with a Cu_3O vertex at an hcp (hexagonal close-packed) hollow site and a Cu_6O vertex at a top site is very similar in energy (<10 meV difference), so we expect both structures to exist on the surface. The configuration of the oxygen atoms (examined in detail for the dBB networks below) in these clusters above three Cu adatoms is similar as that of an oxygen atom chemisorbed at a hollow site on Cu(111), which is consistent with the similar STM appearance of the vertices as chemisorbed oxygen atoms on Cu(111) at the same bias.¹²⁷

A full discussion of the copper–oxygen clusters considered in our calculations is shown in [Figure 3.8](#).

[Figure 3.8](#) shows a model of the 14x14 unit cell for the DBTP 2D network with the copper-oxygen clusters

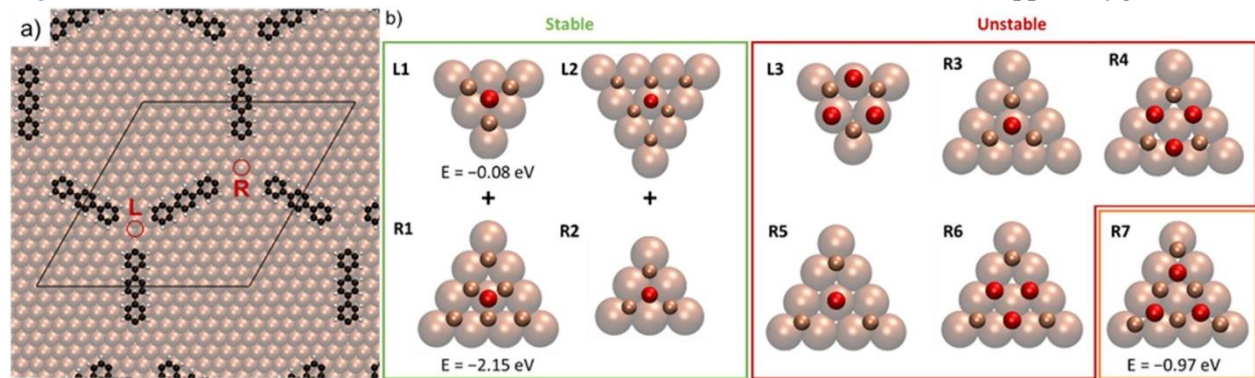


Figure 3.8 Copper-oxygen clusters considered in on-surface DFT calculations for the DBTP 2D OM network. a) model of the full DBTP 2D OM network with the position of the clusters indicated by L (left) and R (right). b) structures considered for the left and right clusters. O atoms are in red and Cu atoms in brown, and the adjacent surface atoms are shown partially transparent. For clarity, the remaining surface atoms are omitted. The formation energy of selected clusters is reported below the cluster labels.

removed. The experimental edge length of 2.04 nm of the hexagonal network indicates that the vertices are centered at different surface sites: if the vertex indicated by ‘L’ in [Figure 3.8a](#) is at an fcc-hollow, hcp-hollow, or top site, the vertex indicated by ‘R’ must be at a top, fcc-hollow, or hcp-follow, respectively.

Calculations to identify possible structures of the DBTP 2D network were performed in stages to keep the computational cost moderate. First, the stability of individual clusters was assessed using a three-layer 8×8 slab with the terphenylene linkers replaced by phenyl groups. If a cluster was stable in isolation, it was then checked in an OM segment (with a length corresponding to the experimental value) in the same 8×8 supercell. The formation energy was then determined for the stable Cu_xO_y clusters relative to individual Cu and O adatoms. Third, the clusters selected for the model proposed in the main text were optimized in the full DBTP 2D network on the two-layer 14×14 slab.

[Figure 3.8b](#) shows the clusters considered in our calculations. Two pairs of clusters were identified as the most probable and are highlighted by a green box. L1 and R1 are the clusters in the model shown in the main text, located at a fcc-hollow and a top site, respectively. L2 and R2 are very similar clusters centered at a top and a hcp-hollow site, respectively. These pairs differ in energy from L1 and R1 by <10 meV, so both are to be expected in the experiment.

The five clusters highlighted by a red box were found to be unstable in DFT calculations, either alone or in an OM segment (with a comparable cluster as the second in the pair.) Additional clusters can be

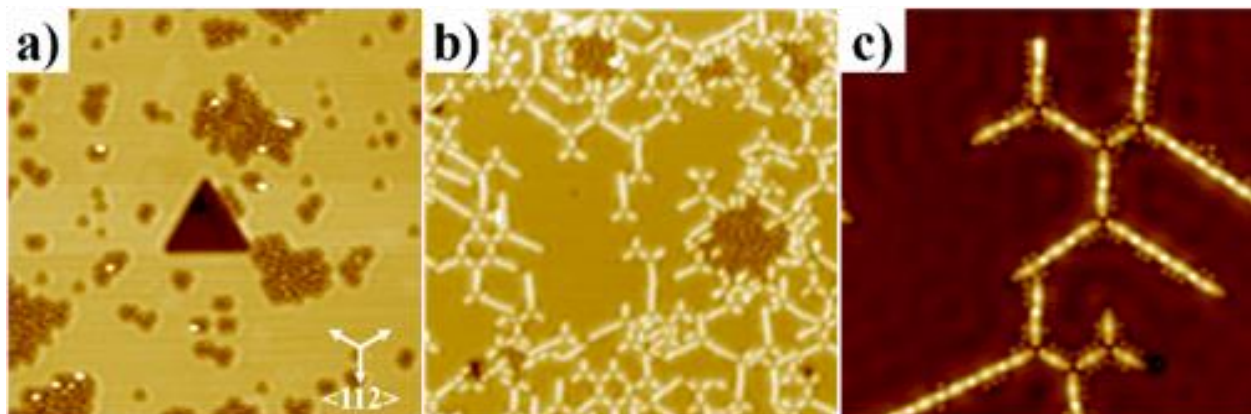


Figure 3. 9 LT STM images for deposition of O₂ before DBTP on Cu(111). a) Image of partially oxidized copper surface formed by deposition of O₂ on Cu(111) at RT. ($V_t = -1.0$ V, $I_t = 0.1$ nA) The orientation is indicated by arrows and is the same for all images. b) Surface after deposition of DBTP on pre-oxidized Cu(111) at RT. ($V_t = -1.0$ V, $I_t = 0.05$ nA) c) Magnified STM image of linear and threefold symmetric structures coexisting on the surface. ($V_t = -0.1$ V, $I_t = 1.0$ nA) (Image sizes of (a–c) are 50 × 50, 50 × 50, and 20 × 20 nm², respectively)

envisioned by a 60° rotation around the center, which converts between ‘R’ or ‘L’ configurations. However, for clusters centered at hollow sites this moves the Cu adatoms to top positions, which were found to be unstable, while clusters at top sites are largely unchanged. Cluster R7 (highlighted in orange) can form a stable OM segment with L1 as the partner cluster, but has a much smaller formation energy (in absolute value) than R1. In addition, the similar configuration of the O adatom in R1 as L1 is consistent with the similar appearance of the two vertices by STM.

To investigate the competition between the formation of 2D OM networks and 1D OM chains, we dosed oxygen on the Cu(111) surface before depositing DBTP. [Figure 3.9a](#) shows the surface after dosing O_2 at RT, where the same triangular oxygen adsorption features are observed as in [Figure 3.2b](#). Deposition of DBTP on the partially oxidized Cu(111) surface leads to the formation of both linear chains and three-fold vertices (as shown in [Figure 3.9b-c](#)), with a corresponding reduction in the number of chemisorbed oxygen features. The linear OM chains appeared immobile in our STM measurements from 77 K to RT, yet could be further transformed into the 2D phase by annealing to 473 K (as shown in [Figure 3.10](#)). This observation indicates that mobile terphenylene fragments, produced by dehalogenation after adsorption at RT or by annealing, are required to form three-fold vertices and therefore the 2D networks. The order of the 2D OM networks does not depend on the deposition sequence of DBTP versus O_2 , but is likely affected by the ratio

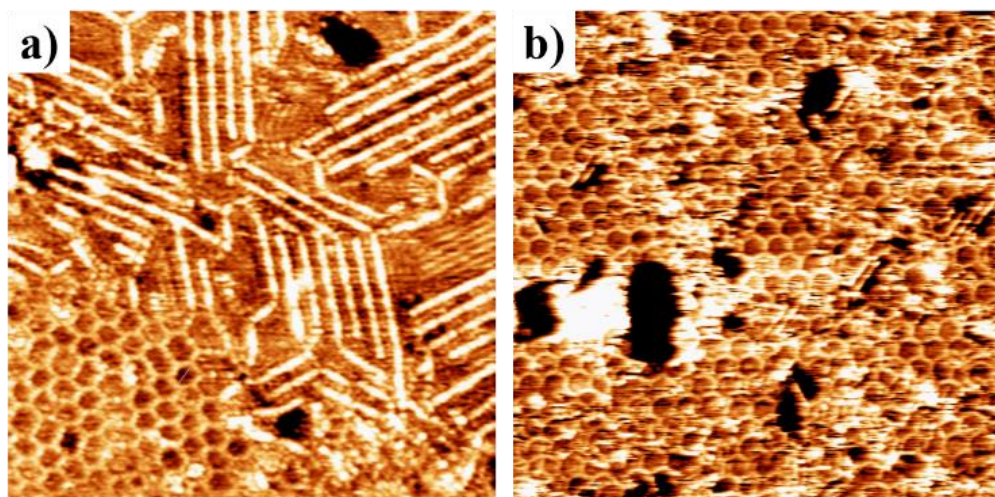


Figure 3. 10 Overview RT STM images of transformation from 1D OM chains to 2D hexagonal networks. a) 2D networks and 1D OM chains coexisted when DBTP was deposited on pre-oxidized Cu (111). b) After annealing the sample at 453 K for 20 minutes, the remaining OM chains transformed to 2D hexagonal OM networks, which further supports that the 2D network structures are thermodynamically favored (a: $V_t = -0.97$ V, $I_t = 0.94$ nA; 60×60 nm 2 , b: $V_t = -0.93$ V, $I_t = 0.40$ nA; 60×60 nm 2)

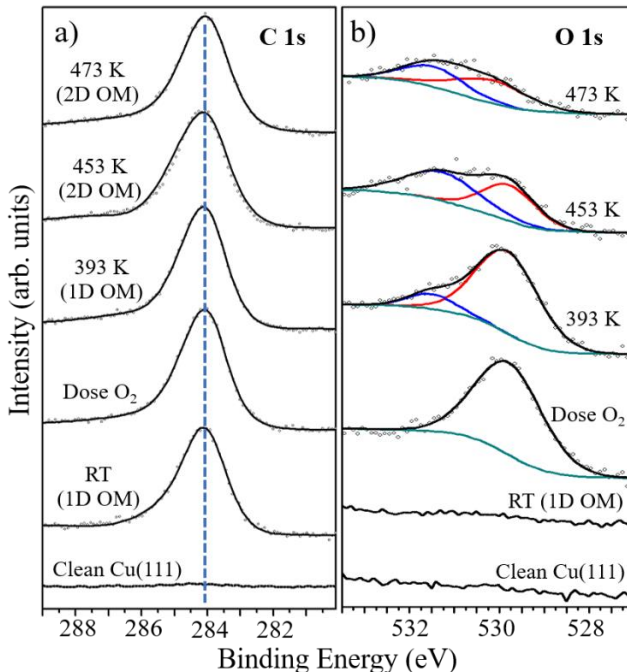


Figure 3.11 a) C 1s and b) O 1s XPS spectra obtained during the transformation from OM chains obtained with DBTP to 2D hexagonal networks on Cu(111). The C 1s peak shape and position do not change with annealing. The O 1s spectra initially show one component for chemisorbed oxygen atoms (red, background in green), and a second component for oxygen atoms forming C-Cu-O bonds appears with annealing (blue).

of each adsorbed species.

C 1s and O 1s XPS spectra were recorded between RT and 473 K to follow the chemical states of these elements throughout the transformation, as shown in [Figure 3.11](#). The C 1s spectrum measured after dosing DBTP and then O₂ at RT shows a broad peak that does not change when annealing up to 473 K, from which we infer that the terminal carbon atoms remain bonded to Cu atoms during the transformation. The O 1s spectrum recorded at RT presents a single component at a binding energy (BE) of 529.7 eV, which we assign to oxygen atoms chemisorbed on the copper surface.¹⁵⁶ After annealing the sample at 393 K for 15 min, a second low-intensity component (blue curve) at a BE of 531.5 eV is visible, which we attribute to the formation of (ph)₃-Cu-O bonds. Dimer formation from OM chains at 393 K has been reported previously,^{47, 50} indicating that some (ph)₃-Cu bonds in OM chains can break already at this temperature. The O 1s spectra for successive annealing to 453 K shows that the (ph)₃-Cu-O peak increases at the expense of the chemisorbed O peak. The total intensity of the O 1s spectra decreases during annealing due to desorption of chemisorbed oxygen, which takes place also when only O₂ was dosed onto clean Cu(111) (as shown in [Figure 3.12](#)). The XPS data support our proposed model of the 2D networks, in which the bonding of the

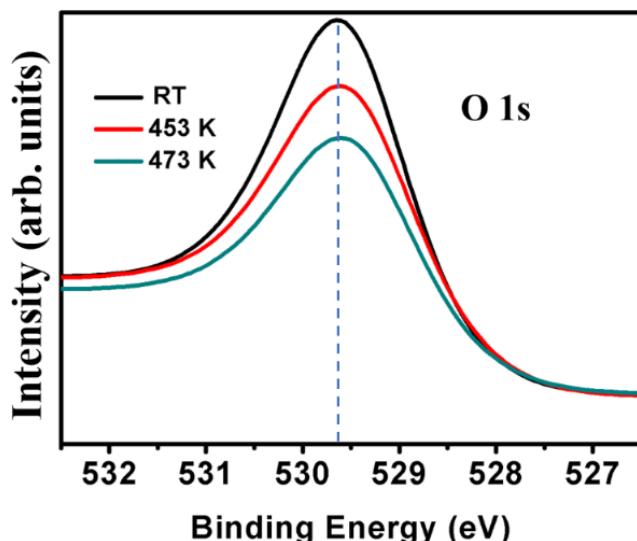


Figure 3. 12 O 1s XPS spectra obtained during a sequential annealing without precursors DBTP on Cu (111). From the spectra, it is clear that there is a decrease in the area but no shift in the peak position induced by gradual annealing. That is to say, a fraction of the chemisorbed oxygen atoms desorbed from the surface during annealing but the remaining oxygen atoms did not form any other phases.

carbon atom does not change during the 1D to 2D transformation, and a new oxygen peak appears, corresponding to the interaction of oxygen atoms with the organometallic copper atoms.

3.2.2 Size and symmetry controlling by using shorter precursor dBB and adjusting the substrates with Cu(111) and Cu(100)

In the last section, we discussed the effect of oxygen on the OM intermediate state in surface-confined Ullmann-type coupling. Introducing oxygen before the deposition of DBTP or after the formation of OM chains on Cu(111) leads to the transformation to a new 2D hexagonal OM network stabilized with Cu-O clusters after annealing at 453 K. To confirm the versatility of this structural transformation, we conducted experiments in a similar procedure with a shorter precursor 1,4-dibromobenzene (dBB), as shown in [Figure 3.1](#). Furthermore, we explored the influences of substrate symmetry on this structural transformation by using the fourfold symmetric Cu(100) surface.

Dosing dBB onto pre-oxidized Cu(111) at RT, as shown in [Figure 3.13a](#), leads to the formation of both 1D and 2D OM structures, similar to those obtained by depositing DBTP on pre-oxidized Cu(111). Annealing the sample at 453 K for 20 min transforms the 1D OM chains to 2D hexagonal networks. The networks formed from dBB have more homogeneous and larger domains than those obtained by DBTP, as

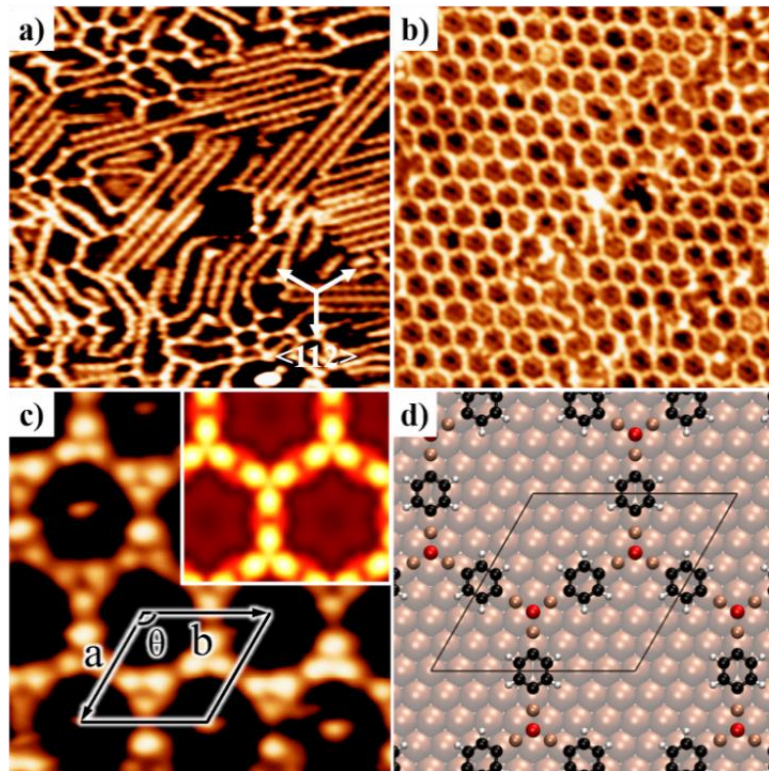


Figure 3. 13 RT STM images for 2D network formation from dBB on Cu(111). a) Coexisting 1D and 2D structures after deposition of dBB on pre-oxidized Cu(111) at RT. ($V_t = -1.0$ V, $I_t = 1.0$ nA) b) Hexagonal network obtained by annealing at 453 K for 10 min. ($V_t = -1.0$ V, $I_t = 1.0$ nA) c) Small-scale STM image of the hexagonal structures at positive bias; Inset: DFT-simulated STM image. ($V_t = 1.0$ V, $I_t = 1.0$ nA) d) DFT optimized model for the 2D networks (red: oxygen, orange: copper, grey: carbon, white: hydrogen). Image sizes of a-c are 25×25 , 25×25 , 5.5×5.5 nm 2 , respectively)

shown in [Figure 3.13b](#), which is attributed to the higher diffusivity of phenylene than terphenylene. The unit cell lattice ($a = b = 1.77 \pm 0.05$ nm, $\theta = 120^\circ \pm 2^\circ$) of the networks is commensurate with 7 copper atoms (1.78 nm) in the close-packed directions $<110>$ of Cu(111).

The positive-bias STM image in [Figure 3.13c](#) shows that the morphology is similar to the networks formed from DBTP shown in [Figure 3.2c-e](#), with a depression at the center of three bright segments attributed to an oxygen atom. For dBB, two separated bright dots could be resolved in each bright segment, which we attribute to the two copper adatoms connected by the less-bright benzene ring, similar to the observation with the molecule of 1,3,5tribromo-benzene by Fan *et al.*¹⁵⁷ We propose a model (as shown in [Figure 3.13d](#) and [Figure 3.7b](#)), in which both vertices are similar to the smaller cluster of DBTP with one central oxygen atom connecting the three OM fragments. The difference in edge length of DBTP and dBB (2.04 nm vs 1.02 nm) compared with the known molecular lengths (1.14 vs 0.28 nm) is consistent with the difference in cluster sizes between the proposed DBTP and dBB 2D structures. In addition, the unit cell

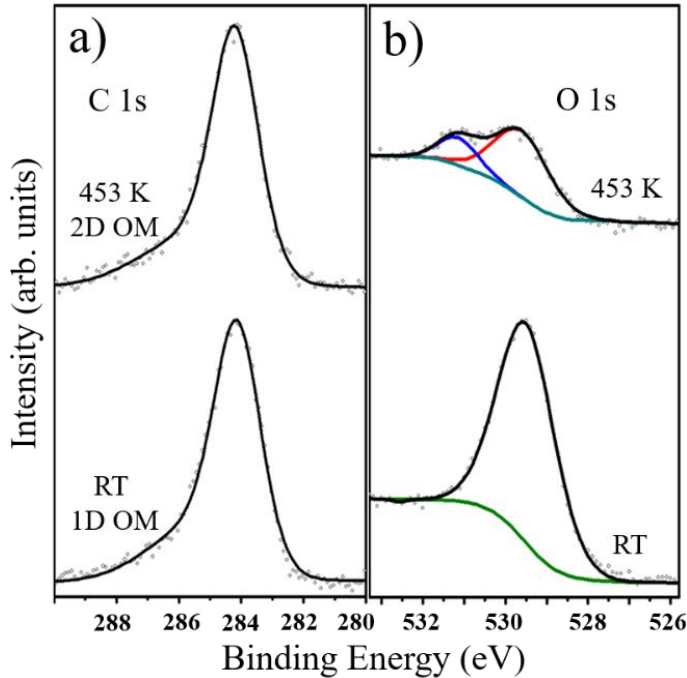


Figure 3.14 C 1s and O 1s XPS spectra obtained during the transformation from 1D OM chains (from dBB) to 2D hexagonal networks. In the C 1s spectra, we are not able to see the change after annealing, while in the O 1s spectra, a new component can be deconvoluted at the binding energy of 531.5 eV. Therefore, the XPS spectra measured for dBB have the same essential features as those measured for DBTP, indicating a common general structure of the 2D OM networks for the two precursors.

dimension of 1.77 nm optimized by DFT for a free-standing network agrees very well with the experimental value, and STM simulations (Inset of [Figure 3.13c](#)) reproduce the appearance of the copper adatoms as bright dots in positive bias. This model is supported by XPS measurements (as shown in [Figure 3.14](#)), which show that during the 1D–2D transformation, there is no detectable change in the C 1s spectra and a new peak appears in the O 1s spectra at 531.5 eV associated with the formation of ph-Cu-O bonds.

To identify the interactions that stabilize the oxygen containing 2D OM networks, we calculated the relative energies of different phases starting from the OM chains (as shown in [Figure 3.15](#)). The results indicate that forming isolated Cu-terminated phenylene units is slightly endothermic ($\Delta E = 0.30$ eV per molecule) and that the stabilization of the organometallic copper adatoms by oxygen is the largest driving force toward the 2D networks ($\Delta E = -1.07$ eV per molecule).

Charge analysis calculations indicate that the oxygen configuration in the 2D network is similar to that of the initial chemisorbed oxygen, in that the oxygen interacts primarily with the three closest Cu atoms with a mixed ionic-covalent bonding character (as shown in [Figure 3.16](#)). Calculations comparing the charge densities of the 2D OM network versus the oxygen atoms and the organometallic fragments in

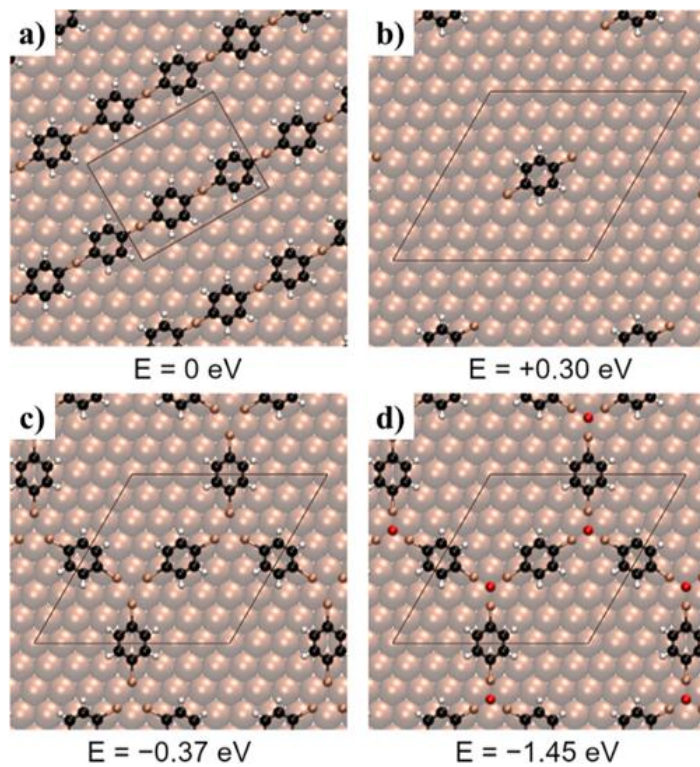


Figure 3. 15 DFT-calculated structures and energies of phases between 1D OM chains and 2D OM networks formed by dBB. a) Initial 1D OM phase, taken as the energy reference b) Isolated Cu-terminated phenylene group c) 2D hexagonal network of phenylene units d) 2D OM network with oxygen clusters observed in experiment. Energies are expressed per phenylene unit to allow for comparison between phases. For steps a→b and c→d, where the number of Cu and O adatoms changes, the formation energies were determined by comparison to isolated adatoms (not shown).

isolation show differences consistent with polar covalent bond formation, with charge accumulation between the O and Cu adatoms, accumulation on the O adatom itself, and loss on the Cu adatoms (as shown in [Figure 3.16a-c](#)). Bader charge analysis¹⁵⁸ indicates that the majority ($\approx 90\%$) of the charge on the oxygen originates from the three closest Cu adatoms. Similar features were exhibited in calculations of a single chemisorbed O adatom (as shown in [Figure 3.16d-f](#)).

Bader charge analysis comparing the 2DOM network to the isolated oxygen atoms and organometallic fragments on the surface indicates a difference in charge of -1.03 e for the oxygen atom, $+0.31\text{ e}$ for each Cu adatom, and $+0.02\text{ e}$ for each of the three closest Cu surface atoms. For the chemisorbed oxygen, there is a charge difference of -0.94 e for the oxygen and $+0.27\text{ e}$ for each of the three adjacent copper atoms. The lower absolute charge on oxygen chemisorbed on the surface than in the organometallic network contradicts the XPS measurements. We attribute this discrepancy to the tendency in calculations using the PBE functional of excessively delocalized charge, an inaccuracy that may be more significant in the

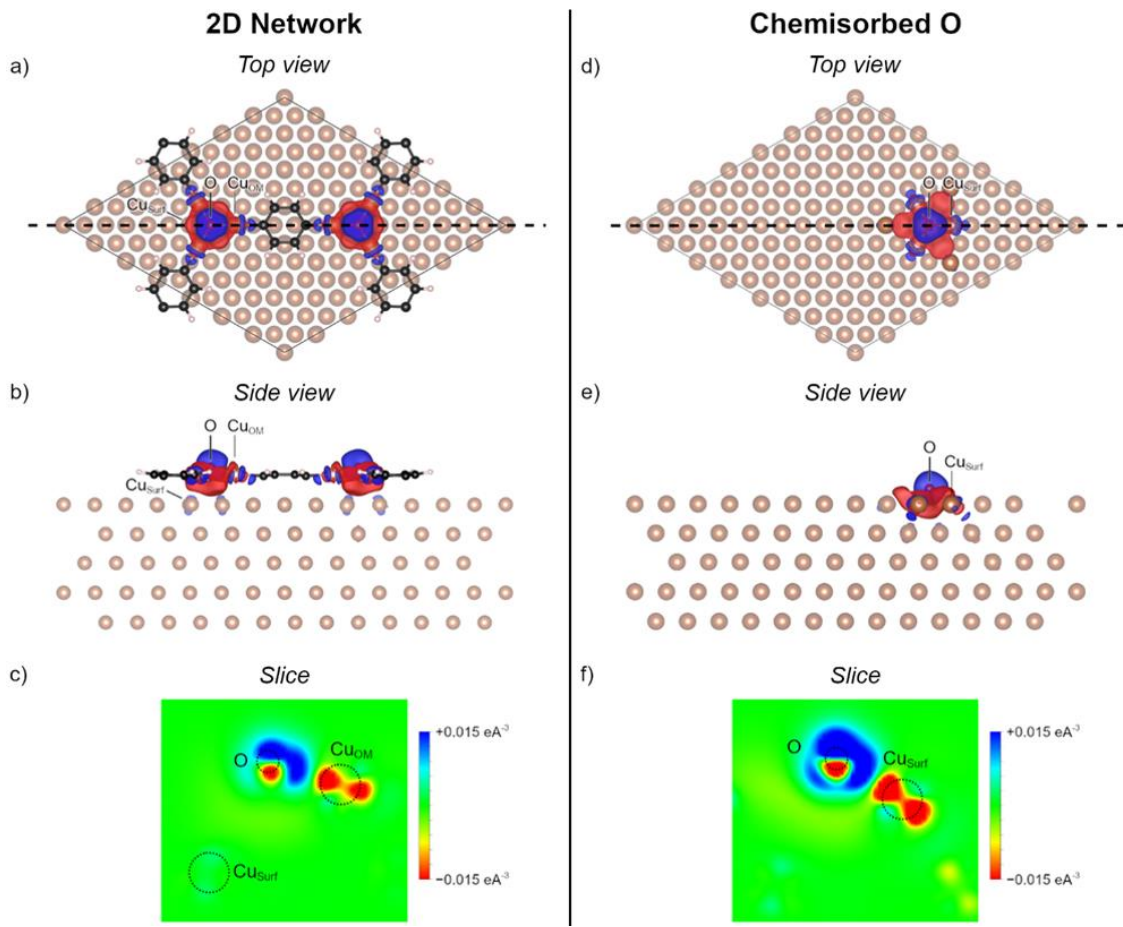


Figure 3.16 Charge density differences induced by oxygen atoms in the 2D OM network and chemisorbed on the bare substrate. a-b) Visualizations of the charge density differences (isosurfaces of 0.0015 eA^{-3}) in the 2D network, showing charge accumulation (blue) on the O adatom and between the O and Cu adatoms and charge loss (red) on the OM Cu adatoms. c) map of the charge density difference in a plane intersecting the O-Cu_{OM} bond, showing the accumulation and loss more clearly. This plane is indicated by the dashed line in (a), viewed from the side. d-f) Visualization of the charge density difference induced by a chemisorbed oxygen atom, presented identically as in a)-c) and showing overall similar features.

chemisorbed oxygen calculation where the oxygen is closer to the surface.

We studied this structural transformation with dBB on Cu(100) to investigate the effect of the substrate symmetry. [Figure 3.17a](#) shows that dBB dehalogenates after deposition at RT to form OM chains in two equivalent directions. After dosing O₂ gas at RT, a slightly higher annealing temperature of 490 K is required to transform the OM chains into square networks, as shown in [Figure 3.17b](#), which have smaller and less-homogeneous domains than those obtained on Cu(111). Both the higher annealing temperature and lower domain quality could result from the higher diffusion barrier (1.0 eV) for oxygen atoms on Cu(100).¹⁵⁹ The observation of the same structural transformation induced by oxygen for DBTP and dBB on Cu(111) and

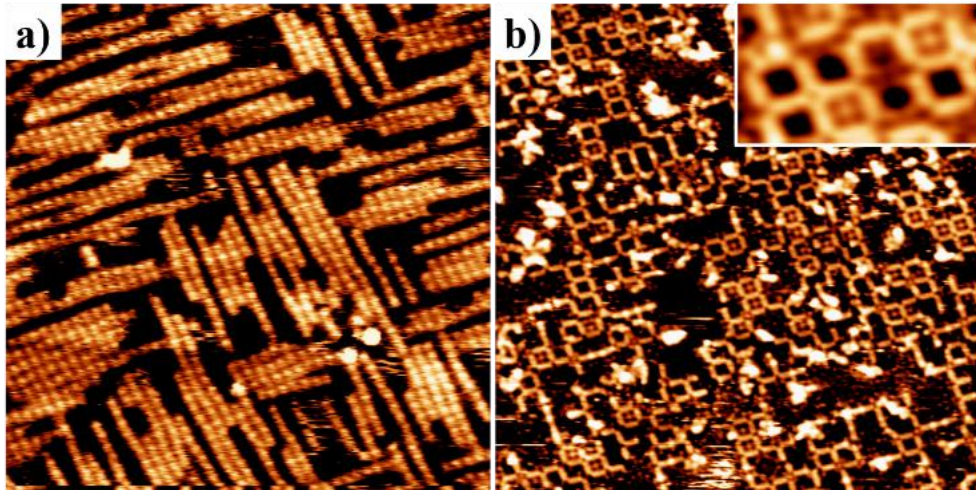


Figure 3. 17 RT STM images for 2D network formation from dBB on Cu(100). a) OM chains formed by deposition of dBB on Cu(100) at RT. ($V_t = -0.8$ V, $I_t = 8.0$ nA) b) Square networks obtained by dosing O_2 and annealing at 490 K for 20 minutes, shown in detail in the inset. (b and inset: $V_t = -1.2$ V, $I_t = 1.0$ nA) (Image sizes of a-b and inset are 30×30 , 30×30 , 5.5×3 nm 2 , respectively)

dBB on Cu(100) indicates that it could be a versatile approach to tune the size and symmetry of 2D OM networks.

3.3 Conclusions

We systematically investigated the effects of dosing oxygen on surface-confined Ullmann-type coupling by introducing chemisorbed oxygen atoms before or after the deposition of two halogenated precursors (DBTP and dBB) on two copper surfaces with different symmetries, Cu(111) and Cu(100). By combining STM and XPS measurements with DFT calculations, we identified an unexpected structural transformation from 1D OM chains to 2D OM networks. Instead of the typical polymerization pathway for thermally-activated Ullmann-type coupling on copper, oxygen atoms suppress polymerization and lead to 2D OM networks, in which copper-oxygen clusters connect three or four copper-terminated aromatic fragments. The size and symmetry of the 2D networks could be rationally controlled by tuning the precursors and using substrates with different symmetry, respectively. In future work, we will investigate the generality of this transformation for other precursors and surfaces to fabricate unique surface nanostructures, with potential applications in host-guest chemistry.

3.4 Experimental and Theoretical Methods

All the experiments were conducted in ultra-high vacuum (UHV) systems with a base pressure of 2×10^{-10} mbar. The Cu(111) and Cu(100) crystals (MaTecK GmbH) were cleaned by repeated cycles of Ar⁺ sputtering and annealing (750 K). The cleanliness was checked by both STM and XPS. Using organic molecular beam deposition, the precursor 4,4''-dibromo-p-terphenyl (98%, Sigma-Aldrich) was deposited at 388 K for three minutes on a clean Cu(111) surface held at RT, yielding a sub-monolayer coverage. The precursor 1,4-dibromobenzene (98%, Sigma-Aldrich) was dosed through a leak-valve for two minutes with a pressure of 1×10^{-8} mbar, leading to monolayer coverage. 60 Langmuir (L) of O₂ was dosed at 5×10^{-7} mbar through a leak-valve onto Cu(111) and Cu(100) held at RT.

STM measurements were performed at low-temperature, 4.6 K, (Omicron LT-STM) or at RT (Omicron VT-STM), in constant-current mode with an electrochemically etched tungsten tip in both cases. LT-STM images were analyzed with the SPIP program and RT STM images with WSxM¹⁶⁰ and calibrated with the known lattice constant of the substrates and the close-packed bromine atoms on the substrates. The bias voltages of STM images were measured from the tip to the sample. XPS measurements were performed in the same UHV system as the Omicron VT-STM, using an Al K α source X-ray lamp (pass energy 20 eV) and a hemispherical electron analyzer with 5 channeltrons detector. The XPS spectra were fitted using Voigt lines and Shirley background.

Theoretical calculations were performed with the Vienna Ab-initio Simulation Package (VASP)^{161, 162}. Plane-wave DFT calculations were made using the Perdew-Burke-Ernzerhof¹⁶³ generalized-gradient approximation (PBE-GGA) for exchange-correlation potential, the projector augmented wave (PAW) method,^{164, 165} and a basis set with an energy cut off of 450 eV. The zero-damping DFT-D3 method of Grimme,¹⁶⁶ was used for van der Waals (vdW) correction of potential energy.

Calculations for the DBTP 2D OM network used a Cu(111) slab corresponding to a (14 0 | 0 14) epitaxy matrix, constructed with a lattice constant of 0.363 nm and a 1.8 nm vacuum layer. Due to the large size of the cell, only two surface layers were used with the atomic positions in both layers fixed. Calculations for dBB used five-layer slabs with the bottom two atomic layers fixed, corresponding to a (7 0 | 0 7) epitaxy matrix for the 2D OM network and (3 3 | -4 4) epitaxy matrix for the OM chains. For the dBB calculations,

geometrical optimizations and STM simulations were performed at the gamma k-point, Bader charge calculations with a 2x2x1 k-mesh, and the formation energies were computed using a 6x6x1 k-mesh and 8x8x1 k-mesh for the supercells for the dBB 2D OM network and OM chains, respectively. For DBTP, a 5x5x1 k-mesh was used for the formation energy calculations. Images of the calculated structures were generated using the VMD software,¹⁶⁷ and STM images were simulated via the Tersoff-Hamann approximation¹⁶⁸ using the calculated wavefunction of the relaxed structures obtained from VASP and visualized using the Hive software.¹⁶⁹

Chapter 4. Oxygen-Promoted Synthesis of Armchair Graphene Nanoribbons on Cu(111)

Penghui Ji, Oliver MacLean, Gianluca Galeotti, Dominik Dettmann, Giulia Berti, Kewei Sun, Haiming Zhang, Federico Rosei, and Lifeng Chi

Authors' contribution: L. Chi and F. Rosei initiated and supervised the project. P. Ji conducted the experiments and the data processing. P. Ji wrote the initial manuscript. O. MacLean performed DFT simulation. All the authors modified the manuscript.

4.1 Introduction

On-surface synthesis has received great attention as a method to create atomically-precise one-dimensional (1D) and two-dimensional (2D) polymers with intriguing properties.^{6, 11, 45, 142, 170-173} In particular, graphene nanoribbons (GNRs), a category of quasi-1D nanomaterials derived from graphene, have been widely studied due to their tunable electronic properties and potential applications in semiconductor devices, such as field-effect transistors and spintronics.^{1, 121, 174-176} A series of top-down approaches have been pursued to produce GNRs,¹⁷⁷⁻¹⁷⁹ yet a lack of control over the ribbon width and edge structure has hindered their further developments. In 2010, Cai *et al.*¹⁴² reported the fabrication of an atomically-precise armchair GNR (AGNR) on the Au(111) surface using a bottom-up approach. The basic mechanism involves thermally-activated dehalogenation, surface-assisted polymerization and finally cyclodehydrogenation. In the following decade, this bottom-up approach has been extended to synthesize a wide variety of GNRs, including AGNRs with different widths,^{143-145, 180, 181} zigzag GNRs,^{120, 121} GNR heterojunctions,¹⁸²⁻¹⁸⁶ chiral GNRs¹⁸⁷⁻¹⁹¹ and chemically-doped GNRs.¹⁹²⁻¹⁹⁵ Based on the periodic similarity of their electronic structures, AGNRs can be classified into three families, 3p, 3p+1 and 3p+2 (representing the number of carbon atoms in the narrow direction).¹⁷⁴ So far, few studies have focused on GNR synthesis on Cu(111) due to the stronger surface interaction, despite the lower temperature for dehalogenation.^{187, 188, 196-198} It has been shown that chiral GNRs can be synthesized on Cu(111)¹⁸⁸ using the same precursor that yields non-chiral 7-AGNR on Au(111)¹⁴² and that dehalogenation can be reversible on

Au(111) but not Cu(111),¹⁷² which implies that the reaction pathway and products achieved could be controlled through the choice of substrate.

A second approach to tailor the reaction pathway in surface-confined synthesis is to introduce different atomic species, which has been considered in only a few recent studies. Exposure to iodine creates a monolayer intercalated between the polymers and the Ag(111) surface that decouples their electronic interactions.¹⁰² In addition, hydrogen was shown to remove halogen by-products and to induce covalent coupling, and sulfur to switch the surface-confined Ullmann reaction on or off.^{105-107, 110, 199} We recently investigated the effect of oxygen on the synthesis of 3-AGNRs by surface-confined Ullmann coupling and determined that it, instead, caused a 1D to 2D transformation of the organometallic (OM) structures.⁵⁴ Here, our objective was to investigate the synthesis of 3p-AGNRs on Cu(111), extending from the previous study on Au(111),¹⁸⁰ and to examine the effect of oxygen on lateral fusion of 3-AGNRs, inspired by their potential to promote C–H activation.¹¹¹

Our investigation demonstrated the successful synthesis of 3p-AGNRs on Cu(111) via lateral fusion of poly(para-phenylene) (i.e. 3-AGNR). Introduction of co-adsorbed atomic oxygen substantially reduced the temperature required to induce the lateral fusion reaction. The identification of this catalytic effect could benefit on-surface synthesis that applies dehydrogenation reactions, including of GNRs, and highlights the potential of additional atomic adsorbates to steer surface reactions.

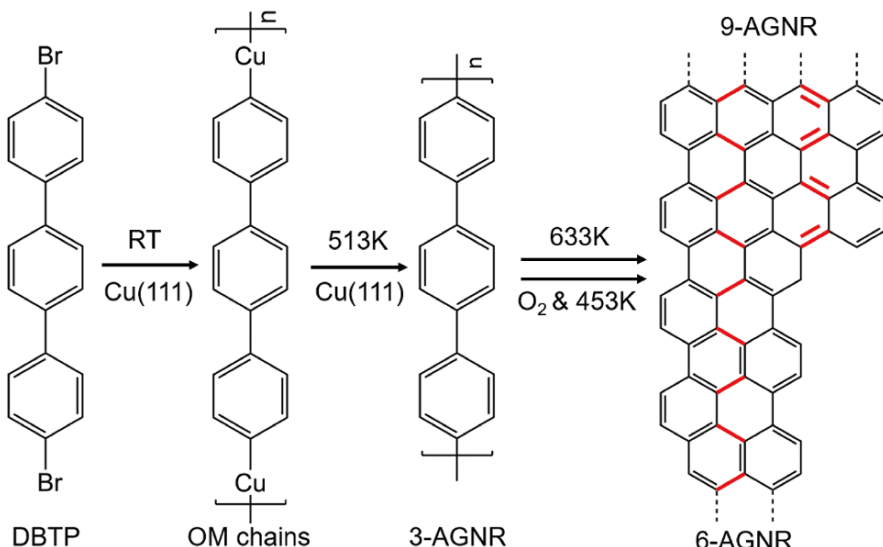


Figure 4. 1 Synthesis of 3p-AGNRs on the pure Cu(111) and partially oxidized Cu(111). Bonds formed during lateral fusion are shown in red.

4.2 Results and Discussions

The synthetic route to AGNRs on pure Cu(111) or with the introduction of oxygen is shown in [Figure 4.1](#). The OM chains consisting of alternating terphenyl segments and copper atoms can be formed after the deposition of DBTP ($\text{Br}(\text{ph})_3\text{-Br}$) on Cu(111) held at RT in UHV.⁵⁰ Annealing the sample at 513 K for 20 min breaks the C-Cu bonding, transforming the OM chains into 3-AGNRs through C-C coupling, which undergo lateral cyclodehydrogenation at 633 K for 20 min to form wider 3p-AGNRs. However, the introduction of O_2 gas after the formation of 3-AGNRs allows lateral fusion to proceed at 453 K within 20 min, which is 180 K lower than that in the absence of oxygen.

4.2.1 The synthesis of 3P sub-family AGNRs on Cu(111)

Representative STM images of different steps in the synthesis of 3p-AGNRs on Cu(111) are shown in [Figure 4.2](#), which follows a similar reaction pathway as on Au(111).¹⁸⁰ Deposition of DBTP on Cu(111) at

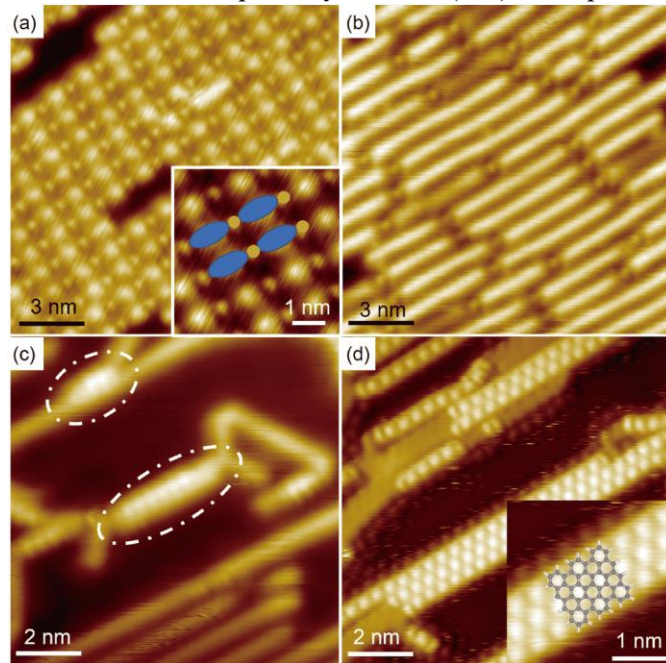


Figure 4. 2 LT STM images ($T = 4.6 \text{ K}$) of the synthesis of 3p-AGNRs on Cu(111). (a) STM image of OM chains formed by the dehalogenation of DBTP. Yellow circles and blue ellipses indicate copper atoms and terphenylene segments in the magnified image in the inset ($V_b = 1 \text{ V}$, $I_t = 0.1 \text{ nA}$; inset: $V_b = 1 \text{ V}$, $I_t = 0.1 \text{ nA}$). (b) 3-AGNRs synthesized after annealing at 513 K ($V_b = 1 \text{ V}$, $I_t = 0.1 \text{ nA}$). (c) Lateral fusion between 3-AGNRs occurring after annealing at 593 K, contributing to the formation of 6-AGNRs ($V_b = 1 \text{ V}$, $I_t = 1 \text{ nA}$). (d) Co-adsorbed 3-AGNRs and wider AGNRs after annealing at 633 K ($V_b = -0.1 \text{ V}$, $I_t = 1 \text{ nA}$).

RT leads to the formation of linear OM chains by $(\text{ph})_3\text{-Cu-(ph)}_3$ bonding, as shown [Figure 4.2a](#), inset of which is the magnified image with superimposed sketchy model (Yellow circles and blue ellipses are copper atoms and terphenylene segments, respectively). Annealing at 513 K induces the breaking of C-Cu bonding and C-C coupling into 3-AGNRs, which are terminated by residual C–Cu bonds, as shown in [Figure 4.2b](#). To achieve the diffusion of 3-AGNRs and subsequent lateral cyclodehydrogenation, we gradually increased the annealing temperature. As shown by the white ellipses in [Figure 4.2c](#), wider ribbons (6-AGNR) start to form by the lateral fusion of 3-AGNRs after annealing at 593 K. A greater amount of wider 3p-AGNRs (including 9-AGNR and 12-AGNR) are synthesized after heating the sample at 633 K for 20 minutes, as shown in [Figure 4.2d](#). A noteworthy feature of these STM images is the increased height and contrast that can be observed in certain segments of the ribbons. We attribute this to the intercalation of Br atoms underneath the ribbons, which is supported by the similar appearance of 3-AGNR that was observed lying above Br atoms between two adjacent 3-AGNRs upon annealing the sample at 533 K (see [Figure 4.3](#)) and by STM simulations (see [Figure 4.4](#)). As a result, the ribbons with Br atoms underneath exhibit bright periodic dots, while the others have a comparably darker homogeneous appearance. A similar variation in the contrast was observed for intercalation of iodine atoms between polymers and Ag(111).¹⁰² This intercalation is further supported by the agreement between the polymer's longitudinal periodicity of 4.4 Å and Br atoms in the known $(\sqrt{3} \times \sqrt{3})\text{R}30^\circ$ overlayer structure on Cu(111) (see [Figure 4.5](#)).²⁰⁰ We performed density functional theory (DFT) calculations to address whether Br intercalation facilitates the lateral fusion

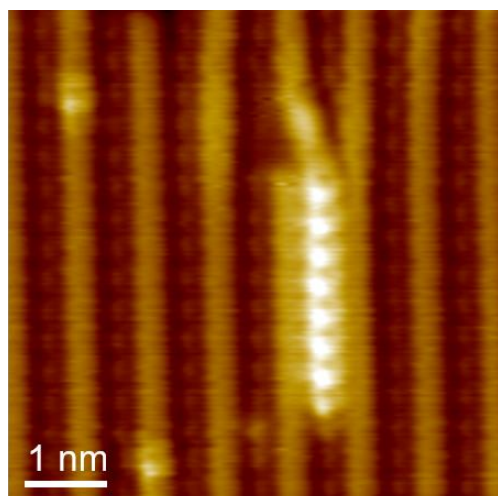


Figure 4. 3 LT STM image of annealing 3-AGNR on Cu(111) at 533 K. As a result, one 3-AGNR lies above the Br atoms to exhibit increased height and contrast. ($V_b = -0.1$ V, $I_t = 1$ nA)

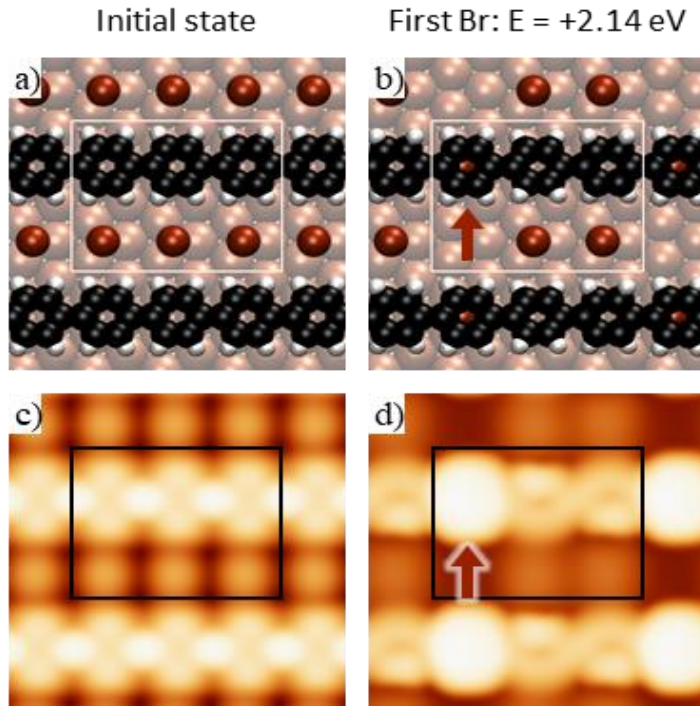


Figure 4. a, b) Calculated structures for the initial self-assembly of 3-AGNRs and Br atoms (a) and after intercalation of one Br atom (b). (c, d) Simulated STM images for the structures above, showing that the intercalated Br causes the upper phenylene to appear bright. Black and white rectangles indicate the supercell and red arrows show the position of the intercalated Br (atom colors: Br: dark red, C: black, H: white, Cu: light brown).

reaction, by enabling 3-AGNRs to cross over the rows of Br atoms prior to fusion. However, intercalation of a single Br atom (for every three phenylene monomers) is endothermic by 2.1 eV (as shown in [Figure 4.4](#) and [Figure 4.6](#)), and therefore could occur only rarely prior to lateral fusion. Instead, we propose that the intercalation results from trapping of Br atoms during the zipping reaction.

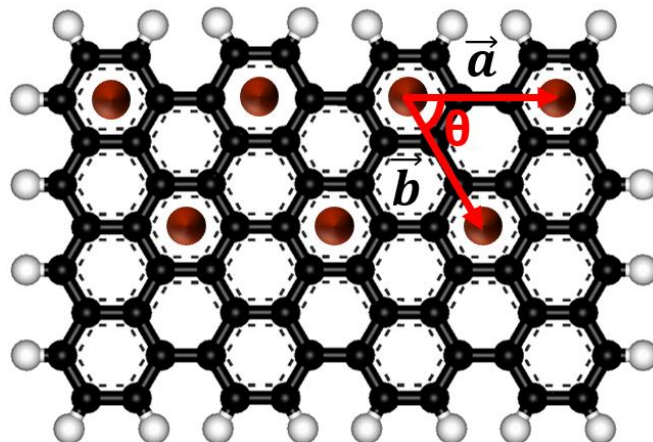


Figure 4.5 Proposed model of 9-AGNR on top of Br atoms. Br atoms are distributed as the known $(\sqrt{3} \times \sqrt{3}) R30^\circ$ overlayer structure on Cu(111) and the lattice matches well with the longitudinal periodicity of 9-AGNR (4.4 Å). (Brown, black and white balls are Br, C and H atoms.)

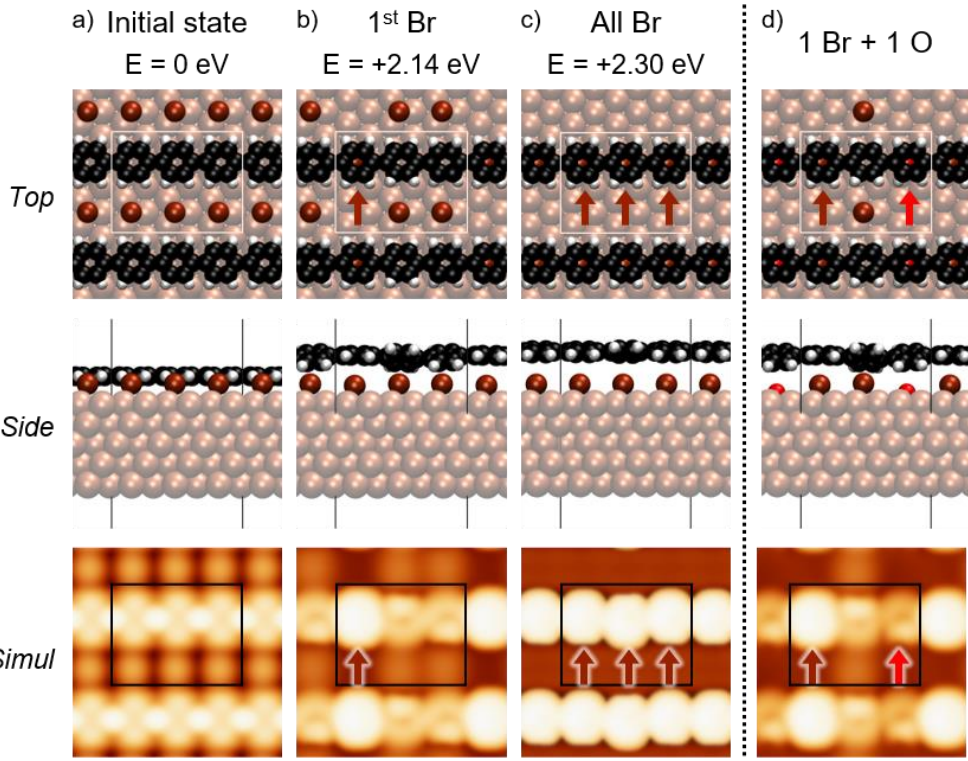


Figure 4.6 Calculated structures and STM simulations for atom intercalation below 3-AGNRs. Top views (Top), side views (Side), and simulated STM images (Simul) for the states of the initial 3-AGNR and Br self-assembly (a), intercalation of 1 Br per three phenylenes (b), intercalation of 1 Br under each phenylene (c), and 1 Br and 1 O atom. The supercell is indicated by white or black rectangles, and dark red and bright red arrows show the positions of Br and O atoms under the polymer, respectively. The column labels include the relative energy of the lifted states.

In summary, 3p-AGNRs can be synthesized on Cu(111) with lateral fusion of 3-AGNR, which is similar to the synthesis on Au(111). However, we observed the intercalation of Br atoms between the ribbons and substrate after the formation of wider 3p-AGNRs, which has never been reported before.

4.2.2 The effects of oxygen on the synthesis of 3P sub-family AGNRs on Cu(111)

To investigate the effects of oxygen on the synthesis of 3p-AGNRs on Cu(111), after forming 3-AGNRs (see [Figure 4.7a](#)), O₂ was dosed on the sample held at 403 K to form areas of oxidized Cu (as shown in [Figure 4.7b](#) and [Figure 4.8](#)) as well as dark Cu vacancy islands.^{127, 128} [Figure 4.7b](#) shows that the 3-AGNRs remain intact during exposure to O₂ and can extend across the bare surface and oxidized domains. Heating at 423 K causes a small percentage of 3-AGNRs to exhibit enhanced contrast, which was attributed to the onset of Br intercalation (see [Figure 4.9](#)). We consider it unlikely that intercalated O atoms are the cause of the increased contrast of the ribbons, since the smaller O atom would lead to a significantly different

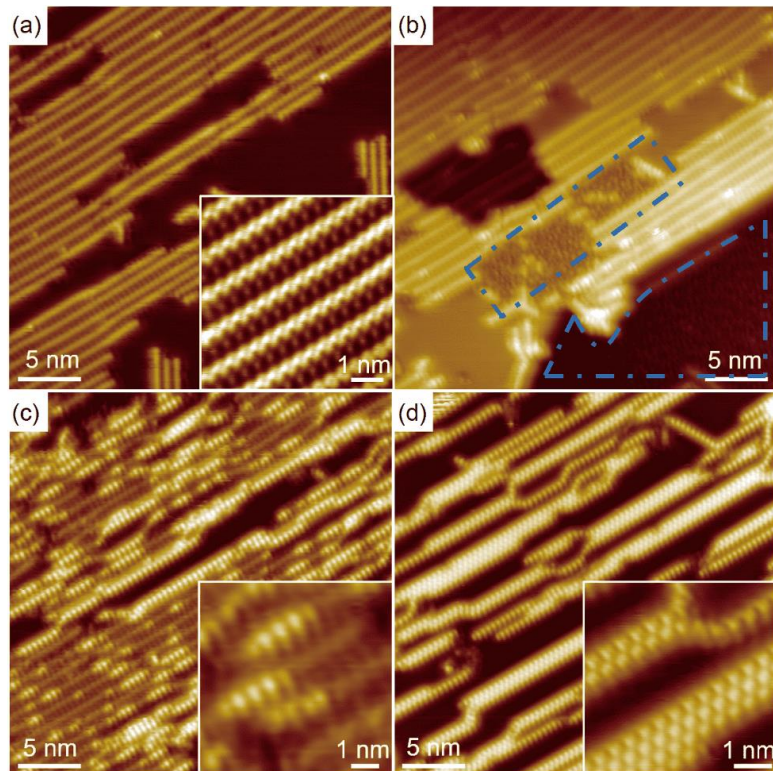


Figure 4. 7 LT STM images ($T = 4.6$ K) of 3p-AGNRs synthesized on Cu (111) with the introduction of O_2 . (a) Image of 3-AGNRs formed after annealing OM chains at 513 K ($V_b = -1$ V, $I_t = 0.1$ nA). Inset is a high-resolution image of 3-AGNRs ($V_b = -0.05$ V, $I_t = 1$ nA). (b) Dose 60 Langmuir (L) of O_2 when sample is held at 403 K (Dashed blue lines mark the oxidized area; $V_b = -1$ V, $I_t = 0.1$ nA). (c) Brighter features appear after annealing at 453 K lasting 15 min ($V_b = -1$ V, $I_t = 0.1$ nA). Inset is a magnified image ($V_b = -0.1$ V, $I_t = 0.1$ nA). (d) 3p-AGNRs synthesized after annealing the sample at 453 K lasting 60 min ($V_b = -0.1$ V, $I_t = 1$ nA). Inset is a magnified image ($V_b = -0.1$ V, $I_t = 1$ nA) (color online).

appearance of the ribbons than Br (supported by STM simulations in [Figure 4.6](#)). After annealing at 453 K, we observed a substantial increase in the number of 3-AGNRs chains showing high contrast and parts of 3-

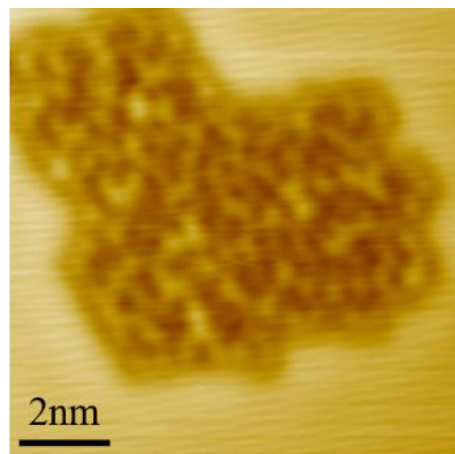


Figure 4. 8 Magnified STM image after dosing O_2 on Cu(111) decorated with 3-AGNR at 403 K, leading to the formation of oxidized Cu phase. ($V_b = -1$ V, $I_t = 0.1$ nA)

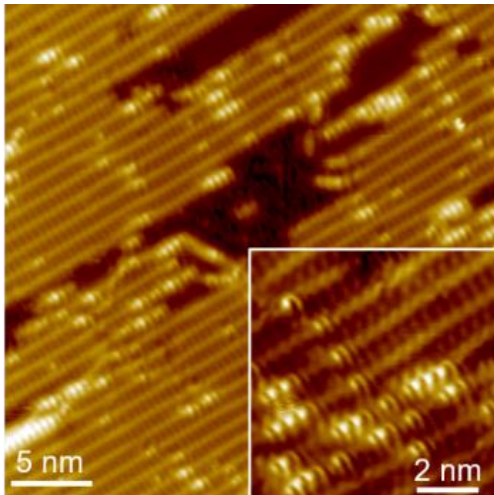


Figure 4. 9 LT-STM image of annealing 3-AGNR on oxidized Cu(111) at 423 K, leading to the onset of Br intercalation. ($V_b = -1$ V, $I_t = 0.1$ nA) Inset is magnified image. ($V_b = -0.1$ V, $I_t = 1$ nA)

AGNRs diffuse to become closer to each other ([Figure 4.7c](#)). Further annealing at 453 K yielded a range of AGNRs with widths up to 12-AGNR, as shown by [Figure 4.7d](#), in which all ribbons have a bright, high-contrast appearance. Compared to the reaction on bare Cu(111), the introduction of oxygen lowers the formation temperature of AGNRs by approximately 180 K. [Figure 4.7d](#) also shows that the wider ribbons are formed by zipping two narrower ones, which is similar to what is observed on Au(111) (as shown in [Figure 4.10](#)).¹⁸⁰ To support the catalytic effect of oxygen on the synthesis of GNRs and follow the chemical states of each element throughout the reactions, we conducted XPS measurements starting from the deposition of DBTP. To ensure that the states of the surface polymers were the same for the XPS measurements as the LT STM images shown in [Figures 4.2](#) and [Figure 4.7](#), we recorded accompanying RT-

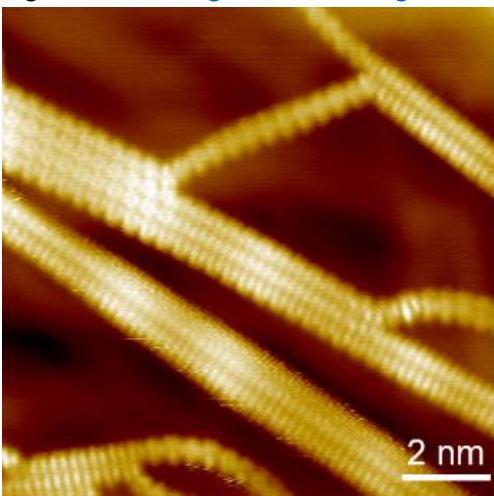


Figure 4. 10 LT STM image of 3P-AGNRs on Au(111). 6, 9 and 12-AGNRs are formed by zipping of 3-AGNRs. ($V_b = -0.1$ V, $I_t = 1$ nA).

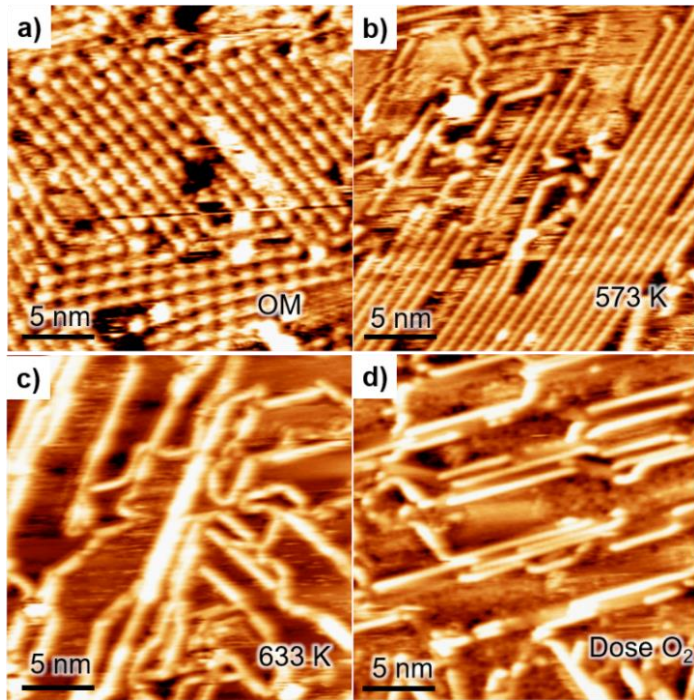


Figure 4. 11 RT STM images of the synthesis of 3P-AGNRs on Cu(111). a) OM (organometallic) chains formed as the deposition of 4, 4"-dibromo-p-terphenyl (DBTP) on Cu(111) at RT. ($V_b = -1$ V, $I_t = 1$ nA). b) 3-AGNRs formed after annealing at 573 K. ($V_b = -1$ V, $I_t = 1$ nA) c) Wider AGNRs are fabricated after annealing at 633 K. ($V_b = -1$ V, $I_t = 0.5$ nA) d) After the formation of wider AGNRs, O₂ was dosed on the sample held at 423 K to form oxidized Cu phases and more Br atoms intercalate between the ribbons and substrates. ($V_b = -1$ V, $I_t = 1$ nA)

STM images (see [Figures 4.11](#) and [Figure 4.12](#)).

Initially, we repeated the synthesis of AGNRs without oxygen. As shown in [Figure 4.11a](#), the deposition of DBTP at RT forms OM chains exhibiting a broad peak in the C 1s spectrum at a binding energy (BE) of 284.6 eV (see [Figure 4.13a](#)). Transformation of the OM chains into 3-AGNR by annealing to 513 K for 20 min induces a shift to a higher BE of 284.8 eV, where both the peak position and upward shift after C–C coupling are consistent with previous results.²⁰¹ From both XPS measurements and RT-STM images (as shown in [Figure 4.11b](#) and [Figure 4.13a](#)), 3-AGNRs do not change by annealing up to 573 K. As shown in [Figure 4.11c](#), annealing at 633 K drives the formation of wider AGNRs. Similarly, we can observe the increased contrast ascribed to the intercalation of Br atoms. At 633 K, C 1s core level shifts back to lower BE of 284.4 eV, which can be attributed to two possible effects: one is the formation of wider conjugated AGNRs, which caused an upshift in the BE of the C 1s spectrum on Au(111);²⁰² the other one is the intercalation of Br atoms between the polymer and substrate, since a large downward shift in the BE was observed for intercalation of iodine atoms.¹⁰² Accordingly, we assign the downshift at 633 K to the

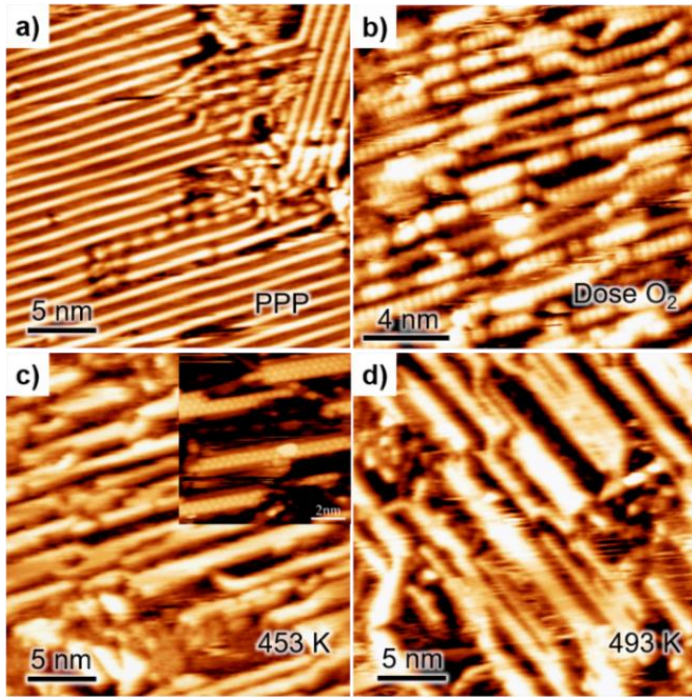


Figure 4.12 RT STM images of the synthesis of 3P-AGNRs on oxidized Cu(111). a) 3-AGNRs are formed after annealing the OM chains on Cu(111) at 513 K. ($V_b = -1$ V, $I_t = 1$ nA). b) O₂ gas was dosed on the sample held at 423 K, leading to the intercalation of Br atoms between 3-AGNRs and Cu substrate. ($V_b = -1$ V, $I_t = 1$ nA) c) Wider AGNRs are fabricated after annealing at 453 K. ($V_b = -1$ V, $I_t = 1$ nA) Inset is high-resolution image which exhibits the increased height and contrast. ($V_b = -1$ V, $I_t = 1$ nA) d) Higher annealing at 493 K causes no apparent difference, and the ribbons remain intact. ($V_b = -1$ V, $I_t = 1$ nA)

intercalation of Br atoms.

After the formation of wider AGNRs, we dosed 60 L of O₂ on the sample held at 423 K to assess whether oxygen will affect the ribbons and Br atoms. As shown in [Figure 4.11d](#), parts of the bare Cu(111) areas are oxidized and more Br atoms intercalate between the ribbons and substrate, which causes the C 1s core level to further shift to a lower BE of 284.2 eV.

We then investigated the effect of introducing O₂ before the lateral fusion of 3-AGNRs on Cu(111) by XPS (see [Figure 4.13b-c](#)). Annealing to 513 K leads to the same broad peak for the 3-AGNRs at the BE of 284.8 eV as shown previously, and corresponding O 1s XPS measurements confirm the absence of oxygen on the surface. Dosing O₂ onto the sample held at 423 K induces a large downward shift (0.6 eV) of the C 1s peak, consistent with the previous decrease assigned to the lifting of the ribbons by Br atoms. The O 1s spectrum after dosing (see [Figure 4.13c](#), 423 K) is consistent with a low coverage of oxidized Cu,²⁰³ implying the absence of significant C–O bond formation, as supported also by the C 1s spectra. From the

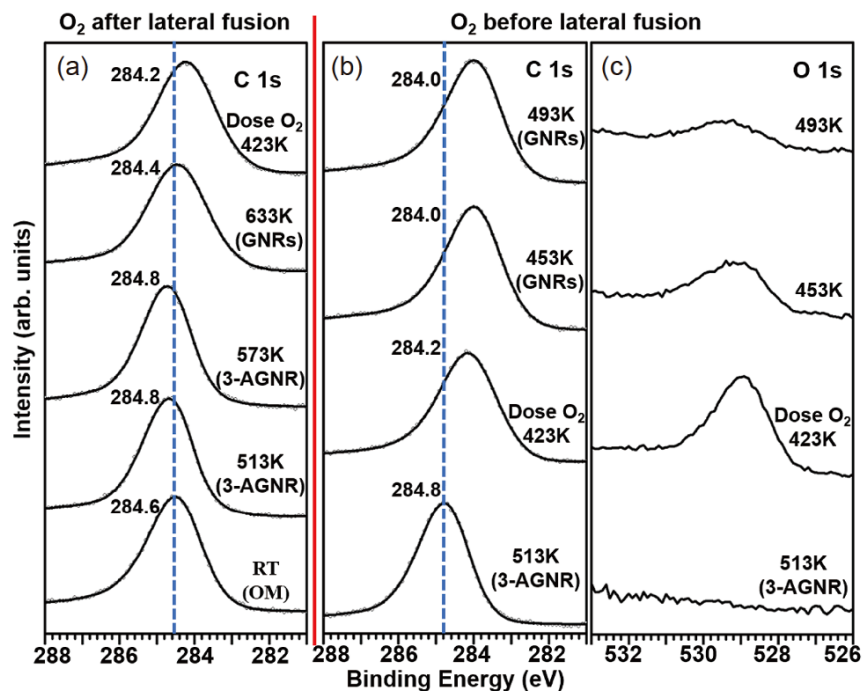


Figure 4.13 a) C 1s XPS spectra of the synthesis of 3p-AGNRs on Cu(111) at increasing temperatures. (b, c) C 1s and O 1s XPS spectra of the synthesis of 3p-AGNRs on Cu(111) with oxygen introduced after the formation of 3-AGNR.

corresponding RT STM images (see [Figure 4.12](#)), no wider AGNRs were observed until we annealed the sample at 453 K, which induced more intercalation of Br atoms and a further downward shift (0.2 eV) of the C 1s core level. After annealing at 493 K, no significant difference in the STM images and C 1s XPS spectra could be distinguished. Annealing at 453 K and 493 K causes a decrease in the intensity of the O 1s spectra, assigned to desorption of O atoms, and a broadening of the peak towards higher binding energy, which is attributed to a partial change in the oxidized Cu phase. The Br 3p spectra shows no evident change by annealing or oxygen deposition, indicating that intercalation does not significantly affect the electronic state of the Br atoms. The XPS measurements are consistent with our STM observations where the introduction of oxygen on Cu(111) promotes the lateral synthesis of AGNRs, as well as the intercalation of Br atoms. In addition, the lack of a significant change in the STM and XPS results suggest that the AGNRs are stable in the presence of oxygen up to at least 493 K.

To further confirm that the large downward shift in C 1s BE is induced by Br intercalation but not oxygen adsorption, we dosed O₂ at RT on Cu(111) after the formation of 3-AGNRs. From the XPS and STM measurements (see [Figure 4.14](#)), no change in the C 1s spectrum and no intercalation of Br can be observed. Annealing at 423 K induces a small degree of Br intercalation and a small decrease (0.2 eV) in the C 1s BE.

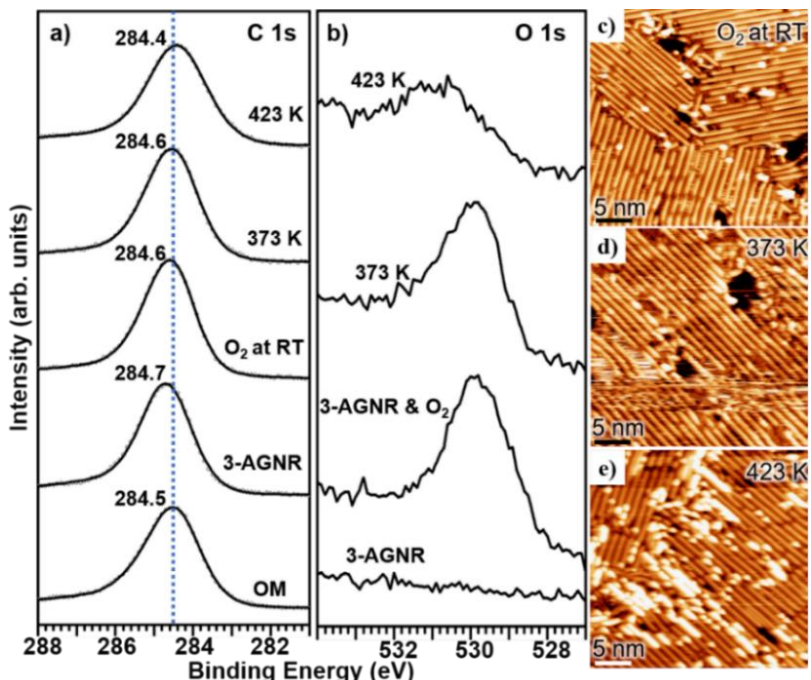


Figure 4. 14 a)-b) C 1s and O 1s XPS spectra of introducing oxygen on the sample held at RT after the formation of 3-AGNRs. c) RT STM image of dosing O₂ on the 3-AGNRs covered Cu(111). (V_b = - 1 V, I_t = 1 nA) d) Annealing at 373 K makes no difference on the 3-AGNRs. (V_b = - 1 V, I_t = 1 nA) e) Annealing at 423 K drives few intercalation of Br atoms between 3-AGRNs and Cu(111) substrate. (V_b = - 1 V, I_t = 1 nA)

From STM and XPS measurements, we learned that introducing O₂ promoted the intercalation of Br atoms and lateral fusion of 3-AGNRs. We propose that oxygen's catalytic effect in cyclodehydrogenation is through the abstraction of H atoms from the AGNRs, similar to the activation of methane by oxygen on Cu(111).¹¹¹ A second possible mechanism is that oxygen adsorption reduces the space available to the 3-AGNRs, causing them to approach more closely and therefore cyclize more readily. Though oxygen also promotes the lifting of 3-AGNRs by Br atoms, this is unlikely to facilitate the lateral fusion reaction, which is expected to be initiated at sites where the AGNR is in contact with the catalytic surface. Diffusion of Br and O atoms is rapid at 453 K, so a possible enhancement in diffusion by lifting of AGNRs cannot account for the considerably higher rate of lateral fusion in the presence of oxygen. Inspired by the repulsive interaction of chemisorbed O atoms on Ag(111),²⁰⁴ we propose that the intercalation of Br atoms could be driven by a repulsive interaction between O and Br atoms on Cu(111). Elucidation of the detailed mechanism of oxygen promoted AGNR fusion and the application of oxygen to cyclodehydrogenation in general calls for further in-depth experimental and theoretical investigations.

4.2.3 STS measurements of 3P sub-family AGNRs on Au(111) & Cu(111)

To date, most STS measurements of the electronic structures of GNRs have been conducted on the Au(111) surface. The large number of STS investigations on a range of GNRs has enabled the creation of a reference database that can be compared against in new investigations. Therefore, before measurements on Cu(111), we conducted STS on 3p-AGNRs synthesized on Au(111) for comparison.

The synthetic strategy of 3p-AGNRs on Au(111) is same as that on Cu(111) with the precursor DBTP (see [Figure 4.1](#)). As the STM image shown in [Figure 4.10](#), 6, 9,12-AGNRs can be simultaneously synthesized on Au(111) by the lateral fusion of 3-AGNR. A dI/dV curve measured on bare Au (111) (red curve in [Figure 4.15a](#)) shows the Shockley surface state near -0.4 eV, which is consistent with previous observations.²⁰⁵ Besides serving as a background reference, this suggests the tip is in good condition for the remaining STS measurements. The dI/dV curve measured on the edge of a 6-AGNR (blue curve in [Figure 4.15a](#)) shows peaks at -1.65 eV and +1.6 eV, which we initially assigned to the maximum of the valence band and minimum of the conduction band (VB and CB). Similarly, from the dI/dV curve measured on the edge of 9-AGNR shown in [Figure 4.15h](#), the peaks at -1.1 eV and +1.1 eV can be

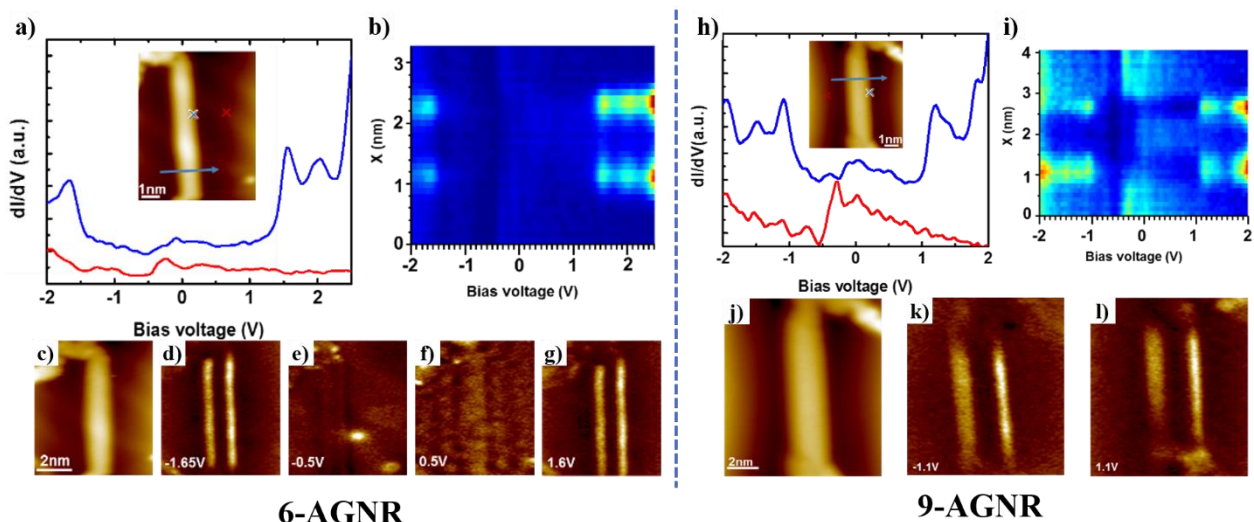


Figure 4. 15 a)-g) STS measurements of 6-AGNR on Au(111). a) dI/dV curves measured on the edge of 6-AGNR (blue line) and on bare Au (111) site (red line). b) 2D STS map comprised of 32 dI/dV curves measured across the ribbons, the direction is denoted with a blue arrow in panel a. c) STM image of 6-AGNR for mapping. d-g) dI/dV maps of 6-AGNR acquired at d) -1.65 eV, e) -0.5 eV, f) 0.5 eV, g) 1.6 eV, respectively. h)-l) STS measurements of the electronic structure of 9-AGNR on Au (111). h) dI/dV curves measured on the edge of 9-AGNR (blue line) and on a bare Au (111) site (red line). i) 2D STS map comprised of 36 dI/dV curves measured across 9-AGNR, the direction is denoted with a blue arrow in panel a. j) STM image of 9-AGNR for mapping. k-l) dI/dV maps of 9-AGNR acquired at the bias voltage of d) -1.1 eV, e) 1.1 eV.

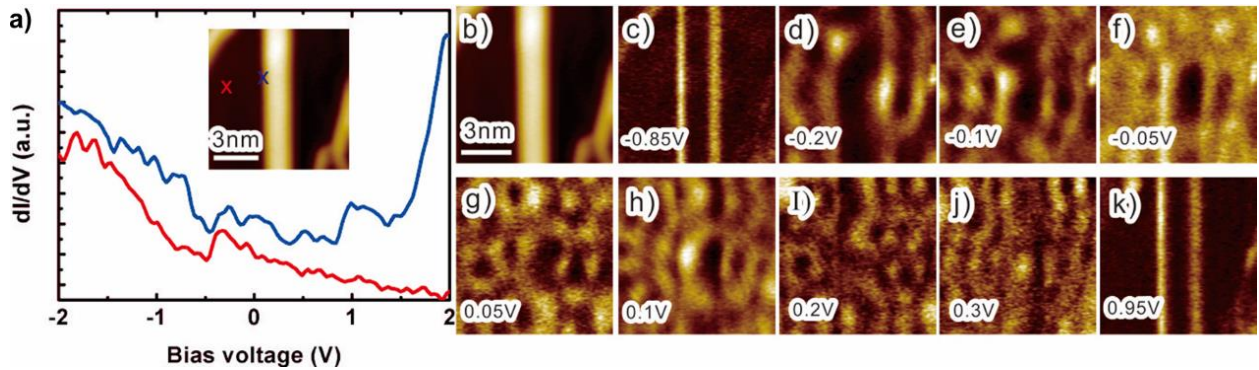


Figure 4. 16 STS measurements of the electronic structure of 12-AGNR on Au (111) substrate. a) dI/dV spectra acquired at a bare Au (111) (red curve) site and on the edge of 12-AGNR (blue curve). b) STM image of original 12-AGNR for mapping. c-k) dI/dV maps of 9-AGNR obtained at the bias voltage of c) -0.85 eV, d) -0.2 eV, e) -0.1 eV, f) -0.05 eV, g) 0.05 eV, h) 0.1 eV, i) 0.2 eV, j) 0.3 eV, k) 0.95 eV, respectively.

interpreted as the position of VB and CB. However, according to the published investigation of 9-AGNR,¹⁸¹ a much weaker VB signal at -0.3 eV can be detected with more detailed STS and angle resolved photoemission spectroscopy (ARPES) measurements, which we had assigned instead to the contribution of a surface state. Therefore, although the states at -1.65 eV in 6-AGNR and at -1.1 eV in 9-AGNR appear more intense than the states of the true VB, we corrected them as the position of VB-1. We re-assigned the VB for 6-AGNR and 9-AGNR to about -0.3 eV.

The spatial distribution of the electronic state can also contribute to the determination of AGNRs' band gaps. The 2D STS maps in [Figure 4.15 b & I](#) are composed of 32 continuous dI/dV curves recorded along the blue line in the inset of [Figure 4.15 a & h](#), revealing the latitudinal features of the electronic structures across the 6-AGNR and 9-AGNR. From the 2D STS maps, the states of VB-1 and CB can be easily discerned, whereas weak features can be observed in the position of VB. In addition, to gain insight into the spatial distribution of electronic structures, we conducted dI/dV mapping at the position of CB and VB-1. From the dI/dV mapping, we can observe the enhanced local density of states near the edge of ribbons, which are typical phenomena in AGNRs adsorbed on Au(111) surfaces.¹⁴³⁻¹⁴⁵ However, this phenomenon has not been well explained so far. Another feature observed in the dI/dV maps is an oscillating contrast at energies between CB and VB (see [Figure 16d-j](#)), which is caused by the quantum interference of the Au(111) surface state.¹²³ As a result of the STS measurements, we can obtain the band gaps of 6-AGNR and 9-AGNR are 1.9 eV and 1.4 eV. Similarly, as shown by the STS measurements of 12-AGNR on Au(111) in [Figure 4.16](#), we can assign -0.2 eV and 0.95 eV as the position of VB and CB, which yields a band gap of

Band Gaps	AGNR on Au(111)	5-AGNR ²⁰⁶	6-AGNR	7-AGNR ¹²⁵	8-AGNR ¹⁴⁴	9-AGNR	10-AGNR ¹⁴⁴	12-AGNR	13-AGNR ¹⁴²
GW Approximation (eV)		1.68	2.75	3.95	1.25	2.09	3.12	1.68	2.58
Experimental Results (eV)		0.20	1.90	2.30	1.00	1.40	2.00	1.15	1.40

Table 4. 1 Table of the band gaps (experimental vs theoretical) in the AGNRs with different widths on Au(111).

1.15 eV.

[Table 4.1](#) reports the experimental band gaps of AGNRs (6, 9 and 12-AGNRs are from our own results, while 5, 7, 8, 10 and 13-AGNRs are from the reports by other groups where the references are shown in the table) with different widths on Au(111). Overall, the band gaps are width-dependent and inversely proportional to the widths in each sub-families (3p, 3p + 1 and 3p + 2, where p is an integer), which is consistent with the theoretical predictions.¹⁷⁴ An exception is 5-AGNR, which was reported to exhibit metallic behavior when the length of the ribbon reaches to a certain value.²⁰⁷ All the experimental values of the band gaps are considerably smaller than the theoretical predictions, which used a first-principles many-electron Green's function approach within the GW approximation.¹⁷⁴ The difference could be calibrated by the image charge corrections which accounts for the screening effects by the metal substrate.²⁰⁸

In general, copper surfaces have stronger interactions (such as charge transfer, rehybridization, etc.) with supported materials than gold surfaces.^{124, 125} Hence, the electronic structures of GNRs measured on Cu(111) surface should have more interference from the substrate and be further away from their intrinsic properties. Accordingly, besides the investigation on pure Cu(111), we proposed to study the electronic structures of 3p-AGNRs on oxidized Cu(111), which exhibits semiconductive properties.

First, we did STS measurements of 6, 9, 12-AGNRs on pure Cu(111). The original STM image is shown in [Figure 4.17a](#) where 3-AGNR and its lateral fusion products (6, 9, 12 -AGNR) can be observed simultaneously on the same sample. The dI/dV curve obtained on the bare Cu(111) (see red curve in [Figure 4.17b](#)) shows a peak at about -0.4 eV, which is consistent with reported Shockley surface state of Cu(111).¹²³ In contrast to the STS measurements on Au(111), no enhanced occupied states can be discerned from the dI/dV curves recorded on 6, 9, 12-AGNRs. This could be because the spectroscopic features overlap with and are suppressed by the strong surface states in Cu(111). As a second contrast with the case of Au(111),

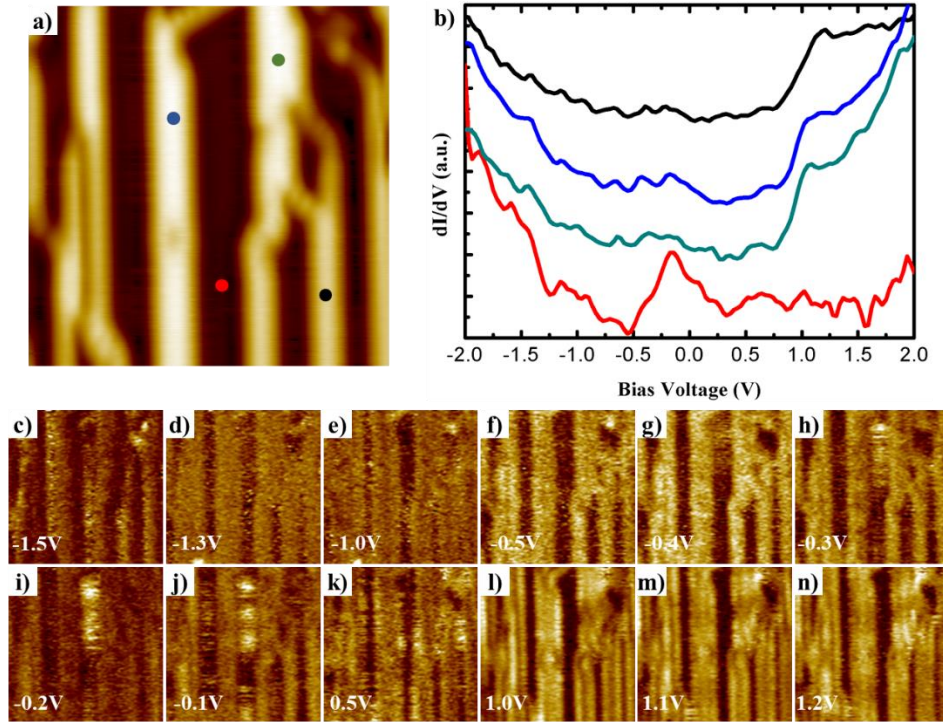


Figure 4. 17 STS measurements of the electronic structure of 6, 9, 12-AGNR on Cu (111) substrate. a) Original STM image of 3, 6, 9, 12-AGNRs on Cu(111). b) dI/dV spectra acquired at a bare Cu (111) (red) site and on top of 6-AGNR (black), 9-AGNR (blue) and 12-AGNR (green). (c-n) dI/dV maps of AGNRs obtained at the bias voltage of c) -1.5 eV, d) -1.3 eV, e) -1.0 eV, f) -0.5 eV, g) -0.4 eV, h) -0.3 eV, i) -0.2 eV, j) -0.1 eV, k) 0.5 eV, l) 1.0 V, m) 1.1 eV, n) 1.2 eV, respectively.

there is no difference in the position of CB between the AGNRs with different widths on Cu(111). The CB of all the 3p-AGNRs on Cu(111) is located at about 1.0 eV. From the series of dI/dV mappings at different energy in [Figure 1.17c-n](#), the occupied state starts to appear at -0.3 eV and empty state at 1.0 eV for all the 3p-AGNRs. It means that the band gaps of 6, 9, 12-AGNRs on Cu(111) are all about 1.3 eV. In future work, by synthesizing aligned ribbons on high-index copper surfaces, the position of the VB could be confirmed using ARPES. In conclusion, the electronic structures between Au(111) and Cu(111) are different and the band gaps of different 3p-AGNRs on Cu(111) are consistent. Both observations could be ascribed by the renormalization of 3p-AGNRs' electronic levels, which is caused by the change of electronic correlation energy when the ribbons are adsorbed on different surfaces.¹⁴⁹

Due to the semiconductive properties of different phases of copper oxides, the oxidization of the top layers of Cu(111) was expected to be capable of decoupling the electronic interactions by the substrates. According to our investigations, the oxidized copper layer can be achieved by oxidizing the Cu(111) surface held at 423 K while dosing O₂ gas in UHV. This step can be conducted after the formation of AGNRs. To

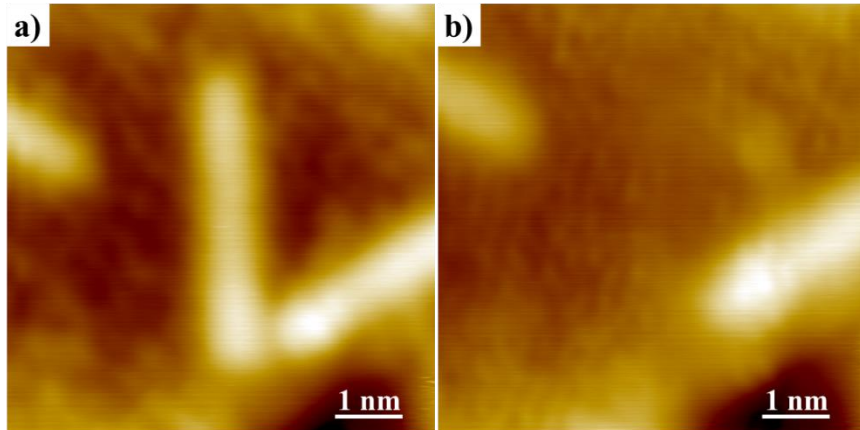


Figure 4. 18 STM images before and after dragging a 6-AGNR on Cu(111) by STM tip manipulation. The surface under the dragged ribbon exhibits the appearance of oxidized Cu(111).

ensure the area under the formed ribbons are oxidized, we always oxidized the whole sample after the formation of AGNRs. It can also be confirmed by removing the AGNRs with STM tip manipulation. One end of a AGNR can be picked up by approaching and retracting the STM tip with a low bias (about -50 mV), then the ribbon can be removed by lateral displacement of the tip. Finally, the ribbon is released away from its original site by a 3.0 V voltage pulse. As shown in [Figure 4.18](#), manipulation to remove the 6-AGNR left a bare area which exhibits the features of oxidized Cu(111). Accordingly, it demonstrates that the AGNRs can be synthesized on pure Cu(111) and remain intact after the introduction of O₂ gas to oxidize the Cu(111). Moreover, the area of Cu(111) under the ribbons is also oxidized, implying that the oxidized copper layers form between the AGNRs and bulk Cu(111).

With the realization of AGNRs on oxidized Cu(111), we conducted STS measurements to study the electronic structures of 3, 6, 9-AGNRs. As shown in [Figure 4.19a](#), multiple 3p-AGNRs with different widths are present on the oxidized Cu(111) surface. The dI/dV curves measured on bare oxidized Cu(111) and 3, 6, 9-AGNRs are shown in [Figure 4.19b](#), respectively. From the surface state exhibited on bare oxidized Cu(111) at the bias of 0.5 eV,²⁰⁹ we confirmed that the tip is in good condition. In the dI/dV curve of 3-AGNR, there is a peak at about 1.2 eV, which is also consistent with reported result on Cu(111). From the comparison of the electronic structure of 3-AGNR on Cu(111) and oxidized Cu(111), there is no difference can be discerned. We further did STS measurements of 6, 9-AGNRs, there is a clear peak at about 1.1 eV for both of these two ribbons, which was assigned as the position of CB. However, the resolution of the dI/dV curve obtained from our machine is insufficient to discern a peak corresponding to

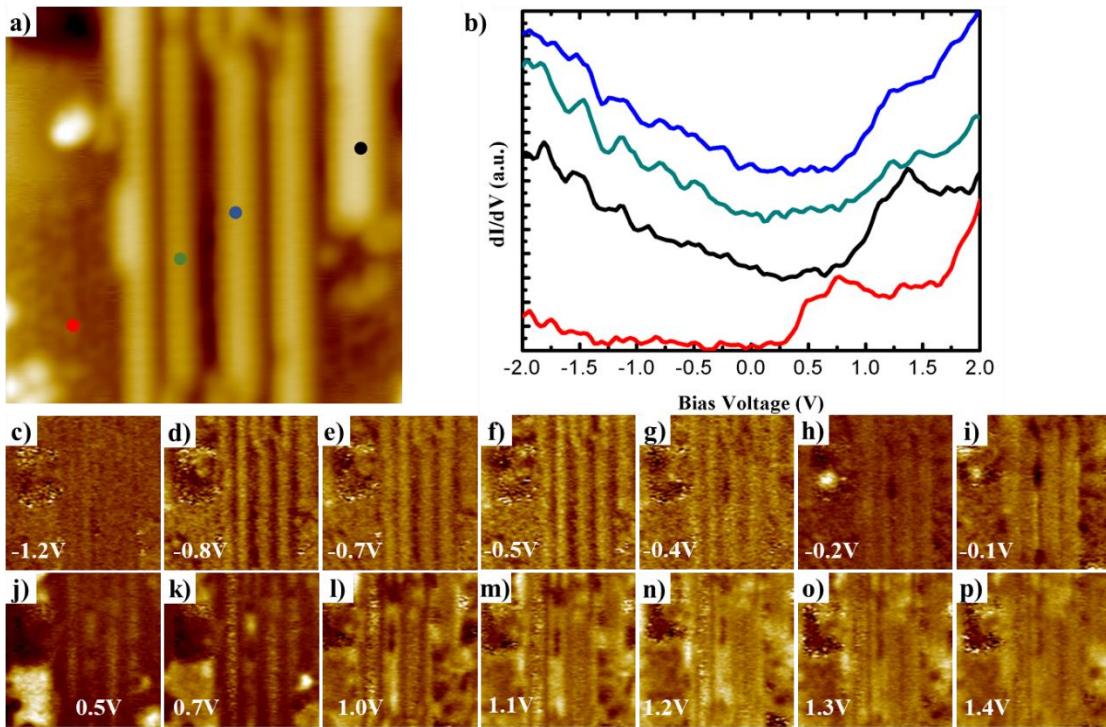


Figure 4. 19 STS measurements of the electronic structure of 3, 6, 9-AGNRs on Au (111) substrate. a) Original STM image of 3, 6, 9-AGNRs on Cu(111). b) dI/dV spectra acquired at oxidized Cu (111) (red) site and on top of 3-AGNR (green), 6-AGNR (blue) and 9-AGNR (black). c-k) dI/dV maps of 9-AGNR obtained at the bias voltage of c) -1.2 eV, d) -0.8 eV, e) -0.7 eV, f) -0.5 eV, g) -0.4 eV, h) -0.2 eV, i) -0.1 eV, j) 0.5 eV, k) 0.7 eV, l) 1.0 eV, m) 1.1 V, n) 1.2 V, o) 1.3 V, p) 1.4 V, respectively. the VB. Compared to the position of CB on pure Cu(111), there is no difference for 6-AGNR and 9-AGNR on oxidized Cu(111), implying that the oxidized layers in our case could not decouple the electronic interference caused by the conductive Cu(111) substrate. Comparing the dI/dV curve of oxidized Cu(111) to a more heavily oxidized Cu(111) surface, the enhanced state lies at lower bias energy.²⁰⁹ This means the band gap of the oxidized layers in our case should be smaller than the more heavily oxidized phases. Accordingly, in the future we will try to synthesize AGNRs directly on fully oxidized Cu(111) surfaces and investigate the decoupling effect of this semiconductive surface.

4.3 Conclusions

In summary, combining STM and XPS measurements, we systematically investigated the synthesis of 3p-AGNRs on Cu(111) and the effects of oxygen during the synthesis. Similar to the case of Au(111), 3p-AGNRs can be formed on Cu(111) by lateral fusion of 3-AGNRs after annealing at 633 K. On Cu(111), the ribbons exhibit increased contrast, which is attributed to the intercalation of Br atoms. Introducing O₂

enables 3p-AGNR formation at a considerably lower temperature of 453 K, which is attributed to the catalysis of C–H activation, without introducing defects or affecting the AGNR length. Our results show that the lateral fusion reaction can be successfully carried out on the more reactive Cu(111) surface. The catalytic effect of O₂ could be beneficial to GNR synthesis and cyclodehydrogenation reactions in general.

In addition, we performed STS measurements of the 3p-AGNRs on pure Cu(111) and oxidized Cu(111) surfaces. On both of these two surfaces, despite their different intrinsic electronic structures, 3p-AGNRs with different widths exhibited similar features in STS measurements. We ascribe this to the strong electronic interference from the copper substrate and the insufficient oxidization of top layers. On pure Cu(111), the energy band gaps of 6,9,12-AGNRs are determined as 1.4 eV, whereas on oxidized Cu(111) no feature can be discerned to determine the position of VB, so the band gaps on oxidized Cu(111) could not be measured. In the future, the STS measurements of AGNRs on more heavily oxidized copper surfaces are called to explore the intrinsic electronic properties.

4.4 Experimental and Theoretical Methods

All experiments were conducted in ultrahigh vacuum (UHV) systems with a base pressure of 2×10^{-10} mbar. The Cu(111) single-crystal (MaTeCK GmbH) was cleaned by repeated cycles of Ar⁺ sputtering and annealing (750 K). The precursor 4,4''-dibromo-p-terphenyl (DBTP, 98%, Sigma-Aldrich) was deposited by organic molecular beam epitaxy using an evaporator temperature of 388 K. The O₂ gas was dosed at 5×10^{-7} mbar through a leak-valve onto Cu(111) held at the desired temperature.

Imaging by scanning tunneling microscopy (STM) was performed at low-temperature (LT), (77 K, Omicron LTSTM) or at room temperature (RT) (Omicron VT-STM), in constant-current mode with a home-made tungsten tip in both cases. All the STM images were calibrated with the known lattice constant of Cu(111). X-ray photoelectron spectroscopy (XPS) measurements were conducted in the same UHV system as the Omicron VT-STM, using an Al K α source X-ray lamp (pass energy 20 eV) and a hemispherical electron analyzer with 5 channeltrons detector. The XPS spectra were fitted using Voigt line shapes and Shirley background. All dI/dV data were collected by using the lock-in technique. The sample bias was modulated by a 727.451 Hz, 20 mV (rms) sinusoidal voltage under open-feedback conditions.

Theoretical calculations were performed with the Vienna Ab-initio Simulation Package (VASP)^{161, 162} using the Perdew-Burke-Ernzerhof¹⁶³ generalized-gradient approximation (PBE-GGA) for the exchange-correlation potential, the projector augmented wave (PAW) method,^{164, 165} and a plane-wave cutoff of 450 eV. The zero-damping DFT-D3 method of Grimme¹⁶⁶ was used for the van der Waals (vdW) correction of the potential energy. The Cu(111) slab was constructed for a (4, 0 | -6, 3) epitaxy matrix using a lattice constant of 0.363 nm and a 1.8 nm vacuum layer, with five atomic layers and the positions of atoms in the bottom two layers fixed. The calculated geometries were optimized using a $4 \times 8 \times 1$ k-point mesh until the force on each atom was below 0.02 eV/Å, and STM simulations were then performed with a $6 \times 12 \times 1$ k-point mesh. Images of the calculated structures were generated using the VMD software,¹⁶⁷ and STM images were simulated via the Tersoff-Hamann approximation¹⁶⁸ using the calculated wave-function of the relaxed structures obtained from VASP and visualized using the Hive software.¹⁶⁹

Chapter 5. Tandem Desulfurization/C-C Coupling Reaction of Tetrathienylbenzenes on Cu(111): Synthesis of Pentacene and an Exotic Ladder Polymer

Penghui Ji, Dominik Dettmann, Ying-Hsuan Liu, Giulia Berti, Navathej Preetha Genesh, Daling Cui, Oliver MacLean, Dmitrii F. Perepichka, Lifeng Chi and Federico Rosei

Authors' contribution: D. F. Perepichka, L. Chi and F. Rosei initiated and supervised the project. P. Ji conducted the experiments and the data processing. P. Ji wrote the initial manuscript. D. Dettmann performed DFT simulation. D. F. Perepichka and Ying-Hsuan Liu provide the precursors. All the authors modified the manuscript.

The synthesis of novel low-dimensional conjugated molecules and polymers has attracted tremendous attention due to their unique properties ranging from ultra-high carrier mobility to carbon magnetism and topological states. Surface-confined reactions represent a powerful approach to synthesize these intriguing materials with atomic precision, yet the toolbox of chemical reactions available for on-surface synthesis, and thus the structural space of resulting materials, remains very limited. New coupling chemistries must be identified and refined to propel this emerging field towards practical applications. In particular, to synthesize a broad range of molecular nanomaterials at-will requires the ability to carry out hierarchical synthesis combining different reactions.

In previous two chapters, we focused on investigations of Ullmann-type coupling, demonstrating its potential to produce OM structures with tunable dimensionalities and synthesize graphene nanoribbons on Cu(111) surface. In this chapter, we will explore desulfurization of thiophene derivatives which is a promising and underexplored route to create unsaturated carbons that can couple to form extended structures. Compared with Ullmann-type coupling, desulfurative coupling offers access to different materials, as it involves the linking of alkenes rather than arenes.

5.1 Introduction

Polycyclic aromatic hydrocarbons (PAHs) and related carbon-based polymers are being widely studied due to their unique electronic properties and their wide applications in modern devices, including solar cells and organic field-effect transistors.^{210, 211} Surface-confined reactions provide a versatile approach to synthesize low-dimensional carbon-based materials by constraining precursors to a surface and exploiting the catalytic effects of metal substrates.^{5, 6, 9, 12, 44, 90, 212-215} In a similar vein, the surface can be used to control the self-assembly of PAHs and other macromolecules.^{8, 216-218}

In 2007, Grill *et al.* reported the synthesis of 2D covalently bonded nanostructures on Au(111) through a bottom-up approach, using dehalogenative coupling of the tetrabrominated porphyrin precursor.³⁷ Since then, a wide range of chemical reactions have been investigated on surfaces using tailored molecular precursors, including polymerization reactions such as Ullmann and Glaser coupling and intramolecular reactions such as cyclodehydrogenation or decarbonylative aromatization.^{17, 19, 20, 38, 43, 54, 57, 219-222} With the rapid development of surface-confined reactions, an impressive array of atomically precise carbon-based nanomaterials have been synthesized, including large PAHs,^{220, 223-225} graphene nanoribbons (GNRs),^{142, 144,} ^{145, 187, 197, 226} and 1D and 2D π -conjugated polymers.^{11, 45, 50} Among these, ladder polymers have emerged as particularly interesting materials due to the appealing electronic properties that arise from their unusual chemical structures.^{227, 228}

The desulfurization of thiophene derivatives is a metal-catalyzed degradation reaction widely used in gas purification.²²⁹ Until now, only a few studies have investigated the fundamentals of this reaction with ultra-high vacuum (UHV) techniques on single-crystal surfaces.²³⁰⁻²³² Early studies from our laboratories demonstrated that the unsaturated carbons created by opening of thiophene rings can couple intramolecularly to form new benzene rings ([Figure 5.1a](#)), a surface reaction with no analogue in solution.^{230, 231} Depending on the molecular structure, these carbons can also undergo intermolecular coupling to form extended oligomers.²³¹ However, the fused tetrathienoanthracene molecules used in these studies require a multistep synthesis in solution and are highly insoluble, which limits their further synthetic modification. We reasoned that tetrathienylbenzene precursors ([Figure 5.1b-c](#)) represent viable alternatives to fused

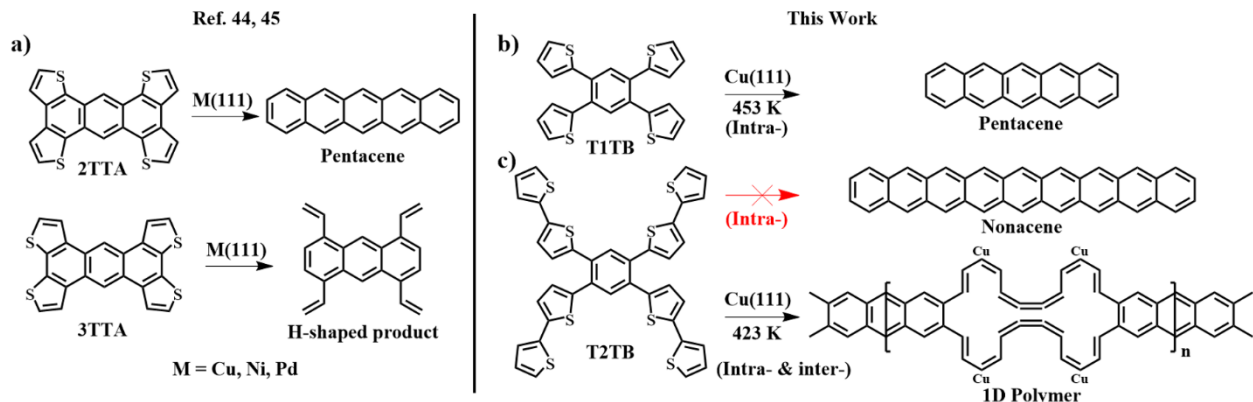


Figure 5. 1 a) Surface-confined reactions of fused tetrathienoanthracene molecules on different metal surfaces, producing pentacene or H-shaped products. b) Surface-confined reaction of T1TB producing pentacene on Cu(111) and c) of T2TB producing a 1D ladder polymer instead of nonacene on Cu(111).

tetrathienoanthracene to form pentacene and potentially longer acenes, with the benefit of simpler synthesis in solution.²³³

Here, we report the desulfurization-induced intra- and intermolecular coupling on Cu(111) of two tetrathienylbenzene precursors with differing numbers of thiophene units. The investigations were conducted using UHV scanning tunneling microscopy (STM), X-ray photoelectron spectroscopy (XPS) and density functional theory (DFT) calculations. As shown in [Figure 5.1](#), pentacene is formed through the desulfurization and intramolecular cyclization of 1,2,4,5-tetra(thien-2-yl)benzene (T1TB) on Cu(111). However, nonacene does not form by repeated intramolecular cyclization from 1,2,4,5-tetrakis(2,2'-bithien-5-yl)benzene (T2TB) on Cu(111). Instead, ordered one-dimensional (1D) ladder polymers composed of alternating anthracene and fused annulene moieties are obtained through a combination of intra- and intermolecular C-C coupling. The unexpected 1D polymer stands out for its exotic ladder structure, which was not previously observed in either solution or surface-confined polymerization. This polymer exhibits desirable electronic properties, including a narrow band gap of 1.38 eV and a low effective mass of charge carriers ($0.18 m_e$ for the holes and $0.14 m_e$ for electrons) similar to that of many GNRs,^{121, 174} suggesting potential applicability in semiconductor devices.

5.2 Results and Discussions

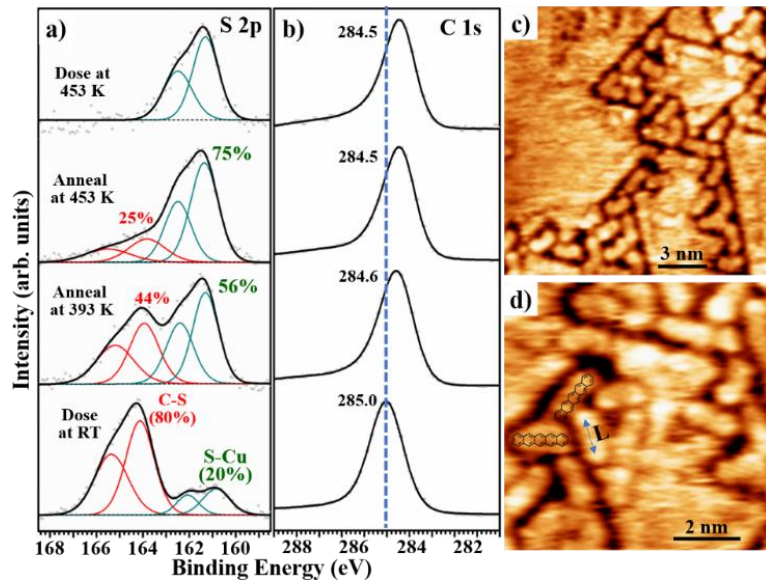


Figure 5.2 a) S 2p and b) C 1s XPS spectra obtained when T1TB was deposited on Cu(111) surface held at 453 K or at RT followed by a sequence of annealing. c-d) STM images of depositing T1TB on Cu(111) held at 453 K. ($V_t = -1$ V, $I_t = 1$ nA). The peak-to-peak length of the rod-like structures (labeled by “L” in d)) is 1.04 ± 0.06 nm.

5.2.1 Synthesis of pentacene on Cu(111) with T1TB

We began our investigation by depositing T1TB on Cu(111) at room temperature (RT) and annealing at 453 K for 15 minutes to induce the reaction. After deposition, the S 2p XPS spectrum (Figure 5.2a) shows two doublets at 164.1 and 161.3 eV, which can be attributed to C-S bonds in T1TB and Cu-S bonds formed by thiophene ring-opening, respectively. The small extent (20%) of C-S bond breaking at RT, already observed in the previous work,¹⁵⁴ might be due to the impact of T1TB on highly reactive step edges or adatoms. No features can be discerned by STM at RT (Figure 5.3a), likely due to the high diffusivity of

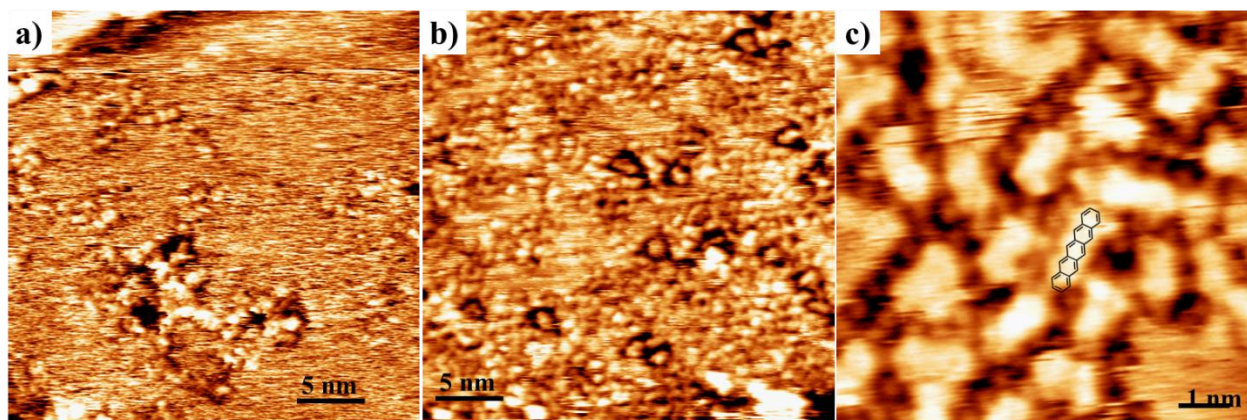


Figure 5.3 STM images after a) Deposition of T1TB on Cu(111) at RT. ($V_b = -1$ V, $I_t = 1$ nA) b) Annealing the sample at 453 K, leading to the formation of isolated, disordered monomers. ($V_b = -1$ V, $I_t = 1$ nA) c) STM image of the formation of pentacene from T1TB on Cu(111), which are co-assembled with dissociated sulfur atoms. ($V_b = -1$ V, $I_t = 1$ nA)

T1TB on Cu(111), which was previously observed for analogous TTA molecules on Cu(111).²³¹ Sequential annealing up to 453 K induces desulfurization of most thiophene groups in T1TB, as indicated by the increase in the S-Cu component at 161.3 eV. Correspondingly, the C 1s peak ([Figure 5.2b](#)) shifts downward by 0.5 eV. However, STM imaging shows only disordered structures and no features that could be identified as pentacene ([Figure 5.3b](#)).

To promote intramolecular over intermolecular coupling, T1TB was deposited on the Cu(111) surface at 453 K. S 2p XPS measurements show only surface-bonded sulfur atoms, indicating complete opening and desulfurization of the thiophene rings. The STM images in [Figure 5.2c-d](#) show rod-like structures whose appearance and length ([Figure 5.2d](#)) are consistent with previous observations on pentacene on Cu(111).²³⁴ In addition, the same rod-like features of 1.04 ± 0.06 nm length were previously observed from 2TTA and identified as pentacene.²³¹ The co-adsorbed dissociated sulfur atoms can also be resolved in some cases ([Figure 5.3c](#)).

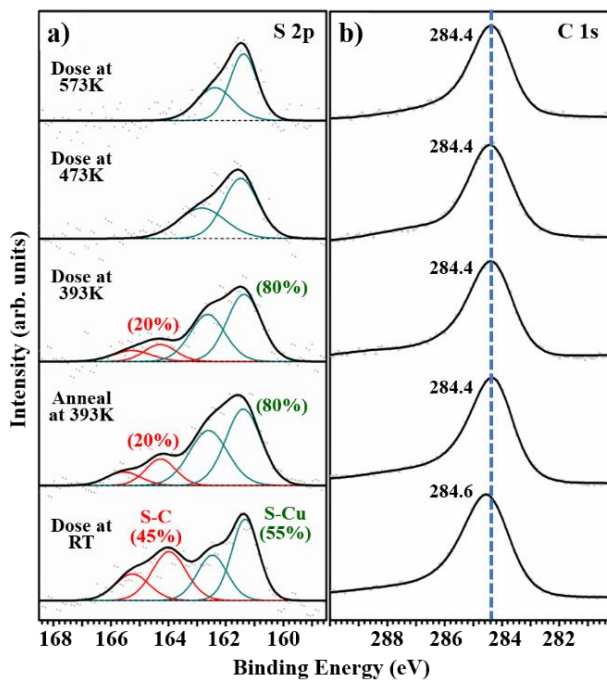


Figure 5. 4 a) S 2p and b) C 1s XPS spectra obtained when T2TB was deposited on Cu(111) surface held at 393, 473 and 573 K, or at RT followed by annealing at 393 K.

5.2.2 Synthesis of ladder polymer on Cu(111) with T2TB

To see if higher acenes could be formed through a cascade of multiple desulfurization and intramolecular cyclization steps, we synthesized an extended precursor (T2TB) with four bithiophene arms. Depositing T2TB on Cu(111) at RT results in a partial thiophene ring opening. The S 2p XPS spectrum in [Figure 5.4a](#) shows two broad S 2p peaks at 164.1 eV and 161.3 eV, indicating desulfurization of ~55% of the thiophene rings. As was the case for T1TB, no ordered features or intact T2TB molecules could be observed by STM ([Figure 5.5a](#)). Annealing the sample at 393 K increases the extent of desulfurization to about 80% and induces further conversion of C-S to C-C bonds, and at the same time the C 1s peak shifts from 284.6 to 284.4 eV ([Figure 5.4b](#)). The STM image in [Figure 5.5b](#) shows randomly-coupled, disordered structures, but no ordered products.

As in the case of T1TB, T2TB was deposited on the Cu(111) surface at elevated temperatures to promote intramolecular reaction. From the XPS measurements shown in [Figure 5.4a-b](#), deposition of T2TB on Cu(111) at 393 K leads to a similar extent of desulfurization (80%) and C 1s peak position (284.4 eV) as annealing to 393 K after RT deposition. Desulfurization is near-complete when T2TB is deposited on Cu(111) at 473 K, while complete C-S bond breaking can be achieved by depositing T2TB on Cu(111) held at 573 K. For both 473 K and 573 K, the C 1s peak is still at the same BE of 284.4 eV.

Although XPS measurements exhibit no significant difference between hot-substrate deposition at 393 K and RT deposition followed by subsequent annealing at 393 K, a clear difference is observed in STM images. Deposition of T2TB at 393 K leads to ordered 1D structures composed of alternating straight

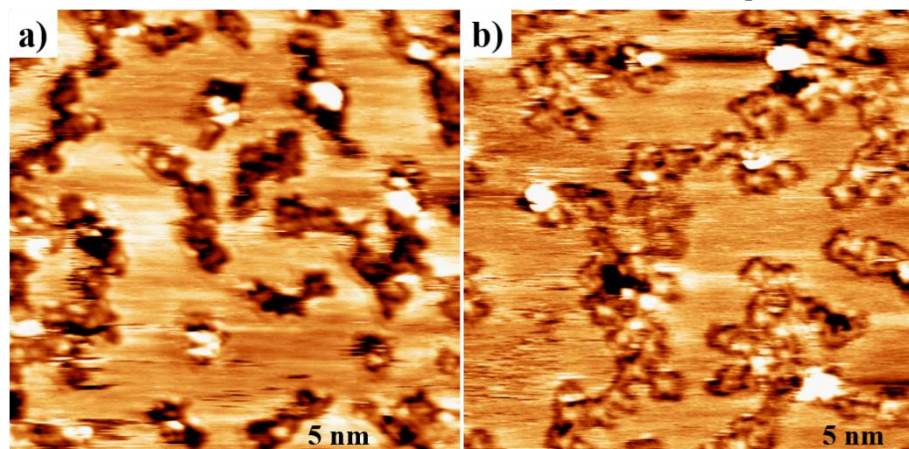


Figure 5. 5 STM images after a) Deposition of T2TB on Cu(111) at RT. ($V_b = -1$ V, $I_t = 1$ nA) b) Annealing the sample at 393 K, leading to the formation of randomly coupled structures. ($V_b = -1$ V, $I_t = 1$ nA)

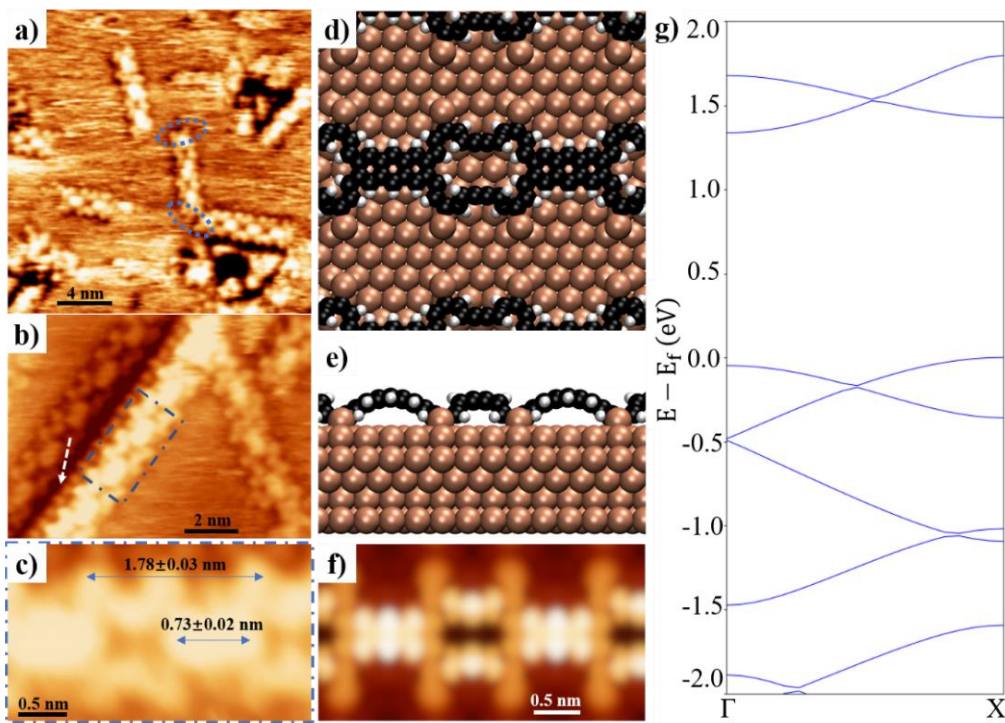


Figure 5.6 a-c) Overview and magnified STM images after depositing T2TB on Cu(111) held at 393 K. Blue ellipses in (a) indicate the uncoupled carbon at the end of the chains which could be saturated by the atoms in the surface. For all STM images: $V_t = -1$ V, $I_t = 1$ nA d-e) Top and side view of DFT optimized model. (brown: copper, black: carbon, white: hydrogen) f) Corresponding DFT-simulated STM image. g) Calculated electronic band structure for the freestanding 1D polymer where the Cu adatoms are replaced with H atoms.

segments connected by curved chains ([Figure 5.6a-c](#)), in striking contrast to the disordered structures obtained by annealing to 393 K ([Figure 5.5b](#)). These structures are aligned with the high-symmetry directions of the substrate. The length of their unit cell (marked by the long arrow in Figure 3c) is 1.78 ± 0.05 nm, which is commensurate with 7 Cu atoms (1.78 nm) in the close-packed $\langle 110 \rangle$ directions of Cu(111). Regular small, round features can be observed next to the 1D structures along the step edge (marked by a white arrow in [Figure 5.6b](#)), which we attribute to dissociated sulfur atoms, consistent with a previous study on S atom adsorption on Cu(111).²³⁵ As shown in the series of STM images of [Figure 5.7](#), this 1D structure can form at a broad range of substrate temperatures from 343 to 493 K, but at 573 K only disordered structures are obtained. Extended chains up to 30 nm (16 repeating units) were observed along the step edge of Cu(111), suggesting a potential aligning effect of step edges on the polymerization process ([Figure 5.7c](#)).²³⁶

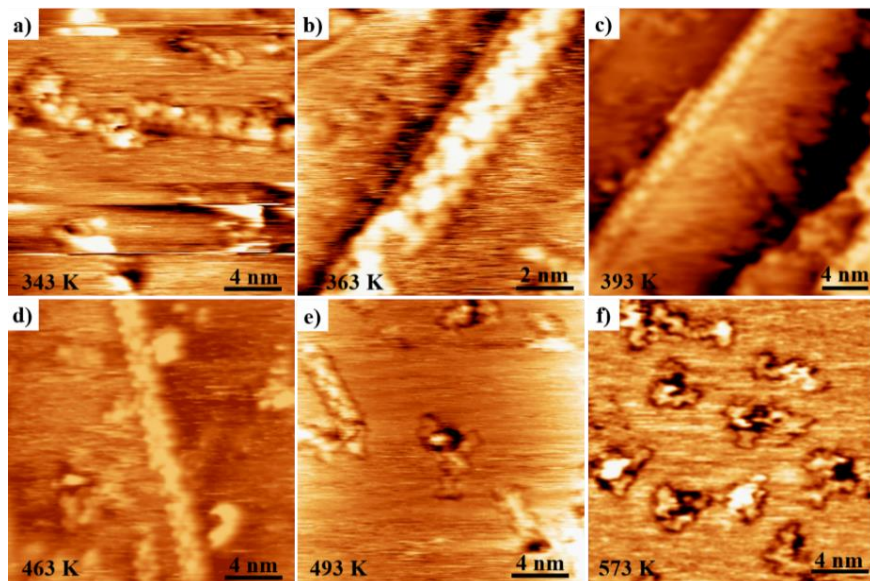


Figure 5. A series of STM images after depositing T2TB on Cu(111) at a) 343 K, b) 363 K, c) 393 K, d) 463 K, e) 493 K, f) 573 K. 1D polymers can be synthesized at all these temperatures except for 633 K. In addition, the polymer can extend up to 30 nm (16 repeating units) along the step edge (see Figure c). (For all the images: $V_b = -1$ V, $I_t = 1$ nA)

To elucidate the chemical structure of these 1D chains, we measured the length of the straight segments (marked by the short arrow in [Figure 5.6c](#)) to be 0.73 ± 0.06 nm, which coincides with the dimension of the expected intermediate anthracene moieties (0.72 nm). The ring opening and desulfurization of thiophene rings adjacent to the benzene core of T2TB should trigger intramolecular C-C cyclization, resulting in the fusion of two new benzene rings to the central moiety, as observed for T1TB (as well as for 2TTA molecules^{230, 231}). However, contrary to our original expectation, no further intramolecular cyclization due to desulfurization of the terminal thiophene rings take place. Instead, the four remaining hexatriene chains undergo intermolecular coupling to ‘stitch’ the anthracene moieties in a ladder polymer chain, via giant (28 carbon atom) macrocycles.

We conducted DFT calculations to determine the adsorption geometry of this ladder polymer. [Figure 5.6d-e](#) shows the structure that gives the best agreement with experiment, which is symmetric and aligned with the high-symmetry directions of the Cu(111) surface. The proposed polymer is composed of alternating fused anthracenes and [28]-annulene rings, in which four carbon atoms are bonded to outer Cu adatoms. The corresponding STM simulation ([Figure 5.6f](#)) agrees well with the main features of the STM images, in particular the bright anthracene segment and the pattern of the curved connecting chains. The polymer structure is consistent with two resonance forms, in which the connecting moiety is a cumulene or diyne.

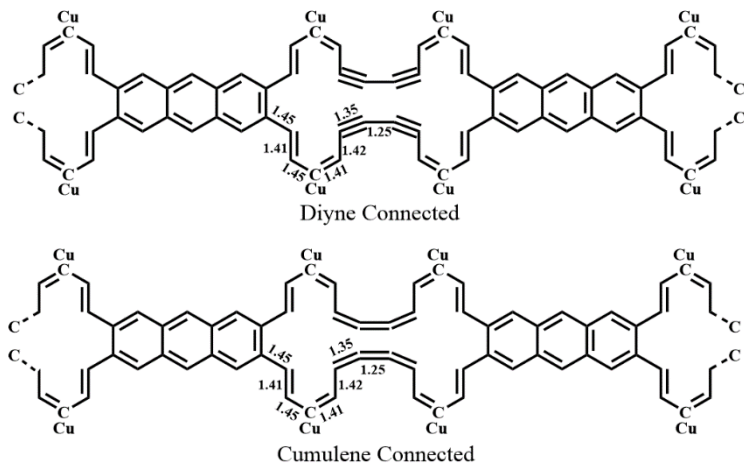


Figure 5.8 Two possible resonant structures for the 1D ladder polymer: the upper one is connected by a diyne moiety while the lower one is connected by a cumulene. The labels indicate bond distances, which agree more closely with the bonding pattern in the cumulene structure.

The bond length alternation in the calculated structure indicates that the cumulene resonance form is dominant (see [Figure 5.8](#)). We also considered the structure that has the non-hydrogenated carbon atoms bonded directly to surface Cu atoms rather than adatoms ([Figure 5.9](#)). Although this structure has the same symmetry and dimensions, the STM simulation does not reproduce the experimental appearance of the connecting chains. Several other structures were considered, as shown in [Figure 5.10](#).

Comparison of the polymer unit cell length derived from experiment (1.78 nm) with the calculated optimal length of 1.97 nm for the free-standing polymer indicates that the polymer adsorbed on the surface is compressed. This strain causes the anthracene backbones to curve upwards, as shown by the side view in

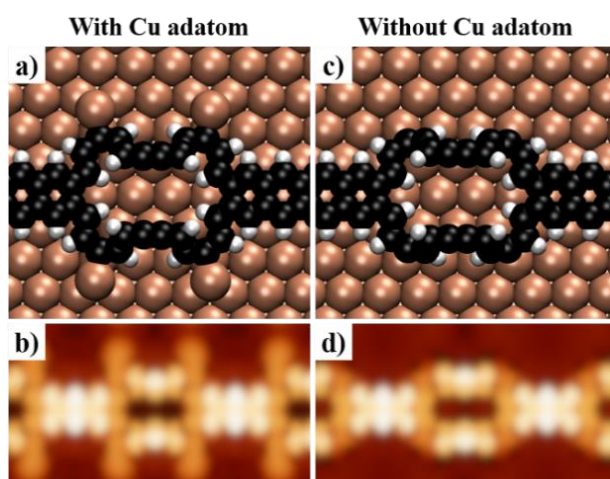


Figure 5.9 a-b) Top-view of the density functional theory (DFT) optimized model and STM simulation for the Cu adatom stabilized structure. c-d) Top-view of the DFT-optimized model and STM simulation for the structure without Cu adatoms.

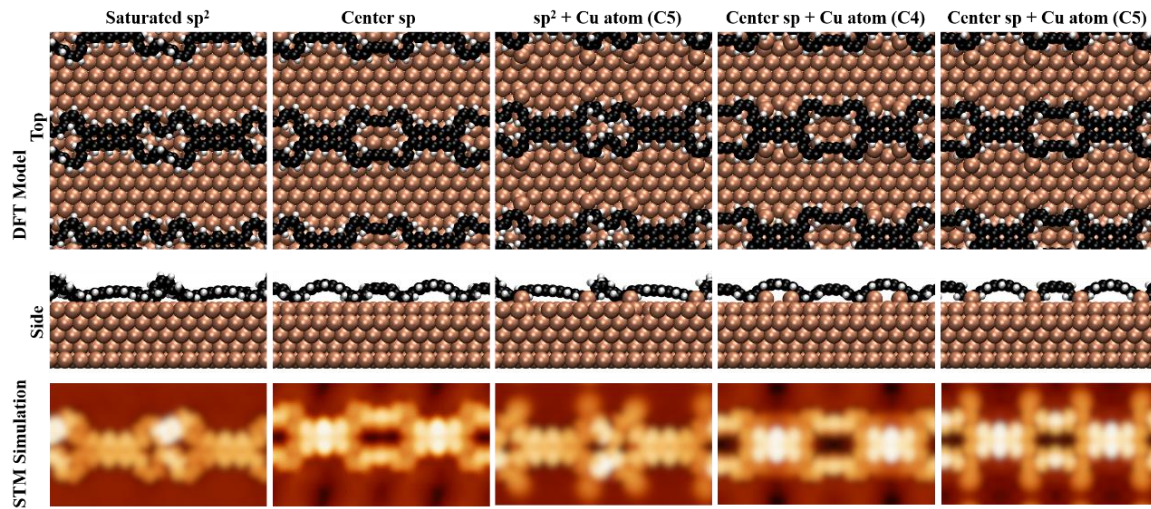


Figure 5.10 Top- and side-views of DFT optimized structures considered for the 1D polymer (consisting of fused anthracene and annulenes) and the corresponding STM simulations. The first column shows a structure with all the C atoms in the annulene saturated with H and sp^2 hybridization. In the second, the center C atoms in the polygon are sp hybridized. The third column structure has sp^2 C atoms with C5 saturated by a Cu adatom. The fourth column has center sp C atoms with Cu adatom saturation at C4. The last column is the proposed structure with sp central C atoms and a Cu adatom at C5. (The C4 and C5 sites are marked in Scheme 2 of the main text.)

Figure 5.6e. We hypothesize that this compression enables the polymer to optimize its registry with the surface, placing the Cu adatoms in preferred hollow sites and enabling an interaction between the C3=C4

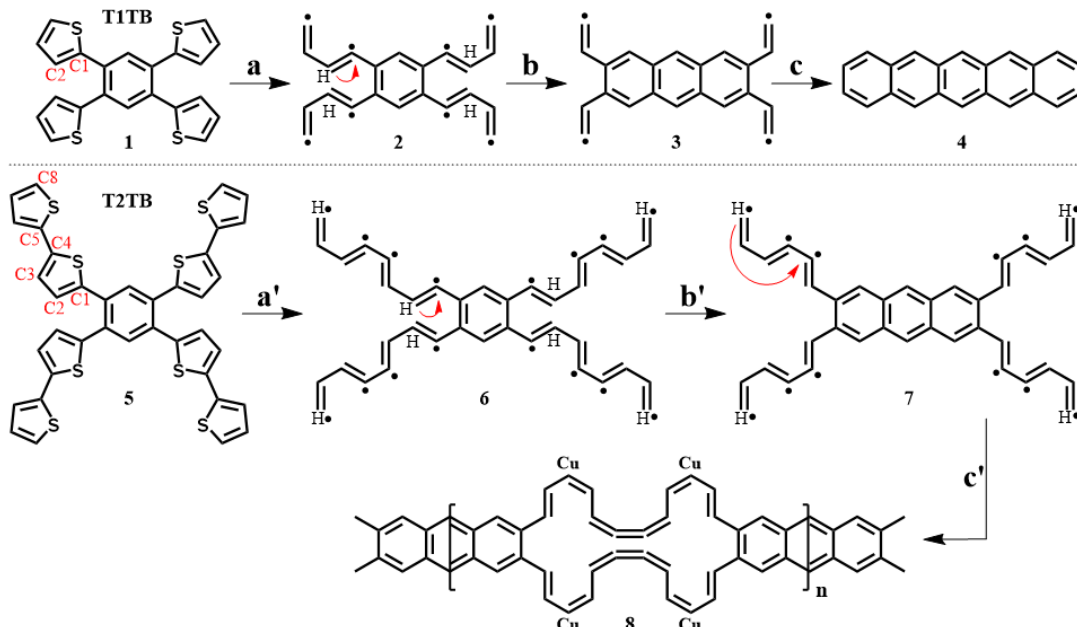


Figure 5.11 Proposed skeletal models of the reaction pathways for the transformation from T1TB to pentacene and T2TB to 1D extended polymer. (a, a': desulfurization; b, b': hydrogen transfer (C2 to C1) and intramolecular cyclization; c: further intramolecular cyclization; c': further hydrogen transfer (C8 to C4) and intermolecular cyclization). The red arrows show hydrogen transfer. ‘•’ Indicate unpaired electrons (stabilized by bonding to Cu), formed after desulfurization. Only hydrogens undergoing the shift during the reaction are shown.

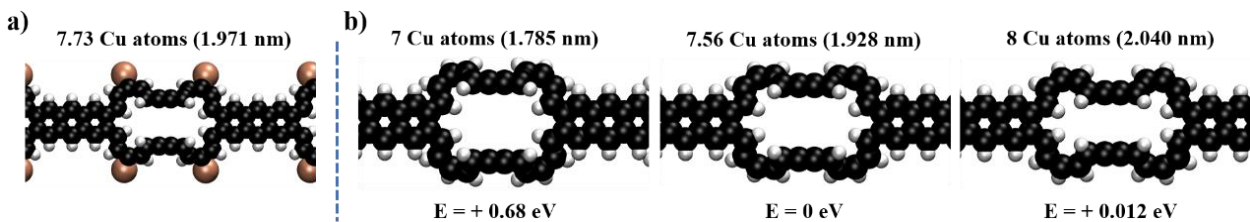


Figure 5. 12 a) DFT calculated structure for the flat free-standing polymer. b) DFT calculated structures and energies of H-saturated polymers in gas phase, which commensurate with 7, 7.56 and 8 Cu atoms in the close-packed direction of Cu(111). The polymer in b) is the most stable one in gas phase, and its energy is set as the reference. The H-saturated polymer was taken as representative of the uncompressed freestanding polymer as the organometallic Cu atoms would have a different chemical state in vacuum than an adsorbed adatom.

double bond (labeled in [Figure 5.11](#)) and a Cu surface atom. This interaction is evidenced by the increase in C-C bond length of 0.04 Å and a lifting of the surface Cu atom by 0.08 Å compared to the separated polymer and surface. These effects could counteract the moderate strain energy induced by compression, computed to be 0.68 eV([Figure 5.12b](#)). We also note that the repeat unit of this polymer has the same number of hydrogen atoms as the initial monomer, but these are bonded to different C atoms, suggestive of hydrogen transfer reactions. Intramolecular hydrogen transfer reactions are common in organic chemistry²³⁷ and also have been reported for a related transformation on surface, heptacene formation on Ag(001).²³⁸

We explored the electronic properties and degree of conjugation of this new 1D ladder polymer using DFT (HS E06 functional) for the relaxed, freestanding polymer (shown in [Figure 5.12](#)) in which the Cu adatoms were replaced with hydrogen. The band structure ([Figure 5.6g](#)) reveals dispersive bands along the carbon backbone and a direct band gap of 1.38 eV. The significant band dispersions, especially for the conduction band (at 1.38 eV), indicate efficient π -conjugation across this 1D ladder polymer. Correspondingly, the effective masses of the frontier bands ($0.18 m_e$ for holes and $0.14 m_e$ for electrons) are low and in the range measured for many GNRs (cf., 0.40, 0.10 and $0.14 m_e$ for 7-, 9-armchair GNR and 12-zigzag GNR respectively).^{121, 174, 181} The combination of a device-suitable band gap and low effective masses is promising for optoelectronic and semiconductor device application.^{239, 240}

To address the origin of divergent reaction pathways between T1TB and T2TB on Cu(111), we propose the step-by-step reaction scheme ([Figure 5.11](#)). The core difference in behavior of these two analogous precursors is the competition between the intramolecular and intermolecular C-C coupling after desulfurization. Desulfurization of T1TB results in four butadiene chains, each with two dangling bonds,

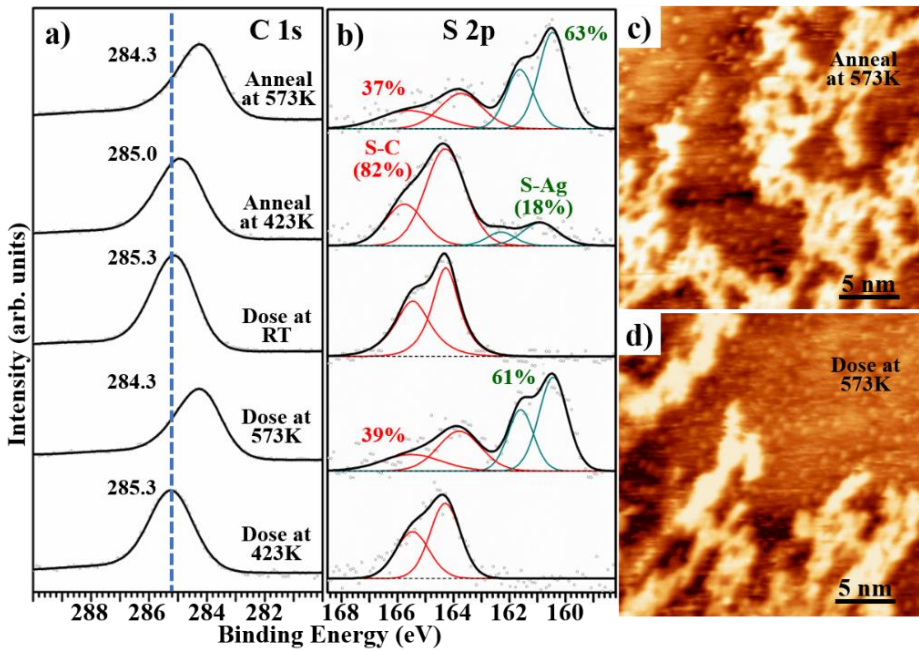


Figure 5.13 a) C 1s and b) S 2p XPS spectra obtained after T2TB was deposited on Ag(111) surface at 423 K and 573 K, or on Ag(111) at RT followed by a sequential annealing. c) STM image after annealing Ag(111) pre-decorated with T2TB at 573 K. ($V_t = -1$ V, $I_t = 1$ nA) d) STM image after depositing T2TB on Ag(111) at 573 K. ($V_t = -1$ V, $I_t = 1$ nA)

attached to the core benzene ring (step a). In the next step b, the hydrogen transfers from C2 to C1 (1,2-shift), which enables an intramolecular cyclization through C2 forming an anthracene ring. The remaining four vinylene radicals in intermediate 3 can flip and couple to each other to form two more benzene rings, resulting in a pentacene moiety, as shown by step c. In the case of T2TB, steps a' and b' are same as a and b, resulting in the formation of the anthracene ring. However, the longer hexatriene chains on the anthracene intermediate 7 are more strongly bound to the surface, which restricts the further cascade of cyclization that could otherwise produce nonacene. These chains of adjacent molecules, however, could undergo intermolecular coupling to form an exotic 1D ladder polymer, as shown in step c'.

To adjust the competition between intramolecular and intermolecular coupling and see if different structures can be formed, we further studied the behavior of T2TB on less reactive substrates, namely Ag(111) and Au(111), with the same procedure as on Cu(111). XPS measurements show the T2TB molecules remain intact when deposited on Ag(111) held at 423 K, while the pristine molecules are still not imaged by STM. As seen in the STM image and XPS spectra (Figure 13), the deposition of T2TB on Ag(111) at 573 K can break 61% of the C-S bonds, driving the formation of disordered structures that follow the features as the sample with post-annealing at the same temperature. Therefore, although the opening of

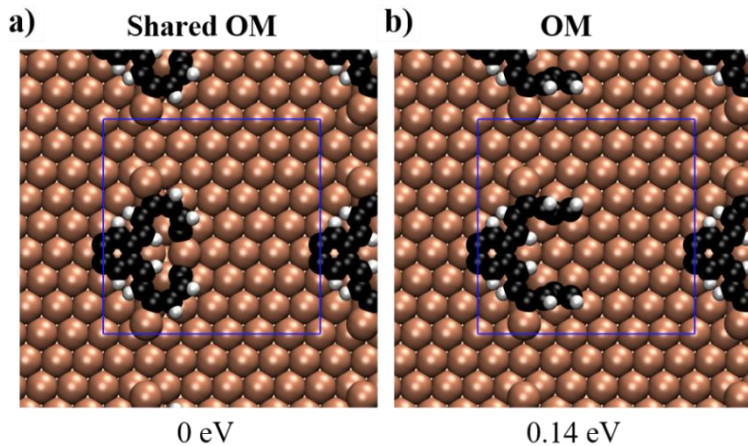


Figure 5. 14 DFT calculations for possible structures of the unreacted chain terminus on Cu(111). To model the chain end, the other chain and a portion of the anthracene were removed and the benzene coordinates frozen. a) The more-stable closed structure with the terminal C atoms sharing a Cu adatom. b) Two terminal alkene chains adsorbed separately. The geometry in (a) could be adopted by the reaction intermediate after cyclization to anthracene, forming a symmetric monomer.

thiophene rings and the breaking of C-S bonds can be achieved, no ordered structures are obtained when depositing T2TB on Ag(111). Hence, we attribute the observation of an ordered 1D ladder polymer on Cu(111) to a favorable molecule-substrate registry that is particular to the Cu(111) lattice. Calculations of the terminus of the 1D polymer on Cu(111) identified a symmetric structure ([Figure 5.14](#)) with the alkene chains forming a closed ring connected by a Cu adatom, which could be adopted by reaction intermediates.

When T2TB was deposited onto Au(111) at RT or higher temperature, we did not observe any obvious change in the XPS spectra for C 1s and S 2p (see [Figure 5.15](#)). The precursors remain intact at 623 K,

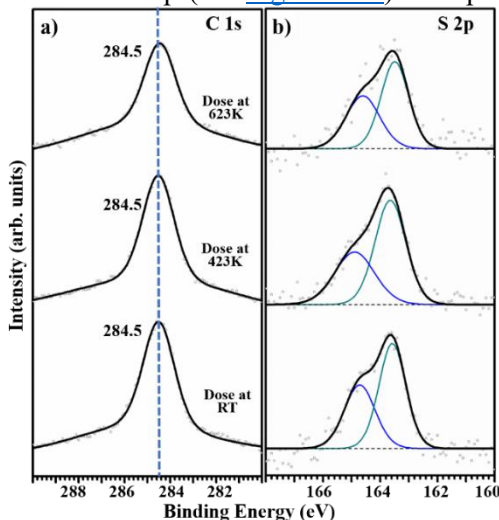


Figure 5. 15 a) C 1s and b) S 2p XPS spectra obtained when T2TB was deposited on Au(111) surface held at RT or higher temperature.

implying no C-S bonds are broken and no polymer forms. We did not try higher temperatures because the backbone of the precursor may already be broken.

5.3 Conclusions

We investigated the surface-confined reactions of two tetrathienylbenzene homologues (T1TB and T2TB) on coinage metal surfaces using STM, XPS and DFT calculations. Thiophene ring opening occurs when T1TB is deposited on Cu(111) at 453 K, driving the transformation into pentacene through intramolecular cyclization. Compared to the previous studies with tetrathienoanthracene, the use of T1TB significantly simplifies the precursor synthesis (one step from commercial reagents, see SI) and yields pentacene with the correct C/H ratio, despite the greater number of degrees of freedom in the reaction.

However, when T2TB is deposited on hot Cu(111) (343–493 K) the desulfurization is followed by a tandem of C–C coupling reactions: an intramolecular cyclization forming an anthracene ring and intermolecular coupling of the remaining carbon chains. This leads to the formation of 1D extended polymers whose chemical and electronic structures were identified through a combination of STM imaging and DFT calculations. That is to say, the reaction pathway can be steered by addition of one thiophene group in the precursor without changing the core structure and symmetry. The transformation from T2TB to 1D polymer was not observed on Ag(111) and Au(111), indicating the crucial nature of the substrate for this reaction. Our investigation provides new insights into the pathways of on-surface ring-opening coupling reactions, a promising but underexplored tool of synthetic on-surface chemistry. Furthermore, desulfurization of thiophene could be combined with other reactions to significantly broaden the carbon nanomaterials possible through on-surface synthesis. Future work is called for to identify the competing forces that drive the reaction towards intra- or intermolecular coupling and the role of the surface.

5.4 Experimental and Theoretical Methods

All experiments were conducted in a UHV system with a base pressure of 2×10^{-10} mbar. The Cu(111), Ag(111) and Au(111) single crystals (MaTecK GmbH) were cleaned by repeated cycles of Ar⁺ sputtering and annealing (~750 K) for 30 minutes. The precursor T1TB was deposited by organic molecular beam

epitaxy at 393 K (evaporator) on Cu(111) held at RT or 453 K, and T2TB was deposited at 483 K (evaporator) on the surface held at various temperatures, including RT, 373, 423, 453, 573 and 623 K. The details on the synthesis of T1TB and T2TB are presented in the Supporting Information.

Imaging by STM was performed at RT (Omicron VT-STM), in constant-current mode with a home-made electrochemically etched tungsten tip. All the STM images were treated with plane subtraction, line-by-line flattening and contrast adjustment by using the software WSxM,¹⁶⁰ and calibrated with the known lattice constant ($a = 2.55 \text{ \AA}$) of Cu(111) in the close-packed directions. XPS measurements were conducted in the same UHV system, using a non-monochromatized Al K α source (pass energy 20 eV) and a hemispherical electron analyzer with a 5 channeltron detector. The XPS spectra were fitted using Voigt line shapes and linear or Shirley backgrounds.

Theoretical calculations were performed using the Vienna *Ab initio* Simulation Package (VASP)^{161, 162} using the Perdew-Burke-Ernzerhof¹⁶³ generalized-gradient approximation (PBE-GGA) for the exchange-correlation potential, the projector augmented wave (PAW) method,^{164, 165} and a plane-wave cutoff of 450 eV. The zero-damping DFT-D3 method of Grimme¹⁶⁶ was used for the van der Waals (vdW) correction of the potential energy. The Cu(111) slab was constructed using a lattice constant of 0.363 nm and a 1.8 nm vacuum layer, with five atomic layers and the positions of atoms in the bottom two layers fixed. The calculated geometries were optimized using a $1 \times 1 \times 1$ k-point mesh until the force on each atom was below 0.02 eV/ \AA . STM simulations were then performed with a $1 \times 1 \times 1$ k-point mesh. Images of the calculated structures were generated using the VMD software,¹⁶⁷ and STM images were simulated via the Tersoff-Hamann approximation¹⁶⁸ using the calculated wave-function of the relaxed structures obtained from VASP and visualized using the Hive software.¹⁶⁹ The band structure of the free-standing polymer was computed using the HSE06 functional using a $3 \times 3 \times 1$ k-mesh with 20 points along Γ -X.²⁴¹

Chapter 6. Conclusions and Future Plans

6.1 Conclusions

In this thesis, my projects focused on the investigation of surface science, in particular surface-confined reactions. We explored new strategies to steer the reaction to produce new desirable structures. On top of this, the desulfurization reaction of thiophene-based molecules was studied, which is a promising and underexplored route to create unsaturated carbons that can couple to form extended structures.

First, we systematically investigated the effects of dosing oxygen on surface-confined Ullmann-type coupling by introducing chemisorbed oxygen atoms before or after the deposition of two halogenated precursors (DBTP and dBB) on two copper surfaces with different symmetries, Cu(111) and Cu(100). As a result, we achieved the structural transformation from 1D OM chains to 2D OM networks linked by Cu-O clusters. Furthermore, the size and symmetry of this newly formed 2D OM networks can be rationally controlled by adjusting the length of halogenated precursors and the substrate symmetry. On top of facilitating the fundamental understanding of the surface-confined Ullmann-type coupling, this work provides a new method to steer surface-confined reactions and therefore to synthesize low-dimensional nanostructures with tunable chemical and electronic structures.

On the basis of the investigation of surface-confined Ullmann-type coupling with precursor DBTP, we further investigated the synthesis of armchair-edged GNRs on Cu(111) and the effects of co-adsorbed oxygen on this synthesis. In the absence of oxygen, annealing OM chains first drives the formation of 3-AGNR. Furthermore, we demonstrated that higher annealing can induce the lateral fusion of 3-AGNR, leading to the formation of wider 3p-AGNRs. In the meantime, we observed the intercalation of dissociated Br atoms between ribbons and the substrate, which was ascribed to the diffusion of 3-AGNR over the rows of Br atoms prior to the fusion. When the oxygen was introduced after the formation of 3-AGNR, the wider 3p-AGNRs can be formed through annealing at 453 K, which is 180 K lower than that in the absence of oxygen. This implies the catalytic effect of oxygen in the activation of C-H bonds during the lateral cyclodehydrogenation. We expect this work will contribute to the on-surface synthesis of more nanomaterials that involves the dehydrogenation reaction in general.

Apart from Ullmann-type coupling, we studied the desulfurization reaction of thiophene derivatives to

explore its potentials in synthesizing conjugated polymers. By using UHV-STM and XPS, supported by DFT calculations, we demonstrated the formation of pentacene through the intramolecular cyclization of T1TB on Cu(111). However, nonacene does not form by repeated intramolecular cyclization from T2TB on Cu(111). Instead, ordered one-dimensional ladder polymers composed of alternating anthracene and fused annulene moieties are produced through a combination of intra- and intermolecular C-C coupling. This unexpected 1D polymer stands out for its favorable electronic properties and its exotic ladder structure that was not previously observed in either solution or surface-confined polymerization. Our investigation provides valuable insights into the pathways of on-surface ring-opening coupling reactions, a promising and underexplored synthetic approach. Future work is called for to understand the interplay between the molecule-molecule coupling and the role of the surface to achieve the desired rational design of low-dimensional carbon nanostructures with intriguing electronic properties.

In the future work, we would extend what we have already achieved to explore more strategies to realize smarter control over the surface-confined reactions. In addition, more thiophene-based molecules will be designed to produce more conjugated polymers through the desulfurization/C-C coupling reaction. The details will be presented in the following section.

6.2 Steering the formation of 2DCPs with 2DOM network templating

On the one hand, we have demonstrated the oxygen-induced 1D to 2D transformation of OM structures. The pore size and symmetry of the formed 2DOM networks can be finely adjusted by using halogenated precursor with different length and substrates with different symmetry. On the other hand, some reductive gases have been reported to be capable of removing the unwanted by-products on surfaces. For example,

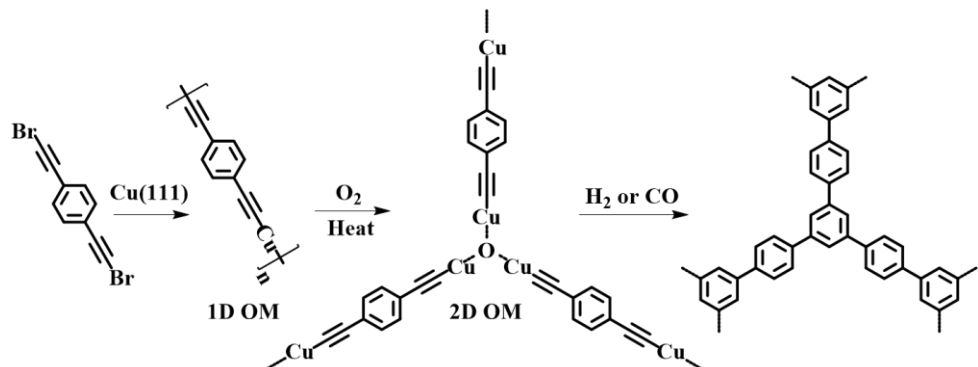


Figure 6. 1 Proposed scheme of the formation of 2DCPs from a precursor functionalized with halogenated acetylene groups.

CO can bind O to release from Cu(111) surface as CO₂ in the reduction of Cu₂O surface oxide,¹¹⁸ and H₂ can remove Br atoms on surface in the phase of HBr. Therefore, I propose to introduce H₂ or CO gas into UHV to remove the O atoms in the formed 2DOM networks at a mild temperature. We expect the 2DOM networks could transform back to pristine 1DOM chains, representing a reversible transformation. Controlling the equilibrium of a reversible reaction would be an essential tool for achieving long-range-ordered 2DOMs. Therefore, we could further adjust the ratio between different gases and the substrate temperature to enlarge the size of the 2DOM networks. However, for the bifunctional aromatic precursors used in this thesis, we anticipate that the introduction of reductive gases at higher temperature will transform the 2DOM networks to 1D polymers instead of 2D π-conjugated polymers (2DCPs).

To achieve the transformation from 2DOMs to more robust 2DCPs after the removal of O, a promising solution is introducing acetylene groups at the end sites of precursor. As reported, the precursor functionalized with acetylene groups can couple to different oligomers on Au(111), including aromatic core structure which is the only case that could form 2DCPs.¹⁸ To constrain the reactions to proceed towards the formation of aromatic core structure, we would add halogen atoms along with the acetylene groups (see the precursor in [Figure 6.1](#)). As a result, the 2DOM networks with acetylene groups and Cu_xO clusters at the connection nodes would form initially (see [Figure 6.1](#)). After further annealing, the newly formed 2DOM

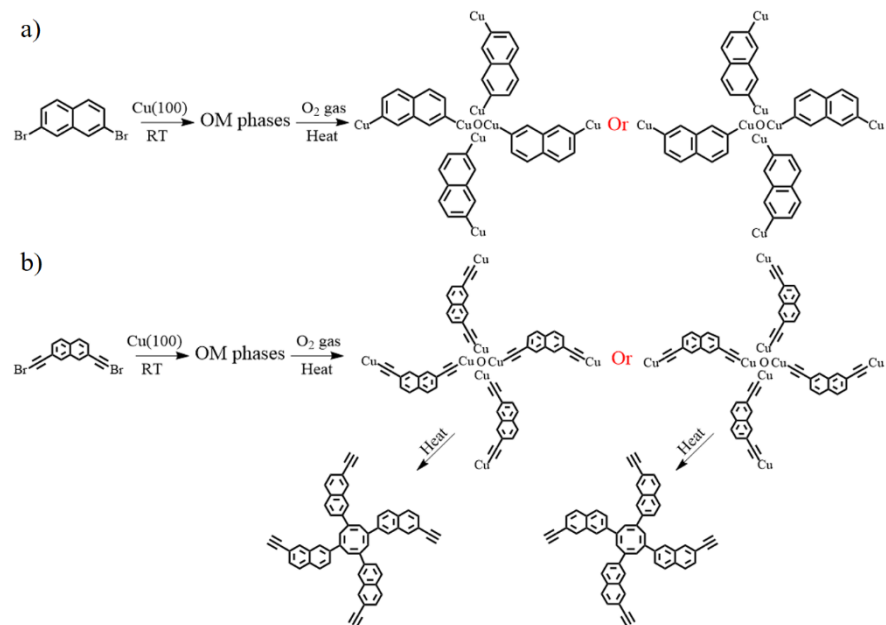


Figure 6. 2 Proposed schemes of a) the formation of 2DOM networks with different chirality from a V-shaped precursor. b) the formation of 2DCPs from a V-shaped precursor functionalized with halogenated acetylene groups.

networks can act as templates to steer the formation of corresponding 2DCPs after the removal of O. With rationally designed precursors, this strategy can be further used to synthesize π -conjugated polymers with desired structures and properties.

6.3 Chiral transfer from 2DOM networks to 2DCPs

Following the same strategy, we will further investigate chiral transfer from 2DOM to 2DCPs on Cu(100), defined as a transformation in which the chirality of the parent phase is retained by the product. To do so, we plan to use a 120° V-shaped halogenated molecule to initially check if the 2DOM networks with different chirality can be formed. As shown in [Figure 6.2a](#), we propose that after the introduction of oxygen on Cu(100), the 1D zigzag OM chains will transform to 2D OM networks with opposite chirality.

On this basis, a V-shaped molecule with halogenated acetylene groups (precursor in [Figure 6.2b](#)) will be further used to achieve the chiral transfer from OM phase to polymerized phase. The molecules would form zigzag shaped 1DOM chains initially after the deposition on Cu(100). As shown in [Figure 6.2b](#), after the introduction of O and heating, the OM chains could transform to 2DOM networks but with distinct chirality. The proposed method to synthesize 2DCPs with alkyne coupling could be applied here to synthesize 2DCPs with inherited chirality. We also expect the transformation from 2DOM networks with heterogeneous chirality to 2DCPs with homogeneous chirality, meaning the achievement of chiral selectivity. We expect that such studies could provide fundamental insights into asymmetric organic synthesis which is particularly important in the pharmaceutical industry where most novel drugs are developed as pure enantiomers.

6.4 Surface-confined reactions of molecules functionalized with thiophene groups

As illustrated in chapter 5, the ring-opening and desulfurization reactions of thiophene groups can induce either intramolecular cyclization or intermolecular C-C coupling, leading to the formation of PAHs or π -conjugated polymers (CPs). On this basis, we propose to synthesize targeted PAHs or CPs with rationally designed thiophene-based precursors. As shown in [Figure 6.3](#), 2D planar PAHs such as nanographenes could be synthesized using a hexakis(oligothienyl)benzene precursor, which can be prepared by trimerization of corresponding di(oligothienyl)-ethynes. The basic mechanism of the surface reaction

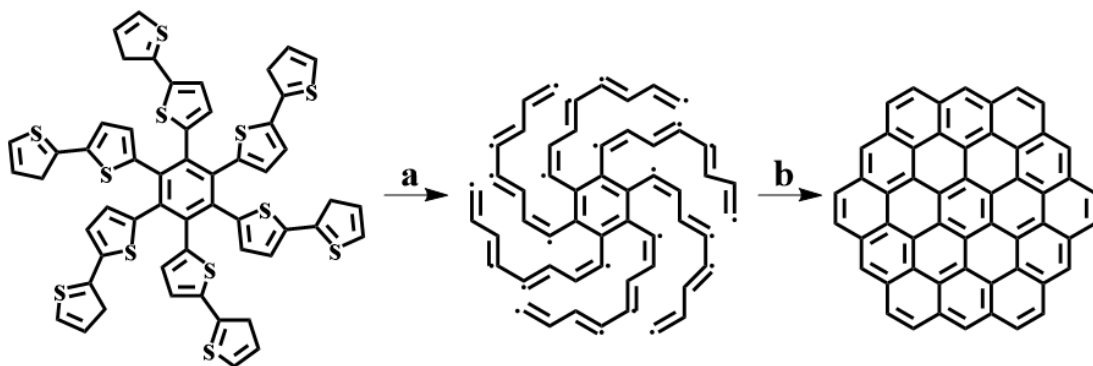


Figure 6. 3 On-surface synthesis of dodecabenzocoronene from thiophene-based precursors. **a:** ring opening and desulfurization. **b:** intramolecular cyclization.

involves ring opening and desulfurization of thiophene groups, leaving a number of unsaturated carbon chains. Further heating will induce the intramolecular C-C coupling to form the conjugated product. The synthesis of this PAH, despite having highly favorable properties, cannot be easily achieved through conventional synthetic methods due to its extremely poor solubility. The nanographene has also been demonstrated as an important material for semiconducting and liquid crystalline devices,²⁴² as well as being the subject of multiple theoretical investigations.²⁴³

Functionalization of the thiophene-based precursor with halogen atoms will be used to synthesize armchair-edged graphene nanoribbons, which have attracted great attention due to their tunable electronic properties and potential applications in nanodevices. As shown in [Figure 6.4](#), due to the lower activation energy, the introduced bromine atoms in the precursor will first lead to intermolecular C-C coupling through the Ullmann-type reaction. After the formation of linear long-range-ordered polymers, ring opening and desulfurization of thiophene groups can be thermally induced at mild temperatures (under 100°C) to produce surface-stabilized radicals in both the benzene ring backbone and dangling carbon chains. A slightly higher annealing is expected to drive the coupling of unsaturated carbon chains and adjacent benzene rings to form a new benzene ring fused with the pristine benzene chains. As a result, AGNRs with

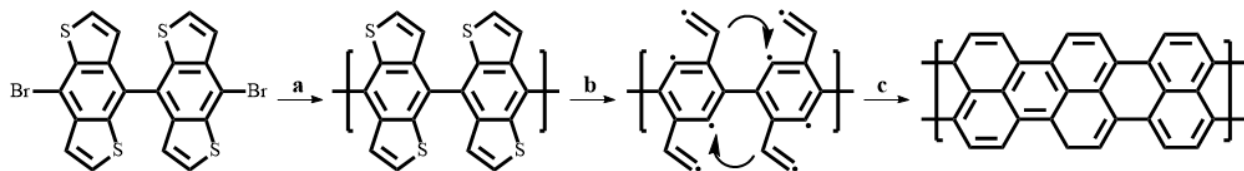


Figure 6. 4 On-surface synthesis of armchair-edged GNRs from thiophene-based precursors. **a:** C-C coupling induced by dehalogenation. **b:** ring opening and desulfurization. **c:** intramolecular cyclization.

5 carbon atoms in the width direction can be formed. We expect this strategy can be further used to synthesize GNRs with different width and edge structure by using rationally designed precursors, with the advantage that it avoids the need for high temperatures (~ 300 °C) to induce cyclodehydrogenation in typical AGNR synthesis.

In addition, to further understand the effect of substrates on the competition of intra- and intermolecular coupling after ring opening, we would study thiophene-based molecules on different substrates than Cu(111), such as more reactive Ni(111) and Pd(111). The different activation energy of desulfurization will further affect the subsequent intra- or intermolecular coupling. We expect the variation of the substrate can be used to rationally control the pathway of the coupling reaction. On top of the use of different substrates to adjust the activation energy of thiophene ring, we plan to replace the thiophene groups with other five-membered aromatic rings with distinct aromaticity and reactivity, such as furan, pyrrole and selenophene. The different properties and features of these aromatic rings can be applied to steer the reaction pathways and to form different products. The co-adsorption of dissociated atoms could also have nontrivial effects on these reactions and products.

Résumé: Synthèse en surface de nanostructures organométalliques et carbonées sous ultravide

7.1 Introduction

7.1.1 Aperçu de la science des surfaces

La chimie des surfaces, y compris l'auto-assemblage de surface et les réactions confinées en surface, a connu un développement rapide grâce à l'invention et à l'adoption généralisée de techniques modernes de science des surfaces, en particulier la microscopie à effet tunnel (STM) et la microscopie à force atomique sans contact (AFM). De nombreuses études dans ce domaine nécessitent un environnement à ultravide (UHV) pour éliminer les effets secondaires des contaminants sur les processus de surface et pour permettre l'utilisation de techniques qui nécessitent des pressions ultra-basses.

L'auto-assemblage de surface s'est avéré être une stratégie efficace pour produire des films organiques fonctionnels monocouches ou multicoches grâce à des interactions relativement faibles (telles que la liaison hydrogène et les forces de van der Waals). En utilisant des blocs de construction moléculaires conçus et différents solvants, l'équilibre entre les interactions molécule-molécule, molécule-sousstrat, molécule-solvant et solvant-sousstrat peut être ajusté pour former des modèles fonctionnels ciblés.²⁴⁴ Cela permet le réglage des propriétés de transport de charge, ce qui est crucial pour l'électronique moléculaire et les nanodispositifs. Les films organiques formés peuvent également être utilisés pour fonctionnaliser la surface pour des applications telles que des modèles spécifiques dans la chimie hôte-invité.²⁴⁵

Contrairement à l'auto-assemblage, les réactions confinées en surface ont été démontrées comme une stratégie prometteuse pour synthétiser des nanostructures liées par des interactions plus fortes (principalement des liaisons covalentes). En raison des effets catalytiques et de confinement de faible dimension des sousstrats métalliques, les réactions sur les interfaces solide-solution ou solide-vide peuvent suivre des voies différentes de la chimie traditionnelle en solution.^{3, 5, 9, 11} Les réactions confinées en surface présentent des caractéristiques de catalyse hétérogène, en ce que les précurseurs initiaux, les états intermédiaires et les produits de réaction restent tous adsorbés sur la surface.^{65, 82, 83, 85, 246} Cette thèse s'est concentrée sur les réactions confinées en surface se déroulant dans un environnement UHV (c'est-à-dire

une interface solide-vide). De plus, les réactions confinées en surface représentent une approche convaincante pour synthétiser des matériaux à base de carbone de faible dimension qui sont inaccessibles par la chimie des solutions en raison de leur insolubilité ou de leur agrégation. Cette approche est à la base d'un nouveau domaine de recherche appelé synthèse en surface. Une large gamme de nanomatériaux robustes de faible dimension avec des propriétés électroniques uniques ont été obtenus par synthèse en surface, y compris des hydrocarbures aromatiques polycycliques exotiques, des fils moléculaires, des polymères π -conjugués 2D (2DCPs) et nanorubans de graphène (GNR).

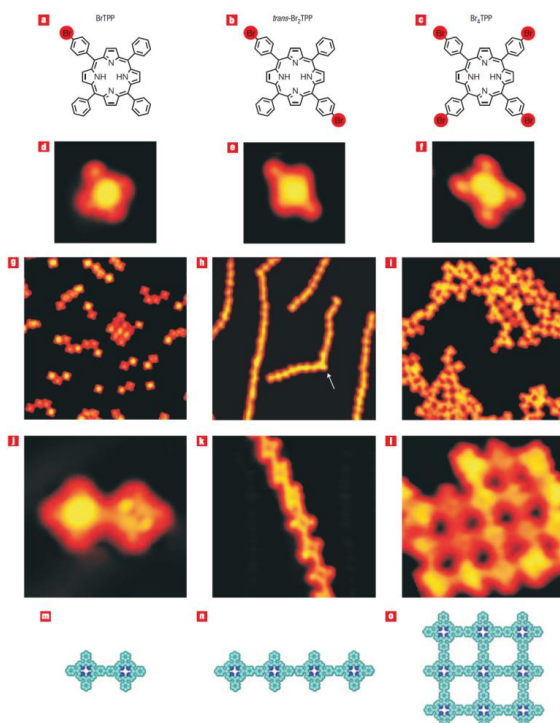


Figure 7.1 Piloter la synthèse de polymères de différentes dimensions en ajoutant des groupements terminaux dans différents sites des précurseurs à base de porphyrines. Adapté de Réf. 37 avec la permission de Springer Nature.

En 2007, Grill et al. ont rapporté la synthèse de nanostructures 2D liées par covalence sur Au(111) par une approche ascendante, utilisant le couplage déhalogénatif du précurseur de porphyrine tétrabromée (voir la Figure 7.1).³⁷ Depuis lors, un large éventail de réactions chimiques traditionnelles ont été étudiées sur des surfaces avec des précurseurs sur mesure, y compris des réactions de polymérisation telles que le couplage de type Ullmann ou le couplage de Glaser et des réactions intramoléculaires telles que la cyclodéshydrogénéation ou la décarbonylation. Ces investigations approfondies ont amélioré notre capacité à synthétiser des nanomatériaux avec les structures souhaitées, permettant des travaux préliminaires examinant leur application dans des dispositifs réels. Cependant, la synthèse de produits souhaitables est

affectée par un grand nombre de paramètres et de conditions de réaction, et nécessite un contrôle environnemental précis, une conception soignée des molécules précurseurs et un choix judicieux du substrat. Par conséquent, le contrôle rationnel de la voie de réaction et des produits reste le principal défi de la synthèse en surface.

Ces réactions peuvent être étudiées sur une gamme de surfaces monocrystallines avec différentes réactivités, constantes de réseau et symétries, y compris des substrats isolants, semi-conducteurs et conducteurs. Cependant, des substrats conducteurs ou semi-conducteurs sont nécessaires pour effectuer la microscopie à effet tunnel, principal outil de caractérisation dans le domaine. Dans cette thèse, nous avons concentré nos expériences sur les surfaces monocrystallines de métal monétaire, y compris Au(111), Ag(111), Cu(111) et Cu(100), qui offrent différentes barrières à la diffusion moléculaire, la capacité catalytique, la constante de réseau et symétrie du substrat.¹²⁴

Outre les effets de gabarit et catalytiques des substrats et les caractéristiques intrinsèques de chaque réaction de surface, il existe plusieurs autres facteurs qui pourraient déterminer les structures et les propriétés des phases intermédiaires et des produits de réactions confinées en surface en UHV, comme la conception rationnelle de la précurseurs, la cinétique (température du substrat lorsque les molécules se fixent sur la surface, ou le taux de dosage des molécules), la couverture des précurseurs et la stoechiométrie des précurseurs multiples. Enfin, il convient de noter que la grande majorité des réactions en surface dans l'UHV sont induites thermiquement, bien que quelques réactions aient été alternativement activées par la lumière, l'irradiation par faisceau d'électrons ou le champ électrique appliqué.

7.1.2 Couplage de type Ullmann confiné en surface

Dans cette thèse, la réaction de type Ullmann sur Cu(111) est la principale réaction étudiée. Bien que plus générale que la réaction d'Ullmann traditionnelle en solution, la réaction de type Ullmann confinée en surface est également définie par un couplage carbone-carbone (C-C) déhalogénatif. À ce jour, c'est l'une des réactions les plus étudiées en raison de son grand potentiel dans la synthèse d'une gamme de polymères conjugués de faible dimension avec une dimensionnalité, des structures et des propriétés spécifiques. Les stratégies de base pour piloter cette réaction en surface incluent la conception des précurseurs

fonctionnalisés, l'optimisation des paramètres de la réaction (couverture moléculaire, température de recuit, etc.), la sélection du substrat et sa symétrie.

La réaction classique d'Ullmann a été proposée pour la première fois par le chimiste allemand Fritz Ullmann en 1901.²⁸ Il a observé qu'un composé contenant du cuivre peut catalyser le couplage de deux halogénures d'aryle en fragments bi-aryle. Au cours des années suivantes, Ullmann a appliqué cette réaction pour synthétiser des N-aryl amines et des éthers.^{29,30} Après une enquête continue sur les espèces de Cu dans la réaction d'Ullmann, les chercheurs ont conclu que les états initiaux de la source de Cu dans la réaction ne sont pas cruciaux car le cuivre sera toujours transféré dans la même phase au cours des processus d'oxydation/réduction. Cependant, le mécanisme de la réaction d'Ullmann a subi une longue période de controverse depuis la première hypothèse dans les années 1960,³¹⁻³³ l'accent était mis sur la question de savoir si les produits finaux étaient générés en solution ou à la surface des espèces de cuivre. De nos jours, le mécanisme généralement accepté est que les espèces de Cu catalysent la dissociation des halogénures d'aryle en atomes d'halogène et en radicaux phénylène, qui couplent immédiatement les atomes de Cu pour former des intermédiaires organométalliques (OM). Après élimination réductrice, les espèces OM se transforment en produits polymérisés finaux.

Pour éliminer les effets secondaires des contaminants présents en solution et obtenir une meilleure compréhension du mécanisme de réaction, l'étude de la réaction d'Ullmann traditionnelle est passée de la solution aux interfaces solides (solide-liquide ou solide-vide). Différent du comportement de la catalyse homogène où les réactions se produisent dans la même phase (liquide), les précurseurs et les adatomes intrinsèques sont contraints en basse dimension lorsque la réaction de type Ullmann a lieu sur des interfaces, portant les caractéristiques des deux homogènes (par exemple, la formation sélective de produits) et la catalyse hétérogène (par exemple, la séparation de catalyseurs homogènes). Cela pourrait favoriser les différentes voies de réaction et la compréhension des réactions sous différents aspects. Combinées à l'atmosphère UHV et au refroidissement à basse température (RT), les techniques modernes de caractérisation de surface sont capables de fournir des informations sur les différents états de cette réaction à l'échelle atomique ou sous-moléculaire. En 1992, pour la première fois, Xi et Bent ont étudié le couplage de type Ullmann confiné en surface avec un précurseur iodobenzène sur Cu(111) en UHV.³⁴ Ils ont en outre

illustré la relation entre la couverture moléculaire et le mécanisme de réaction,³⁵ faisant remarquer que la couverture affecterait l'orientation des molécules d'iodobenzène sur la surface et donc le couplage ultérieur. En 2000, Hla et al. ont rapporté un couplage de type Ullmann induit par la pointe STM sur Cu(111), démontrant la faisabilité de “souder” manuellement les molécules.³⁶ La dissociation du précurseur iodobenzène en phényle et iodé peut être induite en plaçant la pointe au-dessus de la molécule et en appliquant une polarisation. Deux groupes phényle peuvent être rapprochés latéralement par manipulation de la pointe, puis couplés en biphenyle par une excitation supplémentaire de la pointe. Au cours des années suivantes, différents aspects du couplage de type Ullmann en surface ont été étudiés, notamment la synthèse de polymères conjugués aux structures et propriétés souhaitées,^{5, 9, 37-45} les effets de différents substituants halogène dans le précurseur,⁴⁶⁻⁴⁹ formation de différents états intermédiaires,^{40, 50-54} les influences des différents substrats,⁵⁵ et déshalogénéation hiérarchique utilisant les différentes énergies d'activation pour les liaisons C-Br, C-Cl et C-I.⁵⁶⁻⁶²

Basé sur des réactions de type Ullmann confinées en surface, un travail pionnier rapporté par Grill et al. en 2007 ont contribué à la synthèse d'un grand nombre de structures fonctionnelles liées de manière covalente qui ont été introduites précédemment dans cette section (voir [Figure 7.1](#)).³⁷ Après ces travaux, le couplage de type Ullmann confiné en surface s'est principalement concentré sur la synthèse de différents polymères conjugués fonctionnels à grande échelle, tels que les nanorubans de graphène quasi-1D (GNR) et les polymères semi-conducteurs 2D de type graphène.

Avant la formation des polymères conjugués finaux, il existe un certain nombre d'états intermédiaires au cours du processus de couplage de type Ullmann confiné en surface. Non seulement ces états intermédiaires peuvent eux-mêmes avoir des propriétés uniques, mais une compréhension de leur évolution pourrait permettre d'orienter la réaction vers les produits polymérisés finaux souhaités. Fan et al. ont rapporté une transformation de phase induite par les adatomes de surface des états intermédiaires à 113 K sur Cu(111) et à 103 K sur Ag(111).⁵² Le dépôt du précurseur 4,4"-dibromo-m-terphényle sur Cu(111) à 90 K suivi d'un recuit à 113 K peut transformer la phase intermédiaire liée à l'halogène en une phase liée par coordination. Une transformation similaire peut également être obtenue en déposant les précurseurs sur Ag(111) avec un chauffage ultérieur de 88 K à 103 K.

Parmi tous les états intermédiaires, les phases OM sont les plus couramment observées et jouent un rôle crucial dans la polymérisation ultérieure.^{40, 50, 51, 53} En 2013, en utilisant STM et XPS, Di Giovannantonio et al. a d'abord donné un aperçu de l'intermédiaire OM du couplage de type Ullmann en surface sur Cu(110) et de son évolution en polymères.⁴⁰ La même année, Fan et al. a démontré la formation de différents états intermédiaires OM à partir d'une seule catégorie de précurseur mais avec une couverture différente sur Cu(111).⁵¹ De plus, en 2019, Galeotti et al. ont rapporté des intermédiaires OM 2D inattendus qui coexistaient avec la phase OM 1D traditionnelle lorsque le précurseur 1,4-dibromobenzène était déposé sur Cu(110).⁵³ Avec l'augmentation de la température de recuit à 170 °C, le rapport de la phase OM 2D, qui contient un cluster de quatre adatomes de cuivre comme nœud, atteint le pic. Avec un recuit plus élevé, la phase OM 2D se transforme en polymères 1D par couplage de type Ullmann, comme indiqué précédemment. Au cours de l'étude continue du couplage de type Ullmann, davantage d'états intermédiaires OM ont été trouvés, suggérant que la recherche de phases intermédiaires dans le couplage de type Ullmann n'a pas atteint sa fin. Un effort plus important est nécessaire pour parvenir au contrôle rationnel des structures des phases OM afin d'en tirer parti pour orienter la formation de polymères.

Le choix des atomes d'halogène dans le précurseur est un autre facteur clé qui joue un rôle critique dans le pilotage du couplage de type Ullmann en surface. En 2017, Galeotti et al. analysé systématiquement l'influence du type d'halogène sur les superstructures moléculaires, les températures de réaction et la cinétique à l'aide de STM, XPS rapide et spectroscopie de structure fine d'absorption des rayons X proche du bord.⁴⁷ À partir des données XPS rapides, les températures de début et de fin des différentes étapes de réaction peuvent être facilement interprétées. La valeur et la plage de température de réaction sont clairement différentes pour différents précurseurs halogénés. De plus, en 2018, Di Giovannantonio et al. ont rapporté que les monomères fonctionnalisés par l'iode conduisent à la croissance de GNR plus longs que ceux bromés.⁴⁸ En tirant parti des différents seuils de température pour cliver différentes liaisons C-halogène, plusieurs substituants halogène peuvent être ajoutés dans des sites particuliers au sein du même précurseur pour orienter le processus de couplage de type Ullmann confiné en surface. Sur cette base, un protocole de polymérisation hiérarchique a été réalisé en introduisant des liaisons C-Br et C-I dans les mêmes précurseurs.⁵⁷ Les liaisons C-I peuvent être clivées à température ambiante sur Au(111), alors que

le clivage des liaisons C-Br nécessite un chauffage à au moins 185 °C. En optimisant la température de recuit, les défauts des polymères peuvent être réduits efficacement. À l'avenir, nous nous attendons à ce que de plus en plus de nanostructures fonctionnelles puissent être synthétisées par ce protocole hiérarchique avec des précurseurs halogénés de conception subtile.

Bien que le couplage de type Ullmann confiné en surface ait été largement étudié et appliqué dans la synthèse de polymères conjugués fonctionnalisés, des efforts supplémentaires doivent être déployés pour améliorer la qualité et la taille du domaine des structures des intermédiaires et des produits OM, et ajuster les structures pour explorer des phénomènes quantiques plus intéressants. Au-delà de la synthèse sur des substrats métalliques catalytiques, pour atteindre plus d'applications potentielles dans des dispositifs réels, des progrès supplémentaires sont nécessaires pour synthétiser des polymères conjugués sur des surfaces non métalliques avec un couplage de type Ullmann confiné en surface. Très récemment, avec l'induction d'une pointe de microscope à force atomique, Zhong et al. ont rapporté une approche polyvalente pour la construction de structures à liaison covalente de faible dimension bloc par bloc sur des films bicouches de chlorure de sodium sur Cu(111).⁶³ De plus, le transfert post-synthétique pourrait être une solution alternative pour la synthèse de polymères conjugués sur des surfaces non métalliques. Dans cette thèse, pour découpler les interactions du substrat métallique, nous explorerons la possibilité d'oxyder les couches supérieures du substrat Cu(111) qui présente des propriétés semi-conductrices, mais sans effet néfaste sur les produits.

7.1.3 Synthèse en surface de nanorubans de graphène

Avec plus d'investigations et une compréhension approfondie du couplage de type Ullmann confiné en surface, un certain nombre de polymères conjugués 1D ou 2D étendus avec des structures et des propriétés souhaitées ont été synthétisés. Au cours de la dernière décennie, en tant qu'exemple phare de nanomatiériaux de carbone accessibles par couplage de type Ullmann, les nanorubans de graphène (GNR) ont gagné en popularité en raison de leurs applications potentielles dans les dispositifs semi-conducteurs et la spintronique. Une série d'approches descendantes ont été suivies pour produire des GNR,¹⁷⁷⁻¹⁷⁹ pourtant, un manque de contrôle sur la largeur du ruban et la structure des bords a entravé leurs développements ultérieurs. En 2010, Cai et al.¹⁴² ont rapporté la fabrication d'un GNR de fauteuil atomiquement précis

(AGNR) sur la surface Au(111) en utilisant une approche ascendante. Le mécanisme de base implique une déshalogénéation activée thermiquement, une polymérisation assistée en surface (couplage de type Ullmann confiné en surface) et une cyclodéshydrogénéation finale (ou fusion latérale en rubans plus larges). Au cours de la décennie suivante, cette approche ascendante a été étendue pour synthétiser une grande variété de GNR, y compris des AGNR de différentes largeurs (les précurseurs et les AGNR correspondants sont résumés dans la [Figure 7.2](#)),^{143-145, 180, 181} GNR en zigzag,^{120, 121} les hétérojonctions GNR,¹⁸²⁻¹⁸⁶ GNR chiraux¹⁸⁷⁻¹⁹¹ et les GNR dopés chimiquement.¹⁹²⁻¹⁹⁵

Sur la base de la similitude périodique de leurs structures électroniques, les AGNR peuvent être classés en trois familles, 3p, 3p+1 et 3p+2 (représentant le nombre d'atomes de carbone dans la direction étroite).¹⁷⁴ En général, selon l'approximation de la densité locale ou les calculs théoriques des quasi-particules, les bandes interdites des AGNR dans chaque famille sont inversement proportionnelles à leur largeur. Les bandes interdites expérimentales des AGNR obtenues par spectroscopie à effet tunnel sont généralement plus grandes que les prédictions théoriques, qui sont attribuées au blindage par des substrats métalliques. Par conséquent, plusieurs méthodes ont été utilisées pour éliminer l'effet électronique des substrats métalliques, telles que le déplacement du ruban sur les couches de NaCl pré-décorées ou la synthèse directe d'AGNR sur des surfaces semi-conductrices.^{121, 247} De ce fait, la mesure expérimentale sur les structures électroniques des AGNR sera plus proche de la propriété intrinsèque, contribuant à la poursuite de la recherche de leurs applications.

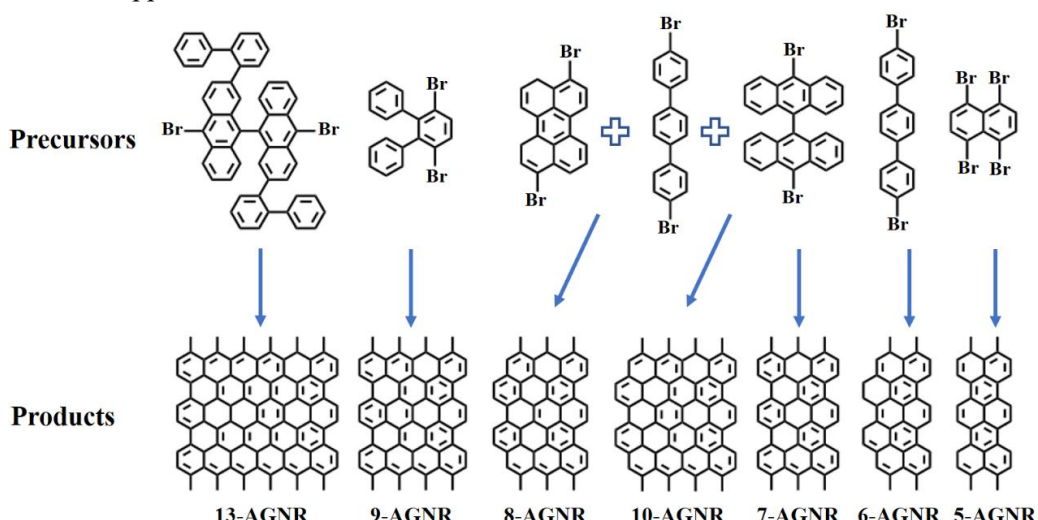


Figure 7. 2 Résumé des AGNR de différentes largeurs synthétisés à partir de différents précurseurs bromés conçus de manière rationnelle sur Au(111).

La conception rationnelle des précurseurs halogénés est le facteur clé dans la synthèse des GNR. Comme le montre la [Figure 7.2](#), des AGNR de différentes largeurs peuvent être synthétisés avec des précurseurs soigneusement conçus. En plus du précurseur, la cinétique de la réaction peut également affecter la structure des produits finaux. En modifiant les sites des substituants halogène dans le précurseur, le rapport entre l'activation des liaisons C-Br et C-H impliquées lors de la polymérisation peut être ajusté.²⁴⁸ Étant donné que l'énergie d'activation des liaisons C-H est considérablement supérieure à celle des liaisons C-Br, moins d'activation C-H impliquée dans la synthèse signifie la formation de GNR plus longs et de meilleure qualité. En conséquence, en raison de la compétition entre l'activation C-H et le couplage C-C après le clivage de la liaison C-Br, le dépôt de précurseurs sur le substrat à température plus élevée conduira à la formation de GNR plus courts. De plus, la cinétique de la réaction peut être ajustée en remplaçant les substituants Br par des atomes I, en raison de l'énergie d'activation différente entre les liaisons C-I et C-Br.

Le choix d'un substrat différent est un autre facteur qui peut affecter la réaction à la formation de GNR. La différence la plus apparente est la nature des différents matériaux de substrat, comme Cu(111) et Au(111). Jusqu'à présent, la plupart des GNR sont synthétisés sur Au(111), alors que peu d'études se sont concentrées sur la synthèse de GNR sur Cu(111) en raison de la plus forte interaction de surface, malgré la plus faible énergie d'activation pour la déshalogénéation.^{187, 188, 196-198} Il a été montré que les GNR chiraux peuvent être synthétisés sur Cu(111)¹⁸⁸ en utilisant le même précurseur qui donne du 7-AGNR non chiral sur Au(111)¹⁴², et la réaction de déshalogénéation lors de la formation peut être réversible sur Au(111) mais pas sur Cu(111).¹⁷² Il est à noter ici que, pour utiliser des spectroscopies spécifiques et répondre aux exigences d'orientation uniforme, les GNR peuvent également être synthétisés sur des surfaces monocrystallines avec un indice de Miller plus élevé où les terrasses plus étroites peuvent contraindre l'orientation du ruban. L'ensemble de ces phénomènes implique que l'importance du substrat dans la synthèse des GNRs.

Comme deuxième objectif de mon doctorat, nous avons étudié la synthèse d'AGNR de la sous-famille 3P sur Cu(111), qui n'a jamais été rapportée. De plus, compte tenu de l'effet catalytique potentiel de l'oxygène sur l'activation C-H, nous avons introduit de l'oxygène atomique de manière extrinsèque lors de la synthèse. Nous nous attendions à ce que l'introduction d'oxygène puisse abaisser la température pour la cyclodéshydrogénéation latérale.

7.1.4 Les effets des co-adsorbats atomiques étrangers sur la réaction confinée en surface

En raison de l'atmosphère extrêmement propre, l'environnement UHV permet d'étudier l'auto-assemblage et les réactions en surface sans pratiquement aucune influence de contaminants. De plus, l'UHV permet de préparer des substrats monocristallins atomiquement plats grâce à des cycles de pulvérisation ionique et de recuit. Sur cette base, il a été démontré qu'un large éventail de paramètres et de conditions de réaction peuvent affecter et orienter la voie des réactions confinées en surface. Parmi tous les paramètres et conditions ajustables, une approche prometteuse et peu étudiée pour contrôler la synthèse en surface consiste à modifier l'atmosphère de réaction en introduisant des gaz réactifs ou divers métaux dans l'environnement d'ultravide (UHV) (voir [Figure 7.3](#)). En ajustant la phase, la quantité et le moment des espèces introduites, cette stratégie ingénieuse peut être appliquée pour étudier les effets de divers co-adsorbats atomiques extrinsèques sur la réaction confinée en surface de manière flexible et contrôlée. En général, les co-adsorbats atomiques peuvent être divisés en deux catégories, les métaux (y compris les petits agrégats atomiques) et les non-métaux (par exemple, l'hydrogène, l'oxygène et les halogènes).

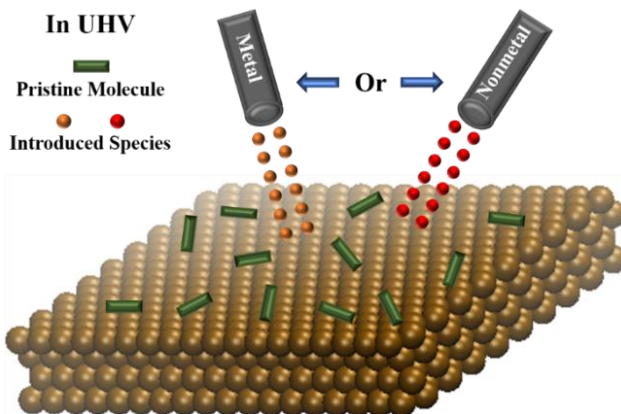


Figure 7.3 Schéma de principe de l'introduction externe d'espèces métalliques ou non métalliques dans l'environnement UHV.

Les métaux sont connus pour jouer un rôle essentiel dans la chimie humide traditionnelle en tant que catalyseurs ou composants essentiels dans les produits (tels que les metal-organic frameworks). Comme mentionné ci-dessus, dans les réactions de type Ullmann confinées en surface, les atomes métalliques intrinsèques extraits des substrats peuvent également entraver le couplage C-C en formant des intermédiaires organométalliques. Ceci suggère le rôle spécifique des atomes métalliques dans les réactions de surface. Il est à noter ici que la question de savoir si les atomes métalliques sont extraits des terrasses ou

proviennent des bords des marches fait toujours l'objet de débats.⁶⁴ Outre les atomes métalliques intrinsèques extraits des substrats, les métaux peuvent également être introduits de manière contrôlée de manière externe sur la surface via des évaporateurs métalliques spécifiques. Les métaux peuvent alors piloter les réactions de deux manières principales, agissant comme catalyseurs pour faciliter les réactions qui présentent les caractéristiques d'une catalyse hétérogène ou participant à la construction de structures finales sous une forme spécifique (par exemple, comme nœuds de connexion dans le métal-réseaux organiques).⁶⁵⁻⁶⁹

Outre les espèces métalliques, les non-métaux introduits de l'extérieur (par exemple, les halogènes, l'oxygène, l'hydrogène, le soufre, le NaCl) peuvent également jouer un rôle critique dans les réactions confinées en surface, qui ont été plus largement étudiées ces dernières années. On rapporte que H₂ est capable d'éliminer les sous-produits halogènes générés lors du couplage de type Ullmann confiné en surface.¹⁰⁵⁻¹⁰⁷ Il a été rapporté que H₂S et H₂ suppriment et réactivent la réaction de type Ullmann en surface, respectivement.¹¹⁰ En outre, il a été démontré que les atomes d'iode forment une monocouche pour s'intercaler aux polymères 2D supportés par la surface Ag(111) ou Au(111), contribuant au découplage électronique entre les matériaux et les substrats supportés en surface.^{102, 103} O₂ était généralement utilisé pour favoriser l'activation des liaisons C-H afin d'abaisser la barrière d'un couplage C-C supplémentaire.^{113, 115} De plus, l'introduction d'oxygène peut décorer la surface en formant de nouvelles phases reconstruites, comme la reconstruction de Cu(110) induite par chimisorption d'oxygène.¹¹⁷ Cependant, jusqu'à présent, il n'y a aucun rapport sur les effets de l'oxygène sur l'une des réactions confinées en surface les plus étudiées, le couplage de type Ullmann. Dans cette thèse, nous discuterons des effets de l'oxygène co-adsorbé sur le couplage de type Ullmann confiné en surface par intrusion de gaz O₂ dans UHV avant ou après la formation d'intermédiaires OM.

7.2 Résultats et discussions

7.2.1 Transformation 1D à 2D induite par l'oxygène de structures organométalliques en surface

Dans ce chapitre, je présenterai nos recherches sur les effets de l'oxygène sur le couplage de type Ullmann

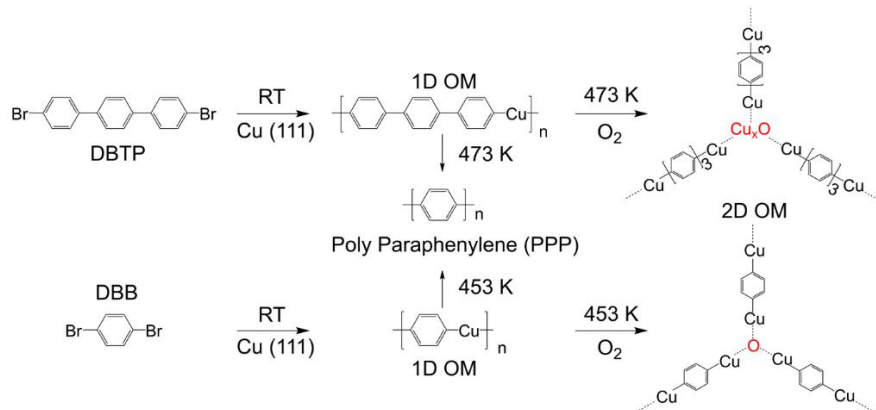


Figure 7.4 Schéma de la transformation de structures organométalliques (OM) de 1D à 2D en introduisant O₂ dans un couplage de type Ullmann confiné en surface.

confiné en surface. Comme le montre le schéma de la [Figure 7.4](#), des intermédiaires organométalliques (OM) se forment après le dépôt de 4,4"-dibromo-p-terphényle (DBTP, ou Br-(ph)₃-Br) ou de 1,4-dibromobenzène (dBB, Br-ph-Br) sur Cu(111) à TA. Une augmentation de la température donne, par couplage de type Ullmann, des fils en poly para-phénylène (PPP). Au lieu de cela, en présence d'oxygène co-adsorbé à la surface, un recuit ultérieur provoque le déroulement de la réaction le long d'une voie inattendue dans laquelle les chaînes OM 1D se transforment en réseaux OM 2D avec des clusters cuivre-oxygène comme nœuds de connexion. En suivant la même approche sur Cu(100), des réseaux OM 2D cuivre-oxygène à symétrie carrée sont également obtenus. La STM UHV et la spectroscopie photoélectronique à rayons X in situ (XPS) ont été utilisées pour étudier les structures 2D, complétées par des calculs de théorie fonctionnelle de la densité (DFT). Nos recherches donnent un aperçu du rôle de l'oxygène dans le couplage de type Ullmann confiné en surface, qui a un effet néfaste sur la synthèse des polymères, tout en permettant la formation de nanostructures 2D de taille et de forme réglables. Le concept pourrait être davantage utilisé dans la chimie hôte-invité en tant que modèles de puits quantiques fournissant des environnements électroniques spécifiques.⁹⁸

Après le dépôt de DBTP sur Cu(111) à température ambiante, par déshalogénéation directe des molécules de DBTP catalysée par le substrat métallique, l'image STM de la [Figure 7.5a](#) montre clairement la formation de chaînes OM linéaires constituées de segments de terphényle alternés et d'atomes de cuivre.^{50, 51, 249} La structure périodique des segments de terphényle et des atomes de cuivre peut être identifiée dans l'image STM agrandie (encart sur la [Figure 7.5a](#)).

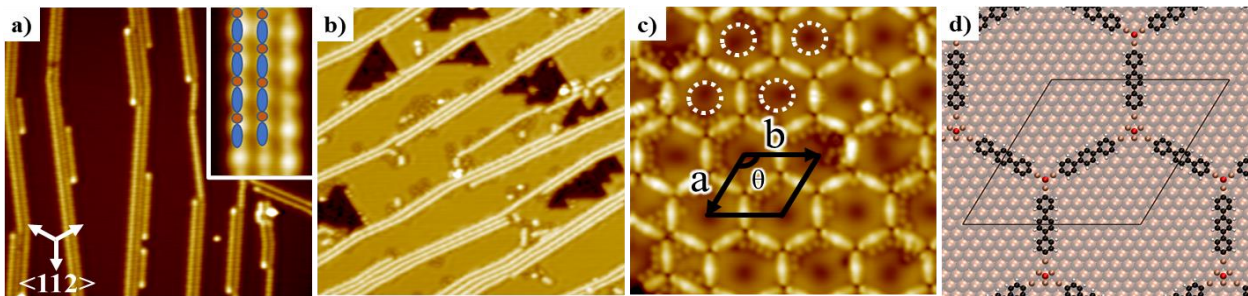


Figure 7.5 a) Vue d'ensemble Image STM des chaînes OM ($\text{ph}_3\text{-Cu-(ph)}_3$) formées par dépôt de DBTP sur Cu(111). Les cercles bruns et les ellipses bleues indiquent les atomes de cuivre et les segments de terphényle dans l'image agrandie de l'encart. b) Dosez O₂ sur l'échantillon maintenu à température ambiante. c) Réseaux hexagonaux formés par recuit à 473 K. d) Modèle optimisé DFT des réseaux. (rouge: oxygène, marron: cuivre, gris: carbone, blanc: hydrogène; les tailles d'image de a-c et e-f sont respectivement de 50 × 50, 50 × 50, 15 × 15)

Suite à la formation de chaînes OM, du gaz O₂ a été dosé sur l'échantillon maintenu à température ambiante. Comme indiqué, la molécule d'O₂ peut se dissocier au-dessus de 170 K sur Cu(111) pour s'adsorber sous forme d'atomes uniques ou de petits agrégats atomiques sur les terrasses ainsi que dans des îles triangulaires sombres formés par l'extraction d'atomes de cuivre de surface (Figure 7.5b).^{127, 151-153} La Figure 7.5b montre en outre que les chaînes OM restent largement intactes après l'introduction de gaz O₂ à température ambiante.

En l'absence d'oxygène, le chauffage des chaînes OM induit un couplage pour former des polymères covalents, et nous avons observé la formation de fils de poly para-phénylène (PPP) après recuit à 473 K, ce qui est cohérent avec les travaux antérieurs.⁵⁰ Cependant, à la même température de recuit, la présence d'oxygène adsorbé induit une transformation structurelle inattendue, dans laquelle les chaînes OM 1D se convertissent en réseaux hexagonaux ordonnés 2D, comme le montre la Figure 7.5c. Les sommets des réseaux 2D apparaissent sous forme de dépressions et les petits points brillants adjacents aux hexagones sont attribués à des atomes de brome chimisorbés. De plus, la variation de contraste dans les pores (marquée par des cercles blancs en pointillés sur la Figure 7.5c) est attribuée au confinement des états de surface sur la surface du cuivre, qui pourrait être davantage utilisée comme modèle de puits quantique pour les systèmes hôte-invité.¹⁵⁵ Les vecteurs de cellule unitaire des réseaux 2D ($a = b = 3.53 \pm 0.05$ nm, $\theta = 120^\circ \pm 2^\circ$) correspondent à 14 atomes de cuivre (3.57 nm) dans les directions <110> compactes de Cu(111), où l'alignement a été déterminé par comparaison avec les bords des îlots triangulaires sombres formés lors du dépôt d'oxygène. La stabilisation de la phase OM 2D supprime la polymérisation à 473 K, mais le couplage

peut être induit par un recuit supplémentaire à 493 K. Cependant, cela ne donne que des chaînes oligomères désordonnées plutôt que de longs polymères.

Des calculs DTF ont été effectués pour identifier la structure de la phase OM 2D. Les observations expérimentales suggèrent que les réseaux 2D sont composés de deux sommets distincts: la longueur des arêtes et l'alignement du réseau hexagonal indiquent que les sommets sont centrés sur différents sites d'adsorption de surface, et les sommets alternés apparaissent comme des dépressions avec une petite différence de hauteur de 11 ± 3 pm. La [Figure 7.5d](#) montre l'une des deux structures calculées cohérentes avec ces observations qui a un sommet Cu₃O centré sur un site creux fcc (cubique à faces centrées) et un sommet Cu₆O sur un site supérieur. Une deuxième structure avec un sommet Cu₃O sur un site creux hcp et un sommet Cu₆O sur un site supérieur est très similaire en énergie (différence <10 meV), nous nous attendons donc à ce que les deux structures existent à la surface. La configuration des atomes d'oxygène (examinée en détail pour les réseaux dBB ci-dessous) dans ces agrégats au-dessus de trois adatomes de Cu est similaire à celle d'un atome d'oxygène chimisorbé sur un site creux sur Cu(111), ce qui est cohérent avec l'apparence STM similaire des sommets sous forme d'atomes d'oxygène chimisorbés au même biais.¹²⁷

Pour étudier la compétition entre la formation de réseaux OM 2D et de chaînes OM 1D, nous avons dosé de l'oxygène sur la surface de Cu(111) avant de déposer du DBTP. Le dépôt de DBTP sur la surface partiellement oxydée de Cu(111) conduit à la formation de chaînes linéaires et de sommets triples, avec une réduction correspondante du nombre de caractéristiques d'oxygène chimisorbé. Les chaînes OM linéaires semblaient immobiles dans nos mesures STM de LT à RT, mais pourraient encore être transformées en phase 2D par recuit à 473 K. Cette observation indique que des fragments de terphénylène mobiles, produits par déshalogénéation après adsorption à TA ou par recuit, sont nécessaire pour former les sommets triples et donc les réseaux 2D. L'ordre des réseaux OM 2D ne dépend pas de la séquence de dépôt de DBTP par rapport à O₂, mais est probablement affecté par le rapport de chaque espèce adsorbée.

Après une enquête plus approfondie, nous avons observé que la taille de la structure 2D peut être ajustée en utilisant un précurseur halogéné plus court, dBB. Le dosage de dBB sur du Cu(111) pré-oxydé à température ambiante, comme le montre la [Figure 7.6a](#), conduit à des structures OM 1D et 2D, similaires à celles obtenues en déposant du DBTP sur du Cu(111) pré-oxydé. Le recuit de l'échantillon à 453 K

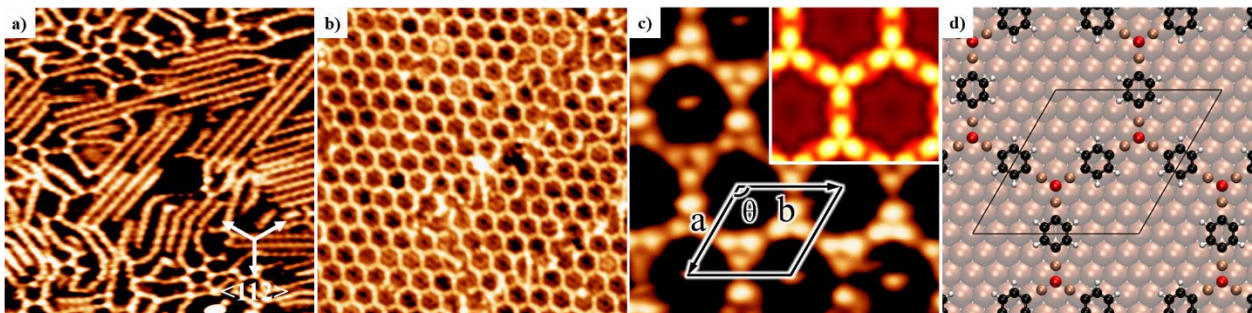


Figure 7.6 a) Image STM de structures 1D et 2D coexistantes après dépôt de dBB sur Cu(111) pré-oxydé à température ambiante. b) Réseau hexagonal obtenu par recuit à 453 K pendant 10 min. c) Image STM à petite échelle des structures hexagonales à polarisation positive; Encart: image STM simulée par DFT. d) Modèle optimisé DFT pour les réseaux 2D (rouge: oxygène, marron: cuivre, gris: carbone, blanc: hydrogène; tailles d'image de a-c 25×25 , 25×25 , $5.5 \times 5.5 \text{ nm}^2$, respectivement)

transforme les chaînes OM 1D en réseaux hexagonaux 2D. Le réseau de cellules unitaires ($a = b = 1.77 \pm 0.05 \text{ nm}$, $\theta = 120^\circ \pm 2^\circ$) des réseaux est proportionnel à 7 atomes de cuivre (1.78 nm) dans les directions rapprochées $<110>$ de Cu(111). L'image STM à polarisation positive de la [Figure 7.6c](#) montre que la morphologie est avec une dépression au centre de trois segments brillants attribués à un atome d'oxygène. Pour dBB, deux points brillants séparés pourraient être résolus dans chaque segment brillant, ce que nous attribuons aux deux adatomes de cuivre reliés par l'anneau de benzène moins brillant, similaire à l'observation de Fan et al.¹⁵⁷ Nous proposons un modèle ([Figure 7.6d](#)), dans lequel les deux sommets sont similaires au plus petit cluster de DBTP avec un atome d'oxygène central reliant les trois fragments OM. La différence de longueur d'arête de DBTP et dBB (2.04 nm contre 1.02 nm) par rapport aux longueurs moléculaires connues (1.14 contre 0.28 nm) est cohérente avec la différence de taille de cluster entre les structures DBTP et dBB 2D proposées. De plus, la dimension de cellule unitaire de 1.77 nm optimisée par DFT pour un réseau autonome s'accorde très bien avec la valeur expérimentale, et les simulations STM (Encadré de la [Figure 7.6c](#)) reproduisent l'apparence des adatomes de cuivre sous forme de points brillants en biais positif.

De plus, nous avons étudié cette transformation structurale avec dBB sur Cu(100) pour étudier l'effet de la symétrie du substrat. La [Figure 7.7a](#) montre que dBB se déshalogène après dépôt à RT pour former des chaînes OM dans deux directions équivalentes. Après dosage du gaz O₂ à température ambiante, une température de recuit légèrement plus élevée de 490 K est nécessaire pour transformer les chaînes OM en réseaux carrés, comme le montre la [Figure 7.7b](#), qui ont des domaines plus petits et moins homogènes que

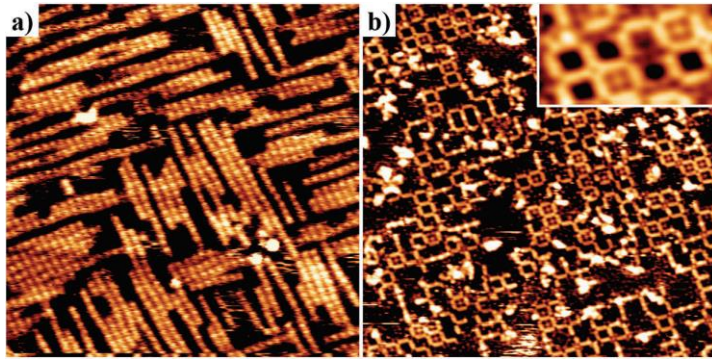


Figure 7.7 Images RT STM pour la formation de réseaux 2D à partir de dBB sur Cu(100). a) Chaînes OM formées par dépôt de dBB sur Cu(100) à TA. ($V_t = 0.8$ V, $I_t = 1.0$ nA). b) Réseaux carrés obtenus par dosage d' O_2 et recuit à 490 K pendant 20 min, détaillés en encadré. ((b) et encart: $V_t = -1.2$ V, $I_t = 1.0$ nA.) (Les tailles d'image de (a,b) et en encart sont de 30×30 , 30×30 , 5.5×3 nm 2)

ceux obtenus sur Cu(111).

En résumé, nous avons systématiquement étudié les effets du dosage de l'oxygène sur le couplage de type Ullmann confiné en surface en introduisant des atomes d'oxygène chimisorbés avant ou après le dépôt de deux précurseurs halogénés (DBTP et dBB) sur deux surfaces de cuivre de symétries différentes, Cu(111) et Cu(100). En combinant les mesures STM et XPS avec les calculs DFT, nous avons identifié une transformation structurelle inattendue des chaînes OM 1D en réseaux OM 2D. Au lieu de la voie de polymérisation typique pour le couplage de type Ullmann activé thermiquement sur le cuivre, les atomes d'oxygène suppriment la polymérisation et conduisent à des réseaux OM 2D, dans lesquels des agrégats cuivre-oxygène relient trois ou quatre fragments aromatiques. La taille et la symétrie des réseaux 2D pourraient être contrôlées rationnellement en ajustant les précurseurs et en utilisant des substrats avec une symétrie différente, respectivement. Dans des travaux futurs, nous étudierons la généralité de cette transformation pour d'autres précurseurs et surfaces afin de fabriquer des nanostructures de surface uniques, avec des applications potentielles dans la chimie hôte-invité.

7.2.2 Synthèse favorisée par l'oxygène de nanorubans de graphène fauteuil sur Cu(111)

Comme mentionné dans la section précédente, les chaînes OM de recuit générées à partir de DBTP peuvent entraîner la transformation en poly(para-phénylène) (c'est-à-dire 3-AGNR) sur Cu(111) en l'absence d'oxygène. De plus, le DBTP peut se transformer en 3-AGNR sur Au(111) sans l'émergence d'un intermédiaire OM. En outre, des nanorubans de graphène de fauteuil de sous-famille 3p plus larges (3p-

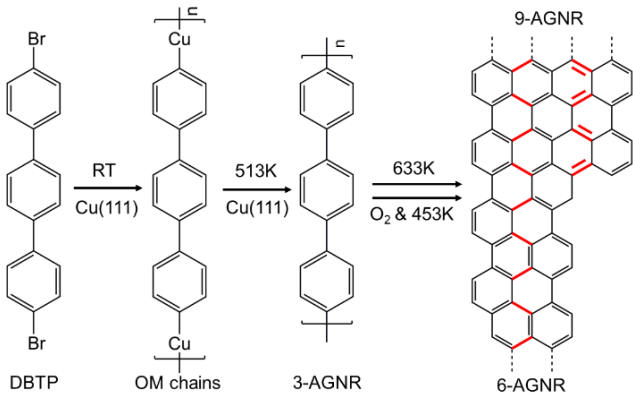


Figure 7.8 Synthèse de 3p-AGNRs sur Cu(111) pur et Cu(111) partiellement oxydé. Les liaisons formées lors de la fusion latérale sont représentées en rouge.

AGNR; la définition de 3p a été fournie à la section 7.1) peuvent être synthétisés par fusion latérale induite thermiquement de 3-AGNR sur Au(111).¹⁸⁰ En suivant une procédure similaire à Au(111), notre premier objectif était donc de réaliser la synthèse de 3p-AGNRs sur le substrat Cu(111) plus réactif et moins cher. Inspiré par l'effet catalytique de l'oxygène sur l'activation C-H, notre deuxième et plus grand objectif était d'étudier l'influence de l'oxygène sur la synthèse des 3p-AGNR sur Cu(111), dans laquelle la cyclodéshydrogénéation latérale est l'étape clé.

La voie de synthèse vers les AGNR est illustrée à la [Figure 7.8](#), où les chaînes OM peuvent être formées après le dépôt de DBTP (Br-(ph)₃-Br) à température ambiante sur Cu(111). Un recuit à 513 K pendant 20 min transforme les chaînes OM en 3-AGNR, qui subissent une cyclodéshydrogénéation latérale à 633 K pendant 20 min pour former des 3p-AGNR plus larges. Cependant, l'introduction de gaz O₂ après la formation de 3-AGNR permet à la fusion latérale de se dérouler à 453 K en 20 min, 180 K de moins qu'en l'absence d'oxygène.

Des images STM représentatives des différentes étapes de la synthèse des 3p-AGNR sur Cu(111) sont présentées à la [Figure 7.9](#), qui suit une voie de réaction similaire à celle sur Au(111).¹⁸⁰ Le dépôt de DBTP sur Cu(111) à température ambiante conduit à la formation de chaînes OM linéaires par liaison (ph)₃-Cu-(ph)₃ (voir [Figure 7.9a](#)). Le recuit à 513 K induit un couplage C-C en 3-AGNR, qui se terminent par des liaisons C-Cu résiduelles. Pour obtenir la diffusion des 3-AGNR et la cyclodéshydrogénéation latérale subséquente, nous avons progressivement augmenté la température de recuit. Comme le montrent les ellipses blanches de la [Figure 7.9c](#), des rubans plus larges (6-AGNR) commencent à se former par la fusion

latérale des 3-AGNR après recuit à 593 K. Une plus grande quantité de 3p-AGNR plus larges (dont 9-AGNR et 12-AGNR) sont synthétisés après chauffage de l'échantillon à 633 K (voir [Figure 7.9d](#)).

Une caractéristique inattendue de ces images STM est la hauteur et le contraste accrus qui peuvent être observés dans certains segments des rubans. Nous attribuons cela à l'intercalation d'atomes de Br sous les rubans, qui est étayée par l'apparence similaire de 3-AGNR observée au-dessus des atomes de Br entre deux 3-AGNR adjacents lors du recuit de l'échantillon à 533 K (encart sur la [Figure 7.9c](#)) et par des simulations STM ([Figure 7.9i](#)). En conséquence, les rubans avec des atomes de Br en dessous présentent des points périodiques brillants, tandis que les autres ont un aspect homogène comparativement plus sombre. Une variation similaire dans le contraste a été observée pour l'intercalation des atomes d'iode entre les polymères et Ag(111).¹⁰² Nous avons effectué des calculs de la théorie fonctionnelle de la densité (DFT) pour déterminer si l'intercalation du Br facilite la réaction de fusion latérale, en permettant aux 3-AGNR de traverser les rangées d'atomes de Br avant la fusion. Cependant, l'intercalation d'un seul atome de Br (pour trois monomères de phénylène) est endothermique de 2.1 eV ([Figure 7.9i-j](#)) et ne peut donc se produire que rarement avant la fusion latérale. Au lieu de cela, nous proposons que l'intercalation résulte du piégeage des atomes de Br pendant la réaction de fermeture éclair.

Pour étudier les effets de l'oxygène sur la synthèse des 3p-AGNR sur Cu(111), après la formation des 3-

Experimental

First row: without oxygen; second row: with oxygen

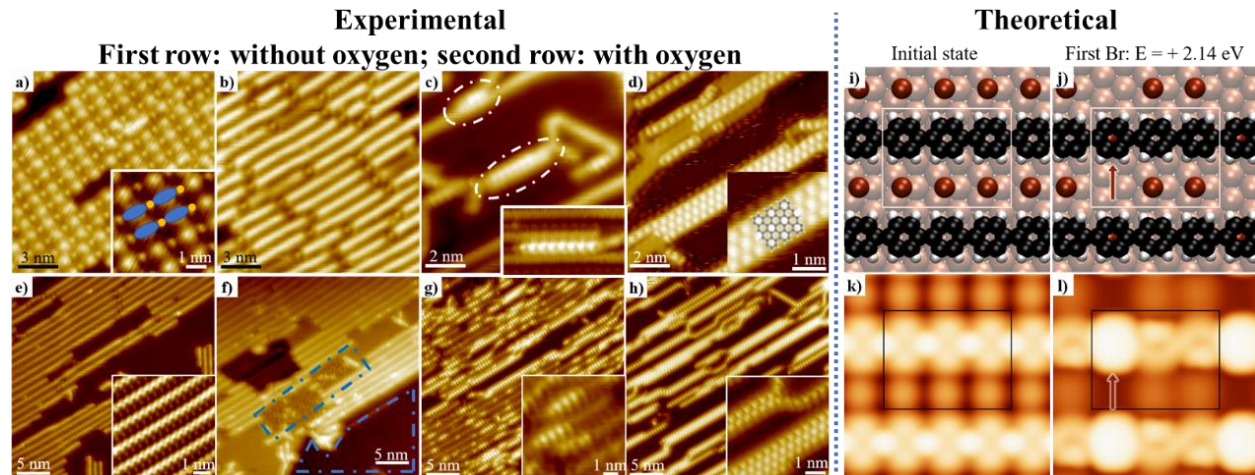


Figure 7.9 a)-d) Images LT STM ($T = 4.6$ K) de la synthèse de 3p-AGNRs sur Cu(111) à partir de la formation de chaînes OM. **e)-f)** Images LT STM de 3p-AGNR synthétisés sur Cu (111) avec introduction d' O_2 après la formation de 3-AGNR. **i)-j)** Structures calculées pour l'auto-assemblage initial des 3-AGNR et des atomes de Br (i) et après intercalation d'un atome de Br (j). **k)-l)** Images STM simulées pour les structures ci-dessus, montrant que le Br intercalé fait apparaître le phénylène supérieur brillant. Les rectangles noirs et blancs indiquent la supercellule. (couleurs des atomes: Br: rouge foncé, C: noir, H: blanc, Cu: marron clair)

AGNR ([Figure 7.9e](#)), O₂ a été dosé sur l'échantillon maintenu à 403 K pour former des zones de Cu oxydé ([Figure 7.9f](#)) ainsi que des îles vides de Cu sombres. La [Figure 7.9e](#) montre que les 3-AGNR restent intacts pendant l'exposition à l'O₂ et peuvent s'étendre à travers la surface nue et les domaines oxydés. Le chauffage à 423 K fait qu'un petit pourcentage de 3-AGNR présente un contraste accru, qui a été attribué au début de l'intercalation du Br. Nous considérons qu'il est peu probable que les atomes d'O intercalés soient la cause du contraste accru des rubans, car le plus petit atome d'O conduirait à une apparence des rubans significativement différente de celle de Br (ce qui est pris en charge par les simulations STM). Après recuit à 453 K, nous avons observé une augmentation substantielle du nombre de chaînes de 3-AGNR présentant un contraste élevé, et des parties des 3-AGNR s'étaient diffusées pour se rapprocher les unes des autres (voir [Figure 7.9g](#)). Un recuit supplémentaire à 453 K a donné une gamme d'AGNR avec des largeurs allant jusqu'à 12-AGNR, comme le montre la [Figure 7.9h](#), dans laquelle tous les rubans ont un aspect brillant et à contraste élevé. Par rapport au Cu(111) nu, l'introduction d'oxygène abaisse la température de formation des GNR d'environ 180 K. La [Figure 7.9h](#) montre également que les rubans plus larges sont formés en glissant deux rubans plus étroits, ce qui est similaire à ce qui est observé sur Au(111).

Pour soutenir l'effet catalytique de l'oxygène sur la synthèse des GNR et suivre les états chimiques de chaque élément tout au long des réactions, nous avons effectué des mesures XPS à partir du dépôt de DBTP. Les mesures XPS ont été effectuées dans un système combiné où la morphologie du même échantillon a également été mesurée par STM à température ambiante, garantissant que les états des polymères de surface étaient les mêmes pour les mesures XPS que les images LT STM illustrées à la [Figure 7.9](#).

Dans un premier temps, nous avons répété la synthèse des AGNR sans oxygène. Comme le montre la [Figure 7.10 a](#), le dépôt de DBTP à RT forme des chaînes OM présentant un large pic dans le spectre C 1s à une énergie de liaison (BE) de 284.6 eV. La transformation des chaînes OM en 3-AGNR par recuit à 513 K pendant 20 min induit un passage à un BE plus élevé de 284.8 eV, où la position du pic et le décalage vers le haut après le couplage C-C sont cohérents avec les résultats précédents.²⁰¹ À partir des mesures XPS et des images RT-STM, les 3-AGNR ne changent pas par recuit jusqu'à 573 K et des rubans plus larges se forment à 633 K. Le recuit à 633 K entraîne le retour du niveau de cœur de C 1 à un BE inférieur de 284,4 eV, ce qui pourrait résulter de deux effets possibles : l'un est la formation d'AGNR conjugués plus larges,

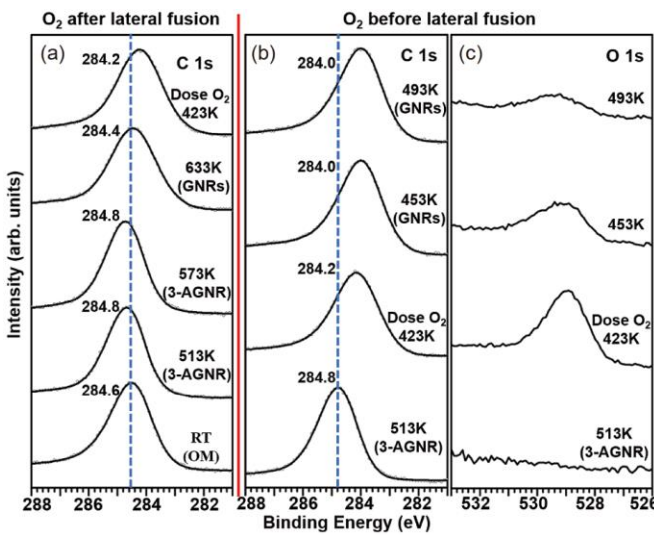


Figure 7. 10 a) Spectres XPS C 1s de la synthèse de 3p-AGNRs sur Cu(111) à des températures croissantes. **b, c)** Spectres XPS C 1s et O 1s de la synthèse de 3p-AGNR sur Cu(111) avec de l'oxygène introduit après la formation de 3-AGNR.

qui ont provoqué un décalage vers le haut du BE du spectre C 1s sur Au(111);²⁰² l'autre est l'intercalation des atomes de Br entre le polymère et le substrat, puisqu'un grand déplacement vers le bas du BE a été observé pour l'intercalation des atomes d'iode.¹⁰² En conséquence, nous attribuons la rétrogradation à 633 K à l'intercalation des atomes de Br.

Après la formation d'AGNR plus larges, nous avons dosé 60 L d'O₂ sur l'échantillon maintenu à 423 K pour évaluer si l'oxygène affectera les rubans et les atomes de Br. En conséquence, des parties des zones nues de Cu(111) sont oxydées et davantage d'atomes de Br s'intercalent entre les rubans et le substrat, ce qui entraîne un déplacement supplémentaire du niveau de noyau C 1s vers un BE inférieur de 284.2 eV.

Nous avons ensuite étudié l'effet de l'introduction d'O₂ avant la fusion latérale des 3-AGNR sur Cu(111) par XPS. Le recuit à 513 K conduit au même pic large pour les 3-AGNR au BE de 284.8 eV comme indiqué précédemment, et les mesures XPS O 1s correspondantes confirment l'absence d'oxygène à la surface. Le dosage d'O₂ sur l'échantillon maintenu à 423 K induit un grand décalage vers le bas (0.6 eV) du pic de C 1s, cohérent avec la diminution précédente attribuée au soulèvement des rubans par les atomes de Br. Le spectre O 1s après dosage ([Figure 7.10c](#), 423 K) est cohérent avec une faible couverture en Cu oxydé,²⁰³ ce qui implique l'absence de formation significative de liaisons C-O, comme en témoignent également les spectres C 1s. Les rubans plus larges se forment après le recuit de l'échantillon à 453 K, ce qui a induit plus d'intercalation d'atomes de Br et un autre déplacement vers le bas (0.2 eV) du niveau du noyau C 1s. Après recuit à 493 K, aucune différence significative dans les spectres XPS C 1s n'a pu être distinguée. Le recuit

à 453 K et 493 K provoque une diminution de l'intensité des spectres O 1s , attribuée à la désorption des atomes O, et un élargissement du pic vers une énergie de liaison plus élevée, qui est attribuée à un changement partiel de la phase Cu oxydée. Les spectres Br 3p ne montrent aucun changement évident par recuit ou dépôt d'oxygène, indiquant que l'intercalation n'affecte pas de manière significative l'état électronique des atomes de Br. Les mesures XPS sont cohérentes avec nos observations STM où l'introduction d'oxygène sur Cu(111) favorise la synthèse latérale d'AGNRs, ainsi que l'intercalation d'atomes de Br. De plus, l'absence de changement significatif dans les résultats STM et XPS suggère que les AGNR sont stables en présence d'oxygène jusqu'à au moins 493 K.

À partir des mesures STM et XPS, nous avons identifié que l'introduction d'O₂ favorisait l'intercalation des atomes de Br et la fusion latérale des 3-AGNR. Nous proposons que l'effet catalytique de l'oxygène dans la cyclodéshydrogénéation se fait par l'abstraction des atomes H des AGNR, similaire à l'activation du méthane par l'oxygène sur Cu(111).¹¹¹ Un deuxième mécanisme possible est que l'adsorption d'oxygène réduit l'espace disponible pour les 3-AGNR, les amenant à se rapprocher plus étroitement et donc à se cycliser plus facilement. Bien que l'oxygène favorise également la levée des 3-AGNR par les atomes de Br, il est peu probable que cela facilite la réaction de fusion latérale, qui devrait être initiée aux sites où l'AGNR est en contact avec la surface catalytique. La diffusion des atomes Br et O est rapide à 453 K, de sorte qu'une éventuelle amélioration de la diffusion par élimination des AGNR ne peut pas expliquer le taux considérablement plus élevé de fusion latérale en présence d'oxygène. Inspiré par l'interaction répulsive des atomes O chimisorbés sur Ag(111),²⁰⁴ nous proposons que l'intercalation des atomes de Br pourrait être entraînée par une interaction répulsive entre les atomes d'O et de Br sur Cu(111). L'élucidation du mécanisme détaillé de la fusion AGNR favorisée par l'oxygène et l'application de l'oxygène à la cyclodéshydrogénéation en général appelle à d'autres investigations expérimentales et théoriques approfondies.

En résumé, en combinant les mesures STM et XPS, nous avons systématiquement étudié la synthèse des 3p-AGNR sur Cu(111) et les effets de l'oxygène lors de la synthèse. Semblable au cas de Au(111), les 3p-AGNR peuvent être formés sur Cu(111) par fusion latérale de 3-AGNR après recuit à 633 K. Sur Cu(111), les rubans présentent un contraste accru, qui est attribué à l'intercalation des atomes de Br. L'introduction

d' O_2 permet la formation de 3p-AGNR à une température considérablement plus basse de 453 K, qui est attribuée à la catalyse de l'activation C-H, sans introduire de défauts ni affecter la longueur de l'AGNR. Nos résultats montrent que la réaction de fusion latérale peut être réalisée avec succès sur la surface Cu(111) plus réactive. L'effet catalytique de l' O_2 pourrait être bénéfique pour la synthèse du GNR et les réactions de cyclodéshydrogénéation en général.

7.2.3 Réaction de désulfuration en tandem/couplage C-C de tétrathienylbenzènes sur Cu(111) : synthèse de pentacène et d'un polymère en échelle exotique

La synthèse des nouvelles molécules et polymères conjugués de faible dimension a attiré énormément d'attention en raison de leurs propriétés uniques allant de la mobilité ultra-elevée des porteurs au magnétisme du carbone et aux états topologiques. Les réactions confinées en surface représentent une approche puissante pour synthétiser ces matériaux intrigants avec une précision atomique, mais la boîte à outils de réactions chimiques disponibles pour la synthèse en surface, et donc l'espace structurel des matériaux résultants, reste très limitée. De nouvelles chimies de couplage doivent être identifiées et affinées pour propulser ce domaine émergent vers des applications pratiques. En particulier, synthétiser à volonté une large gamme de nanomatériaux moléculaires nécessite de pouvoir réaliser des synthèses hiérarchisées combinant différentes réactions.

Dans les deux sections précédentes, nous nous sommes concentrés sur les recherches de couplage de type Ullmann, démontrant son potentiel pour produire des structures OM avec des dimensionnalités accordables et synthétiser des nanorubans de graphène sur la surface Cu(111). Dans ce chapitre, nous explorerons la désulfuration des dérivés du thiophène qui est une voie prometteuse et sous-explorée pour créer des carbones insaturés qui peuvent se coupler pour former des structures étendues. Comparé au couplage de type Ullmann, le couplage désulfuratif offre un accès à différents matériaux, car il implique la liaison d'alcènes plutôt que d'arènes.

Dans des travaux antérieurs, nous avons signalé une réaction confinée en surface sans analogue de la littérature, consistant en la formation de pentacène par couplage C-C intramoléculaire après la désulfuration d'une molécule de thiénoanthracène fusionnée ([Figure 7.11a](#)). Cependant, ce précurseur nécessite une

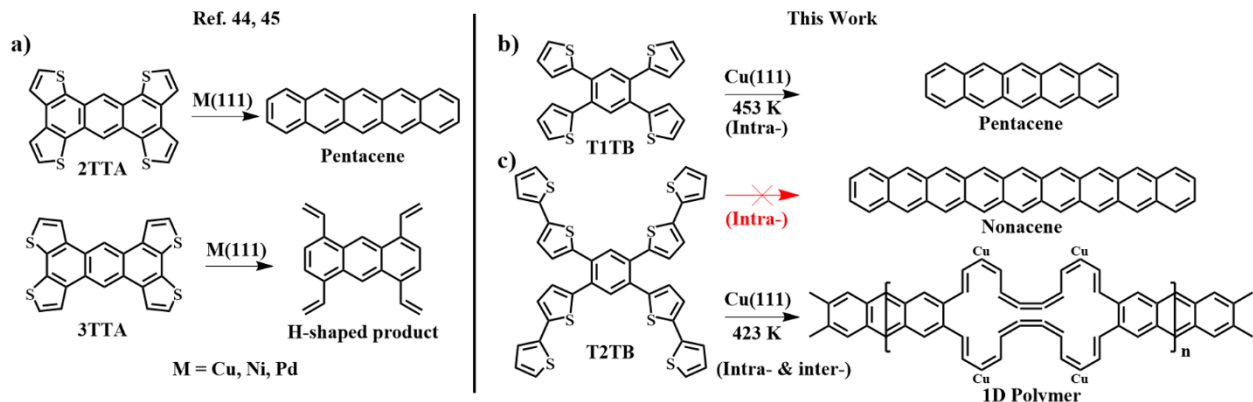


Figure 7.11 a) Réactions confinées en surface de molécules de tétrathiénoanthracène fusionnées sur différentes surfaces métalliques, produisant du pentacène ou des produits en forme de H. b) Réaction confinée en surface de T1TB produisant du pentacène sur Cu(111) et c) de T2TB produisant un polymère en échelle 1D au lieu de nonacène sur Cu(111).

synthèse en plusieurs étapes en solution et est fortement insoluble. Nous avons estimé que les précurseurs de tétrathiénylbenzène ([Figure 7.11b-c](#)) représentent des alternatives viables au tétrathiénoanthracène condensé pour former du pentacène et des acènes potentiellement plus longs, avec l'avantage d'une synthèse plus simple en solution.²³³

Dans cette section, nous rapportons le couplage intra- et intermoléculaire induit par la désulfuration sur Cu(111) de deux précurseurs de tétrathienylbenzène avec des nombres différents d'unités de thiophène. Les investigations ont été menées à l'aide de la microscopie à effet tunnel UHV (STM), de la spectroscopie photoélectronique à rayons X (XPS) et des calculs de la théorie fonctionnelle de la densité (DFT). Comme le montre la [Figure 7.11](#), le pentacène est formé par la désulfuration et la cyclisation intramoléculaire du 1,2,4,5-tétra(thién-2-yl)benzène (T1TB) sur Cu(111). Cependant, le nonacène ne se forme pas par cyclisation intramoléculaire répétée à partir du 1,2,4,5-tétrakis(2,2'-bithien-5-yl)benzène (T2TB) sur Cu(111). Au lieu de cela, des polymères en échelle unidimensionnels (1D) ordonnés composés d'une alternance de fragments anthracène et annulène fusionné sont obtenus par une combinaison de couplage C-C intra- et intermoléculaire. Le polymère 1D inattendu se distingue par sa structure en échelle exotique, qui n'était pas observée auparavant dans la polymérisation en solution ou en surface. Ce polymère présente des propriétés électroniques souhaitables, notamment une bande interdite étroite de 1.38 eV et une faible masse effective de porteurs de charge (0.18 m_e for the holes and 0.14 m_e for electrons) similaire à celle de nombreux GNR,^{121, 174} suggérant une applicabilité potentielle dans les dispositifs à semi-conducteurs.

Nous avons commencé notre étude en déposant T1TB sur Cu(111) à température ambiante (RT) et en recuit à 453 K pendant 15 minutes pour induire la réaction. Après dépôt, le spectre S 2p XPS ([Figure 7.12a](#)) montre deux doublets à 164.1 et 161.3 eV, qui peuvent être attribués respectivement aux liaisons C-S dans T1TB et Cu-S formées par ouverture du cycle thiophène. La faible étendue (20%) de la rupture de la liaison C-S à RT, déjà observée dans les travaux précédents,¹⁵⁴ peut être dû à l'impact de T1TB sur des bords de marche ou des adatomes hautement réactifs. Aucune caractéristique ne peut être discernée par STM à RT ([Figure 7.12e](#)), probablement en raison de la diffusivité élevée de T1TB sur Cu(111), qui a été précédemment observée pour des molécules TTA analogues sur Cu(111).²³¹ Le recuit séquentiel jusqu'à 453 K induit la désulfuration de la plupart des groupes thiophène dans T1TB, comme l'indique l'augmentation de la composante S-Cu à 161.3 eV. En conséquence, le pic C 1s ([Figure 7.12b](#)) se déplace vers le bas de 0.5 eV. Cependant, l'imagerie STM ne montre que des structures désordonnées et aucune caractéristique pouvant être identifiée comme du pentacène ([Figure 7.12f](#)).

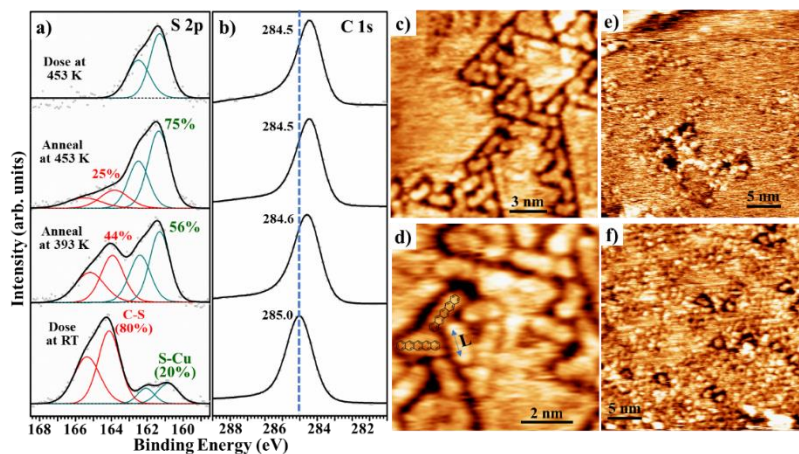


Figure 7. 12 a) S 2p et b) Spectres XPS C 1s obtenus lorsque T1TB a été déposé sur une surface Cu(111) maintenue à 453 K ou à température ambiante, suivi d'une séquence de recuit. c-d) Images STM du dépôt de T1TB sur Cu(111) maintenu à 453 K. La longueur crête à crête des structures en forme de bâtonnet (marquées par "L" en dessin de 1.04 ± 0.06 nm. e) Dépôt de T1TB sur Cu(111) à TA. f) Recuit de l'échantillon à 453 K, conduisant à la formation de monomères désordonnés isolés. (Pour toutes les images STM: $V_t = -1$ V, $I_t = 1$ nA)

Pour favoriser le couplage intramoléculaire par rapport au couplage intermoléculaire, T1TB a été déposé sur la surface de Cu(111) à 453 K. Les mesures XPS S 2p ne montrent que des atomes de soufre liés à la surface, indiquant une ouverture et une désulfuration complètes des anneaux de thiophène. Les images STM de la [Figure 7.12c-d](#) montrent des structures en forme de tige dont l'apparence et la longueur ([Figure 7.12d](#)) sont cohérentes avec les observations précédentes sur le pentacène sur Cu(111).²³⁴ De plus, les mêmes

caractéristiques en forme de bâtonnet de 1.04 ± 0.06 nm de longueur ont été précédemment observées à partir de 2TTA et identifiées comme du pentacène.²³¹

Pour voir si des acènes supérieurs pouvaient être formés par une cascade d'étapes multiples de désulfuration et de cyclisation intramoléculaire, nous avons synthétisé un précurseur étendu (T2TB) avec quatre bras de bithiophène. Le dépôt de T2TB sur Cu(111) à température ambiante entraîne une ouverture partielle du cycle thiophène. Le spectre S 2p XPS de la [Figure 7.13a](#) montre deux larges pics S 2p à 164.1 eV et 161.3 eV, indiquant une désulfuration d'environ 55 % des cycles thiophène. Comme c'était le cas pour le T1TB, aucune caractéristique ordonnée ou aucune molécule T2TB intacte n'a pu être observée par STM. Le recuit de l'échantillon à 393 K augmente l'étendue de la désulfuration à environ 80 % et induit une conversion supplémentaire des liaisons C-S en C-C, et en même temps le pic C 1s passe de 284.6 à 284.4 eV ([Figure 7.13b](#)). L'image STM montre des structures désordonnées couplées de manière aléatoire, mais aucun produit ordonné.

Comme dans le cas de T1TB, T2TB a été déposé sur la surface de Cu(111) à des températures élevées pour favoriser la réaction intramoléculaire. D'après les mesures XPS illustrées à la [Figure 7.13a-b](#), le dépôt

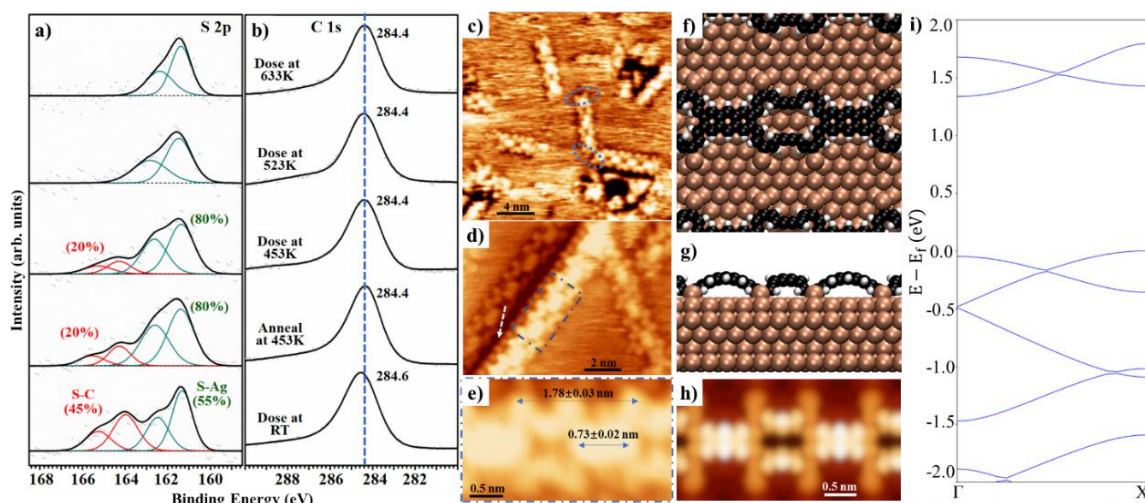


Figure 7. 13 a) S 2p et **b)** Spectres XPS C 1s obtenus lorsque T2TB a été déposé sur une surface Cu(111) maintenue à 393, 473 et 573 K, ou à RT suivi d'un recuit à 393 K. **ce)** Vue d'ensemble et images STM agrandies après dépôt T2TB sur Cu(111) maintenu à 393 K. Les ellipses bleues en (c) indiquent le carbone non couplé à l'extrémité des chaînes qui pourrait être saturé par les atomes de la surface. Pour toutes les images STM: $V_t = -1$ V, $I_t = 1$ nA) **f-g)** Vue de dessus et de côté du modèle optimisé DFT. (marron: cuivre, noir: carbone, blanc: hydrogène) **h)** Image STM simulée par DFT correspondante. **i)** Structure de bande électronique calculée pour le polymère 1D autonome où les adatomes de Cu sont remplacés par des atomes de H.

de T2TB sur Cu(111) à 393 K conduit à une mesure similaire de désulfuration (80 %) et à la position du pic C 1s (284.4 eV) comme recuit à 393 K après dépôt RT. La désulfuration est presque complète lorsque T2TB est déposé sur Cu(111) à 473 K, tandis que la rupture complète de la liaison CS peut être obtenue en déposant T2TB sur Cu(111) maintenu à 573 K. Pour 473 K et 573 K, le C 1s le pic est toujours au même BE de 284.4 eV.

Bien que les mesures XPS ne présentent aucune différence significative entre le dépôt de substrat chaud à 393 K et le dépôt RT suivi d'un recuit ultérieur à 393 K, une nette différence est observée dans les images STM. Le dépôt de T2TB à 393 K conduit à des structures 1D ordonnées composées de segments droits alternés reliés par des chaînes courbes ([Figure 7.13c-e](#)), en contraste frappant avec les structures désordonnées obtenues par recuit à 393 K. Ces structures sont alignées avec les directions de haute symétrie du substrat. La longueur de leur cellule unitaire (marquée par la longue flèche sur la [Figure 7.13e](#)) est de 1.78 ± 0.05 nm, ce qui correspond à 7 atomes de Cu (1.78 nm) dans les directions compactes <110> de Cu(111). De petites caractéristiques rondes régulières peuvent être observées à côté des structures 1D le long du bord de la marche (marquées par une flèche blanche sur la [Figure 7.13d](#)), que nous attribuons aux atomes de soufre dissociés, conformément à une étude précédente sur l'adsorption d'atomes de S sur Cu(111).²³⁵

Pour élucider la structure chimique de ces chaînes 1D, nous avons mesuré la longueur des segments droits (marqués par la flèche courte sur la [Figure 7.13e](#)) à 0.73 ± 0.06 nm, ce qui coïncide avec la dimension des fragments anthracène intermédiaires attendus (0.72 nm). L'ouverture du cycle et la désulfuration des cycles thiophène adjacents au noyau benzénique du T2TB devraient déclencher une cyclisation C-C intramoléculaire, entraînant la fusion de deux nouveaux cycles benzéniques avec le fragment central, comme observé pour le T1TB (ainsi que pour les molécules 2TTA^{230, 231}). Cependant, contrairement à nos attentes initiales, aucune autre cyclisation intramoléculaire due à la désulfuration des anneaux thiophène terminaux n'a lieu. Au lieu de cela, les quatre chaînes hexatriènes restantes subissent un couplage intermoléculaire pour "assembler" les fragments anthracènes dans une chaîne polymère en échelle, via des macrocycles géants (28 atomes de carbone).

Nous avons effectué des calculs DFT pour déterminer la géométrie d'adsorption de ce polymère en échelle. La Figure 7.13f-g montre la structure qui donne le meilleur accord avec l'expérience, qui est symétrique et alignée avec les directions de haute symétrie de la surface Cu(111). Le polymère proposé est composé d'anthracènes condensés alternés et de cycles [28]-annulène, dans lesquels quatre atomes de carbone sont liés à des atomes de Cu externes. La simulation STM correspondante (Figure 7.13h) concorde bien avec les principales caractéristiques des images STM, en particulier le segment anthracène brillant et le motif des chaînes de connexion courbes.

Nous avons exploré les propriétés électroniques et le degré de conjugaison de ce nouveau polymère en échelle 1D en utilisant DFT (HSE06 fonctionnel) pour le polymère détendu et autonome dans lequel les atomes de Cu ont été remplacés par de l'hydrogène. La structure des bandes (Figure 7.13i) révèle des bandes dispersives le long du squelette carboné et une bande interdite directe de 1.38 eV. Les dispersions de bande importantes, en particulier pour la bande de conduction (à 1.38 eV), indiquent une π -conjugaison à travers ce polymère en échelle 1D. De même, les masses effectives des bandes frontières ($0.18 m_e$ for holes and $0.14 m_e$ for electrons) sont faibles et dans la gamme mesurée pour de nombreux GNR (cf., 0.40, 0.10 et $0.14 m_e$ pour GNR 7, 9 fauteuils et GNR 12 zigzag respectivement).^{121, 174, 181} La combinaison d'une bande interdite adaptée aux dispositifs et de faibles masses effectives est prometteuse pour les applications de dispositifs optoélectroniques et semi-conducteurs.^{239, 240}

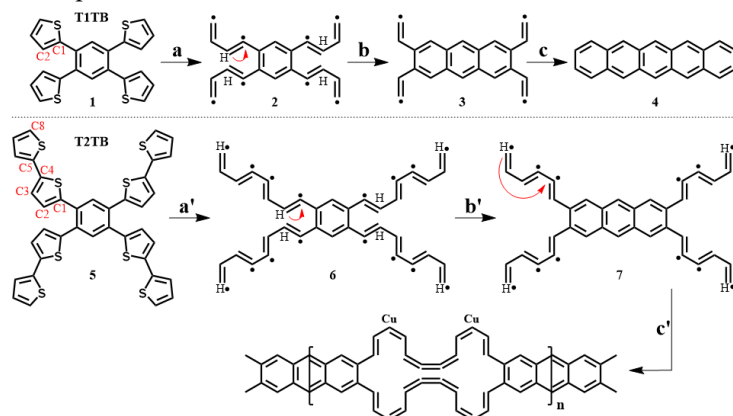


Figure 7. 14 Modèles squelettiques proposés des voies de réaction pour la transformation du T1TB en pentacène et du T2TB en polymère étendu 1D. (a, a': désulfuration; b, b': transfert d'hydrogène (C2 vers C1) et cyclisation intramoléculaire; c: poursuite de la cyclisation intramoléculaire; c': poursuite du transfert d'hydrogène (C8 vers C4) et cyclisation intermoléculaire). Les flèches rouges montrent le transfert d'hydrogène. '*' Indique des électrons non appariés (stabilisés par liaison à Cu), formés après désulfuration. Seuls les hydrogènes subissant le déplacement au cours de la réaction sont représentés.

Pour aborder l'origine des voies de réaction divergentes entre T1TB et T2TB sur Cu(111), nous proposons le schéma de réaction étape par étape ([Figure 7.14](#)). La principale différence de comportement de ces deux précurseurs analogues est la compétition entre le couplage C-C intramoléculaire et intermoléculaire après désulfuration. La désulfuration de T1TB donne quatre chaînes de butadiène, chacune avec deux liaisons pendantes, attachées au noyau benzénique (étape a). À l'étape suivante b, l'hydrogène passe de C2 à C1 (décalage 1,2), ce qui permet une cyclisation intramoléculaire à travers C2 formant un cycle anthracène. Les quatre radicaux vinylène restants dans l'intermédiaire 3 peuvent basculer et se coupler les uns aux autres pour former deux autres cycles benzéniques, ce qui donne un fragment pentacène, comme le montre l'étape c. Dans le cas du T2TB, les étapes a' et b' sont identiques à a et b, entraînant la formation du cycle anthracène. Cependant, les chaînes hexatriène plus longues sur l'intermédiaire anthracène 7 sont plus fortement liées à la surface, ce qui limite la cascade supplémentaire de cyclisation qui pourrait autrement produire du nonacène. Ces chaînes de molécules adjacentes pourraient toutefois subir un couplage intermoléculaire pour former un polymère en échelle 1D exotique, comme indiqué à l'étape c'.

Nous avons ensuite étudié le comportement de T2TB sur des substrats moins réactifs, à savoir Ag(111) et Au(111), avec la même procédure que sur Cu(111). Les mesures STM et XPS sur Ag(111) montrent que la désulfuration ne conduit qu'à des réseaux désordonnés de type polymère. Nous attribuons l'observation d'un polymère échelle 1D ordonné sur Cu(111) à un registre molécule-substrat favorable qui est particulier au réseau Cu(111). La réactivité de Au(111) s'est avérée trop faible pour catalyser la désulfuration, car aucune réaction n'a été observée par XPS pour le dépôt de T2TB à des températures de substrat allant jusqu'à 623 K.

En un mot, nous avons étudié les réactions confinées en surface de deux homologues de tétrathiénylbenzène (T1TB et T2TB) sur des surfaces métalliques de monnaie à l'aide de calculs STM, XPS et DFT. L'ouverture du cycle thiophène se produit lorsque T1TB est déposé sur Cu(111) à 453 K, entraînant la transformation en pentacène par cyclisation intramoléculaire. Cependant, lorsque T2TB est déposé sur du Cu(111) chaud (343-493 K), la désulfuration est suivie d'un tandem de réactions de couplage C-C: une cyclisation intramoléculaire formant un cycle anthracène et un couplage intermoléculaire des chaînes carbonées restantes. Cela conduit à la formation de polymères étendus 1D dont les structures chimiques et

électroniques ont été identifiées grâce à une combinaison d'imagerie STM et de calculs DFT. C'est-à-dire que la voie de réaction peut être dirigée par l'ajout d'un groupe thiophène dans le précurseur sans modifier la structure et la symétrie du noyau. La transformation de T2TB en polymère 1D n'a pas été observée sur Ag(111) et Au(111), indiquant la nature cruciale du substrat pour cette réaction.

7.3 Conclusions et perspectives

Nous avons systématiquement étudié les effets du dosage de l'oxygène sur le couplage de type Ullmann confiné en surface en introduisant des atomes d'oxygène chimisorbés avant ou après le dépôt de deux précurseurs halogénés (DBTP et dBB) sur deux surfaces de cuivre de symétries différentes, Cu(111) et Cu(100). En conséquence, nous avons réalisé la transformation structurelle des chaînes OM 1D en réseaux OM 2D liés par des clusters Cu-O. De plus, la taille et la symétrie de ces réseaux OM 2D nouvellement formés peuvent être contrôlées de manière rationnelle en ajustant la longueur des précurseurs halogénés et la symétrie du substrat. En plus de faciliter la compréhension fondamentale du couplage de type Ullmann confiné en surface, ce travail fournit une nouvelle méthode pour piloter les réactions confinées en surface et donc synthétiser des nanostructures de faible dimension avec des structures chimiques et électroniques accordables.

Sur la base de l'étude du couplage de type Ullmann confiné en surface avec le précurseur DBTP, nous avons étudié plus avant la synthèse des GNR à bords de fauteuil sur Cu(111) et les effets de l'oxygène co-adsorbé sur cette synthèse. En l'absence d'oxygène, le recuit des chaînes OM entraîne la formation de 3-AGNR. De plus, nous avons démontré qu'un recuit plus élevé peut induire la fusion latérale de 3-AGNR, conduisant à la formation de 3p-AGNR plus larges. Dans l'intervalle, nous avons observé l'intercalation d'atomes de Br dissociés entre les rubans et le substrat, qui a été attribuée au piégeage des atomes de Br lors de la fusion latérale. Lorsque l'oxygène a été introduit après la formation de 3-AGNR, les 3p-AGNR plus larges peuvent être formés par recuit à 453 K, soit 180 K de moins qu'en l'absence d'oxygène. Ceci suggère un effet catalytique de l'oxygène dans l'activation des liaisons C-H lors de la cyclodéshydrogénélation latérale. Nous espérons que ce travail contribuera à la synthèse en surface de plus de nanomatériaux impliquant la réaction de déshydrogénération en général.

Outre le couplage de type Ullmann, nous avons étudié la réaction de désulfuration des dérivés du thiophène pour explorer ses potentiels dans la synthèse de polymères conjugués. En utilisant UHV-STM et XPS, soutenus par des calculs DFT, nous avons démontré la formation de pentacène par la cyclisation intramoléculaire de T1TB sur Cu(111). Cependant, le nonacène ne se forme pas par cyclisation intramoléculaire répétée à partir de T2TB sur Cu(111). Au lieu de cela, des polymères en échelle unidimensionnels ordonnés composés d'une alternance de fragments anthracène et annulène fusionné sont produits par une combinaison de couplage C-C intra- et intermoléculaire. Ce polymère 1D inattendu se distingue par ses propriétés électroniques favorables et sa structure en échelle exotique qui n'a pas été observée auparavant dans la solution ou la polymérisation confinée en surface. Notre recherche fournit de nouvelles informations sur les voies des réactions de couplage par ouverture de cycle en surface, un outil prometteur mais sous-exploré de la chimie synthétique en surface. De plus, la désulfuration du thiophène pourrait être combinée à d'autres réactions pour élargir considérablement les nanomatériaux de carbone possibles grâce à la synthèse en surface. Des travaux futurs sont nécessaires pour comprendre l'interaction entre le couplage molécule-molécule et le rôle de la surface pour parvenir à la conception rationnelle souhaitée de nanostructures de carbone de faible dimension avec des propriétés électroniques intrigantes.

7.4 Projets futurs

D'une part, nous avons démontré la transformation 1D à 2D induite par l'oxygène des structures OM. D'autre part, certains gaz réducteurs (CO ou H₂) pourraient être utilisés pour éliminer les sous-produits indésirables sur les surfaces. Par conséquent, nous prévoyons d'utiliser H₂ ou CO pour éliminer les atomes O dans les réseaux 2DOM. Nous nous attendons à ce que les réseaux 2DOM se transforment en chaînes 1DOM vierges, ce qui représente une transformation réversible. Le contrôle de l'équilibre d'une réaction réversible serait un outil essentiel pour réaliser des 2DOM ordonnés à longue portée.

Pour réaliser la transformation des 2DOM en polymères π -conjugués 2D plus robustes (2DCPs) après l'élimination de l'O, une solution prometteuse consiste à introduire des groupes acétylène aux sites terminaux du précurseur. Comme indiqué, le précurseur fonctionnalisé avec des groupes acétylène peut se coupler à une structure de noyau aromatique qui est le seul cas susceptible de former des 2DCPs.¹⁸ Pour

contraindre les réactions à se poursuivre vers la formation d'une structure de noyau aromatique, nous ajouterions des atomes d'halogène avec les groupes acétylène. Par conséquent, les réseaux 2DOM avec des groupes acétylène et des clusters Cu_xO aux nœuds de connexion se formeraient initialement, ce qui peut en outre servir de modèle pour diriger la formation de 2DCPs après la suppression de O.

En suivant la même stratégie, nous étudierons plus en détail le transfert chiral (transfert de chiralité diverse vers la chiralité diversifiée ou uniforme correspondante) de 2DOM à 2DCP sur Cu(100). Nous prévoyons que de telles études pourraient fournir des informations fondamentales sur la synthèse organique asymétrique, ce qui est particulièrement important dans l'industrie pharmaceutique où la plupart des nouveaux médicaments sont développés sous forme d'énanthiomères purs.

References

1. Talirz, L.; Ruffieux, P.; Fasel, R., On-surface synthesis of atomically precise graphene nanoribbons. *Adv. Mater.* **2016**, 28, 6222-6231.
2. Wang, H.; Wang, H. S.; Ma, C.; Chen, L.; Jiang, C.; Chen, C.; Xie, X.; Li, A.-P.; Wang, X., Graphene nanoribbons for quantum electronics. *Nat. Rev. Phys.* **2021**, 3, 791-802.
3. Perepichka, D. F.; Rosei, F., Extending polymer conjugation into the second dimension. *Science* **2009**, 323, 216-217.
4. Lipton-Duffin, J.; Miwa, J.; Kondratenko, M.; Ciciora, F.; Sumpter, B.; Meunier, V.; Perepichka, D.; Rosei, F., Step-by-step growth of epitaxially aligned polythiophene by surface-confined reaction. *PNAS* **2010**, 107, 11200-11204.
5. Dong, L.; Liu, P. N.; Lin, N., Surface-activated coupling reactions confined on a surface. *Acc. Chem. Res.* **2015**, 48, 2765-2774.
6. Zhang, H.; Chi, L., Gold–Organic Hybrids: On-Surface Synthesis and Perspectives. *Adv. Mater.* **2016**, 28, 10492-10498.
7. Ebrahimi, M.; Rosei, F., Materials science: Organic analogues of graphene. *Nature* **2017**, 542, 423-424.
8. Goronzy, D.; Ebrahimi, M.; Rosei, F.; Arramel; Fang, Y.; De Feyter, S.; Tait, S. L.; Wang, C.; Beton, P. H.; Wee, A. T.; Weiss, P. S.; Perepichka, D. F., Supramolecular Assemblies on Surfaces: Nanopatterning, Functionality, and Reactivity. *ACS Nano* **2018**, 12, 7445-7481.
9. Clair, S.; de Oteyza, D. G., Controlling a chemical coupling reaction on a surface: tools and strategies for on-surface synthesis. *Chem. Rev.* **2019**, 119, 4717-4776.
10. MacLean, O.; Rosei, F., Two-dimensional polymers grow up. *Science* **2019**, 366, 1308-1309.
11. Cui, D.; Perepichka, D. F.; MacLeod, J. M.; Rosei, F., Surface-confined single-layer covalent organic frameworks: design, synthesis and application. *Chem. Soc. Rev.* **2020**, 49, 2020-2038.
12. Grill, L.; Hecht, S., Covalent on-surface polymerization. *Nat. Chem.* **2020**, 12, 115-130.
13. Glaser, C., Beiträge zur kenntniss des acetylenylbenzols. *Berichte der deutschen chemischen Gesellschaft* **1869**, 2, 422-424.
14. Hay, A. S., Oxidative coupling of acetylenes. II1. *J. Org. Chem.* **1962**, 27, 3320-3321.
15. Sun, K.; Nishiuchi, T.; Sahara, K.; Kubo, T.; Foster, A. S.; Kawai, S., Low-Temperature Removal of Dissociated Bromine by Silicon Atoms for an On-Surface Ullmann Reaction. *J. Phys. Chem. C* **2020**, 124, 19675-19680.
16. Zhang, Y.-Q.; Kepčija, N.; Kleinschrodt, M.; Diller, K.; Fischer, S.; Papageorgiou, A. C.; Allegretti, F.; Björk, J.; Klyatskaya, S.; Klappenberger, F., Homo-coupling of terminal alkynes on a noble metal surface. *Nat. Commun.* **2012**, 3, 1-8.
17. Gao, H. Y.; Wagner, H.; Zhong, D.; Franke, J. H.; Studer, A.; Fuchs, H., Glaser coupling at metal surfaces. *Angew. Chem. Int. Ed.* **2013**, 52, 4024-4028.
18. Gao, H.-Y.; Franke, J. r.-H.; Wagner, H.; Zhong, D.; Held, P.-A.; Studer, A.; Fuchs, H., Effect of metal surfaces in on-surface glaser coupling. *J. Phys. Chem. C* **2013**, 117, 18595-18602.
19. Zhong, D.; Franke, J.-H.; Podiyannachari, S. K.; Blömker, T.; Zhang, H.; Kehr, G.; Erker, G.; Fuchs, H.; Chi, L., Linear alkane polymerization on a gold surface. *Science* **2011**, 334, 213-216.

20. Sun, K.; Chen, A.; Liu, M.; Zhang, H.; Duan, R.; Ji, P.; Li, L.; Li, Q.; Li, C.; Zhong, D.; Müllen, K.; Chi, L., Surface-Assisted Alkane Polymerization: Investigation on Structure–Reactivity Relationship. *J. Am. Chem. Soc.* **2018**, *140*, 4820-4825.
21. Zhang, J.; Chang, C. r.; Yang, B.; Cao, N.; Peng, C.; Zhang, H.; Tang, D. T. D.; Glorius, F.; Erker, G.; Fuchs, H., Step-Edge Assisted Direct Linear Alkane Coupling. *Chem. Eur. J* **2017**, *23*, 6185-6189.
22. Li, X.; Yadav, P.; Loh, K. P., Function-oriented synthesis of two-dimensional (2D) covalent organic frameworks—from 3D solids to 2D sheets. *Chem. Soc. Rev.* **2020**, *49*, 4835-4866.
23. Weigelt, S.; Busse, C.; Bombis, C.; Knudsen, M. M.; Gothelf, K. V.; Strunskus, T.; Wöll, C.; Dahlbom, M.; Hammer, B.; Lægsgaard, E., Covalent interlinking of an aldehyde and an amine on a Au (111) surface in ultrahigh vacuum. *Angew. Chem. Int. Ed.* **2007**, *46*, 9227-9230.
24. Weigelt, S.; Busse, C.; Bombis, C.; Knudsen, M. M.; Gothelf, K. V.; Lægsgaard, E.; Besenbacher, F.; Linderoth, T. R., Surface synthesis of 2D branched polymer nanostructures. *Angew. Chem. Int. Ed.* **2008**, *47*, 4406-4410.
25. Gong, Z.; Yang, B.; Lin, H.; Tang, Y.; Tang, Z.; Zhang, J.; Zhang, H.; Li, Y.; Xie, Y.; Li, Q., Structural variation in surface-supported synthesis by adjusting the stoichiometric ratio of the reactants. *ACS Nano* **2016**, *10*, 4228-4235.
26. Jiang, L.; Papageorgiou, A. C.; Oh, S. C.; Sağlam, O. z.; Reichert, J.; Duncan, D. A.; Zhang, Y.-Q.; Klappenberger, F.; Guo, Y.; Allegretti, F., Synthesis of pyrene-fused pyrazaacenes on metal surfaces: toward one-dimensional conjugated nanostructures. *ACS Nano* **2016**, *10*, 1033-1041.
27. Bilbao, N.; Yu, Y.; Verstraete, L.; Lin, J.; Lei, S.; De Feyter, S., The impact of grafted surface defects on the on-surface Schiff-base chemistry at the solid–liquid interface. *Chem. Commun.* **2018**, *54*, 9905-9908.
28. Ullmann, F.; Bielecki, J., Ueber synthesen in der biphenylreihe. *Berichte der deutschen chemischen Gesellschaft* **1901**, *34*, 2174-2185.
29. Ullmann, F., Ueber eine neue Bildungsweise von Diphenylaminderivaten. *Berichte der deutschen chemischen Gesellschaft* **1903**, *36*, 2382-2384.
30. Ullmann, F.; Sponagel, P., Ueber die phenylierung von phenolen. *Berichte der deutschen chemischen Gesellschaft* **1905**, *38*, 2211-2212.
31. Weingarten, H., Mechanism Of The Ullmann Condensation1. *J. Org. Chem.* **1964**, *29*, 3624-3626.
32. Bunnett, J. F.; Kim, J. K., Evidence for a radical mechanism of aromatic" nucleophilic" substitution. *J. Am. Chem. Soc.* **1970**, *92*, 7463-7464.
33. Jenkins, C.; Kochi, J., Homolytic and ionic mechanisms in the ligand-transfer oxidation of alkyl radicals by copper (II) halides and pseudohalides. *J. Am. Chem. Soc.* **1972**, *94*, 856-865.
34. Xi, M.; Bent, B. E., Iodobenzene on Cu (111): formation and coupling of adsorbed phenyl groups. *Surf. Sci.* **1992**, *278*, 19-32.
35. Xi, M.; Bent, B. E., Mechanisms of the Ullmann coupling reaction in adsorbed monolayers. *J. Am. Chem. Soc.* **1993**, *115*, 7426-7433.
36. Hla, S.-W.; Bartels, L.; Meyer, G.; Rieder, K.-H., Inducing all steps of a chemical reaction with the scanning tunneling microscope tip: towards single molecule engineering. *Phys. Rev. Lett.* **2000**, *85*, 2777.
37. Grill, L.; Dyer, M.; Lafferentz, L.; Persson, M.; Peters, M. V.; Hecht, S., Nano-architectures by covalent assembly of molecular building blocks. *Nat. Nanotechnol.* **2007**, *2*, 687.
38. Lipton-Duffin, J. A.; Ivasenko, O.; Perepichka, D. F.; Rosei, F., Synthesis of polyphenylene molecular

- wires by surface-confined polymerization. *Small* **2009**, *5*, 592-597.
39. Cai, J.; Ruffieux, P.; Jaafar, R.; Bieri, M.; Braun, T.; Blankenburg, S.; Muoth, M.; Seitsonen, A. P.; Saleh, M.; Feng, X.; Müllen, K.; Fasel, R., Atomically precise bottom-up fabrication of graphene nanoribbons. *Nature* **2010**, *466*, 470.
40. Di Giovannantonio, M.; El Garah, M.; Lipton-Duffin, J.; Meunier, V.; Cardenas, L.; Fagot Revurat, Y.; Cossaro, A.; Verdini, A.; Perepichka, D. F.; Rosei, F., Insight into organometallic intermediate and its evolution to covalent bonding in surface-confined Ullmann polymerization. *ACS Nano* **2013**, *7*, 8190-8198.
41. Sambiagio, C.; Marsden, S. P.; Blacker, A. J.; McGowan, P. C., Copper catalysed Ullmann type chemistry: from mechanistic aspects to modern development. *Chem. Soc. Rev.* **2014**, *43*, 3525-3550.
42. Ruffieux, P.; Wang, S.; Yang, B.; Sánchez-Sánchez, C.; Liu, J.; Dienel, T.; Talirz, L.; Shinde, P.; Pignedoli, C. A.; Passerone, D.; Dumslaff, T.; Feng, X.; Müllen, K.; Fasel, R., On-surface synthesis of graphene nanoribbons with zigzag edge topology. *Nature* **2016**, *531*, 489.
43. Vasseur, G.; Fagot-Revurat, Y.; Sicot, M.; Kierren, B.; Moreau, L.; Malterre, D.; Cardenas, L.; Galeotti, G.; Lipton-Duffin, J.; Rosei, F.; Di Giovannantonio, M.; Contini, G.; Le Fèvre, P.; Bertran, F.; Liang, L.; Meunier, V.; F. Perepichka, D., Quasi one-dimensional band dispersion and surface metallization in long-range ordered polymeric wires. *Nat. Commun.* **2016**, *7*, 10235.
44. Lackinger, M., Surface-assisted Ullmann coupling. *Chem. Commun.* **2017**, *53*, 7872-7885.
45. Galeotti, G.; De Marchi, F.; Hamzehpoor, E.; MacLean, O.; Rao, M. R.; Chen, Y.; Besteiro, L.; Dettmann, D.; Ferrari, L.; Frezza, F.; Sheverdyaeva, P.; Liu, R.; Kundu, A.; Moras, P.; Ebrahimi, M.; Gallagher, M.; Rosei, F.; Perepichka, D. F.; Contini, G., Synthesis of mesoscale ordered two-dimensional π -conjugated polymers with semiconducting properties. *Nat. Mater.* **2020**, *19*, 874-880.
46. Bronner, C.; Marangoni, T.; Rizzo, D. J.; Durr, R. A.; Jørgensen, J. H.; Fischer, F. R.; Crommie, M. F., Iodine versus bromine functionalization for bottom-up graphene nanoribbon growth: role of diffusion. *J. Phys. Chem. C* **2017**, *121*, 18490-18495.
47. Galeotti, G.; Di Giovannantonio, M.; Lipton-Duffin, J.; Ebrahimi, M.; Tebi, S.; Verdini, A.; Floreano, L.; Fagot-Revurat, Y.; Perepichka, D. F.; Rosei, F.; Contini, G., The role of halogens in on-surface Ullmann polymerization. *Faraday Discuss.* **2017**, *204*, 453-469.
48. Di Giovannantonio, M.; Deniz, O.; Urgel, J. I.; Widmer, R.; Dienel, T.; Stoltz, S.; Sánchez-Sánchez, C.; Muntwiler, M.; Dumslaff, T.; Berger, R., On-Surface Growth Dynamics of Graphene Nanoribbons: The Role of Halogen Functionalization. *ACS Nano* **2018**, *12*, 74-81.
49. Kawai, S.; Nakatsuka, S.; Hatakeyama, T.; Pawlak, R.; Meier, T.; Tracey, J.; Meyer, E.; Foster, A. S., Multiple heteroatom substitution to graphene nanoribbon. *Sci. Adv.* **2018**, *4*, eaar7181.
50. Wang, W.; Shi, X.; Wang, S.; Van Hove, M. A.; Lin, N., Single-molecule resolution of an organometallic intermediate in a surface-supported Ullmann coupling reaction. *J. Am. Chem. Soc.* **2011**, *133*, 13264-13267.
51. Fan, Q.; Wang, C.; Han, Y.; Zhu, J.; Kuttner, J.; Hilt, G.; Gottfried, J. M., Surface-assisted formation, assembly, and dynamics of planar organometallic macrocycles and zigzag shaped polymer chains with C–Cu–C bonds. *ACS Nano* **2013**, *8*, 709-718.
52. Fan, Q.; Liu, L.; Dai, J.; Wang, T.; Ju, H.; Zhao, J.; Kuttner, J.; Hilt, G.; Gottfried, J. M.; Zhu, J., Surface Adatom Mediated Structural Transformation in Bromoarene Monolayers: Precursor Phases in Surface Ullmann Reaction. *ACS Nano* **2018**, *12*, 2267-2274.

53. Galeotti, G.; Di Giovannantonio, M.; Cupo, A.; Xing, S.; Lipton-Duffin, J.; Ebrahimi, M.; Vasseur, G.; Kierren, B.; Fagot-Revurat, Y.; Tristant, D.; Meunier, V.; Perepichka, D. F.; Rosei, F.; Contini, G., An unexpected organometallic intermediate in surface-confined Ullmann coupling. *Nanoscale* **2019**, 11, 7682-7689.
54. Ji, P.; Galeotti, G.; De Marchi, F.; Cui, D.; Sun, K.; Zhang, H.; Contini, G.; Ebrahimi, M.; MacLean, O.; Rosei, F.; Chi, L., Oxygen-Induced 1D to 2D Transformation of On-Surface Organometallic Structures. *Small* **2020**, 16, 2002393.
55. Judd, C. J.; Haddow, S. L.; Champness, N. R.; Saywell, A., Ullmann coupling reactions on Ag (111) and Ag (110); substrate influence on the formation of covalently coupled products and intermediate metal-organic structures. *Sci. Rep.* **2017**, 7, 1-7.
56. Lafferentz, L.; Eberhardt, V.; Dri, C.; Africh, C.; Comelli, G.; Esch, F.; Hecht, S.; Grill, L., Controlling on-surface polymerization by hierarchical and substrate-directed growth. *Nat. Chem.* **2012**, 4, 215-220.
57. Eichhorn, J.; Nieckarz, D.; Ochs, O.; Samanta, D.; Schmittel, M.; Szabelski, P. J.; Lackinger, M., On-surface Ullmann coupling: the influence of kinetic reaction parameters on the morphology and quality of covalent networks. *ACS Nano* **2014**, 8, 7880-7889.
58. Steiner, C.; Gebhardt, J.; Ammon, M.; Yang, Z.; Heidenreich, A.; Hammer, N.; Görling, A.; Kivala, M.; Maier, S., Hierarchical on-surface synthesis and electronic structure of carbonyl-functionalized one- and two-dimensional covalent nanoarchitectures. *Nat. Commun.* **2017**, 8, 1-11.
59. Bronner, C.; Durr, R. A.; Rizzo, D. J.; Lee, Y.-L.; Marangoni, T.; Kalayjian, A. M.; Rodriguez, H.; Zhao, W.; Louie, S. G.; Fischer, F. R., Hierarchical on-surface synthesis of graphene nanoribbon heterojunctions. *ACS Nano* **2018**, 12, 2193-2200.
60. Ebeling, D.; Zhong, Q.; Schlöder, T.; Tschakert, J.; Henkel, P.; Ahles, S.; Chi, L.; Mollenhauer, D.; Wegner, H. A.; Schirmeisen, A., Adsorption Structure of Mono-and Diradicals on a Cu (111) Surface: Chemoselective Dehalogenation of 4-Bromo-3 "-iodo-p-terphenyl. *ACS Nano* **2018**, 13, 324-336.
61. Merino-Díez, N.; Pérez Paz, A.; Li, J.; Vilas-Varela, M.; Lawrence, J.; Mohammed, M. S.; Berdonces-Layunta, A.; Barragán, A.; Pascual, J. I.; Lobo-Checa, J., Hierarchy in the Halogen Activation During Surface-Promoted Ullmann Coupling. *ChemPhysChem* **2019**, 20, 2305-2310.
62. Shi, K. J.; Yuan, D. W.; Wang, C. X.; Shu, C. H.; Li, D. Y.; Shi, Z. L.; Wu, X. Y.; Liu, P. N., Ullmann reaction of aryl chlorides on various surfaces and the application in stepwise growth of 2D covalent organic frameworks. *Org. Lett.* **2016**, 18, 1282-1285.
63. Zhong, Q.; Ihle, A.; Ahles, S.; Wegner, H. A.; Schirmeisen, A.; Ebeling, D., Constructing covalent organic nanoarchitectures molecule by molecule via scanning probe manipulation. *Nat. Chem.* **2021**, 1-7.
64. Zhang, Z.; Perepichka, D. F.; Khaliullin, R. Z., Adatoms in the Surface-Confined Ullmann Coupling of Phenyl Groups. *J. Phys. Chem. Lett.* **2021**, 12, 11061-11069.
65. Lin, T.; Shang, X. S.; Adisoejoso, J.; Liu, P. N.; Lin, N., Steering on-surface polymerization with metal-directed template. *J. Am. Chem. Soc.* **2013**, 135, 3576-3582.
66. Adisoejoso, J.; Lin, T.; Shang, X. S.; Shi, K. J.; Gupta, A.; Liu, P. N.; Lin, N., A Single-Molecule-Level Mechanistic Study of Pd-Catalyzed and Cu-Catalyzed Homocoupling of Aryl Bromide on an Au (111) Surface. *Chem. Eur. J.* **2014**, 20, 4111-4116.
67. Kong, H.; Zhang, C.; Xie, L.; Wang, L.; Xu, W., Constitutional Dynamics of Metal–Organic Motifs on a Au (111) Surface. *Angew. Chem. Int. Ed.* **2016**, 55, 7157-7160.

68. Zhao, W.; Dong, L.; Huang, C.; Win, Z. M.; Lin, N., Cu-and Pd-catalyzed Ullmann reaction on a hexagonal boron nitride layer. *Chem. Commun.* **2016**, 52, 13225-13228.
69. Zhang, R.; Lyu, G.; Li, D. Y.; Liu, P. N.; Lin, N., Template-controlled Sonogashira cross-coupling reactions on a Au (111) surface. *Chem. Commun.* **2017**, 53, 1731-1734.
70. Haruta, M., Size-and support-dependency in the catalysis of gold. *Catal. Today* **1997**, 36, 153-166.
71. Bamwenda, G. R.; Tsubota, S.; Nakamura, T.; Haruta, M., The influence of the preparation methods on the catalytic activity of platinum and gold supported on TiO₂ for CO oxidation. *Catal. Lett.* **1997**, 44, 83-87.
72. Xu, X.; Vesecky, S. M.; Goodman, D. W., Infrared reflection-absorption spectroscopy and STM studies of model silica-supported copper catalysts. *Science* **1992**, 258, 788-790.
73. Chen, M.; Kumar, D.; Yi, C.-W.; Goodman, D. W., The promotional effect of gold in catalysis by palladium-gold. *Science* **2005**, 310, 291-293.
74. Molnar, A., Efficient, selective, and recyclable palladium catalysts in carbon– carbon coupling reactions. *Chem. Rev.* **2011**, 111, 2251-2320.
75. Shi, K. J.; Zhang, X.; Shu, C. H.; Li, D. Y.; Wu, X. Y.; Liu, P. N., Ullmann coupling reaction of aryl chlorides on Au (111) using dosed Cu as a catalyst and the programmed growth of 2D covalent organic frameworks. *Chem. Commun.* **2016**, 52, 8726-8729.
76. Lewis, E.; Murphy, C.; Pronschinske, A.; Liriano, M.; Sykes, E., Nanoscale insight into C–C coupling on cobalt nanoparticles. *Chem. Commun.* **2014**, 50, 10035-10037.
77. Shi, K.-J.; Shu, C.-H.; Wang, C.-X.; Wu, X.-Y.; Tian, H.; Liu, P.-N., On-surface Heck reaction of aryl bromides with alkene on Au (111) with palladium as catalyst. *Org. Lett.* **2017**, 19, 2801-2804.
78. Kim, K.; Lee, T.; Kwon, Y.; Seo, Y.; Song, J.; Park, J. K.; Lee, H.; Park, J. Y.; Ihee, H.; Cho, S. J., Lanthanum-catalysed synthesis of microporous 3D graphene-like carbons in a zeolite template. *Nature* **2016**, 535, 131-135.
79. Cirera, B.; Björk, J.; Otero, R.; Gallego, J. M.; Miranda, R.; Ecija, D., Efficient Lanthanide Catalyzed Debromination and Oligomeric Length-Controlled Ullmann Coupling of Aryl Halides. *J. Phys. Chem. C* **2017**, 121, 8033-8041.
80. Hellwig, R.; Uphoff, M.; Paintner, T.; Björk, J.; Ruben, M.; Klappenberger, F.; Barth, J. V., Ho-Mediated Alkyne Reactions at Low Temperatures on Ag (111). *Chem. Eur. J* **2018**, 24, 16126-16135.
81. Messina, P.; Dmitriev, A.; Lin, N.; Spillmann, H.; Abel, M.; Barth, J. V.; Kern, K., Direct observation of chiral metal-organic complexes assembled on a Cu (100) surface. *J. Am. Chem. Soc.* **2002**, 124, 14000-14001.
82. Schlickum, U.; Decker, R.; Klappenberger, F.; Zoppellaro, G.; Klyatskaya, S.; Ruben, M.; Silanes, I.; Arnau, A.; Kern, K.; Brune, H., Metal– organic honeycomb nanomeshes with tunable cavity size. *Nano Lett.* **2007**, 7, 3813-3817.
83. Stepanow, S.; Lin, N.; Payer, D.; Schlickum, U.; Klappenberger, F.; Zoppellaro, G.; Ruben, M.; Brune, H.; Barth, J. V.; Kern, K., Surface-Assisted Assembly of 2D Metal–Organic Networks That Exhibit Unusual Threefold Coordination Symmetry. *Angew. Chem.* **2007**, 119, 724-727.
84. Gambardella, P.; Stepanow, S.; Dmitriev, A.; Honolka, J.; De Groot, F. M.; Lingenfelder, M.; Gupta, S. S.; Sarma, D.; Bencok, P.; Stancescu, S., Supramolecular control of the magnetic anisotropy in two-dimensional high-spin Fe arrays at a metal interface. *Nat. Mater.* **2009**, 8, 189-193.

85. Kühne, D.; Klappenberger, F.; Decker, R.; Schlickum, U.; Brune, H.; Klyatskaya, S.; Ruben, M.; Barth, J. V., High-Quality 2D Metal–Organic Coordination Network Providing Giant Cavities within Mesoscale Domains. *J. Am. Chem. Soc.* **2009**, 131, 3881-3883.
86. Henningsen, N.; Rurali, R.; Limbach, C.; Drost, R.; Pascual, J.; Franke, K., Site-dependent coordination bonding in self-assembled metal–organic networks. *J. Phys. Chem. Lett.* **2010**, 2, 55-61.
87. Shi, Z.; Lin, N., Structural and Chemical Control in Assembly of Multicomponent Metal–Organic Coordination Networks on a Surface. *J. Am. Chem. Soc.* **2010**, 132, 10756-10761.
88. Li, Y.; Lin, N., Combined scanning tunneling microscopy and kinetic Monte Carlo study on kinetics of Cu-coordinated pyridyl-porphyrin supramolecular self-assembly on a Au (111) surface. *Phys. Rev. B* **2011**, 84, 125418.
89. Li, Y.; Xiao, J.; Shubina, T. E.; Chen, M.; Shi, Z.; Schmid, M.; Steinrück, H.-P.; Gottfried, J. M.; Lin, N., Coordination and metalation bifunctionality of Cu with 5, 10, 15, 20-tetra (4-pyridyl) porphyrin: toward a mixed-valence two-dimensional coordination network. *J. Am. Chem. Soc.* **2012**, 134, 6401-6408.
90. Shchyrba, A.; Wäckerlin, C.; Nowakowski, J.; Nowakowska, S.; Björk, J.; Fatayer, S.; Girovsky, J.; Nijs, T.; Martens, S. C.; Kleibert, A., Controlling the dimensionality of on-surface coordination polymers via endo-or exoligation. *J. Am. Chem. Soc.* **2014**, 136, 9355-9363.
91. Li, C.; Zhang, X.; Li, N.; Wang, Y.; Yang, J.; Gu, G.; Zhang, Y.; Hou, S.; Peng, L.; Wu, K., Construction of Sierpiński Triangles up to the Fifth Order. *J. Am. Chem. Soc.* **2017**, 139, 13749-13753.
92. Zhou, X.; Bebensee, F.; Shen, Q.; Bebensee, R.; Cheng, F.; He, Y.; Su, H.; Chen, W.; Xu, G. Q.; Besenbacher, F., On-surface synthesis approach to preparing one-dimensional organometallic and poly-p-phenylene chains. *Mater. Chem. Front.* **2017**, 1, 119-127.
93. Urgel, J. I.; Cirera, B.; Wang, Y.; Auwärter, W.; Otero, R.; Gallego, J. M.; Alcamí, M.; Klyatskaya, S.; Ruben, M.; Martín, F., Surface-Supported Robust 2D Lanthanide-Carboxylate Coordination Networks. *Small* **2015**, 11, 6358-6364.
94. Lin, N.; Dmitriev, A.; Weckesser, J.; Barth, J. V.; Kern, K., Real-time single-molecule imaging of the formation and dynamics of coordination compounds. *Angew. Chem. Int. Ed.* **2002**, 41, 4779-4783.
95. Dmitriev, A.; Spillmann, H.; Lin, N.; Barth, J. V.; Kern, K., Modular Assembly of Two-Dimensional Metal–Organic Coordination Networks at a Metal Surface. *Angew. Chem.* **2003**, 115, 2774-2777.
96. Stepanow, S.; Lin, N.; Vidal, F.; Landa, A.; Ruben, M.; Barth, J. V.; Kern, K., Programming supramolecular assembly and chirality in two-dimensional dicarboxylate networks on a Cu (100) surface. *Nano Lett.* **2005**, 5, 901-904.
97. Classen, T.; Fratesi, G.; Costantini, G.; Fabris, S.; Stadler, F. L.; Kim, C.; de Gironcoli, S.; Baroni, S.; Kern, K., Templated growth of metal–organic coordination chains at surfaces. *Angew. Chem. Int. Ed.* **2005**, 44, 6142-6145.
98. Nowakowska, S.; Wäckerlin, A.; Kawai, S.; Ivas, T.; Nowakowski, J.; Fatayer, S.; Wäckerlin, C.; Nijs, T.; Meyer, E.; Björk, J.; Stöhr, M.; Gade, L. H.; Jung, T. A., Interplay of weak interactions in the atom-by-atom condensation of xenon within quantum boxes. *Nat. Commun.* **2015**, 6, 6071.
99. Stepanow, S.; Lingenfelder, M.; Dmitriev, A.; Spillmann, H.; Delvigne, E.; Lin, N.; Deng, X.; Cai, C.; Barth, J. V.; Kern, K., Steering molecular organization and host–guest interactions using two-dimensional nanoporous coordination systems. *Nat. Mater.* **2004**, 3, 229-233.
100. Xie, L.; Zhang, C.; Ding, Y.; Xu, W., Structural Transformation and Stabilization of Metal–Organic

- Motifs Induced by Halogen Doping. *Angew. Chem.* **2017**, 129, 5159-5163.
101. Lahrood, A. R.; Björk, J.; Heckl, W. M.; Lackinger, M., 1, 3-Diiodobenzene on Cu (111)—an exceptional case of on-surface Ullmann coupling. *Chem. Commun.* **2015**, 51, 13301-13304.
102. Rastgoo-Lahrood, A.; Björk, J.; Lischka, M.; Eichhorn, J.; Kloft, S.; Fritton, M.; Strunskus, T.; Samanta, D.; Schmittel, M.; Heckl, W. M.; Lackinger, M., Post-Synthetic Decoupling of On-Surface-Synthesized Covalent Nanostructures from Ag (111). *Angew. Chem. Int. Ed.* **2016**, 55, 7650-7654.
103. Rastgoo-Lahrood, A.; Lischka, M.; Eichhorn, J.; Samanta, D.; Schmittel, M.; Heckl, W. M.; Lackinger, M., Reversible intercalation of iodine monolayers between on-surface synthesised covalent polyphenylene networks and Au (111). *Nanoscale* **2017**, 9, 4995-5001.
104. Galeotti, G.; Fritton, M.; Lackinger, M., Carbon-Carbon Coupling on Inert Surfaces by Deposition of En Route Generated Aryl Radicals. *Angew. Chem. Int. Ed.* **2020**, 59, 22785-22789.
105. Bronner, C.; Björk, J.; Tegeder, P., Tracking and removing Br during the on-surface synthesis of a graphene nanoribbon. *J. Phys. Chem. C* **2015**, 119, 486-493.
106. Tran, B. V.; Pham, T. A.; Grunst, M.; Kivala, M.; Stöhr, M., Surface-confined [2+ 2] cycloaddition towards one-dimensional polymers featuring cyclobutadiene units. *Nanoscale* **2017**, 9, 18305-18310.
107. Abyazisani, M.; MacLeod, J. M.; Lipton-Duffin, J., Cleaning up after the Party: Removing the byproducts of on-surface Ullmann coupling. *ACS Nano* **2019**, 13, 9270-9278.
108. Zuzak, R.; Jančářík, A.; Gourdon, A.; Szymonski, M.; Godlewski, S., On-Surface Synthesis with Atomic Hydrogen. *ACS Nano* **2020**, 14, 13316-13323.
109. Schauermann, S.; Schröder, C.; Schmidt, M. C.; Haugg, P. A.; Baumann, A.-K.; Smyczek, J., Understanding Ligand-Directed Heterogeneous Catalysis: When the Dynamically Changing Nature of the Ligand Layer Controls the Hydrogenation Selectivity. *Angew. Chem.* **2021**, 133, 16485-16490.
110. Rodríguez-Fernández, J.; Schmidt, S. B.; Lauritsen, J. V., Sulfur-driven switching of the Ullmann coupling on Au (111). *Chem. Commun.* **2018**, 54, 3621-3624.
111. Niu, T.; Jiang, Z.; Zhu, Y.; Zhou, G.; van Spronsen, M. A.; Tenney, S. A.; Boscoboinik, J. A.; Stacchiola, D., Oxygen-Promoted Methane Activation on Copper. *J. Phys. Chem. B* **2017**, 122, 855-863.
112. Orozco, N.; Kyriakou, G.; Beaumont, S. K.; Fernandez Sanz, J.; Holgado, J. P.; Taylor, M. J.; Espinós, J. P.; Márquez, A. M.; Watson, D. J.; Gonzalez-Elipe, A. R.; Lambert, R. M., Critical Role of Oxygen in Silver-Catalyzed Glaser–Hay Coupling on Ag (100) under Vacuum and in Solution on Ag Particles. *ACS Catal.* **2017**, 7, 3113-3120.
113. Zhang, Y.-Q.; Paintner, T.; Hellwig, R.; Haag, F.; Allegretti, F.; Feulner, P.; Klyatskaya, S.; Ruben, M.; Seitsonen, A. P.; Barth, J. V.; Klappenberger, F., Synthesizing highly regular single-layer alkynyl-silver networks at the micrometer scale via gas-mediated surface reaction. *J. Am. Chem. Soc.* **2019**, 141, 5087.
114. Fabris, S.; Stepanow, S.; Lin, N.; Gambardella, P.; Dmitriev, A.; Honolka, J.; Baroni, S.; Kern, K., Oxygen dissociation by concerted action of di-iron centers in metal–organic coordination networks at surfaces: modeling non-heme iron enzymes. *Nano Lett.* **2011**, 11, 5414-5420.
115. De Marchi, F.; Galeotti, G.; Simenas, M.; Tornau, E.; Pezzella, A.; MacLeod, J.; Ebrahimi, M.; Rosei, F., Room-temperature surface-assisted reactivity of a melanin precursor: silver metal–organic coordination versus covalent dimerization on gold. *Nanoscale* **2018**, 10, 16721-16729.
116. De Marchi, F.; Galeotti, G.; Simenas, M.; Ji, P.; Chi, L.; Tornau, E.; Pezzella, A.; MacLeod, J.; Ebrahimi, M.; Rosei, F., Self-assembly of 5, 6-dihydroxyindole-2-carboxylic acid: polymorphism of a

- eumelanin building block on Au (111). *Nanoscale* **2019**, *11*, 5422-5428.
117. Jensen, F.; Besenbacher, F.; Lægsgaard, E.; Stensgaard, I., Surface reconstruction of Cu (110) induced by oxygen chemisorption. *Phys. Rev. B* **1990**, *41*, 10233.
118. Yang, F.; Choi, Y.; Liu, P.; Stacchiola, D.; Hrbek, J.; Rodriguez, J. A., Identification of 5–7 defects in a copper oxide surface. *J. Am. Chem. Soc.* **2011**, *133*, 11474-11477.
119. Gottardi, S.; Müller, K.; Bignardi, L.; Moreno-López, J. C.; Pham, T. A.; Ivashenko, O.; Yablonskikh, M.; Barinov, A.; Björk, J.; Rudolf, P., Comparing graphene growth on Cu (111) versus oxidized Cu (111). *Nano Lett.* **2015**, *15*, 917-922.
120. Ruffieux, P.; Wang, S.; Yang, B.; Sánchez-Sánchez, C.; Liu, J.; Dienel, T.; Talirz, L.; Shinde, P.; Pignedoli, C. A.; Passerone, D.; Dumslaff, T.; Feng, X.; Müllen, K.; Fasel, R., On-surface synthesis of graphene nanoribbons with zigzag edge topology. *Nature* **2016**, *531*, 489-493.
121. Wang, S.; Talirz, L.; Pignedoli, C. A.; Feng, X.; Müllen, K.; Fasel, R.; Ruffieux, P., Giant edge state splitting at atomically precise graphene zigzag edges. *Nat. Commun.* **2016**, *7*, 11507.
122. Voigtländer, B., *Scanning probe microscopy: Atomic force microscopy and scanning tunneling microscopy*. Springer: 2015.
123. Crommie, M.; Lutz, C.; Eigler, D., Imaging standing waves in a two-dimensional electron gas. *Nature* **1993**, *363*, 524.
124. Bjork, J.; Hanke, F.; Stafstrom, S., Mechanisms of halogen-based covalent self-assembly on metal surfaces. *J. Am. Chem. Soc.* **2013**, *135*, 5768-5775.
125. Heimel, G.; Duhm, S.; Salzmann, I.; Gerlach, A.; Strozecka, A.; Niederhausen, J.; Bürker, C.; Hosokai, T.; Fernandez-Torrente, I.; Schulze, G., Charged and metallic molecular monolayers through surface-induced aromatic stabilization. *Nat. Chem.* **2013**, *5*, 187.
126. Linden, S.; Zhong, D.; Timmer, A.; Aghdassi, N.; Franke, J.; Zhang, H.; Feng, X.; Müllen, K.; Fuchs, H.; Chi, L., Electronic structure of spatially aligned graphene nanoribbons on Au (788). *Phys. Rev. Lett.* **2012**, *108*, 216801.
127. Wiame, F.; Maurice, V.; Marcus, P., Initial stages of oxidation of Cu (1 1 1). *Surf. Sci.* **2007**, *601*, 1193-1204.
128. Jensen, F.; Besenbacher, F.; Lægsgaard, E.; Stensgaard, I., Oxidation of Cu (111): two new oxygen induced reconstructions. *Surf. Sci.* **1991**, *259*, L774-L780.
129. Hipps, K.; Scudiero, L.; Barlow, D. E.; Cooke, M. P., A self-organized 2-dimensional bifunctional structure formed by supramolecular design. *J. Am. Chem. Soc.* **2002**, *124*, 2126-2127.
130. Weigelt, S.; Busse, C.; Bombis, C.; Knudsen, M. M.; Gothelf, K. V.; Strunskus, T.; Wöll, C.; Dahlbom, M.; Hammer, B.; Lægsgaard, E.; Besenbacher, F.; Linderoth, T. R., Covalent interlinking of an aldehyde and an amine on a Au (111) surface in ultrahigh vacuum. *Angew. Chem. Int. Ed.* **2007**, *46*, 9227-9230.
131. Lafferentz, L.; Eberhardt, V.; Dri, C.; Africh, C.; Comelli, G.; Esch, F.; Hecht, S.; Grill, L., Controlling on-surface polymerization by hierarchical and substrate-directed growth. *Nat. Chem.* **2012**, *4*, 215.
132. Kalashnyk, N.; Mouhat, K.; Oh, J.; Jung, J.; Xie, Y.; Salomon, E.; Angot, T.; Dumur, F.; Gigmes, D.; Clair, S., On-surface synthesis of aligned functional nanoribbons monitored by scanning tunnelling microscopy and vibrational spectroscopy. *Nat. Commun.* **2017**, *8*, 1-9.
133. Steiner, C.; Gebhardt, J.; Ammon, M.; Yang, Z.; Heidenreich, A.; Hammer, N.; Görling, A.; Kivala, M.; Maier, S., Hierarchical on-surface synthesis and electronic structure of carbonyl-functionalized one-

- and two-dimensional covalent nanoarchitectures. *Nat. Commun.* **2017**, *8*, 14765.
134. Sun, Q.; Zhang, R.; Qiu, J.; Liu, R.; Xu, W., On-Surface Synthesis of Carbon Nanostructures. *Adv. Mater.* **2018**, *30*, 1705630.
135. Williams, C. G.; Wang, M.; Hopwood, J. P.; Tempas, C. D.; Morris, T. W.; Wisman, D. L.; Kesmodel, L. L.; Ciszek, J. W.; Tait, S. L., Surface-catalyzed dehydrogenation and intermolecular CC bond formation at peripheral alkyl units on Cu (100) and Au (111). *Surf. Sci.* **2019**, *683*, 23-30.
136. Fan, Q.; Wang, C.; Han, Y.; Zhu, J.; Hieringer, W.; Kuttner, J.; Hilt, G.; Gottfried, J. M., Surface-Assisted Organic Synthesis of Hyperbenzene Nanotroughs. *Angew. Chem. Int. Ed.* **2013**, *52*, 4668-4672.
137. Li, Q.; Gao, J.; Li, Y.; Fuentes-Cabrera, M.; Liu, M.; Qiu, X.; Lin, H.; Chi, L.; Pan, M., Self-assembly directed one-step synthesis of [4] radialene on Cu (100) surfaces. *Nat. Commun.* **2018**, *9*, 3113.
138. Gutzler, R.; Cardenas, L.; Lipton-Duffin, J.; El Garah, M.; Dinca, L. E.; Szakacs, C. E.; Fu, C.; Gallagher, M.; Vondráček, M.; Rybachuk, M.; F. Perepichka, D.; Rosei, F., Ullmann-type coupling of brominated tetrathienoanthracene on copper and silver. *Nanoscale* **2014**, *6*, 2660-2668.
139. Di Giovannantonio, M.; Tomellini, M.; Lipton-Duffin, J.; Galeotti, G.; Ebrahimi, M.; Cossaro, A.; Verdini, A.; Kharche, N.; Meunier, V.; Vasseur, G.; Fagot-Revurat, Y.; Perepichka, D. F.; Rosei, F.; Contini, G., Mechanistic picture and kinetic analysis of surface-confined Ullmann polymerization. *J. Am. Chem. Soc.* **2016**, *138*, 16696-16702.
140. Fritton, M.; Duncan, D. A.; Deimel, P. S.; Rastgoo-Lahrood, A.; Allegretti, F.; Barth, J. V.; Heckl, W. M.; Björk, J.; Lackinger, M., The role of kinetics vs. thermodynamics in surface-assisted Ullmann coupling on gold and silver surfaces. *J. Am. Chem. Soc.* **2019**, *141*, 4824-4832.
141. Kim, W. J.; Xing, S.; Kremer, G.; Sicot, M.; Kierren, B.; Malterre, D.; Contini, G.; Rault, J.; Le Fèvre, P.; Bertran, F.; Rocca, D.; Fagot-Revurat, Y.; Lebègue, S. b., Electronic Structure of Heavy Halogen Atoms Adsorbed on the Cu (111) Surface: A Combined ARPES and First Principles Calculations Study. *J. Phys. Chem. C* **2019**, *123*, 26309-26314.
142. Cai, J.; Ruffieux, P.; Jaafar, R.; Bieri, M.; Braun, T.; Blankenburg, S.; Muoth, M.; Seitsonen, A. P.; Saleh, M.; Feng, X.; Müllen, K.; Fasel, R., Atomically precise bottom-up fabrication of graphene nanoribbons. *Nature* **2010**, *466*, 470-473.
143. Chen, Y.-C.; De Oteyza, D. G.; Pedramrazi, Z.; Chen, C.; Fischer, F. R.; Crommie, M. F., Tuning the band gap of graphene nanoribbons synthesized from molecular precursors. *ACS Nano* **2013**, *7*, 6123-6128.
144. Zhang, H.; Lin, H.; Sun, K.; Chen, L.; Zagranjarski, Y.; Aghdassi, N.; Duhm, S.; Li, Q.; Zhong, D.; Li, Y.; Müllen, K.; Fuchs, H.; Chi, L., On-surface synthesis of rylene-type graphene nanoribbons. *J. Am. Chem. Soc.* **2015**, *137*, 4022-4025.
145. Sun, K.; Ji, P.; Zhang, J.; Wang, J.; Li, X.; Xu, X.; Zhang, H.; Chi, L., On-Surface Synthesis of 8-and 10-Armchair Graphene Nanoribbons. *Small* **2019**, *15*, 1804526.
146. Wang, S.; Sun, Q.; Gröning, O.; Widmer, R.; Pignedoli, C. A.; Cai, L.; Yu, X.; Yuan, B.; Li, C.; Ju, H.; Zhu, J.; Ruffieux, P.; Fasel, R.; Xu, W., On-surface synthesis and characterization of individual polyacetylene chains. *Nat. Chem.* **2019**, *11*, 924-930.
147. Li, Q.; Yang, B.; Lin, H.; Aghdassi, N.; Miao, K.; Zhang, J.; Zhang, H.; Li, Y.; Duhm, S.; Fan, J.; Chi, L., Surface-controlled mono/diselective ortho C–H bond activation. *J. Am. Chem. Soc.* **2016**, *138*, 2809-2814.
148. Niu, T.; Jiang, Z.; Zhu, Y.; Zhou, G.; van Spronsen, M. A.; Tenney, S. A.; Boscoboinik, J. A.; Stacchiola,

- D., Oxygen-promoted methane activation on copper. *J. Phys. Chem. B* **2018**, 122, 855-863.
149. Neaton, J. B.; Hybertsen, M. S.; Louie, S. G., Renormalization of molecular electronic levels at metal-molecule interfaces. *Phys. Rev. Lett.* **2006**, 97, 216405.
150. Kolmer, M.; Ahmad Zebari, A. A.; Prauzner-Bechcicki, J. S.; Piskorz, W.; Zasada, F.; Godlewski, S.; Such, B.; Sojka, Z.; Szymonski, M., Polymerization of Polyanthrylene on a Titanium Dioxide (011)-(2× 1) Surface. *Angew. Chem. Int. Ed.* **2013**, 52, 10300-10303.
151. Sueyoshi, T.; Sasaki, T.; Iwasawa, Y., Molecular and atomic adsorption states of oxygen on Cu (111) at 100–300 K. *Surf. Sci.* **1996**, 365, 310-318.
152. Matsumoto, T.; Bennett, R.; Stone, P.; Yamada, T.; Domen, K.; Bowker, M., Scanning tunneling microscopy studies of oxygen adsorption on Cu (1 1 1). *Surf. Sci.* **2001**, 471, 225-245.
153. Xu, Y.; Mavrikakis, M., Adsorption and dissociation of O₂ on Cu (111): thermochemistry, reaction barrier and the effect of strain. *Surf. Sci.* **2001**, 494, 131-144.
154. Galeotti, G.; De Marchi, F.; Taerum, T.; Besteiro, L.; El Garah, M.; Lipton-Duffin, J.; Ebrahimi, M.; Perepichka, D.; Rosei, F., Surface-mediated assembly, polymerization and degradation of thiophene-based monomers. *Chem. Sci.* **2019**, 10, 5167-5175.
155. Lobo-Checa, J.; Matena, M.; Müller, K.; Dil, J. H.; Meier, F.; Gade, L. H.; Jung, T. A.; Stöhr, M., Band formation from coupled quantum dots formed by a nanoporous network on a copper surface. *Science* **2009**, 325, 300-303.
156. Eren, B.; Lichtenstein, L.; Wu, C. H.; Bluhm, H.; Somorjai, G. A.; Salmeron, M., Reaction of CO with preadsorbed oxygen on low-index copper surfaces: An ambient pressure X-ray photoelectron spectroscopy and scanning tunneling microscopy study. *J. Phys. Chem. C* **2015**, 119, 14669-14674.
157. Fan, Q.; Wang, T.; Liu, L.; Zhao, J.; Zhu, J.; Gottfried, J. M., Tribromobenzene on Cu (111): Temperature-dependent formation of halogen-bonded, organometallic, and covalent nanostructures. *J. Chem. Phys.* **2015**, 142, 101906.
158. Bader, R. F., Atoms in molecules. *Acc. Chem. Res.* **1985**, 18, 9-15.
159. Yagyu, K.; Liu, X.; Yoshimoto, Y.; Nakatsuji, K.; Komori, F., Dissociative adsorption of oxygen on clean Cu (001) surface. *J. Phys. Chem. C* **2009**, 113, 5541-5546.
160. Horcas, I.; Fernández, R.; Gomez-Rodriguez, J.; Colchero, J.; Gómez-Herrero, J.; Baro, A., WSXM: a software for scanning probe microscopy and a tool for nanotechnology. *Rev. Sci. Instrum.* **2007**, 78, 013705.
161. Kresse, G.; Hafner, J., Ab initio molecular dynamics for liquid metals. *Phys. Rev. B* **1993**, 47, 558.
162. Kresse, G.; Furthmüller, J., Efficient iterative schemes for ab initio total-energy calculations using a plane-wave basis set. *Phys. Rev. B* **1996**, 54, 11169.
163. Perdew, J. P.; Ernzerhof, M.; Burke, K., Rationale for mixing exact exchange with density functional approximations. *J. Chem. Phys.* **1996**, 105, 9982-9985.
164. Blöchl, P. E., Projector augmented-wave method. *Phys. Rev. B* **1994**, 50, 17953.
165. Kresse, G.; Joubert, D., From ultrasoft pseudopotentials to the projector augmented-wave method. *Phys. Rev. B* **1999**, 59, 1758.
166. Grimme, S.; Antony, J.; Ehrlich, S.; Krieg, H., A consistent and accurate ab initio parametrization of density functional dispersion correction (DFT-D) for the 94 elements H-Pu. *J. Chem. Phys.* **2010**, 132, 154104.
167. Humphrey, W.; Dalke, A.; Schulten, K., VMD: visual molecular dynamics. *J. Mol. Graph.* **1996**, 14,

33-38.

168. Tersoff, J.; Hamann, D. R., Theory of the scanning tunneling microscope. *Phys. Rev. B* **1985**, 31, 805.
169. Vanpoucke, D. E.; Brocks, G., Formation of Pt-induced Ge atomic nanowires on Pt/Ge (001): A density functional theory study. *Phys. Rev. B* **2008**, 77, 241308.
170. Wang, X.-Y.; Yao, X.; Müllen, K., Polycyclic aromatic hydrocarbons in the graphene era. *Sci. China Chem.* **2019**, 62, 1099-1144.
171. Zheng, C.; Zhu, J.; Yang, C.; Lu, C.; Chen, Z.; Zhuang, X., The art of two-dimensional soft nanomaterials. *Sci. China Chem.* **2019**, 62, 1145-1193.
172. Stoltz, S.; Di Giovannantonio, M.; Urgel, J. I.; Sun, Q.; Kinikar, A.; Borin Barin, G.; Bommert, M.; Fasel, R.; Widmer, R., Reversible Dehalogenation in On-Surface Aryl–Aryl Coupling. *Angew. Chem. Int. Ed.* **2020**, 132, 14210-14214.
173. Yu, M.; Chen, C.; Liu, Q.; Mattioli, C.; Sang, H.; Shi, G.; Huang, W.; Shen, K.; Li, Z.; Ding, P.; Guan, P.; Wang, S.; Sun, Y.; Jinping, H.; Gourdon, A.; Kantorovich, L.; Besenbacher, F.; Chen, M.; Song, F.; Rosei, F., Long-range ordered and atomic-scale control of graphene hybridization by photocycloaddition. *Nat. Chem.* **2020**, 12, 1035-1041.
174. Yang, L.; Park, C.-H.; Son, Y.-W.; Cohen, M. L.; Louie, S. G., Quasiparticle energies and band gaps in graphene nanoribbons. *Phys. Rev. Lett.* **2007**, 99, 186801.
175. Sakaguchi, H.; Kawagoe, Y.; Hirano, Y.; Iruka, T.; Yano, M.; Nakae, T., Width-Controlled Sub-Nanometer Graphene Nanoribbon Films Synthesized by Radical-Polymerized Chemical Vapor Deposition. *Adv. Mater.* **2014**, 26, 4134-4138.
176. Sakaguchi, H.; Song, S.; Kojima, T.; Nakae, T., Homochiral polymerization-driven selective growth of graphene nanoribbons. *Nat. Chem.* **2017**, 9, 57.
177. Li, X.; Wang, X.; Zhang, L.; Lee, S.; Dai, H., Chemically derived, ultrasmooth graphene nanoribbon semiconductors. *Science* **2008**, 319, 1229-1232.
178. Wang, X.; Ouyang, Y.; Li, X.; Wang, H.; Guo, J.; Dai, H., Room-temperature all-semiconducting sub-10-nm graphene nanoribbon field-effect transistors. *Phys. Rev. Lett.* **2008**, 100, 206803.
179. Jiao, L.; Zhang, L.; Wang, X.; Diankov, G.; Dai, H., Narrow graphene nanoribbons from carbon nanotubes. *Nature* **2009**, 458, 877-880.
180. Basagni, A.; Sedona, F.; Pignedoli, C. A.; Cattelan, M.; Nicolas, L.; Casarin, M.; Sambi, M., Molecules–oligomers–nanowires–graphene nanoribbons: a bottom-up stepwise on-surface covalent synthesis preserving long-range order. *J. Am. Chem. Soc.* **2015**, 137, 1802-1808.
181. Talirz, L.; Söde, H.; Dumslaff, T.; Wang, S.; Sanchez-Valencia, J. R.; Liu, J.; Shinde, P.; Pignedoli, C. A.; Liang, L.; Meunier, V.; C. Plumb, N.; Shi, M.; Feng, X.; Narita, A.; Müllen, K.; Fasel, R.; Ruffieux, P., On-surface synthesis and characterization of 9-atom wide armchair graphene nanoribbons. *ACS Nano* **2017**, 11, 1380-1388.
182. Ma, C.; Liang, L.; Xiao, Z.; Puretzky, A. A.; Hong, K.; Lu, W.; Meunier, V.; Bernholc, J.; Li, A.-P., Seamless staircase electrical contact to semiconducting graphene nanoribbons. *Nano Lett.* **2017**, 17, 6241-6247.
183. Wang, S.; Kharche, N.; Costa Girão, E.; Feng, X.; Müllen, K.; Meunier, V.; Fasel, R.; Ruffieux, P., Quantum dots in graphene nanoribbons. *Nano Lett.* **2017**, 17, 4277-4283.
184. Rizzo, D. J.; Veber, G.; Cao, T.; Bronner, C.; Chen, T.; Zhao, F.; Rodriguez, H.; Louie, S. G.; Crommie,

- M. F.; Fischer, F. R., Topological band engineering of graphene nanoribbons. *Nature* **2018**, 560, 204-208.
185. Cai, J.; Pignedoli, C. A.; Talirz, L.; Ruffieux, P.; Söde, H.; Liang, L.; Meunier, V.; Berger, R.; Li, R.; Feng, X., Graphene nanoribbon heterojunctions. *Nat. Nanotechnol.* **2014**, 9, 896.
186. Chen, Y.-C.; Cao, T.; Chen, C.; Pedramrazi, Z.; Haberer, D.; De Oteyza, D. G.; Fischer, F. R.; Louie, S. G.; Crommie, M. F., Molecular bandgap engineering of bottom-up synthesized graphene nanoribbon heterojunctions. *Nat. Nanotechnol.* **2015**, 10, 156-160.
187. Han, P.; Akagi, K.; Federici Canova, F.; Mutoh, H.; Shiraki, S.; Iwaya, K.; Weiss, P. S.; Asao, N.; Hitosugi, T., Bottom-up graphene-nanoribbon fabrication reveals chiral edges and enantioselectivity. *ACS Nano* **2014**, 8, 9181-9187.
188. Sánchez-Sánchez, C.; Dienel, T.; Deniz, O.; Ruffieux, P.; Berger, R.; Feng, X.; Müllen, K.; Fasel, R., Purely armchair or partially chiral: Noncontact atomic force microscopy characterization of dibromo-bianthryl-based graphene nanoribbons grown on Cu (111). *ACS Nano* **2016**, 10, 8006-8011.
189. Jacobse, P. H.; Simonov, K. A.; Mangnus, M. J.; Svirskiy, G. I.; Generalov, A. V.; Vinogradov, A. S.; Sandell, A.; Mårtensson, N.; Preobrajenski, A. B.; Swart, I., One Precursor but Two Types of Graphene Nanoribbons: On-Surface Transformations of 10, 10'-dichloro-9, 9'-bianthryl on Ag (111). *J. Phys. Chem. C* **2019**, 123, 8892-8901.
190. Tao, C.; Jiao, L.; Yazyev, O. V.; Chen, Y.-C.; Feng, J.; Zhang, X.; Capaz, R. B.; Tour, J. M.; Zettl, A.; Louie, S. G., Spatially resolving edge states of chiral graphene nanoribbons. *Nat. Phys.* **2011**, 7, 616-620.
191. Wang, X.-Y.; Urgel, J. I.; Barin, G. B.; Eimre, K.; Di Giovannantonio, M.; Milani, A.; Tommasini, M.; Pignedoli, C. A.; Ruffieux, P.; Feng, X., Bottom-up synthesis of heteroatom-doped chiral graphene nanoribbons. *J. Am. Chem. Soc.* **2018**, 140, 9104-9107.
192. Cloke, R. R.; Marangoni, T.; Nguyen, G. D.; Joshi, T.; Rizzo, D. J.; Bronner, C.; Cao, T.; Louie, S. G.; Crommie, M. F.; Fischer, F. R., Site-specific substitutional boron doping of semiconducting armchair graphene nanoribbons. *J. Am. Chem. Soc.* **2015**, 137, 8872-8875.
193. Carbonell-Sanromà, E.; Hieulle, J.; Vilas-Varela, M.; Brandimarte, P.; Iraola, M.; Barragán, A.; Li, J.; Abadia, M.; Corso, M.; Sánchez-Portal, D., Doping of graphene nanoribbons via functional group edge modification. *ACS Nano* **2017**, 11, 7355-7361.
194. Pawlak, R.; Liu, X.; Ninova, S.; D'Astolfo, P.; Drechsel, C.; Sangtarash, S.; Häner, R.; Decurtins, S.; Sadeghi, H.; Lambert, C. J., Bottom-up Synthesis of Nitrogen-Doped Porous Graphene Nanoribbons. *J. Am. Chem. Soc.* **2020**, 142, 12568-12573.
195. Kawai, S.; Saito, S.; Osumi, S.; Yamaguchi, S.; Foster, A. S.; Spijker, P.; Meyer, E., Atomically controlled substitutional boron-doping of graphene nanoribbons. *Nat. Commun.* **2015**, 6, 1-6.
196. Han, P.; Akagi, K.; Federici Canova, F.; Shimizu, R.; Oguchi, H.; Shiraki, S.; Weiss, P. S.; Asao, N.; Hitosugi, T., Self-assembly strategy for fabricating connected graphene nanoribbons. *ACS Nano* **2015**, 9, 12035-12044.
197. Sun, K.; Ji, P.; Zhang, H.; Niu, K.; Li, L.; Chen, A.; Li, Q.; Müllen, K.; Chi, L., A new on-surface synthetic pathway to 5-armchair graphene nanoribbons on Cu (111) surfaces. *Faraday Discuss.* **2017**, 204, 297-305.
198. Teeter, J. D.; Costa, P. S.; Pour, M. M.; Miller, D. P.; Zurek, E.; Enders, A.; Sinitskii, A., Epitaxial growth of aligned atomically precise chevron graphene nanoribbons on Cu (111). *Chem. Commun.* **2017**, 53, 8463-8466.

199. Zuzak, R.; Jancarik, A.; Gourdon, A.; Szymonski, M.; Godlewski, S., On-Surface Synthesis with Atomic Hydrogen. *ACS Nano* **2020**, 14, 13316-13323.
200. Jones, R. G.; Kadodwala, M., Bromine adsorption on Cu (111). *Surf. Sci.* **1997**, 370, L219-L225.
201. Chen, M.; Xiao, J.; Steinrück, H.-P.; Wang, S.; Wang, W.; Lin, N.; Hieringer, W.; Gottfried, J. M., Combined photoemission and scanning tunneling microscopy study of the surface-assisted Ullmann coupling reaction. *J. Phys. Chem. C* **2014**, 118, 6820-6830.
202. Batra, A.; Cvetko, D.; Kladnik, G.; Adak, O.; Cardoso, C.; Ferretti, A.; Prezzi, D.; Molinari, E.; Morgante, A.; Venkataraman, L., Probing the mechanism for graphene nanoribbon formation on gold surfaces through X-ray spectroscopy. *Chem. Sci.* **2014**, 5, 4419-4423.
203. Stadnichenko, A.; Sorokin, A.; Boronin, A., XPS, UPS, and STM studies of nanostructured CuO films. *J. Struct. Chem.* **2008**, 49, 341-347.
204. Carlisle, C.; Fujimoto, T.; Sim, W.; King, D., Atomic imaging of the transition between oxygen chemisorption and oxide film growth on Ag {1 1 1}. *Surf. Sci.* **2000**, 470, 15-31.
205. Everson, M.; Jaklevic, R.; Shen, W., Measurement of the local density of states on a metal surface: Scanning tunneling spectroscopic imaging of Au (111). *J. Vac. Sci. Technol.* **1990**, 8, 3662-3665.
206. Merino-Díez, N.; Garcia-Lekue, A.; Carbonell-Sanromà, E.; Li, J.; Corso, M.; Colazzo, L.; Sedona, F.; Sánchez-Portal, D.; Pascual, J. I.; de Oteyza, D. G., Width-dependent band gap in armchair graphene nanoribbons reveals Fermi level pinning on Au (111). *ACS Nano* **2017**, 11, 11661-11668.
207. Kimouche, A.; Ervasti, M. M.; Drost, R.; Halonen, S.; Harju, A.; Joensuu, P. M.; Sainio, J.; Liljeroth, P., Ultra-narrow metallic armchair graphene nanoribbons. *Nat. Commun.* **2015**, 6, 1-6.
208. Ruffieux, P.; Cai, J.; Plumb, N. C.; Patthey, L.; Prezzi, D.; Ferretti, A.; Molinari, E.; Feng, X.; Müllen, K.; Pignedoli, C. A., Electronic structure of atomically precise graphene nanoribbons. *Acs Nano* **2012**, 6, 6930-6935.
209. Therrien, A. J.; Hensley, A. J.; Zhang, R.; Pronschinske, A.; Marcinkowski, M. D.; McEwen, J.-S.; Sykes, E. C. H., Characterizing the geometric and electronic structure of defects in the “29” copper surface oxide. *J. Chem. Phys.* **2017**, 147, 224706.
210. Zhang, L.; Cao, Y.; Colella, N. S.; Liang, Y.; Bredas, J.-L.; Houk, K. N.; Briseno, A. L., Unconventional, chemically stable, and soluble two-dimensional angular polycyclic aromatic hydrocarbons: from molecular design to device applications. *Acc. Chem. Res.* **2015**, 48, 500-509.
211. Wang, Y.; Liu, B.; Koh, C. W.; Zhou, X.; Sun, H.; Yu, J.; Yang, K.; Wang, H.; Liao, Q.; Woo, H. Y., Facile Synthesis of Polycyclic Aromatic Hydrocarbon (PAH)-Based Acceptors with Fine-Tuned Optoelectronic Properties: Toward Efficient Additive-Free Nonfullerene Organic Solar Cells. *Adv. Energy Mater.* **2019**, 9, 1803976.
212. Zhang, X.; Zeng, Q.; Wang, C., On-surface single molecule synthesis chemistry: a promising bottom-up approach towards functional surfaces. *Nanoscale* **2013**, 5, 8269-8287.
213. Klappenberger, F.; Zhang, Y.-Q.; Björk, J.; Klyatskaya, S.; Ruben, M.; Barth, J. V., On-surface synthesis of carbon-based scaffolds and nanomaterials using terminal alkynes. *Acc. Chem. Res.* **2015**, 48, 2140-2150.
214. Wang, T.; Huang, J.; Lv, H.; Fan, Q.; Feng, L.; Tao, Z.; Ju, H.; Wu, X.; Tait, S. L.; Zhu, J., Kinetic strategies for the formation of graphyne nanowires via Sonogashira coupling on Ag (111). *J. Am. Chem. Soc.* **2018**, 140, 13421-13428.

215. Wang, Z.; Liu, X.; Lu, Y.; Wang, Z.; Bortolini, C.; Chen, M.; Wei, S.; Li, W.; Zhu, J.; Ju, H.; Rosei, F.; Dong, M.; Wang, L., Direct on-surface synthesis of gold–phthalocyanine via cyclization of cyano-groups with gold adatoms. *Mater. Chem. Front.* **2019**, 3, 1406-1410.
216. Wiggins, B.; Hipps, K. W., Investigation of metal free naphthalocyanine vapor deposited on Au (111). *J. Phys. Chem. C* **2014**, 118, 4222-4230.
217. Hipps, K.; Mazur, U., Kinetic and thermodynamic control in porphyrin and phthalocyanine self-assembled monolayers. *Langmuir* **2018**, 34, 3-17.
218. Cui, D.; MacLeod, J. M.; Rosei, F., Planar anchoring of C70 liquid crystals using a covalent organic framework template. *Small* **2019**, 15, 1903294.
219. Dettmann, D.; Galeotti, G.; MacLean, O.; Tomellini, M.; Di Giovannantonio, M.; Lipton-Duffin, J.; Verdini, A.; Floreano, L.; Fagot-Revurat, Y.; Perepichka, D. F.; Rosei, F.; Contini, G., Identification of Topotactic Surface-Confined Ullmann-Polymerization. *Small* **2021**, 17, 2103044.
220. Urgel, J. I.; Mishra, S.; Hayashi, H.; Wilhelm, J.; Pignedoli, C. A.; Di Giovannantonio, M.; Widmer, R.; Yamashita, M.; Hieda, N.; Ruffieux, P.; Yamada, H.; Fasel, R., On-surface light-induced generation of higher acenes and elucidation of their open-shell character. *Nat. Commun.* **2019**, 10, 1-9.
221. Zhong, Q.; Ihle, A.; Ahles, S.; Wegner, H. A.; Schirmeisen, A.; Ebeling, D., Constructing covalent organic nanoarchitectures molecule by molecule via scanning probe manipulation. *Nat. Chem.* **2021**, 13, 1133-1139.
222. Pham, T. A.; Song, F.; Nguyen, M.-T.; Li, Z.; Studener, F.; Stöhr, M., Comparing Ullmann coupling on noble metal surfaces: On-surface polymerization of 1, 3, 6, 8-tetrabromopyrene on Cu (111) and Au (111). *Chem.-Eur. J* **2016**, 22, 5937-5944.
223. Krüger, J.; García, F.; Eisenhut, F.; Skidin, D.; Alonso, J. M.; Gutián, E.; Pérez, D.; Cuniberti, G.; Moresco, F.; Peña, D., Decacene: On-Surface Generation. *Angew. Chem. Int. Ed.* **2017**, 129, 12107-12110.
224. Zuzak, R.; Dorel, R.; Kolmer, M.; Szymonski, M.; Godlewski, S.; Echavarren, A. M., Higher Acenes by On-Surface Dehydrogenation: From Heptacene to Undecacene. *Angew. Chem. Int. Ed.* **2018**, 57, 10500-10505.
225. Krüger, J.; Pavliček, N.; Alonso, J. M.; Pérez, D.; Gutián, E.; Lehmann, T.; Cuniberti, G.; Gourdon, A.; Meyer, G.; Gross, L., Tetracene formation by on-surface reduction. *ACS Nano* **2016**, 10, 4538-4542.
226. Ji, P.; MacLean, O.; Galeotti, G.; Dettmann, D.; Berti, G.; Sun, K.; Zhang, H.; Rosei, F.; Chi, L., Oxygen-promoted synthesis of armchair graphene nanoribbons on Cu (111). *Sci. China Chem.* **2021**, 64, 636-641.
227. Lee, J.; Kalin, A. J.; Yuan, T.; Al-Hashimi, M.; Fang, L., Fully conjugated ladder polymers. *Chem. Sci.* **2017**, 8, 2503-2521.
228. Li, D.-Y.; Qiu, X.; Li, S.-W.; Ren, Y.-T.; Zhu, Y.-C.; Shu, C.-H.; Hou, X.-Y.; Liu, M.; Shi, X.-Q.; Qiu, X., Ladder Phenylenes Synthesized on Au (111) Surface via Selective [2+ 2] Cycloaddition. *J. Am. Chem. Soc.* **2021**, 143, 12955-12960.
229. Breysse, M.; Djega-Mariadassou, G.; Pessaire, S.; Geantet, C.; Vrinat, M.; Pérot, G.; Lemaire, M., Deep desulfurization: reactions, catalysts and technological challenges. *Catal. Today* **2003**, 84, 129-138.
230. Dinca, L. E.; Fu, C.; MacLeod, J. M.; Lipton-Duffin, J.; Brusso, J. L.; Szakacs, C. E.; Ma, D.; Perepichka, D. F.; Rosei, F., Unprecedented transformation of tetrathienoanthracene into pentacene on Ni (111). *ACS Nano* **2013**, 7, 1652-1657.

231. Dinca, L. E.; MacLeod, J. M.; Lipton-Duffin, J.; Fu, C.; Ma, D.; Perepichka, D. F.; Rosei, F., Tailoring the reaction path in the on-surface chemistry of thienoacenes. *J. Phys. Chem. C* **2015**, 119, 22432-22438.
232. Borca, B.; Michnowicz, T.; Pétuya, R.; Pristl, M.; Schendel, V.; Pentegov, I.; Kraft, U.; Klauk, H.; Wahl, P.; Gutzler, R.; Arnau, A. s.; Schlickum, U.; Kern, K., Electric-field-driven direct desulfurization. *ACS Nano* **2017**, 11, 4703-4709.
233. Brusso, J. L.; Hirst, O. D.; Dadvand, A.; Ganesan, S.; Cicoira, F.; Robertson, C. M.; Oakley, R. T.; Rosei, F.; Perepichka, D. F., Two-dimensional structural motif in thienoacene semiconductors: Synthesis, structure, and properties of tetrathienoanthracene isomers. *Chem. Mater.* **2008**, 20, 2484-2494.
234. Smerdon, J.; Bode, M.; Guisinger, N.; Guest, J., Monolayer and bilayer pentacene on Cu (111). *Phys. Rev. B* **2011**, 84, 165436.
235. Walen, H.; Liu, D.-J.; Oh, J.; Lim, H.; Evans, J. W.; Kim, Y.; Thiel, P. A., Reconstruction of steps on the Cu (111) surface induced by sulfur. *J. Chem. Phys.* **2015**, 142, 194711.
236. Ma, C.; Xiao, Z.; Lu, W.; Huang, J.; Hong, K.; Bernholc, J.; Li, A.-P., Step edge-mediated assembly of periodic arrays of long graphene nanoribbons on Au (111). *Chem. Commun.* **2019**, 55, 11848-11851.
237. Samec, J. S.; Bäckvall, J.-E.; Andersson, P. G.; Brandt, P., Mechanistic aspects of transition metal-catalyzed hydrogen transfer reactions. *Chem. Soc. Rev.* **2006**, 35, 237-248.
238. Colazzo, L.; Mohammed, M. S.; Dorel, R.; Nita, P.; Fernández, C. G.; Abufager, P.; Lorente, N.; Echavarren, A. M.; De Oteyza, D. G., On-surface synthesis of heptacene on Ag (001) from brominated and non-brominated tetrahydroheptacene precursors. *Chem. Commun.* **2018**, 54, 10260-10263.
239. Jacobberger, R. M.; Arnold, M. S., High-performance charge transport in semiconducting armchair graphene nanoribbons grown directly on germanium. *ACS Nano* **2017**, 11, 8924-8929.
240. Saraswat, V.; Jacobberger, R. M.; Arnold, M. S., Materials Science Challenges to Graphene Nanoribbon Electronics. *ACS Nano* **2021**, 15, 3674-3708.
241. Heyd, J.; Peralta, J. E.; Scuseria, G. E.; Martin, R. L., Energy band gaps and lattice parameters evaluated with the Heyd-Scuseria-Ernzerhof screened hybrid functional. *J. Chem. Phys.* **2005**, 123, 174101.
242. Craats, A. v. d.; Warman, J.; Fechtenkötter, A.; Brand, J. D.; Harbison, M.; Müllen, K., Record charge carrier mobility in a room-temperature discotic liquid-crystalline derivative of hexabenzocoronene. *Adv. Mater.* **1999**, 11, 1469-1472.
243. Aryanpour, K.; Roberts, A.; Sandhu, A.; Rathore, R.; Shukla, A.; Mazumdar, S., Subgap two-photon states in polycyclic aromatic hydrocarbons: Evidence for strong electron correlations. *J. Phys. Chem. C* **2014**, 118, 3331-3339.
244. Kudernac, T.; Lei, S.; Elemans, J. A.; De Feyter, S., Two-dimensional supramolecular self-assembly: nanoporous networks on surfaces. *Chem. Soc. Rev.* **2009**, 38, 402-421.
245. De Feyter, S.; De Schryver, F. C., Two-dimensional supramolecular self-assembly probed by scanning tunneling microscopy. *Chem. Soc. Rev.* **2003**, 32, 139-150.
246. Chen, M.; Goodman, D., The structure of catalytically active gold on titania. *science* **2004**, 306, 252-255.
247. Kolmer, M.; Steiner, A.-K.; Izidorczyk, I.; Ko, W.; Engelund, M.; Szymonski, M.; Li, A.-P.; Amsharov, K., Rational synthesis of atomically precise graphene nanoribbons directly on metal oxide surfaces. *Science* **2020**, 369, 571-575.
248. de Oteyza, D. G.; García-Lekue, A.; Vilas-Varela, M.; Merino-Díez, N.; Carbonell-Sanromà, E.; Corso,

M.; Vasseur, G.; Rogero, C.; Gutián, E.; Pascual, J. I., Substrate-independent growth of atomically precise chiral graphene nanoribbons. *ACS Nano* **2016**, 10, 9000-9008.

249. Di Giovannantonio, M.; El Garah, M.; Lipton-Duffin, J.; Meunier, V.; Cardenas, L.; Fagot Revurat, Y.; Cossaro, A.; Verdini, A.; Perepichka, D. F.; Rosei, F.; Contini, G., Insight into organometallic intermediate and its evolution to covalent bonding in surface-confined Ullmann polymerization. *ACS Nano* **2013**, 7, 8190-8198.

APPENDIX

Publications during the Ph.D.

1. **P. Ji**, D. Dettmann, Y. Liu, G. Berti, D. Cui, O. MacLean*, D. F. Perepichka*, L. Chi* and F. Rosei*, Tandem Desulfurization/C-C Coupling Reaction of Tetrathienylbenzenes on Cu(111): Synthesis of Pentacene and New Exotic Ladder Polymer, *ACS Nano*, **2022**
2. **P. Ji**, O. MacLean*, G. Galeotti, D. Dettmann, G. Berti, K. Sun, H. Zhang, F. Rosei*, L. Chi*, Oxygen-Promoted Synthesis of Armchair Graphene Nanoribbons on Cu (111), *Sci. China Chem.*, **2021**, 64, 636-641.
3. **P. Ji**, G. Galeotti, F. De Marchi, D. Cui, K. Sun, H. Zhang,*, G. Contini, M. Ebrahimi, O. MacLean*, F. Rosei*, L. Chi*, Oxygen-Induced 1D to 2D Transformation of On-Surface Organometallic Structures, *Small*, **2020**, 16, 2002393.
4. K. Sun‡, **P. Ji‡ (co-first author)**, J. Zhang, J. Wang, X. Li, X. Xu, H. Zhang*, L. Chi* On-Surface Synthesis of 8-and 10-Armchair Graphene Nanoribbons, *Small*, **2019**, 15, 1804526.
5. K. Sun, A. Chen, M. Liu, H. Zhang*, R. Duan, **P. Ji**, L. Li, Q. Li, C. Li, D. Zhong, K. Müllen, L. Chi*, Surface-Assisted Alkane Polymerization: Investigation on Structure–Reactivity Relationship, *J. Am. Chem. Soc.*, **2018**, 140, 4820-4825.
6. Q. Wang, A. Franco-Cañellas, **P. Ji**, C. Bürker, R. Wang, K. Broch, P. K. Thakur, T. Lee, H. Zhang, A. Gerlach, L. Chi*, S. Duhm*, F. Schreiber*, Bilayer Formation vs Molecular Exchange in Organic Heterostructures: Strong Impact of Subtle Changes in Molecular Structure, *J. Phys. Chem. C*, **2018**, 122, 9480-9490.
7. K. Sun, **P. Ji**, H. Zhang*, K. Niu, L. Li, A. Chen, Q. Li, K. Müllen, L. Chi*, A new on-surface synthetic pathway to 5-armchair graphene nanoribbons on Cu (111) surfaces, *Faraday Discuss.*, **2017**, 204, 297-305.
8. H. Zhang, Z. Gong, K. Sun, R. Duan, **P. Ji**, L. Li, C. Li, K. Müllen, L. Chi*, Two-dimensional chirality transfer via on-surface reaction, *J. Am. Chem. Soc.*, **2016**, 138, 11743-11748.

Contributions to the international conferences during the Ph.D.

2019, 12, 1-6, Boston, Massachusetts, USA. *2019 MRS Fall Meeting & exhibit*

Title (oral): Oxygen-Induced 1D to 2D Transformation of On-Surface Organometallic Structures

2018, 07, 8-11, Montreal, QC, Canada. *EMP 18, Energy, Materials and Photonics 18*

Title (poster): Electronic Structures of Surface-Supported 3P Sub-Family Graphene Nanoribbons

2017, 08, 29-31, Beijing, China. *ChinaNANO 2017, The 7th International Conference on Nanoscience & Technology*

Title (poster): Electronic Structures of Surface-Supported 3P Sub-Family Graphene Nanoribbons.